Phd thesis

to obtain the title of

Docteur de l'université Pierre et Marie Curie, spécialité physique
Dottore di ricerca dell'università del Salento in bio-molecular nanotechnologies

by

Mathieu Manceau

Single CdSe/CdS dot-in-rods fluorescence properties





Defended on December 03, 2014, in front of the jury composed of

Philippe Tamarat	Reviewer
Marco Genovese	Reviewer
Catherine Schwob	Examinator
Luigi Carbone	Examinator
Massimo De Vittorio	PhD advisor
Alberto Bramati	PhD advisor

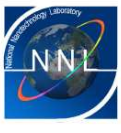







Acknowledgments

This work has been realized at the laboratoire Kastler Brossel (Paris, France) and the National Nanotechnologies Laboratory (Lecce, Italy). First I would like to thank Paul Indelicato and Antoine Heidmann, successiveley at the head of the LKB, for welcoming me in such a great working environment.

I thank my supervisor Alberto Bramati for his guidance during these three years of work. On top of helping me in the every day laboratory job, I am grateful for the many opportunities he gave me; I was able to work on so many different projects involving different laboratories (in Italy, in Germany, in France). I met a tremendous amount of researchers and PhD students during this thesis, this gave me the opportunity to see different aspects and vision of the scientific working process. This attests the great confidence Alberto has in his PhD students and I am deeply grateful for this. Elisabeth Giacobino should also be acknowledged as she played a major role in me being involved in many of these projects. I am also very grateful for the interest Elisabeth demonstrated during these three years of work and her precious help during the articles writing process.

A special thanks to Stefano Vezzoli with whom I shared the experiment for about half my PhD. Many of the results presented in this thesis can be traced back to his precious work. Thanks a lot Stefano for this among many, many other things!

I also had the chance to work at the end of my PhD with Quentin Glorieux who joined the group. I thank him for the great interest he showed for my work, his motivation, the careful reading and the various important inputs he gave to this manuscript.

I thank also Jean-Pierre Hermier for being available for discussions on the physics of nanocrystals at Versailles or in conference, as well as for giving me experimental devices when necessary. The same goes for Louis Biadala who was always motivated to discuss results and problems on the physics of nanocrystals for the short amount of time we met here and there. I am also grateful towards our colleagues at INSP, Agnès Maître, Laurent Coolen and Clotilde Lethiec for discussions and their work on the polarization that greatly contributed to the results presented in this manuscript.

I would like to thank all the members of the group: Thomas Boulier for sharing with me in such a good atmosphere the day to day work during these three years and a great number of noteworthy afterwork apéro, dinner, and parties! Romain Hivet, Emiliano Cancellieri, Godefroy Leménager, Clément Godfrin, the space team Jean-Michel Villain and Salma Aziam, Feng Li, Arthur Trifonov.

My (unfortunately short) stays in Italy were fantastics. I thank Massimo De Vittorio and Ferruccio Pisanello for welcoming me so nicely in Lecce and for their inputs to this work. Needless to say that this thesis would be nothing without somebody synthesizing

nanocrystals, so I am grateful to Luigi Carbone for his reactivity in answering questions and sending new samples. A special thanks to Gianni Lerario with whom I spent some great times in Lecce and Puglia.

I was lucky during this thesis to collaborate with many researchers. I would like to thank Markus Sondermann, Maria Chekhova and Gerd Leuchs for welcoming me in Erlangen and for giving me the opportunity to work on new experiments. I thank also Christophe Couteau, Wei Geng, Emmanuelle Lacaze and Laurent Pelliser.

Finally, I am grateful to so many people outside work. Among them I would like to acknowledge Simon for keeping me in a good physical condition during these three years thanks to our weekly chatting/running meeting, his various advices on how to keep a good mental health during the PhD and some outstanding nightlife moments and Karaoke singing together! The FC Marx Dormoy also contributed to my good fitness at the end of my PhD, I thank its president for that and various good advices on how to run a PhD. I thank also another member of the football team, Julien, for the nice BBQs in Bagnolet and the couple of amazing Jazz concerts. I am grateful to all the couples that had the great idea to get married during this last year. Among them a special thanks to Martin and Alena, we spent a wonderful time in Marseille as well as in New York.

I thank the family Tuambilangana for their support and all the amazing weekends in Cherbourg, always a source of rest, fun, good times and way back with kilograms of fresh products! Many thanks to Kasia and Jean-Michel for all the good things we have done together during this three years close from each other. How lucky we were to be so close for once! Jean you are always a source of inspiration and motivation for me, thanks for all. I thank my parents for their kindness, help and support during all this time, you are wonderful. My thoughts and feelings go finally to you my beloved Christelle, my source of motivation along the way, many thanks for your support during these years.

Contents

Introduction **11**

I CdSe/CdS colloidal nanocrystals **15**

Introduction . . . 15

I.1 Electronic structure of CdSe nanocrystals . . . 16

I.1.1 From bulk CdSe to quantum confined nanocrystals . . . 17

I.1.2 Fine structure of the band-edge exciton . . . 25

I.2 Optical transitions and relaxation processes . . . 30

I.2.1 Highly excited states and absorption . . . 31

I.2.2 Non-radiative relaxation processes in nanocrystals . . . 31

I.2.3 Quantum states and radiative relaxation . . . 37

I.2.4 Quantum yields . . . 39

I.3 Core/shell nanocrystals . . . 39

I.3.1 Classification of core/shell heterostructures . . . 40

I.3.2 CdSe/CdS nanocrystals: quasi-type II heterostructures and wave-function engineering . . . 42

I.3.3 Nanorods . . . 43

I.3.4 CdSe/CdS dot-in-rods . . . 47

I.4 Studied Samples . . . 57

I.4.1 Samples geometry . . . 58

I.4.2 Samples spectra . . . 59

Conclusion . . . 60

II Experimental setup and methods **63**

Introduction . . . 63

II.1 Setup description . . . 64

II.1.1 Standard microscopy setup . . . 64

II.1.2 Polarization microscopy . . . 67

II.1.3 Defocused microscopy . . . 73
II.1.4 Collection efficiency . . . 74
II.2 Measurements and data processing . . . 76
II.2.1 Sample preparation . . . 76
II.2.2 Noise . . . 76
II.2.3 Excitation power and saturation curves . . . 77
II.2.4 Data acquisition and processing . . . 81
Conclusion . . . 84

III CdSe/CdS dot-in-rods blinking statistics 85
Introduction . . . 85
III.1 Blinking: a review . . . 85
III.1.1 Two types of blinking . . . 87
III.1.2 Reduced blinking . . . 93
III.2 Dot-in-rods blinking statistics . . . 96
III.2.1 Type A blinking . . . 96
III.2.2 Blinking timescales and statistics . . . 107
Conclusion . . . 115

IV CdSe/CdS dot-in-rods photon statistics 117
Introduction . . . 117
IV.1 Photon statistics theory . . . 117
IV.1.1 A general approach to the photon statistics . . . 118
IV.1.2 Photon statistics and nanocrystals . . . 122
IV.2 Single photon emission: exciton and negative trion . . . 126
IV.2.1 Saturation and exciton quantum yield . . . 126
IV.2.2 Trion quantum yield and electron delocalization . . . 127
IV.3 Two photon emission: biexciton and charged biexciton . . . 129
IV.3.1 Dot-in-rod geometry and biexciton quantum yield . . . 129
IV.3.2 Blinking and charged biexciton emission . . . 129
IV.4 Measuring the photon statistics with an ICCD camera . . . 139
Conclusion . . . 145

V CdSe/CdS dot-in-rods emission polarization 147
Introduction . . . 147
V.1 Dot-in-rods polarization: an overview . . . 147
V.1.1 Ensemble measurement methods . . . 148
V.1.2 Dielectric effects . . . 148

V.1.3 Fine structure . . . 151
V.1.4 Polarization and c axis . . . 151
V.2 Polarization of the emission and geometrical parameters . . . 153
V.2.1 Measurements procedure . . . 153
V.2.2 Measurements . . . 153
V.3 Discussion . . . 155
V.3.1 Comparison with the literature . . . 155
V.3.2 A model for the emission polarization . . . 155
V.3.3 Simulations of the emission polarization . . . 161
Conclusion . . . 169

VI Coupling nanocrystals to devices: towards integrated nanophotonics 171
Introduction . . . 171
VI.1 Coupling nanocrystals to ZnO nanowires . . . 171
VI.1.1 System description . . . 172
VI.1.2 Passive/Active excitation . . . 174
VI.1.3 Losses and excitation efficiency . . . 175
VI.1.4 Outlook . . . 177
VI.2 Orientation of CdSe/CdS dot-in-rods using liquid crystals . . . 177
VI.2.1 Orientation and positioning of nanoparticles . . . 177
VI.2.2 The liquid crystal samples . . . 178
VI.2.3 Polarization microscopy of dot-in-rods inside a liquid crystal . . . 179
VI.2.4 Outlook . . . 181
Conclusion . . . 182

Conclusions and outlook 185

A CdSe/CdS dot-in-rods emission at cryogenic temperature 189

B Coupling CdSe/CdS dot-in-rods to a parabolic mirror 193

Introduction

Nanometer size materials often present specific peculiarities, these peculiarities cannot be observed with bulk pieces of the same material. Reducing the size of a material in one dimension up to the point where the charge carriers are confined in a smaller region than their De Broglie wavelength leads to a dramatic change in the electronic and optical properties. The last decades, technological progress in the semiconductor industry has lead to a great control of the materials down to the nanometer scale and size effects are now currently studied by scientists.

Systems for which the charge carriers can be confined in the three dimensions of space are called quantum dots. Until twenty years ago one of the most spread and performing methods for building nanocrystals was the epitaxial growth of the so-called Stranski-Krastanov quantum dots. Due to the lattice constant mismatch between two crystalline materials, epitaxial growth of a given material on a different material slab can result in the spontaneous formation of nanometer size islands that can confine the charge carriers. These self-assembled structures are usually pyramidal or lens shaped, with a lateral size in the range of $10-20$ nm and vertical dimensions of few nanometers. These structures, although made of thousands of atoms, are characterized by discrete atomic-like energy levels. This discrete energy states arrangement is completely different from the usual continuum of energy states characterizing the same materials with larger dimensions. Another category of quantum dots made by chemical methods is now thorough-fully studied in the literature. First studies in the eighties by A. I. Ekimov [1] and L. E. Brus [2] have shown the possibility to observe quantum size effects by chemical synthesis of nanoparticles. In the mid nineties, new synthesis procedure lead to higher sample qualities in terms of size control, dispersivity [3] and photoluminescence quantum yields [4]. Synthesis of nanometer size crystals in solution forming the so called colloidal suspension is now a very mature field of research, to the point where many applications for such materials are under study.

Colloidal nanocrystals Colloidal nanocrystals have emerged as interesting light emitters in various fields of applications. Biology is maybe the most successful domain of

applications of colloidal nanocrystals. Nanocrystals are nowadays stable fluorophores, with a narrow emission spectra at room temperature that can be synthetically tuned. The emission stability is particularly important in biological experiments, where photobleaching is a limiting factor for imaging [5]. The broad absorption spectrum of colloidal nanocrystals implies that different samples with different emission wavelengths can be excited at the same time by the same source, allowing for simultaneous, multiplexed imaging of biological samples [6]. The possibility to change the ligands at the nanocrystal surface is also of great importance in biology for sensing purposes [7]. In optics, they are now currently used as light emitters [8] for light emitting diode devices, photodetectors [9] or in solar cell systems [10]. Nanocrystals have also been demonstrated to be a gain medium for lasing [11]. These light emitters can also display very low multiexciton emission probabilities implying that single particles could be used as single photon or few photon sources [12, 13] at room temperature for quantum information protocols [14].

Among colloidal nanocrystals, Cadmium Selenide (CdSe) is probably the most studied material for its optical properties. By changing the size of the nanocrystals, CdSe emission can cover almost all the visible spectrum. The synthesis of this material give rise to size homogeneous, high quality samples. The first studies of single spherical CdSe nanoparticles revealed the emission properties hidden by previous ensemble measurements, such as emission intermittency [15] (blinking) or spectral diffusion [16]. Reducing these effects has been an intense research topic in the community in order to obtain fluorescent particles with a steady emission rate and emission line. Another drawback of spherical CdSe nanocrystals is their poor degree of polarization [17] and lack of defined orientation when deposited on a substrate.

The development of new synthesis method has progressively helped in overcoming these drawbacks. First, CdSe nanocrystals were capped by a thin spherical layer of another semiconductor material, Zinc Sulfide (ZnS) [4, 18], to form heterostructures. An increase in the photoluminescence quantum yield was observed. Later on, capping CdSe nanocrystals with thick shells of Cadmium Sulfide (CdS) has considerably enhanced the average emission rate [19] by reducing the emission intermittency. In the meantime, synthesis of elongated particles with a cylindrical shape, called nanorods, opened the way to shape control of colloidal nanocrystals. Tuning the shape can change the optical properties of the emitter: CdSe nanorods have for example a high degree of linear polarization [20] conversely to spherical CdSe particles. New heterostructures are now synthesized which show various specific emission properties. Among others, we can cite dot-in-bulks [21] that are spherical CdSe nanocrystals embedded into a large bulk-like CdS shell, or dot-in-plates [22] that are spherical CdSe nanocrystals embedded into a quantum-well-like CdS shell [23].

This thesis joins the recent efforts in tuning the properties of nanocrystals to overcome drawbacks such as emission intermittency, low polarization of emission and starts coupling these emitters with photonic devices. We concentrate our study on a specific type of CdSe/CdS nanocrystals called dot-in-rods, they are made of a CdSe spherical core embedded in a rod-like CdS shell [24, 25].

Subject of this thesis In this thesis we fully characterize the fluorescence properties of CdSe/CdS dot-in-rods at room temperature.

The *first chapter* of this manuscript reviews the theoretical background on colloidal nanocrystals, focusing on the optical properties emerging from the strong quantum confinement. The various phenomena involved in the relaxation of the charge carriers after excitation are introduced. We finish the chapter by a review of Cadmium Selenide/Cadmium Sulfide dot-in-rods specificities. In the *second chapter* we detail the experimental setup and methods used throughout this thesis. We explain how we can efficiently collect the photoluminescence of a single nanocrystal with a confocal microscope. The information we can acquire during a measurement run are also presented together with the methods used to process the data. We also present how we can characterize a sample prior to any specific measurement, more particularly how to determine precisely the saturation of a given sample.

The *third chapter* addresses the blinking phenomenon. First we characterize the blinking of CdSe/CdS dot-in-rods. We demonstrate that for the dot-in-rods studied in this manuscript two states of emission are involved in the emission process, photoionization of the emitter via Auger relaxation processes between multiple carriers being responsible of the emission intermittency. We show that the switching between the two states happens on timescales of the order of milliseconds. The *fourth chapter* presents the characterization of the CdSe/CdS dot-in-rods photon statistics taking into account the emission intermittency. The effects of the geometry of the sample are presented. The possibility of tuning the photon statistics by changing the hole or electron confinement is clearly demonstrated. The end of the chapter is dedicated to an original experiment to determine the photon statistics based on a intensified CCD camera. In *chapter five*, the analysis of the fluorescence properties is focused on the polarization properties: the influence of the geometry on the degree of linear polarization of the emission is investigated.

Finally in the *last chapter* we present two experiments where we couple dot-in-rods with different structures. We demonstrate that we can successfully excite a single emitter using a Zinc Oxyde nanowire. Another experiment shows the possibility to orientate single CdSe/CdS dot-in-rods using control defects formed in liquid crystal structures.

We also briefly present preliminary results on cryogenic measurements and the coupling of dot-in-rods with a parabolic mirror in the appendix.

Chapter I
CdSe/CdS colloidal nanocrystals

Introduction

Reducing the size of semiconductor to nanometer scale can change dramatically its electronic and optical properties compared to the bulk material. In this chapter we review the optical properties of colloidal Cadmium Selenide (CdSe) nanocrystals for which the spatial confinement of the charge carriers happens in the three dimensions. CdSe is the most studied colloidal nanocrystal material owing to its easy and high quality synthesis, together with the fact that it can cover almost the whole visible spectrum. With the progress made at the beginning of the 90's on the synthesis and sample quality [3], the study of their physical properties together with the possible applications started. Later on, the addition of a shell around CdSe nanocrystals to form heterostructures considerably improved the optical properties [18]. The last years, the possibility to engineer shape, size and material interfaces with heterostructures offered a way to modify the electronic and optical properties of CdSe nanoparticles.

In this chapter we first present the electronic structure of bare CdSe spherical nanocrystals. We then consider the different relaxation processes existing in such nanostructures. Once a comprehensive overview of the phenomena leading to the emission of photons by CdSe nanocrystals is achieved, we consider the effects of the addition of a shell surrounding the CdSe core. We finish with a review on the object of this manuscript: CdSe/CdS dot-in-rods made of a CdSe spherical core capped with a rod-like Cadmium Sulfide (CdS) shell.

Synthesis

Various synthesis of nanocrystals were developped since the early eighties: synthesis in solid materials and doped glass [1]; synthesis in liquid via the formation of colloidal solutions [26] were also investigated. A colloidal nanocrystal solution is a suspension of nanometer size crystals stabilized in solution by a layer of organic ligands adsorbed

to its surfaces. CdSe nanocrystals are nowadays produced by organo-metallic synthesis [3]. This synthesis delivers size controlled nanocrystal with a small dispersion and high crystallinity. The colloidal solution obtained presents also several advantages. Being in a liquid solvent, nanocrystals can be easily manipulated: they can be transferred from one solvent to another, embedded in different materials or diluted in order to be observed individually.

In section I.3.4 we detail the specific synthesis used to fabricate the dot-in-rods studied in this work.

Crystal structure

High resolution transmission electron microscopy images reveal that CdSe nanocrystals display a hexagonal crystal structure, more precisely a wurtzite structure [4], like the bulk material. Wurtzite crystal is an anisotropic structure with the so called c axis that is not equivalent to the two remaining axis. This asymmetry of the structure can be used to grow CdSe nanorods for examples whose axis coincides with the c axis of the crystallographic structure [27]. In general, even if meant to be spherical, CdSe nanocrystals are slightly elongated along the c axis [4], with an ellipticity of the order of 10%[1].

A cubic structure called zinc-blende has also been observed for CdSe nanocrystals depending on the synthesis [28, 29]. The three axis of the crystals are equivalent in this case. Polytypism is also possible, such that both structures appear in the same nanocrystal [30].

In the following, we will consider CdSe nanocrystals with a wurtzite structure as it is precisely the intrinsic asymmetry of this structure that is used to grow rod-like CdS shell around the spherical CdSe core to obtain the so-called dot-in-rods particles [25, 31]. Fig.I.1b is a schematics of a CdSe/CdS dot-in-rod with typical geometrical parameters taken from samples studied in this thesis. The long molecules around the nanocrystals are the ligands that passivate the surface and ensure a colloidal suspension of nanocrystals in solution. Fig.I.1c is a view in a plane perpendicular to the c axis, the hexagonal crystal structure in this plane is visible. Fig.I.1a is a transmission electron microscope (TEM) image of a dot-in-rod sample.

I.1 Electronic structure of CdSe nanocrystals

To understand the electronic structure of CdSe nanocrystals, one can start from the electronic properties of the bulk material and then take into account the quantum size

[1]This corresponds to an aspect ratio of 1.1 for an ellipsoid of revolution.

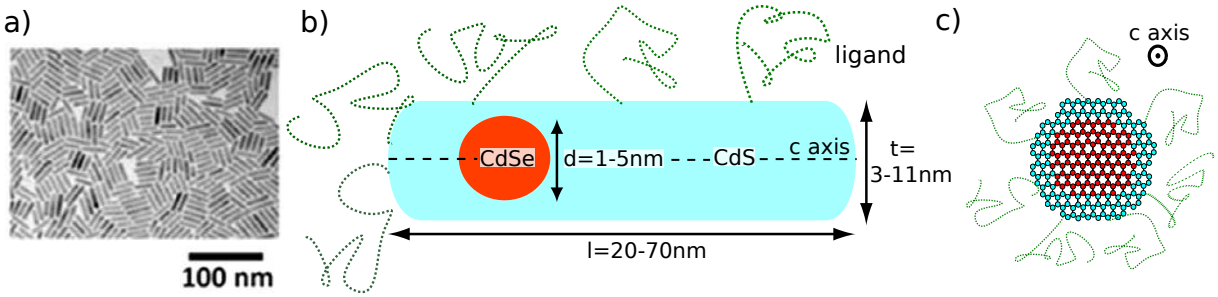

Figure I.1: TEM image and schematics of CdSe/CdS dot-in-rod studied in this thesis with its ligands. *a)TEM image of a CdSe/CdS dot-in-rod sample studied in this manuscript. b)Typical spherical CdSe core can be grown with a diameter d ranging from 1 to 5 nm. The CdS rod shell can have a thickness t going from 3 to 11 nm and length l from 20 to 70 nm. The c axis of the wurtzite crystal structure is oriented along the rod axis as it constitutes the preferential growth axis. The long molecules around the shell symbolize the ligands used to passivate the surface and to ensure the colloidal nature of the solution. c) View in a plane perpendicular to the c axis of the dot-in-rod, the hexagonal lattice of the wurtzite crystal structure is depicted.*

effect [32, 33]. The other way around, treating the nanocrystals as a big molecule made of thousands of atoms is also possible [34–36] but less intuitive in terms of how to understand the arising energy spectrum. By quantum size effect, one means that if the size of the semiconductor structure becomes comparable to or smaller than the De Broglie wavelength of the charge carriers (electrons and holes) for this specific material, then the charges start to feel the finite size of the material: they are confined inside the material. The confinement changes dramatically the energy states of the carriers. Among quantum confined systems, CdSe nanocrystals are part of the quantum dots family. They confine the charge carriers in the three dimensions of space. In this case, the energy spectrum moves from a continuum of allowed states for the bulk material to an atomic-like behavior as the bulk bands become quantized. This discretization of the energy level happens only because of the finite size as the material remains structurally identical to the bulk crystal.

I.1.1 From bulk CdSe to quantum confined nanocrystals

Bulk CdSe band structure

Cadmium Selenide is a II-VI direct bandgap semiconductor. Dispersion relations for the valence band (VB) and conduction band (CB) have a maximum and minimum respectively in $k = 0$ where they can be approximated by parabolic dispersions:

$$E_{VB} = \hbar k^2 / 2m_h^*,$$

$$E_{CB} = E_g + \hbar k^2 / 2m_e^*.$$

m_h^* and m_e^* are the hole and electron effective masses considering they behave as free particles with a parabolic dispersion. The effective mass then simply models the complicated periodic potential felt by the carrier inside the crystal lattice. E_g is the bandgap of the material ($E_g = 1.84$ eV$\simeq$ 690 nm for CdSe [33]).

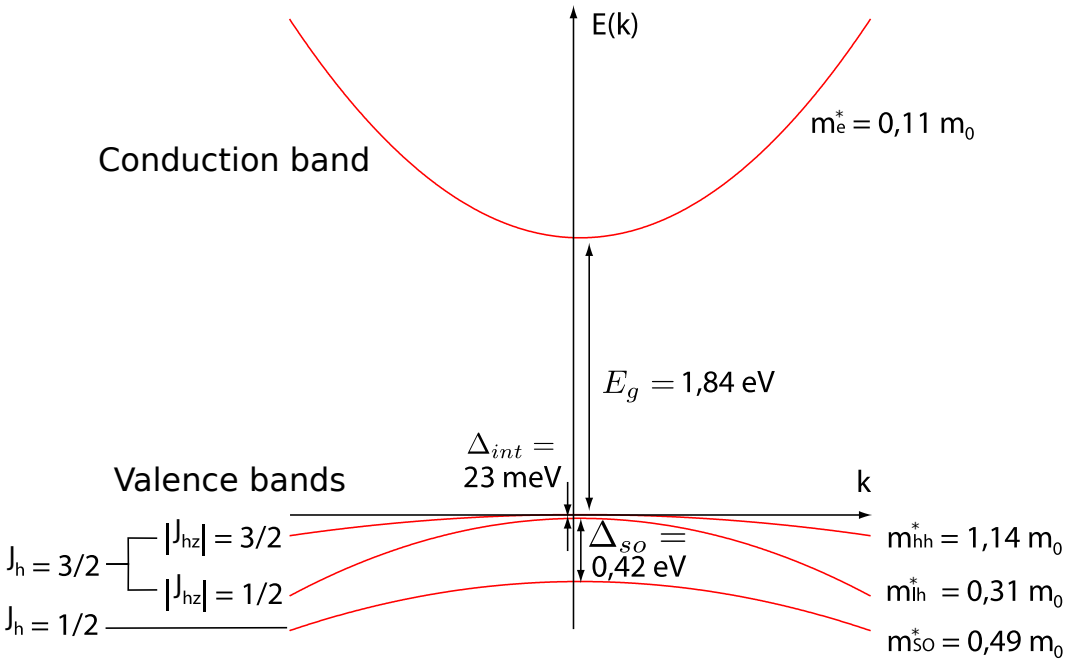

Figure I.2: Bulk CdSe band structure. *Numerical values taken from [33, 37].*

Cadmium ($[Kr]4d^{10}5s^2$) atoms share their $5s$ electrons with Selenium ($[Ar]3d^{10}4s^24p^4$). The conduction band is then made of the empty Cadmium $5s$ orbitals. It is a twofold degenerate band [33] because of the electrons spin. It is well described by the effective mass approximation (effective mass $m_e^* = 0.11m_0$, with m_0 the free electron mass).

The valence band is constituted of the $4p$ orbitals of Selenium filled with the $5s$ Cadmium electrons. It has an orbital angular momentum l_h of 1 as it is essentially made of the more energetic p orbitals. The valence band is sixfold degenerate at $k = 0$ [33]. The sixfold degeneracy is partly lift by the spin-orbit coupling. To consider this effect, the good quantum number to study is the hole total angular momentum $J_h = l_h + s_h$, the sum of the orbital and spin contribution to the angular momentum. J_h is either equal to 1/2 or 3/2, this gives two distinct bands, $J_h = 1/2$ is called the split-off-hole band (SO) and separated by $\Delta_{SO} = 0.42$ eV at $k = 0$ from the higher $J_h = 3/2$ band. This last one is further split for $k \neq 0$ into two sub-bands called the heavy-hole (hh) and light-hole (lh) sub-bands with different associated effective masses owing to different projections J_{hz} of J_h onto the z axis ($|J_{hz}| = 1/2$ or $3/2$). Furthermore, the asymmetry of the wurtzite structure induces an intrinsic crystal field that splits the heavy-hole and light-hole sub-bands by an amount of $\Delta_{int} = 23$ meV. Under the effective mass approximation, effective

masses can be attributed to each of the valence band, m^*_{so}, m^*_{hh} and m^*_{lh} for the split-off, heavy-hole and light-hole bands respectively. Fig.I.2 illustrates the bulk CdSe band structure.

Confinement

After absorption of a high energy photon by a semiconductor material, an exciton, i.e. bound electron-hole pair[2], is created and can be described as a hydrogen-like atom. The binding between the electron and the hole is ensured by the Coulomb interaction. A Bohr radius can be defined for this particle:

$$r_B = \epsilon \frac{m_0}{\mu} r_0, \tag{I.1}$$

with r_0 the Bohr radius of the hydrogen atom, ϵ the material dielectric constant, m_0 the electron rest mass and μ the reduced mass of an electron-hole pair. For CdSe material, the Bohr radius is $r_B \approx 5.6$ nm.The energy associated with the Coulomb interaction evolves as $1/r$, r being the distance between the two particles, while the confinement energy (as will be demonstrated in the following paragraphs) evolves as $1/a^2$, with a the confinement radius (for a spherical nanocrystal a is the radius). One way to picture the fact that an energy can be ascribed to the confinement is that according to the Heisenberg uncertainty principle the momentum of a particle, so its energy, increases if its position becomes well defined. Different confinement regimes are defined by comparing the confinement size with the exciton Bohr radius:

- The weak confinement regime: $r_B < a$. The Coulomb interaction is the dominant interaction and the quantum confinement is treated as a perturbation. This is typically the case for self-assembled quantum dots owing to their large size.
- The strong confinement regime: $r_B > a$. The Coulomb interaction is treated as a perturbation while the confinement is fully taken into account. This is the case for the CdSe nanocrystals.

Using the effective mass approximation previously described, the electronic structure of CdSe nanocrystals can be calculated. We suppose that the parabolic band model for the valence bands and conduction band as above described for the bulk material is still valid in the case of a nanocrystal. This is the case if the nanocrystal diameter is much larger than the lattice constant. For CdSe crystal, the lattice constant is $p = 0.43$ nm such that the approximation is meaningful for nanometer size crystals. Then the charge carriers

[2]We will use the terms of excitons and electron-hole pair indifferently in all this manuscript.

are evolving as free particles with a given effective mass inside a spherical potential well as depicted on Fig.I.3 for the specific case of a CdSe/CdS dot-in rod. For the following calculations the quantum well where the electron and hole are confined will be considered as infinite, a valid hypothesis for the lowest energy level. The case of a finite well has been treated in literature [38] with the consequences of a decrease of the confinement energy and a slight spreading of the wave functions outside the well.

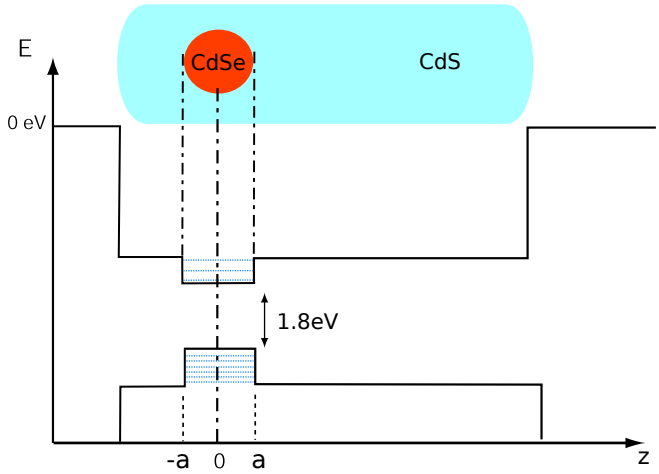

Figure I.3: Potential profile of a CdSe/CdS dot-in-rod.

According to the Bloch's theorem, the electron and hole wavefunctions inside a bulk crystal can be written as:

$$\Psi_{nk}(\vec{r}) = u_{nk}(\vec{r}) \exp(i\vec{k}.\vec{r}), \tag{I.2}$$

where u_{nk} is a function of the crystal lattice periodicity that gives the wavefunction variations on a lattice site, while the other term is a plane wave term, it accounts for a larger scale dependency. k is the wavevector associated to the particle and the index n is associated to a specific band (conduction or valence band). Inside a nanocrystal, an electron or a hole wavefunction in a given band can be written as a linear combination of Bloch functions:

$$\Psi(\vec{r}) = \sum_k C_{nk} u_{nk}(\vec{r}) \exp(i\vec{k}.\vec{r}), \tag{I.3}$$

with the expansion coefficients C_{nk} satisfying the limit conditions of the infinite well problem. In practice, the Bloch's functions are weakly dependent on k because the nanocrystal size a is much larger than the lattice constant p as already stated. In this case $u_{nk} \approx u_{n0}$ and the wavefunction can be simplified:

$$\Psi(\vec{r}) = u_{n0}(\vec{r}) \sum_k C_{nk} \exp(i\vec{k}.\vec{r}) = u_{n0}(\vec{r})\psi(\vec{r}). \tag{I.4}$$

$\psi(\vec{r})$ is called the envelop function. It describes the wavefunction at the nanocrystal scale and satisfies the Schrödinger equation. The confinement effects are described by the envelop function.

Electron confinement

Solving the Schrödinger equation for the envelop function $\psi(\vec{r})$ of an electron inside an infinite potential well yields the following energies [32, 33]:

$$E_e^{nl} = \frac{\hbar k_{nl}^2}{2m_e^*}, \tag{I.5}$$

with k_{nl} the quantized values of k due to the finite size of the system. The envelop function solutions are hydrogen-like orbitals with n the radial quantum number, l and m the angular quantum numbers. By analogy with the atomic case, the electron state is written nL_e and the orbitals L are called S, P....The first quantized electronic state is then called $1S_e$ and as the following energy:

$$E_e^{1S} = \frac{\hbar \pi^2}{2m_e^* a^2}, \tag{I.6}$$

with $k_{10} = \pi/a$. It is twofold degenerate with respect to the spin projection, with a spherical symmetry ($1S$ state).

Hole confinement

The solutions for a hole in an infinite potential well are less straightforward to derive because of the complex valence band structure of bulk CdSe described above. The Hamiltonian of the problem is called the Luttinger Hamiltonian [33,38,39], it takes into account the sixfold degenerate valence bands and therefore includes the interactions and mixing between these bands necessary to understand the experimental results [40].

Each valence sub-band does not produce its own ladder of hole states, but the hole states come from a mixture of the different valence sub-bands (the three ladders are coupled to each other). Without entering into details, the main result of these considerations is that one should take into account two quantum numbers for this problem: the envelop function orbital angular momentum L coming from the confined particle and the total angular momentum J_h from the underlying atomic basis forming the 3 hole sub-bands described in Fig.I.2. Therefore $F = L + J_h$ is the good quantum number considering

the Luttinger Hamiltonian[3]. For a given F, the hole state is a combination of different envelop orbitals L (more precisely L and $L+2$, this is called "S-D" mixing) and the 3 sub-bands angular moment J_h ("valence band mixture").

The hole energy level are written as follow: nL_F. We just briefly introduce the first hole level which has a total angular momentum $F = 3/2$, it is fourfold degenerate with the corresponding projections $F_z = (-3/2, -1/2, 1/2, 3/2)$. Following the introduced notation, it is called $1S_{3/2}$. A global notation that shows the underlying mixture is: $(F, J_h, L) = (3/2, 3/2, 0), (3/2, 3/2, 2), (3/2, 1/2, 2)$.

This energy state enters into the exciton ground state together with the $1S_e$ state to form the $1S_{3/2}1S_e$ exciton state that is essential for the understanding of the photoluminescence properties of CdSe nanocrystals. This point is detailed below in sections I.1.2 and I.2.3.

Excited states

Fig.I.4 presents results obtained in reference [40] from ensemble measurements on different CdSe nanocrystals samples at cryogenic temperature (10 K).

Fig.I.4a (top) shows an absorption spectrum of a CdSe dots sample of radius $a = 2.8$ nm together with the associated emission spectrum obtained from an excitation at 2.7 eV (467 nm), well above the CdSe bandgap. The absorption spectrum displays discrete absorption features corresponding to the quantized exciton lines as expected from the 3D confinement of the charges. A first strong absorption line is visible at 2.1 eV (600 nm) corresponding to the band-edge $1S_{3/2}1S_e$ exciton, followed by a weaker transition a 100 meV further in the blue. The various lines cannot be fully resolved because of homogeneous and inhomogeneous broadening. The inhomogeneous broadening comes from the size distribution of the sample and the homogeneous broadening comes from the coupling of the excitation with the phonon modes of the crystals still present at 10 K. One can notice that conversely to the absorption spectrum, the emission spectrum (dashed line) is characterized by a single peak slightly red-shifted compared to the first absorption peak. The shift between the first and the second absorption lines depends on the size of the nanocrystal but is always much larger than the thermal energy even at room temperature (~ 25 meV), such that the emission comes only from the $1S_{3/2}1S_e$ state. Even if excited well above this transition, the nanocrystal excitation always relax non-radiatively towards the band-edge exciton before emitting a photon (see section I.2.2). CdSe nanocrystals are thus very appealing light emitters as they have a relatively

[3]The electron levels were just derived from the envelop function considering only the confinement, particle in a sphere model, more complex descriptions exist as for the hole. Nevertheless the electron levels are well approximated by the particle in a sphere description.

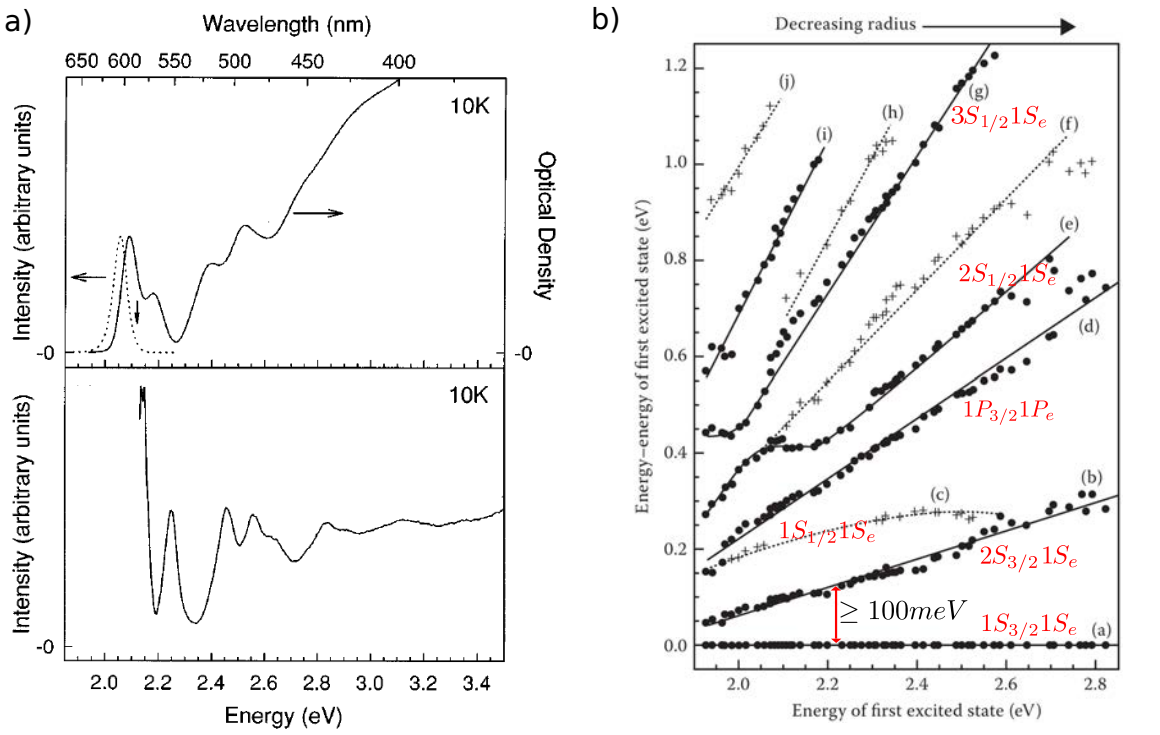

Figure I.4: Absorption, photoluminescence spectra and first exciton transitions energies of CdSe nanocrystals. *a) Graph reproduced from reference [40]. Top: Absorption (solid line) and emission (dashed line) spectra for a sample of radius $a = 2.8$ nm. Bottom: photoluminescence excitation spectrum for the same sample, the emission position corresponding to this measurement is marked by the downward arrow on the absoption spectra above. b) Graph reproduced from reference [40]. The data are derived from photoluminescence excitation spectra of samples with different dot radii at 10 K. Transitions symbolized with dots are strong transitions, easily observable in the absorption spectra while the transitions denoted by crosses are weak transitions. We added the name of a few transitions as explained in [40].*

narrow emission line for a solid state system that is highly tunable with the size of the confinement. The shift between the first absorption peak and the emission peak (referred as Stokes shift) is due to the fine structure [32, 41] of the band edge $1S_{3/2}1S_e$ state. This is explained in the next section I.1.2.

Fig.I.4a (bottom) is a photoluminescence excitation (PLE) spectrum from the same ensemble of nanocrystals. Photoluminescence excitation measurement consists in selecting a spectrally narrow emission window within the inhomogenous emission feature while scanning the frequency of the excitation source. Because excited nanocrystals always relax to their first excited state before emission, the signal that is obtained while scanning the excitation wavelength gives absorption information about the narrow subset of nanocrystals emitting at the wavelength that the experimentalist is looking at. This technique reduces the inhomogeneous broadening compared to a simple absorption spectrum measurement. The absorption spectrum is then much more detailed in this case. Fitting

such spectrum for different samples of various dot radii, Fig.I.4b from reference [40], that presents the first exciton lines energies, is obtained.

The different transitions energy are compared with the first transition energy from the $1S_{3/2}1S_e$ exciton. These measurements contain many information and confirm the complexity of the transitions due to the valence sub-bands structure. The reader should refer to the article by Norris et al. ([40]) for the full details as we will only briefly discuss the figure. As expected, the splitting between the lines increases for smaller dot radii as the confinement is stronger. Very weak transitions that are poorly visible on the PLE measurements are denoted with crosses. The strongest transitions are the $1S_{3/2}1S_e$ and $1P_{3/2}1P_e$ transitions. The oscillator strengths of the interband transitions are proportionals to the electric dipole matrix element P between the vacuum state $|0\rangle$ and the exciton state under consideration $|\Psi_X\rangle$:

$$P = |\langle 0|\vec{\mathcal{E}}.\vec{p}|\Psi_X\rangle|^2, \tag{I.7}$$

with $\vec{\mathcal{E}}$ the electric field operator and $\vec{p}$ the transition dipole moment. In the strong confinement regime the charges are treated separately (Coulomb interaction is treated as a perturbation), P can be expressed by separating the Bloch and envelop function parts of the carriers wavefunctions:

$$P = |p_{cv}|^2 \left| \int \psi_h \psi_e d^3r \right|^2 = |p_{cv}|^2 P_{eh}, \tag{I.8}$$

where p_{cv} is the dipole matrix element for the bulk material and P_{eh} the carriers envelope wavefunctions overlap. Therefore the oscillator strength of a transition depends on the carriers envelop overlap.

As it can be seen on the absorption and PLE curves on Fig.I.4a, it is not possible to distinguish discrete transitions 1 eV above the fundamental interband transition for several reasons:

- the bands are not parabolic anymore but concave implying that energy states are very close to each other,
- the hole density of states is large at higher energies [42],
- the energy states are broadened by their coupling to phonons and overlap [42].

This continuum-like absorption spectrum implies that nanocrystals can easily be excited by various sources. Details about absorption concerning our experiment are given further in section I.2.1.

I.1.2 Fine structure of the band-edge exciton

Photoluminescence of CdSe nanocrystals originates from the band-edge exciton only owing to the fast non-radiative relaxations [43] from higher states. To fully understand the photoluminescence properties, it is necessary to consider the fine structure of the band-edge exciton [32]. The fine structure explains the polarization properties of the emission, the Stokes shift of the emission [44] whose origin was first wrongly attributed to the emission of a surface state [45] and also the very long exciton emission lifetime ($\sim 1\ \mu$s) measured at cryogenic temperatures [45] below $2K$.

Lifted degeneracy

The band-edge exciton is eightfold degenerate (twice with respect to the $1S_e$ electron spin projection and four times with respect to the $1S_{3/2}$ hole total angular momentum projection F_z) for spherical dots with zinc-blende structure. Three effects have to be considered to lift the degeneracy:

- the hexagonal crystal structure,
- the nonsphericity of nanocrystals,
- the electron-hole exchange interaction.

Hexagonal crystal structure When considering a wurtzite structure, the intrinsic asymmetry of this structure generates a crystal field that splits the heavy-hole light-holes sub-bands [46] at $k = 0$ (see section I.1.1 and Fig.I.2). The $1S_{3/2}$ hole state is split in two twofold degenerate sub-levels with $|J_{hz}| = 3/2$ and $|J_{hz}| = 1/2$. The corresponding energy Δ_{int} is independent of the crystal size and is equal to 23 meV for CdSe [46].

Shape anisotropy As already mentioned in section I, the wurtzite CdSe nanocrystals are not perfectly spherical but often slightly elliptical [4]. The ellipticity is characterized by the parameter μ:

$$\mu = c/b - 1, \tag{I.9}$$

with c and b the crystals axis length. If c is greater than b, μ is positive and the crystal is prolate (elongated along the c axis), conversely it is said to be oblate if μ is negative. As the crystal field[4], it splits the fourfold degenerate hole state with respect to the heavy-hole

[4]The shape anisotropy is a modification of the crystal field of a perfect sphere due to the deformation of the lattice.

and light-hole bands total angular momentum projections $|J_{hz}|$. The shape anisotropy splitting is denoted Δ_{sh}. Besides depending on the ellipticity μ, its value depends also on the $1S_{3/2}$ ground state hole energy and thus on the size of the nanocrystal ($1/a^2$ dependence with the nanocrystal radius).

We will call $\Delta = \Delta_{sh} + \Delta_{int}$ the net-splitting of the hole state due to the crystal field and shape anisotropy[5]. The net-splitting can become negative for sufficiently small prolate nanocrystals as the shape anisotropy contribution can be negative, this reverse the hole state order.

Electron-hole exchange interaction Finally, the eightfold degeneracy of the spherical dot band-edge exciton is also broken by the electron-hole exchange interaction [32]. This Coulomb interaction is strongly enhanced in nanocrystals, especially when reaching the strong confinement regime for which the electron and hole wavefunctions overlap considerably [47]. It is proportional to the inverse of the nanocrystal volume ($\sim 1/a^3$).

Fine structure

The Hamiltonian with the previous perturbations splits the eightfold degeneracy into 5 levels. The band-edge exciton total angular momentum F can be either 1 or 2 as the electron and hole total angular momentum are 1/2 and 3/2 respectively. The projections gives five distinct levels:

- $|F = 2, F_z = 0\rangle = |0^L\rangle$, $|F = 2, F_z = \pm 1\rangle = |\pm 1^L\rangle$, $|F = 2, F_z = \pm 2\rangle = |\pm 2\rangle$,
- $|F = 1, F_z = 0\rangle = |0^U\rangle$, $|F = 1, F_z = \pm 1\rangle = |\pm 1^U\rangle$,

with the U and L superscript for upper and lower respectively to distinguish sublevels with the same projection but with different total angular momenta. The diagonalization of the Hamiltonian [32] gives the following associated splitting energies:

[5]Sometimes in the literature the net-splitting is simply referred as the crystal field of the particle under study

$$
\begin{aligned}
E_{\pm 2} &= -3\eta/2 - \Delta/2, \\
E^U_{\pm 1} &= \eta/2 + \sqrt{(2\eta - \Delta)^2/4 + 3\eta^2}, \\
E^U_0 &= \eta/2 + \Delta/2 + 2\eta, \\
E^L_{\pm 1} &= \eta/2 - \sqrt{(2\eta - \Delta)^2/4 + 3\eta^2}, \\
E^L_0 &= \eta/2 + \Delta/2 - 2\eta,
\end{aligned}
\tag{I.10}
$$

with η a function of the nanocrystal radius coming from the exchange interaction and Δ the already defined energy splitting due to the crystal field and shape anistropy. Fig.I.5a depicts the degeneracy splitting of the band-edge exciton state for the 5 fine structure levels. The order of the energy levels and their relative energy difference depend on the nanocrystal shape and size. For a perfectly spherical nanocrystal, the shape anisotropy energy Δ_{sh} equals 0, the order of the energy levels is depicted on Fig.I.5a and the dot size dependence is shown on Fig.I.5b.

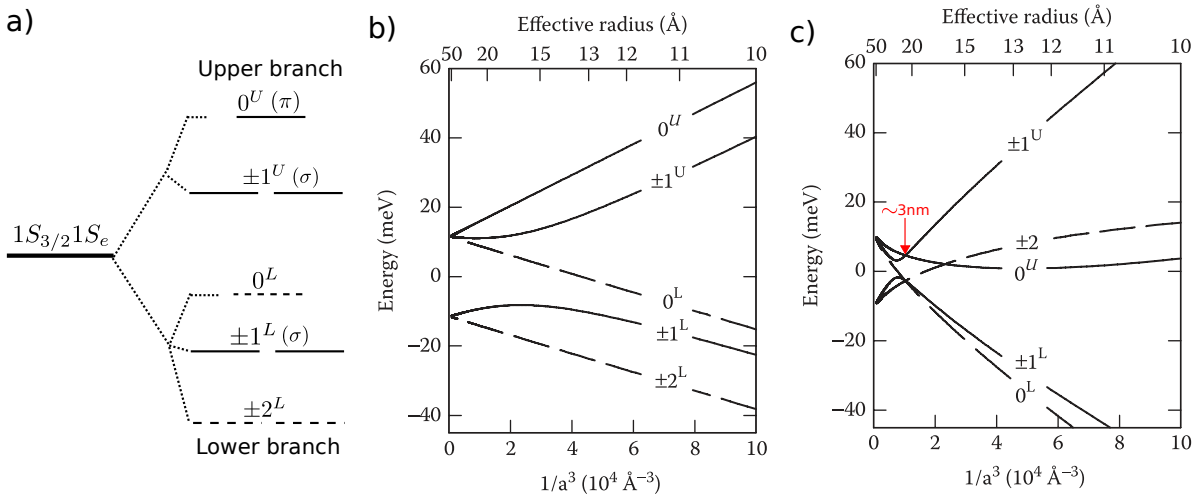

Figure I.5: Fine structure of the $1S_{3/2}1S_e$ band-edge exciton. *a) Schematics of the fine structure. The order of the energy levels and their relative energy difference depend on the nanocrystal shape and size. b) Fine structure for a spherical nanocrystal as a function of the dot size. Reproduced from reference [32]. c) Fine structure for a prolate nanocrystal ($\mu = 0.28$) as a function of the dot size. Reproduced from reference [32].*

However, when taking into account the shape anisotropy, the level order can be swapped as shown on Fig.I.5c where an ellipticity $\mu = 0.28$ is considered. In this specific case, the level swapping is predicted to happen at a radius $a = 3$ nm, the 0^L becomes the lowest level for dots with radii smaller than 3 nm. This happens when the shape

anisotropy term Δ_{sh} compensates the crystal field contribution $\Delta_{int} = 23$ meV, such that the net-splitting Δ is zero.

Fine structure: Dark and Bright transitions All the transitions described above are not optically active. Actually only 3 of them are, they are called bright excitons, while the other are called dark excitons. Optically active (passive) states are represented with full (dashed) lines on Fig.I.5. The $|\pm 2\rangle$ state is optically passive in the dipole approximation because its angular momentum projection ($\pm 2\hbar$) is greater than the angular momentum of a photon ($\hbar$).

For the other states one as to calculate their oscillator strengths. As already presented in section I.1.1 with eq.I.7, the oscillator strength depends on the exciton wavefunction. For the derivation one can refer to reference [32]. The $|0^L\rangle$ and $|0^U\rangle$ states have transition probabilities independent of the dot radius, $|0^L\rangle \propto -i|\Psi_{\uparrow,-1/2}\rangle + |\Psi_{\downarrow,1/2}\rangle$ has 0 oscillator strength because of a destructive interference between the indistinguishable states superposition, it is then optically passive. For the $|0^U\rangle \propto i|\Psi_{\uparrow,-1/2}\rangle + |\Psi_{\downarrow,1/2}\rangle$, the interference are constructive and it is optically active. Fig.I.6 reproduced from reference [32] shows the oscillator strength (normalized to the $|0^U\rangle$ state oscillator strength) as a function of the nanocrystal radius for the spherical and prolate ($\mu = 0.28$) cases.

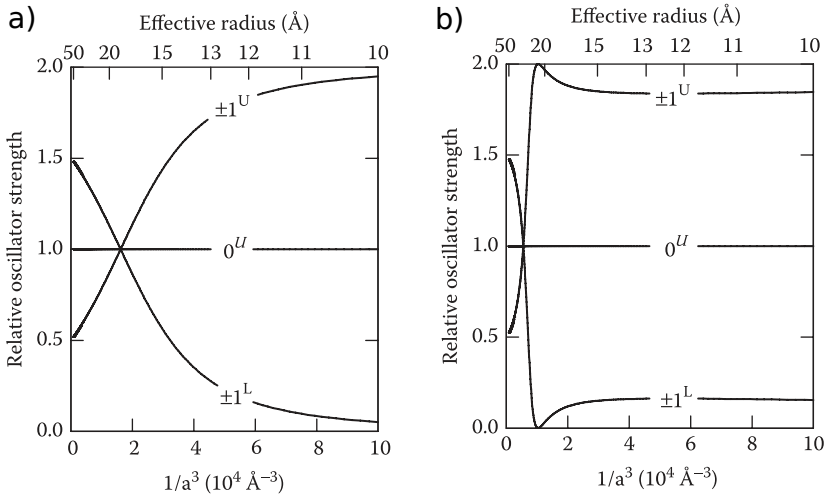

***Figure I.6: Optically active excitons oscillator strength as a function of the nanocrystal radius.**. a) Spherical nanocrystal. b) Prolate nanocrystal ($\mu = 0.28$). Reproduced from reference [32].*

Fine structure and polarization The emission polarization of nanocrystals depends on the fine structure. Transitions with total angular momentum projection of 1 emit circularly polarized photons, σ transitions. $|+1^U\rangle$ and $|+1^L\rangle$ emit σ^+ photons while $|-1^U\rangle$ and $|-1^L\rangle$ emit σ^- photons. The $|0^U\rangle$ transition is a π transition, it emits linearly

polarized photons. Fig.I.5a sums up the associated photon polarizations for each active transition.

From a classical point of view, σ transitions can be seen has two-dimensional (2D) dipole [48], meaning a dipole turning into a plane. It is equivalent to two linear dipoles, oscillating perpendicularly and in quadrature. In the case of CdSe nanocrystals, the sigma transitions from $|\pm 1^{L,U}\rangle$ are 2D dipoles contained into the plane perpendicular to the quantization axis, here the c axis of the crystal [32]. The $|\pm 1^{L}\rangle$ level is degenerate, the emission from these transitions is an incoherent superposition of σ^+ and σ^- components [17, 49], the classical dipole is still a 2D dipole contained inside the plane perpendicular to the c axis but without a defined rotation sense (this is also the case for the $|\pm 1^{U}\rangle$ transitions). It is usually called a degenerate dipole (σ^d). The c axis perpendicular to the 2D dipole plane is also called dark axis. To a π transition is associated a linear dipole [48], this is the case for the $|0^{U}\rangle$ transition that oscillates along the c axis of the crystal [32].

To summarize, the emission polarization:

- $|\pm 1^{L}\rangle$, $|\pm 1^{U}\rangle$: incoherent superpositions of σ^+ and σ^- photons, 2D degenerate dipoles orthogonal to the c-axis.
- $|0^{U}\rangle$: π photons, 1D dipole oscillating along the c-axis.

Depending on the level ordering and their spacing the emission polarization is changed. It was first demonstrated at cryogenic temperature (10 K) that the emission polarization corresponds to a degenerate 2D dipole for spherical CdSe dots [17]. At this temperature, only the $|\pm 1^{L}\rangle$ levels are thermally populated apart from the dark exciton state $|2\rangle$. It was further shown that they also behave as 2D dipoles at room temperatures [49]. Precise measurements realized in reference [50] have shown a fine structure splitting of the bright $|\pm 1^{L}\rangle$ exciton state in some nanocrystals. If the spherical symmetry of the core in the plane perpendicular to the c axis is broken, the $|\pm 1^{L}\rangle$ degenerate exciton becomes $|X\rangle = (|+1^{L}\rangle + |-1^{L}\rangle)/2$ and $|Y\rangle = (|+1^{L}\rangle - |-1^{L}\rangle)/2$, two fine structure states spectrally separated by an energy of up to 3 meV depending on the nanocrystal size and characterized by linearly and orthogonally polarized emission dipoles (still in the plane perpendicular to the c axis).

Fine structure experimental measurements

The existence of a fine structure for the band-edge exciton was first shown experimentally by ensemble measurements. PLE and its corresponding method FLN (Fluorescence Line

Narrowing) to obtain information about the emission spectrum was used in reference [37]. The emission and absorption features confirm the theoretical model for the fine structure levels of different dot sizes developed in reference [32]. Within this model, the measured Stokes shifts are explained by the fact that the absorption is mostly realized by the $|0^U\rangle$ and $|\pm 1^U\rangle$ states that have the largest coupling with the electric field (see Fig.I.6). Below 2 K, after thermalization, the emission happens from the $|\pm 2\rangle$ state. Even though this state is dark in the dipole approximation, it can relax radiatively, the origin of this being still controversial [41, 51, 52]. The low efficiency of these processes explains the very long lifetime decay measured in this case (microsecond timescales). Above 2 K, the $|\pm 1^L\rangle$ transition starts to be thermally populated, a decrease of the lifetime is measured down to approximately 20 ns at room temperature. Lifetime measurements of the emission at 2 K under a magnetic field were also explained by the existence of the dark exciton [41], under a strong magnetic field a faster photoluminescence decay is measured due to the mixing of the dark exciton with the optically allowed higher states.

More recently, the fine structure of the band-edge exciton was revealed with single particle measurements. First, by measuring the photoluminescence decay of spherical CdSe/ZnS nanocrystals with temperature [53], the emission at cryogenic temperature is attributed to the $|\pm 2\rangle$ and $|\pm 1^U\rangle$ states. Similar results were obtained with CdSe/ZnS nanorods [54], an evolution of the fine structure level positions with the nanorod radius was also demonstrated. Direct measurements of the spectral lines have recently been realized on neutral spherical CdSe/ZnS dots [55, 56], CdSe/ZnS nanorods [57, 58] and also charged nanocrystals [59]. For a review of these works see the reference [52] by Fernée et al.

I.2 Optical transitions and relaxation processes

We now review the various relaxation processes taking place inside CdSe nanocrystals. We start from an excitation far above the bandgap. The typical scenario is the creation of one or more electron-hole pairs in the continuum of the energy states that will first relax nonradiatively[6] via interactions with the lattice and carrier scatterings (Auger relaxations). During these processes the carriers will relax towards the band-edge state and/or will be trapped in defects of the crystal or its surface. For a given electronic state of the nanocrystal, the probability that a photon will be emitted is therefore not 100%, the notion of quantum yield is introduced to quantify this.

[6]Relaxations not leading to the emission of a photon

I.2.1 Highly excited states and absorption

Experimentally, we excite nanocrystals with a diode laser at 405 nm (3.06 eV). This is more than 1 eV above the first exciton state even for small nanocrystals. As explained in section I.1.1, at these energies nanocrystals exhibit a continuum-like absorption spectrum (see Fig.I.4a) because of the high density of hole states and their coupling. In this case, the nanocrystals interact with light as small light-scattering spheres, the absorption cross sections being proportionals to the volume of the nanocrystal [60]. They show an absorption cross sections of the order of 10 Å^2 (0.1×10^{-14} cm^2) as measured in solution [60] or via saturation measurements [12]. This can be compared to the 4 Å^2 for Rhodamine 6G molecules for example. When capped with a shell, the absorption cross section is even larger, it can be as high as 1000 Å^2 for thick shell nanocrystals [61].

Depending on the excitation intensity and absorption cross section of a nanocrystal, a certain number of electron-hole pairs will be created inside the quantum dot after excitation. The energy is then released through nonradiative and radiative processes described below.

I.2.2 Non-radiative relaxation processes in nanocrystals

Nanocrystals photoluminescence is only governed by the band-edge exciton even though the excitation is far above the bandgap, this suggests that nonradiative relaxations play a major role in the photophysics of these nanostructures. Moreover, the low multiexciton emission[7] together with emission intermittency[8] imply that nonradiative processes are not only involved in the relaxation of electron-hole pairs towards the band edge but are also in competition with radiative processes.

Interactions with phonons

Interactions of the carriers with the ion lattice takes place during the relaxation of the carriers in their respective bands, this is called intraband (inter-sub-band) relaxations. This interaction is also important to understand the band-edge relaxation of an exciton (interband relaxation), this relaxation can excite one or more phonons.

Intraband relaxations Once carriers are created in the quasi-continuum of energy state they quickly relax towards lower energy states by giving energy to the lattice and

[7]Nanocrystals are good single photon emitters [12], meaning only one exciton recombine radiatively even though multiple excitons are created. This is detailed in Chapter IV of the manuscript.

[8]the emission of a nanocrystal randomly turns on and off, it was discovered thanks to single particle measurements [15], this phenomenon is described in Chapter III of the manuscript.

creating phonons. However, phonons are also affected by the confinement and are quantized in discrete levels. Intraband relaxations due to phonons are therefore predicted to be slower in confined systems than in bulk [62] due to the lower density of phonon modes. Intraband transition should be inhibited if there are no available phonons with the same energy as the transition, leading to the so-called "phonon bottleneck" expected for such structures [43].

For CdSe nanocrystals, as the electron levels are strongly separated (more than a 100 meV between $1S_e$ and $1P_e$ electron states [38]), a phonon bottleneck is expected for these carriers (largest phonon energies are of the order of 20 meV). However, it was experimentally shown that the electron relaxation towards the $1S_e$ level can even be faster than in bulk CdSe [43, 63–65]: hundreds of femtoseconds to picoseconds, depending on the nanocrystals sizes. A Coulomb mediated energy transfer (see next section on Auger recombinations, Fig.I.7a) between electrons and holes is the process at stakes to explain the fast electron relaxation [66, 67]. The hole levels are typically separated by one to tenth of meV. The hole relaxation towards the band edge $1S_{3/2}$ state can therefore be mediated by phonon relaxation (see Fig.I.7b). A slower decay rate at the bottom of the band energy has been observed and attributed to a phonon bottleneck [68], a less efficient multi-phonon process being necessary for the hole relaxation at the bottom of the energy ladder.

Interband relaxations The band-edge exciton relaxation is also affected by the presence of phonons. First, the homogeneous linewidth of the zero-phonon emission line is broadened by the thermal excitation and shows the expected temperature trend [69]. Second, phonon replicas have been clearly observed in CdSe nanocrystals. Longitudinal optical (LO) phonon mode corresponding to out-of-phase movement of the atoms in the lattice, as well as longitudinal acoustic (LA) phonon mode (coherent movements of atoms of the lattice out of their equilibrium positions) have been evidenced on single particle measurements at 2 K [55] as replica lines of the zero phonon line.

Auger processes

Energy transfers between carriers via Coulomb interactions are called Auger processes. They can happen between two carriers or more. In CdSe nanocrystals for which the strong confinement regime applies, even though the Coulombian potential is considered as a perturbation and the accessible energy levels are quantized, Auger processes are strongly enhanced. Therefore, Auger energy transfers play a major role in the photophysics of colloidal nanocrystals, for electron thermalization, multiexciton recombinations, photoluminescence quenching, autoionization. In this section we give an overview

of the Auger mechanisms and their consequences on CdSe nanocrystals photoluminescence. In Chapter III and IV, the multiexciton recombinations and photoluminescence quenching in CdSe/CdS dot-in-rods will be treated in details.

Electron thermalization The fast electron thermalization (picosecond timescales) is realized via an exchange of energy with the hole as experimentally observed in reference [67]. This Auger process between the two carriers is depicted on Fig.I.7a, the electron relax towards the band edge giving its energy to the hole and no phonon bottleneck [9] is thus observed. The hole relax by successive emission of phonons [68].

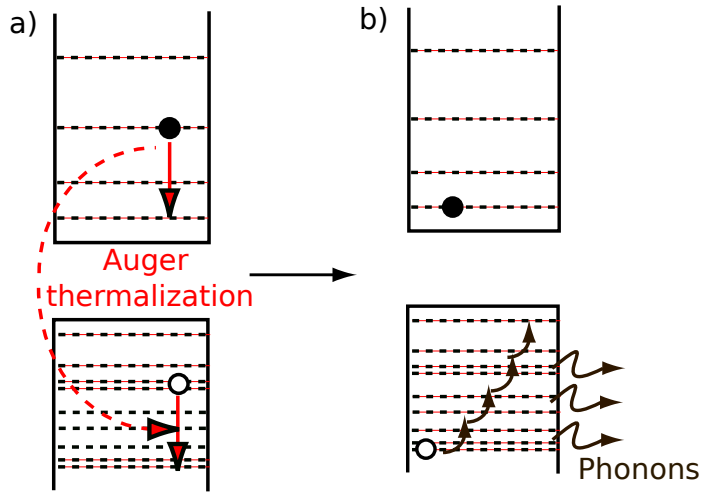

Figure I.7: Electron thermalization by Auger relaxation. *a) Hot electron relaxation towards the band-edge state, the electron transfer its energy to the hole via an Auger process involving electron-hole scattering . b) Hole relaxation by phonon emission.*

Multiexciton relaxations Auger relaxations of electron-hole pairs plays a major role in the optical properties of CdSe nanocrystals. It involves at least three charge carriers and consists in the nonradiative recombination of an electron-hole pair that transfers its energy to a third charge, an electron or a hole. On Fig.I.8 are depicted two cases that will be largely discussed throughout this thesis.

First the nonradiative relaxation of a trion (an electron hole pair plus an extra charge: a charged exciton) through an Auger energy transfer is depicted on Fig.I.8a: the extra charge[10] is promoted to a higher energy state after taking the recombination energy of the electron-hole pair. This process is very efficient in CdSe nanocrystal. Since the first observation of emission intermittency from single particle fluorescence measurements [15],

[9] Slowing down of the electron relaxation due to the lack of accessible single phonon relaxation

[10] Here an electron associated with an electron-hole pair forms a negative trion, the case of a positive trion for which the extra charge is a hole is also possible

the random switching between ON emission periods where photons are detected and OFF periods where the nanocrystal is not emissive has been attributed to the charging of the nanocrystals. The trion emission is quenched by the Auger relaxation mechanism.

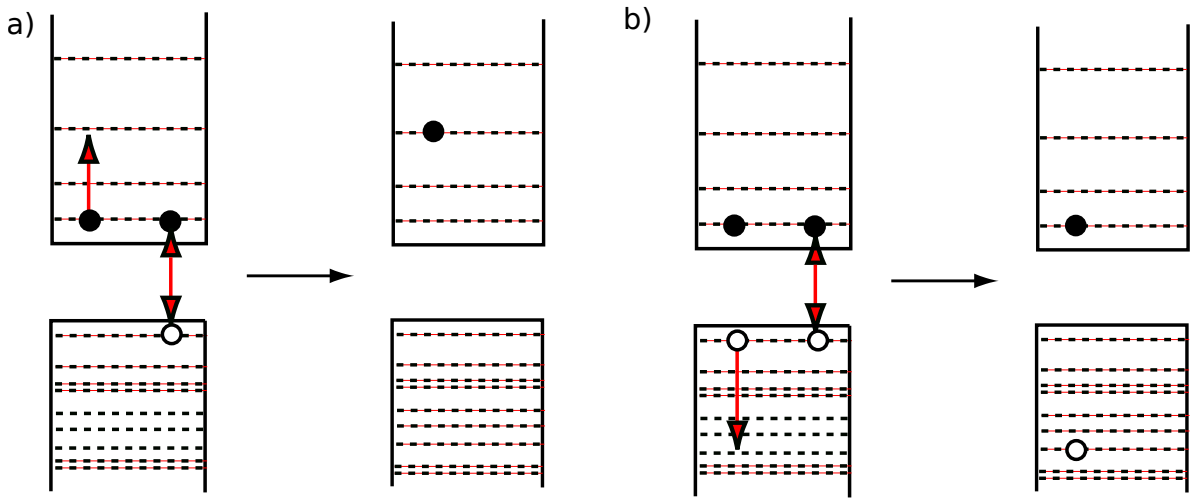

Figure I.8: Examples of multiexcitons Auger recombinations. *a) Auger process involving the decay of a ground-state trion into a hot hole. b) Auger process involving the decay of a ground-state biexciton into a monoexciton.*

The second important case that is described in Fig.I.8b involves the nonradiative recombination of a biexciton (more generally of a multiexciton composed of many electron-hole pairs). One electron-hole pair gives its recombination energy to one charge of a neighbooring electron-hole pair. This mechanism prevents the photon emission from multiple excitons and explains the single photon emission of CdSe nanocrystals observed at room temperature [12,70–72]. Even if pumped on average with more than one electron-hole pair, a CdSe nanocrystal will emit a string of single photons. Negligible multiexciton emission peaks are observable in the emission spectrum conversely to epitaxially grown CdSe quantum dots [73,74] that realizes weak confinement of the charges with negligible Auger effects.

Control of Auger recombination Besides the scientific interest in modeling and understanding the Auger processes in nanocrystals, the control of these phenomena is of a particular importance for nanocrystal applications as they affect all aspects of carrier relaxations. First, the emission intermittency that is detrimental for using these particles as stable light sources. Second, the photodegradation[11] of the photoluminescence due to photooxydation of a charged quantum dot in presence of oxygen [75–77]. Both these processes involve Auger ionization of nanocrystals. Also, colloidal nanocrystals are

[11]degradation of the optical properties, decrease of the quantum efficiency of the emission under light excitation

particularly appealing for lasing technologies. The reduced density of states due to the three dimensional confinement implies a lower threshold for lasing. Moreover, the ability to tune the emission wavelength on a broad spectral window just by changing the size of the particle with the same material is possible, whereas for epitaxial quantum dots the weak control of the confinement dimensions implies that the emission wavelength is mostly material dependent. Moreover, due to their stronger confinement, room temperature operation is possible. However, gain threshold in such structures arises only for an average number of electron-hole pairs per dot $\langle N_{eh} \rangle$ above one [11,78]. Then, optical gain in NCs directly relies on emission from multiexciton states, and hence, Auger recombination represents the dominant intrinsic optical-gain relaxation mechanism and explains the short gain lifetime [78].

In bulk materials, Auger processes are usually weak with a slow recombination rate compared to radiative recombination. They are also strongly material and temperature dependent as the rate scales as E_g/T, with E_g and T the semiconductor bandgap energy and temperature respectively [79]. For CdSe colloidal nanocrystals in the strong confinement regime, multiexciton Auger rates of the order of a few picoseconds to hundreds of picoseconds have been measured [80], this is much faster than radiative recombination happening on nanosecond timescales. The efficiency of the Auger processes in nanocrystals is explained by a higher Coulomb interaction between particles due to the small size and a reduced dielectric screening due to the proximity of a surrounding medium[12] [81]. A second reason explaining the efficiency of Auger scattering for nanometer size particles is the confinement-induced relaxation of the momentum conservation [79]. No wave vector momentum conservation is mandatory in 3D confined systems due to the lack of translation symmetry. No activation energy is necessary as in bulk material for which the conservation of momentum implies possible Auger effects only at high temperatures. This explains the temperature independent Auger processes in direct bandgap semiconductor nanocrystals. Furthermore, the existence of efficient Auger effects for indirect bandgap semiconductor nanocrystals implies that no phonons (thus no momentum conservation) are needed for these processes that would otherwise be inefficient. For a review of the Auger processes in different nanocrystal materials and the various arguments exposed above, see the chapter 5 section 6 of reference [33]. Energy conservation still needs to be fulfilled for Auger processes to happen in nanocrystals. Discretized energy levels hinder Auger processes as available final states are scarce; a state from the continuum-like of higher energies as a final state for Auger relaxation is then highly probable. This explains the possible ionization of a nanocrystal by Auger effect [82], if a charge is promoted into the continuum-like of higher energies, then it is less confined and more susceptible to be

[12] The surrounding medium is typically characterized by a lower dielectric constant.

trapped by surface defects for example.

We now review the different parameters that play a role in the Auger scattering processes efficiency in the strong confinement regime:

- First the size of the structure. The so-called volume scaling of Auger processes [80, 83] was demonstrated for several materials, the Auger rate depending on the volume of the nanocrystals. This is only valid if the physical volume under consideration is the confinement volume of the charges (typically the case for high potential wells), if not, the exciton size needs to be defined. Tuning the exciton size (the electron-hole wavefunction overlap) changes the Auger efficiency as demonstrated for CdSe nanocrystal capped with a giant CdS shell [19]. This will be detailed in section I.3.1.

- As theoretically predicted and calculated in reference [84], it was demonstrated using [85–87] core/shell structures for which the confinement can be tuned, that a smooth confinement potential reduces the efficiency of Auger effects. It is chemically realized by imposing an alloy layer between the two materials at the core-shell interface. Auger recombination is highly probable for a particle whose kinetic energy uncertainty is maximum [79], this is typically the case in defects, at an abrupt potential interface (core shell interface).

- For the same reason than at the interface between two materials, the surface plays a significant role in Auger recombination due to the abrupt potential. Reference [88] explains the extinction of Auger recombination at low temperature in CdSe/CdS nanocrystals as attested by a trion state with 100% efficiency by the localization of the electrons inside the core at low temperature and the absence of interactions with the surface.

Charge trapping

Together with Auger processes, the charge trapping plays a considerable role in the photophysics of colloidal nanocrystals. In this section we will very briefly describe the different trapping sites.

Fig.I.9 depicts the different sites where trapping is possible for a core/shell nanocrystal. Defects can appear at the interface between the two materials because of the strain produced by the lattice mismatch. These interface defects can form localized energy levels inside the bandgap of the dot and thus act as trapping sites for the carriers. It was shown to be the case for CdSe/ZnS spherical particles with an important lattice mismatch of 12%; growth of large ZnS shell induced a decrease of the emission efficiency attributed

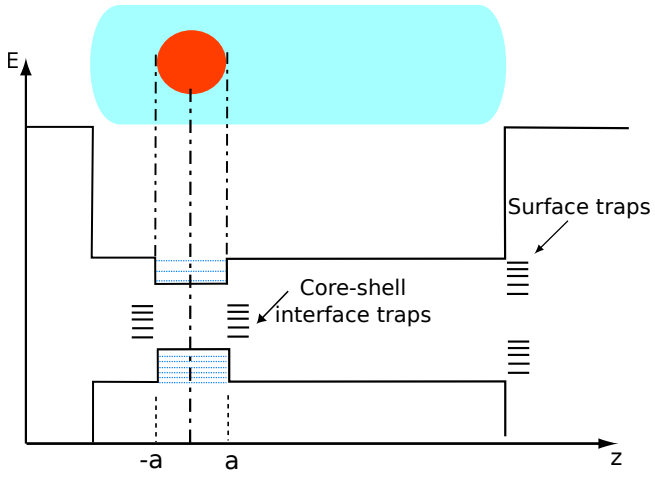

Figure I.9: Typical trapping sites for a core/shell heterostructure like dot-in-rods. *The core/shell interface can have defects, especially if the material lattice parameters mismatch is high. The surface of the nanocrystal exhibits trapping sites due to unsaturated ("dangling") atomic bonds.*

to defects [4]. More important is the surface of nanocrystals. Unsaturated atomic bonds act like surface traps for the carriers. Unsaturated bonds passivation by inorganic or organic molecules (ligands) leads to increased fluorescence efficiency due to a reduced number of surface trapping states [18]. A surface trap is for example an unsaturated anionic dangling bond, Se^{2-}, on the CdSe surface, or S^{2-} for a ZnS or CdS capped CdSe nanocrystal. Finally , trap sites intrinsic to the passivating ligand or local environment of the nanocrystal have also been observed [89, 90].

Trapped states can recombine with their countercharge delocalized inside the nanocrystal. It is usually a non-radiative recombination channel. The recombination can nevertheless be radiative: low fluorescence in the infrared spectrum has been attributed to the radiative recombination of trapped charges [91], the effect being more important for smaller dot sizes as the volume to surface ratio decreases implying a greater importance of surface phenomena.

I.2.3 Quantum states and radiative relaxation

In section I.1.1 and I.2.2 we have described the experimental evidence and the various phenomena leading to an emission characterized only by the band edge exciton state, $1S_{3/2}1S_e$, in CdSe nanocrystals. However, not only the band edge exciton emits photons, other emission states exist and are experimentally observed. The band edge exciton will be denoted X[13] for the rest of this thesis.

[13] X means the band edge exciton $1S_{3/2}1S_e$ in general without considering its fine structure, if talking about a specific sublevel then the notations introduced in section I.1.2 will be used

Multiple electron-hole pairs (multiexcitons) can be created inside a nanocrystal at high excitation power. Bare CdSe nanocrystals have almost no multiexciton emission owing to their extremely efficient Auger recombination. CdSe/CdS dot-in-rods that we will study in details in the rest of this thesis can display multiexciton emission. A multiexciton made of m electron-hole pairs will be denoted mX.

Finally, the last scenario is when an extra charge is present inside the dot, either a hole or an electron. An isolated charge can appear consequently to an Auger autoionization [82] that ejected the complementary particle in a trap. In this case for a singly charged exciton, the term trion is used, either positive (X^+) or negative (X^-) trion depending if the extra charge is a hole or an electron respectively. Charged multiexciton can also exists and will be denoted mX^+ or mX^-. Multiple charging is also a possibility, if n charges are present, then the state will be written as follow: mX^{n+} or mX^{n-}.

A radiative relaxation is characterized by its radiative decay rate γ_r, the rate of spontaneous emission. It can be described by Fermi's golden rule. The rate of emission depends on two factors: the light emitter with its intrinsic properties and the density of electromagnetic modes of the emitter surrounding medium. Concerning the emitter, we already described in section I.1.1 the strength of a given transition, the oscillator strength, which is given by Eq.I.8 for nanocrystals. There is a part depending on the bulk material and another on the electron hole wavefunctions overlap. This last term can be engineered by changing the confinement of the particles or the material used for the shell. The density of the electromagnetic modes can be controlled by changing the dielectric environment around the emitter. For example by inserting the emitter inside a cavity [92], or close to a material with a specific resonance [93] at the emission wavelengths of the emitter. In our case, we will only study the case of the vicinity of a dielectric interface, because it is our typical experimental condition: single nanocrystals are usually deposited on a microscope glass coverslip. In this case, the mode density is independent of the emission frequency on the bandwidth considered here, the radiative decay rate can be calculated using classical considerations [94, 95]. For our purposes in this thesis, one should remember the relationship between the radiative decay rate and the electron hole wavefunctions overlap:

$$\gamma_r \propto |\langle \psi_h | \psi_e \rangle|^2. \tag{I.11}$$

Beyond radiative relaxation, the various states presented above have also their own nonradiative relaxation rates and pathways. Their probability to emit one photon when excited depends on the nanocrystal structure and is different for different states. It is quantified by the quantum yield.

I.2.4 Quantum yields

The quantum yield of a specific excited state inside the nanocrystal gives the probability that this state emits one photon. For a specific state S, it is defined as the radiative relaxation rate γ_r^S of this state over its total relaxation rate γ^S, sum of the radiative and nonradiative (γ_{nr}^S) rates:

$$Q_S = \frac{\gamma_r^S}{\gamma^S} = \frac{\gamma_r^S}{\gamma_r^S + \gamma_{nr}^S}. \tag{I.12}$$

The total relaxation rate γ^S of a state is easily measurable by building a histogram of the photon arrival times on a detector after pulsed excitations[14]. The average arrival time of the photons emitted by the state S after pulsed excitations is called the lifetime of the state and denoted τ_S. This tells us how much time on average a state S takes to relax to the ground state. It corresponds to the inverse of the total relaxation rate γ^S:

$$\tau_S = \frac{1}{\gamma^S}. \tag{I.13}$$

How γ^S is precisely measured is detailed in chapter II.

The exciton quantum yield Q_X has been measured to be unity in high quality CdSe nanocrystals (capped with a thin ZnS layer) under various methods: lifetime measurements [96] and variation of lifetime due to a change in the electromagnetic environment of the emitter [94]. In the rest of this thesis we will always consider $Q_X = 1$. In chapter IV we will show that this is the case for our dot-in-rods. This means that no nonradiative processes quench the photoluminescence of the exciton, implying a very high crystal quality.

Other states than the exciton usually have nonradiative decay channels that quench their photon emission. In this case their associated quantum yields are lower than unity. The nonradiative channel we have to consider is the Auger recombination, it happens when at least 3 carriers are inside the quantum dot. In the following we will write Auger rates as γ_A.

I.3 Core/shell nanocrystals

The capping of CdSe nanocrystals by another material is attractive for controlling the properties of these emitters beyond just changing the size of the confinement. Indeed, the optical properties can drastically change when capping bare CdSe nanocrystals with

[14]The photon arrival times are exponentially distributed, the decay is given by the total relaxation rate γ^S

various materials of different shape.

In general, the addition of a shell greatly enhances the efficiency of emission. The nanocrystal surface is passivated by the ligands adsorbed during the synthesis. However, the ligands do not passivate the whole nanocrystal surface. Many dangling bonds are close to the nanocrystal core, they act as nonradiative decay channels and quench the photoluminescence. Fluorescence quantum yield in core-only nanocrystals is usually less than 10%. Moreover, capped nanocrystals exhibit a better photostability than bare CdSe. Photooxydation reactions will impact the shell and not the core as for bare nanocrystals, such that the access of carriers to the photooxydation sites is less important. Also nanocrystals capped with CdS or ZnS are less keen to photooxydation reactions than uncapped CdSe particles.

We briefly review the different types of core/shell nanocrystals before describing in details CdSe/CdS heterostructures. We also give details on the consequences of the shape anisotropy on optical properties before describing CdSe/CdS dot-in-rods.

I.3.1 Classification of core/shell heterostructures

Capping of the core with a specific shell can impact the carriers wave function. A particle will be strongly confined in the core if the capping material as a bandgap well above the core bandgap. When decreasing the bandgap difference between the two materials, the carriers starts to expand more and more inside the shell. This can potentially result in a change of radiative rate if the overlap decreases. Depending on the capping material and its band alignment compared to the core, a classification of core/shell structures is made in the literature. Two categories are differentiated: type I and type II heterostructures.

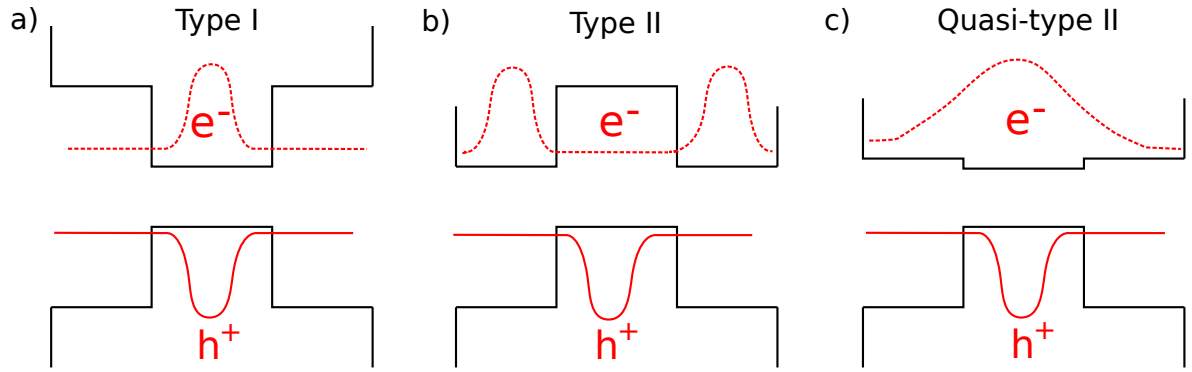

Figure I.10: Core/shell heterostructures classification. *a) Type I heterostructure. b) Type II heterostructure. c) Quasi-type II heterostructure. In red is depicted the wavefunctions of the hole (solid line) and electron (dashed line).*

Fig.I.10 is a schematics of the different type of core-shell heterostructures. Type I heterostructures depicted in Fig.I.10a have a band alignment such that both the valence

and conduction bands of the core material are located within the energy gap of the shell[15]. In this case both electrons and holes wavefunctions are mostly localized inside the core. The typical type I nanocrystal is CdSe/ZnS; valence and conduction bands differences between the two materials being roughly 1eV[16], carriers wavefunctions are strongly localized within the core. For the first synthesis [4, 18], 1-2 monolayers of ZnS were added to 3 nm diameter CdSe nanocrystals. A fairly small red shift ($\sim$ 5 nm) in the observed optical spectra after the shell growth confirmed the strong confinement realized by the ZnS shell: almost no carrier wavefunction leakage and energy position shift by the addition of the shell. An increased emission efficiency from quantum yields of 10% to 50% is noticed even for such small shells.

Type II heterostructures depicted in Fig.I.10b have their lowest energy states for electrons and holes with the corresponding wavefunctions localized in different semiconductors. The energy gradient at the interfaces tends to spatially separate electrons and holes on different sides of the heterojunction. The growth of the shell induce a strong redshift of the spectrum as carriers are spatially separated. Also the lifetime of the emission considerably increases because of the small carrier wavefunctions overlap. Typical type II heterojunctions are often made of Tellurium: CdTe/CdSe, CdSe/ZnTe, but ZnSe/CdS has also shown a type II behaviour [97]. Type II heterostructures are useful for emission in the near-infrared wavelengths[17] [98] (around 800 nm), lasing [99] because of their reduced Auger effects, for photovoltaics applications because of the possibility to collect the separated charges before any recombination.

Finally, heterostructures for which the carrier wavefunctions are only partially overlapping are called quasi-type II. This is the case if one of the bands shows only a slight offset between the two materials as sketched on Fig.I.10c. In this case one of the charge is well confined inside one material while the other is delocalized over the whole structure. CdSe/CdS is the typical example of such an heterostructure. The conduction band offset is known to be small but not precisely determined, different numbers are given in literature ($\pm 0.3eV$). The electron is delocalized inside the entire structure. The hole is confined inside the core due to the large valence bands offset ($0.68eV$).

One way to discriminate between type I and type II heterostructures is to measure the biexciton-exciton spectral shift [100, 101]. The spectral shift is a consequence of the type of interaction between the excitons. A blue shifted biexciton compared to the exciton means a repulsive exciton-exciton interaction. This is the case for type II structures as the repulsive part of the Coulomb interaction is stronger than the attractive part due to the spatial positions of charges. Conversely, for type I heterostructures the biexciton is

[15] Reverse type I also exists where both bands of the shell are within the energy gap of the core
[16] ZnS bandgap: $E_g^{ZnS} = 3.61eV$, CdSe bandgap: $E_g^{CdS} = 1.8eV$.
[17] They nevertheless display a small emission efficiency.

redshifted compared to the exciton. For heterostructures presenting a quasi-type II band structure the situation is less clear. If we retain this criteria to discriminate between the two types of band alignment, they can either act as type I or type II depending on the geometry and synthesis [101].

I.3.2 CdSe/CdS nanocrystals: quasi-type II heterostructures and wavefunction engineering

Even if a discrepancy in the values of the conduction band offset appears in the literature[18], CdSe/CdS nanocrystals are considered as quasi-type II heterostructures as exposed above. During the shell growth, a large redshift of the exciton photoluminescence of some tenths of nanometers are observed and an increase in the emission lifetime. Calculations [102] predict that the growth of a CdS shell barely changes the hole confinement (the hole stays inside the CdSe core), while the electron wavefunction is spreading all over the structure. The larger hole effective mass together with the larger valence bands offset explain the difference with the electron. Since the electron wavefunction can be either totally or partially delocalized into the shell, it is common to describe CdSe/CdS nanocrystals as **quasi-type II heterostructures**. The small conduction band offset of CdSe/CdS nanocrystals allows to engineer the electron wavefunction. Various parameters can change the electron localization inside the heterostructure:

- Core and shell size: a transition between a proper type-I and a type-II condition may be obtained by tuning the core and the shell size [101, 103, 104].
- Shell shape, electric field, dipole moment: an anisotropic rod-like shell can separate the charges [105] by tuning the length. Also a separation of the electron and hole wavefunctions can be obtained by applying an external electric field (Stark effect). An intrinsic electric dipole [106] can be present in such an asymmetric structure as well. Reference [107] reports that morphological differences of the shell (cylindrical, arrow like, tetrapod shapes) greatly modify the optical properties.
- Alloying at the core/shell interface: high growth temperatures and large shell thickness can favor an alloying process at the interface which contributes to modify the band profile and carriers wavefunctions [85, 86].

Finally, CdSe/CdS heterostructures display a high crystal quality. The two materials have the same wurtzite structure and a small lattice mismatch (4%, CdSe lattice pa-

[18]The discrepancy for the conduction band offset in CdSe/CdS nanocrystals in the literature comes from the fact that it can be different from the bulk materials: strain effects can modify the offset [102] for example.

rameter: 4.3Å, CdS lattice parameter: 4.136Å), resulting in a small defect probability. Moreover, the small lattice mismatch gives the possibility to grow thick shells with few strain induced defects.

I.3.3 Nanorods

We now concentrate on various peculiar properties of rod-shaped nanocrystals. This section is not an exhaustive review on nanorods. Instead it aims at providing useful insights for the next section on CdSe/CdS dot-in-rods and the effects of the addition of a CdS rod shell. Therefore only the elements that are useful for the following section are treated.

First we will briefly detail how the electronic levels are affected by the shape by comparing the rod case with the thorough-fully described spherical case of section I.1.2. We then review the peculiar properties of nanorods compared to the spherical particles. Finally, we motivate the use of rod-shaped particles reviewing different experiment where the rod shape is important. For the interested reader, the reference [108] by Khrane et al. presents in great details the physical properties of elongated inorganic nanoparticles.

Electronic properties

The nanorods spectral lines are less separated than those measured on spherical nanocrystals because of a reduced quantum confinement in one dimension for nanorods. Nearly identical spectra [109] were observed between samples of same radii and different lengths (aspect ratio from 3 to 10), while significant differences were measured between rods of same lengths but different radii (with a factor of 2). The rod level structure is dominated by the radius rather than by the length.

The shape of the nanocrystal can have significant influence on the fine structure of the band edge exciton as previously mentioned in section I.1.2 for prolate nanocrystals. Nanorods can be approximated by axially symmetric prolate ellipsoids with ellipticity μ defined as $\mu = (2r_B/b) - 1$, with b the ellipsoid (rod) diameter and r_B the Bohr radius of the exciton because of the lack of confinement in the long axis direction. In this case the Bohr radius of the exciton is taken as a reference because the strong confinement is not anymore realized along the rod axis for which the length c is greater than the Bohr radius (5.6 nm for CdSe). We however still consider strong lateral confinement ($b < 2r_B$).

As depicted in section I.1.2, the crystal field and shape anisotropy splits the fourfold degenerate hole state of the bandedge exciton $1S_{3/2}1S_e$ with respect to the heavy-hole and light-hole bands total angular momentum projections $|Jhz|$: $|Jhz| = 3/2$ and $|Jhz| = 1/2$ respectively. Fig.I.11 summarize the perturbations that lift the eightfold degeneracy into

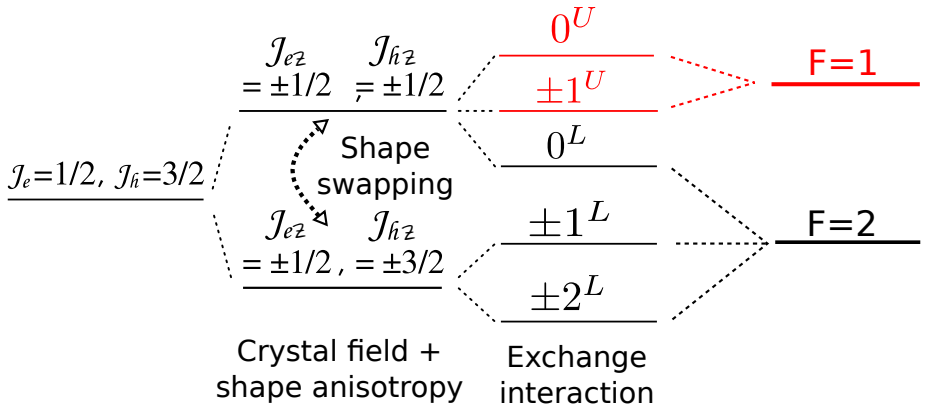

Figure I.11: Schematics of the degeneray lifting. *The asymmetric perturbation (crystal field and shape anisotropy) lift the degeneracy with respect to the hole total angular momentum, the electron hole exchange interaction split further the levels into the five sublevels. The crystal field (Δ_{int}) plus the shape anisotropy (Δ_{sh}) perturbations, called the net-splitting (Δ), can change sign depending on the shape anisotropy value, this leads to a swapping of the heavy-hole and light-hole bands and a reordering of the energy levels, with respect to the spherical nanocrystal case.*

the five fine structure sublevels. If the net-splitting Δ changes its sign compared to the standard nearly spherical case, some sublevels coming from the $|Jhz| = 1/2$ band can pass below some sublevels coming from the $|Jhz| = 3/2$ band and induce a complete level reordering.

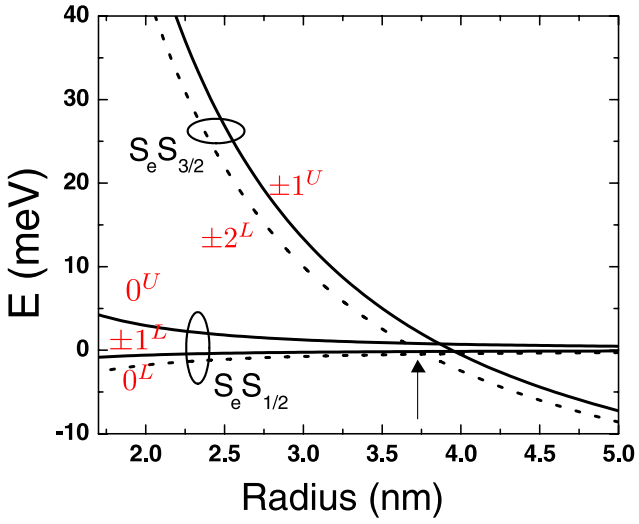

Figure I.12: CdSe rod fine structure. *Theoretical calculation of CdSe rods fine structure as a function of the rod radius. Dark transitions are denoted by dashed lines and allowed transitions by full lines. Figure reproduced from [54].*

Reference [54] has calculated the exciton fine structure for CdSe nanorods depending on the radius of the rod, Fig.I.12a reproduces the theoretical results. When the rod is sufficiently long (longer than the exciton Bohr radius), the shape anisotropy is then given

by the rod radius. Decreasing the rod radius increases the shape anisotropy perturbation Δ_{sh}, level swapping is predicted to happen for a radius of 3.7 nm. Below this number the lowest energy levels become the dark $|0^L\rangle$ level, the optically active $|\pm 1^L\rangle$ and $|0^U\rangle$ levels as for the prolate case. The level splitting is fairly small between these levels and almost rod diameter independent as seen on Fig.I.12. The same reference using lifetime and polarization measurements, as well as references [57, 58] with spectroscopic measurements at low temperatures, gives experimental evidence of the level reordering. Another theoretical work [110] gives also the same energy level ordering: the lowest energy levels being the dark $|0^L\rangle$ level, with the optically active $|\pm 1^U\rangle$ and $|0^U\rangle$ levels above.

The cylindrical shape of rods also reduces the exchange interaction because of a smaller overlap between electrons and holes. Consequently, the energy splitting between the levels in the fine structure is smaller than in the strongly confined spherical case as can be seen on the energy scale of Fig.I.12 compared to Fig.I.5.

Other peculiarities of nanorods

The first particularity noticed about CdSe nanorods has been the high linear polarization of the emission [20]. The linear polarization was attributed to the fine structure energy level swapping and small energy difference between the fine structure energy levels [54] implying a strong emission from the $|0^U\rangle$ state (see Fig.I.12) that emits linearly polarized photons, even at low temperatures [57]. Shabaev et al. [110] have also calculated that the oscillator strength of the $|0^U\rangle$ transition should be larger than the dipole of the underlying $|\pm 1^U\rangle$ transition that should lower the degree of linear polarization due to its 2D nature[19]. In addition, antenna like dielectric effects [110, 111] due to the shape anisotropy have to be taken into account, the electric field of a photon is significantly reduced if the field is perpendicular to the nanorod axis while the photon field remains almost unchanged if it is parallel to the nanorod axis. This dielectric enhancement will affect differently the light emitted by the different fine structure levels that have different polarization as well as emission patterns.

The absorption cross section [112] of nanorods is larger than in the case of spherical particles for two reasons. First because of the larger amount of material for nanorods compared to nanocrystals of the same radius. Also, the cylindrical shape displays a better coupling [112] with the incoming light compared to the spherical shape even for randomly oriented nanorods. A further increase in the absorption is possible in the case of aligned rod samples oriented along the polarization of the excitation field. This can be useful

[19] This point, how the dipole nature affects the measured degree of polarization, is discussed in chapter II when developing the measurement procedure for polarization.

when only a low excitation of the sample can be achieved[20] or for lasing purposes [112].

Nanorods are also interesting for the understanding of the effect of electric fields on the photoluminescence processes. They are subject to quantum confined Stark effect (QCSE) because the elongation allows transformation from strong isotropic quantum confinement typical of spherical nanocrystals to weak confinement. Fig.I.13 presents the effect of QCSE on the electron and hole wavefunctions inside a nanorod. The carriers can be pulled apart under the modification of the band energy due to an applied electric field. By diminishing the wavefunction overlap, the radiative recombination can be made less probable and nanorods photoluminescence can even be switched off [113].

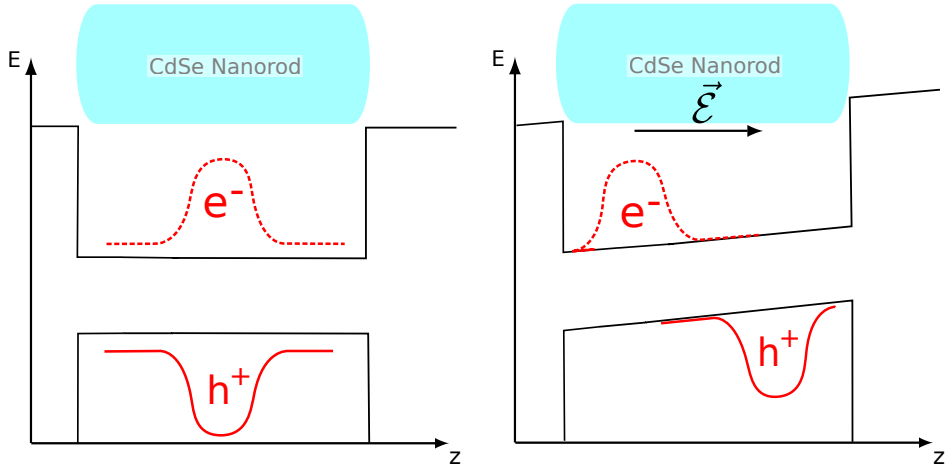

Figure I.13: Schematics of the quantum confined Stark effect implication on the carriers wavefunctions localization. *Application of an electric field $\vec{\mathcal{E}}$ along the rod axis pulls apart the electron and hole wavefunctions. a) Initial state without $\vec{\mathcal{E}}$ field: the wavefunctions are strongly overlapping. b) With an $\vec{\mathcal{E}}$ field the carriers wavefunctions are pushed away.*

Finally, rods have a larger surface than spherical nanocrystals for a given volume, thus the surface should play a greater role for such particles. Local fields induce photoluminescence intermittency for such particles [113] via QCSE. Local electric field in nanorods can originate from charge residing in trap sites at the surface, which can accumulate and change in position with time. Another possible source for a local field is a tilted direction of growth with respect to the c-axis of the wurtzite structure due to stacking faults [114, 115]. This creates polar facets at the lateral sides of the rod and permanent surface charges.

Rod shape and positioning

Besides the interest that tuning the shape can bring to the understanding of the confinement and other fundamental phenomena in nanocrystals, the shape anisotropy is also

[20]In chapter VI we detail an experiment of excitation of CdSe/CdS dot-in-rods through a ZnO nanowire for which the high absorption cross section of dot-in-rods is beneficial.

very interesting for positioning purposes.

The cylindrical shape can be used as a proof of the alignment in a given direction if the nanoparticles can be visualized for example. Furthermore, if an optical dipole can be associated with the rod long axis then simple optical measurements can be employed to determine particle alignment. This last point will be presented in chapter V where we discuss polarization measurements and dot-in-rods alignment in liquid crystals defects. Using the polarization properties of CdSe nanorods, devices with aligned CdSe nanorods [116] can be used as detectors of polarized light or as a lasing material [117] for the emission of polarized light for examples.

The cylindrical shape allows also to fabricate self-assembled arrays as demonstrated in reference [25]. Self assembly can be used for bottom up building of superparticles where one wants to assemble individual particles in a controled manner to form bigger particles [118]. It can be used to generate thin-films of well ordered particles for photovoltaics devices for example. Self assembled arrays with a well-defined orientation of the NC crystallographic axis relative to external parameters, such as an applied magnetic field and the observation direction [119] are also very interesting in order to investigate the optical properties of ensembles without dealing with orientational considerations.

I.3.4 CdSe/CdS dot-in-rods

We have presented the principal ideas about the photophysics of bare CdSe spherical nanocrystals and the effects of adding a capping layer of a given semiconductor around it. Spherical CdSe/CdS nanocrystals presents several differences compared to the bare CdSe model[21] due to the quasi type II band alignment and the possibility of alloying formation at the core shell interface for some synthesis. Moreover, we described some peculiarities of the nanorods crystals caused by their shape anisotropy. With this knowledge, we will review in the following the properties of CdSe/CdS dot-in-rods made of a spherical CdSe core embedded inside a rod-like shell, synthesized using the seeded growth approach developed by Carbone et al. [25].

Synthesis

The controlled synthesis of particles with shapes other than spherical [27] started in 2000 with the synthesis of CdSe nanorods. The specific adsorption of surfactants to the individual crystallographic planes can alter the relative growth rates of different facets, providing a way of controlling the nanocrystal shape. It was soon realized that the optical

[21] CdSe/ZnS nanocrystals are close to the bare CdSe model due to the strong type I confinement conferred by the ZnS shell.

properties were different from spherical CdSe particles and that changing the shape could help in having new optical properties and in testing the theories on quantum confinement. As already stated before, linear polarization of nanorods emission was reported [20].

Soon after, particles of mixed[22] dimensionality [24] were synthesized: the so-called CdSe/CdS dot-in-rods. CdS shells were grown on CdSe cores by slowly adding a solution of cadmium and sulfur precursors to a diluted dispersion of already prepared CdSe cores at temperatures between 120 $°C$ and 150 $°C$.

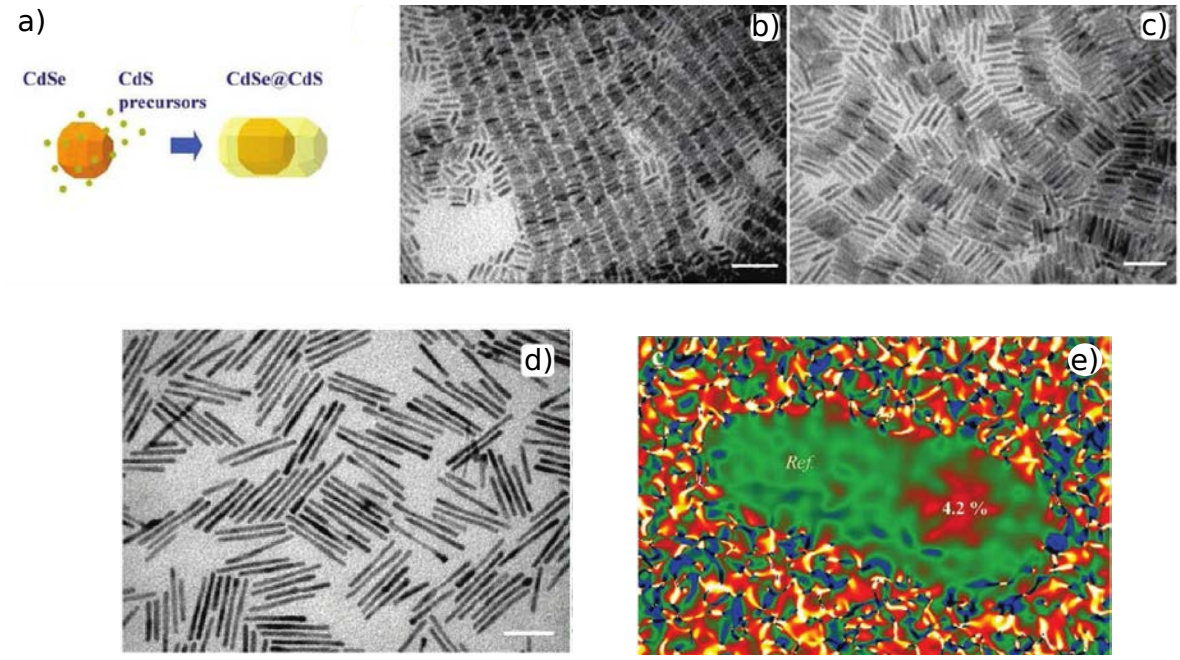

Figure I.14: Synthesis and transmission electron microscope images. Reproduced from reference [25]. *a) Sketch of the seeded growth approach. b) Shell thickness* $t = 4.9 \pm 0.7$ *nm and length* $l = 19 \pm 1$ *nm. c)* $t = 4.2 \pm 0.4$ *nm and* $l = 35 \pm 2$ *nm. d)* $t = 3.8 \pm 0.3$ *nm and* $l = 70 \pm 4$ *nm. e) Mean dilatation mapping from high-resolution electron microscope images.Areas of the same color are regions with the same periodicity. It shows an area corresponding to the CdSe core with lattice parameters altered by* 4.2% *with respect to the reference area, situated at the opposite tip of the rod.*

In 2007, Carbone et al. [25] reported the synthesis of CdSe/CdS dot-in-rods with a new procedure: the seeded-growth approach. It relies on the rapid injection of spherical CdSe seeds and elemental sulfur dissolved in hydrophobic TOP (trioctylphosphine), into a solution of CdO in a mixture of TOPO (trioctylphosphine oxide), hexylphosphonic acid and octadecylphosphonic acid at high temperature ($350-380\ °C$). In reference [25] aspect ratios as high as 30:1 are obtained, much larger than with previous synthetic method. High quantum yields values in solution ($70-75\%$) are measured, comparable to state of the art spherical CdSe/CdS nanocrystals. The seeded-growth synthesis results in more

[22]The term mixed dimensionality was used to state that electron and holes should have very different degree of confinement in this heterostructure.

homogeneous samples compared to previous synthesis and is flexible, many parameters can be tuned in order to control the morphology of the resulting DR. The mean rod diameter can be tuned with the growth temperature, higher temperatures resulting in thicker shell. The rod length can be varied not only by the amount of precursors and/or seeds added, but also by the growth temperature and/or the reaction time. In both cases, the size of the seeds plays an important role: small seeds, for example, tend to form long and thin rods. However, growing a DR with specified parameters of core diameter, rod thickness and rod length requires a careful tuning of all synthesis parameters such that there are limitations to the growth process. For example it is very difficult to grow a thick shell on a small dot. In section I.4 below, we present the samples studied in this thesis that represent the state of the art in growing thick shells for dot-in-rods.

Fig.I.14 presents some TEM images of different synthesis realized by Carbone et al. [25], the thickness t and length l of the rods are given in the caption. The size homogeneity of the various samples is clearly visible. Also an image of the lattice deformation is given in Fig.I.14e which indicates the position of the core. It shows that the CdSe region is rarely localized near the tips of the rods nor at the center, but in most cases between 1/3 and 1/4 of the overall rod length.

Absorption and emission spectra

Typical absorption and emission spectra from an ensemble of dot-in-rods in solution are shown in Fig.I.15. The dark blue line is the absorption curve, it is very similar to the absorption curve (dash, light blue line) of CdS rods only. The very steep absorption onset below 500 nm is characteristic of CdS absorption. The slight shift between the two curves is due to different geometrical parameters of the two samples [120]. In reference [120], they estimate by comparing the absorption spectra of the bare CdSe seeds and of the dot-in-rod that the core contribution to the absorption at high energies ($< 500nm$) is lower than 5%. The CdS shell with its rod shape and large material amount dominates the absorption curve of dot-in-rods. In the inset we show the absorption and emission of bare CdSe seeds used in this synthesis. The absorption peak at lower energy (590 nm) of the CdSe/CdS sample can be associated to the first electronic transition of the CdSe seeds as it is not present in the CdS nanorods. It is red-shifted with respect to the corresponding transition in the seed (557 nm) due to the lower confinement induced by the shell.

Theoretical absorption spectra were calculated in reference [25] for CdSe embedded in a hexagonal prism of CdS and considering a zero conduction band offset. They confirm the experimental spectra and show that the high energy peaks can be ascribed to the absorption from the CdS shell. The lowest energy peak is due to transitions from the holes

confined in the CdSe core and the electrons delocalized throughout the whole nanocrystal structure[23] because of the small conduction band offset.

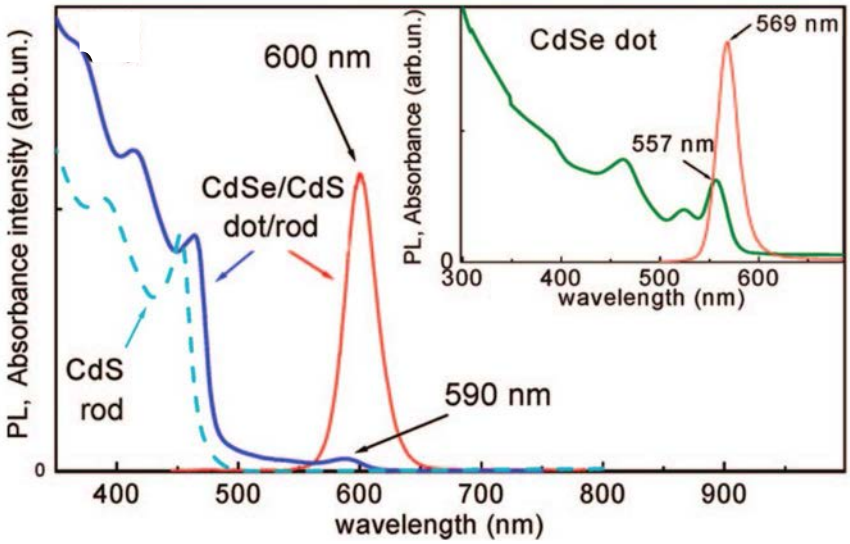

Figure I.15: Absorption and emission spectra of dot-in-rods. *Absorption (blue line) and photoluminescence emission spectra (red line) of CdSe/CdS dot-in-rods. Dashed blue line is the absorption of a CdS rod. Inset: Absorption and photoluminescence of only CdSe cores. Figure reproduced from reference [120].*

The photoluminescence emission originates from states related to the CdSe core. This is experimentally confirmed by two observations:

- The emission peak is red-shifted with respect to the lowest CdSe absorption peak (Stokes shift) by the same amount than in core only CdSe nanocrystals and is shell independent [25,121] . For example, in Fig.I.15, the dot-in-rods photoluminescence peak is at 600 nm and the absorption edge at 590 nm, while it is at 569 nm and 557 nm for bare CdSe dots.

- In reference [25], a phonon replica at 26 meV has been observed in PLE measurements, this is exactly the same energy shift than for spherical CdSe dots.

Relaxation of the hole from the shell towards the core [120] is very efficient (ps timescales) as well as relaxation of the electron towards the band edge [24]. It follows that the exciton photoluminescence emission always comes from the band edge exciton $1S_{3/2}1S_e$ as for bare CdSe dots, a single peak in the photoluminescence emission spectra is therefore visible on Fig.I.15.

One major difference with bare CdSe dots or CdSe/ZnS core/shell structures is the fact that Auger recombination can be drastically reduced in CdSe/CdS heterostructures.

[23]This point is detailed in the following section on electron delocalization.

We have already detailed in section I.2.2 the different strategies that can lead to a modification of Auger processes efficiency: the exciton size, the core/shell interface potential (smooth or abrupt) and the charges distance with the surface. All these parameters can be controlled using a CdS shell as the electron can be delocalized inside the shell, a graded alloying of CdSe and CdS can be favored by the synthesis and finally large shell can be grown thanks to the small lattice mismatch. Hence, the multiexciton emission is clearly visible in these structures at high excitation power and have been reported in different works [61, 101], an example is shown below on Fig.I.16 for three different CdSe/CdS dot-in-rods.

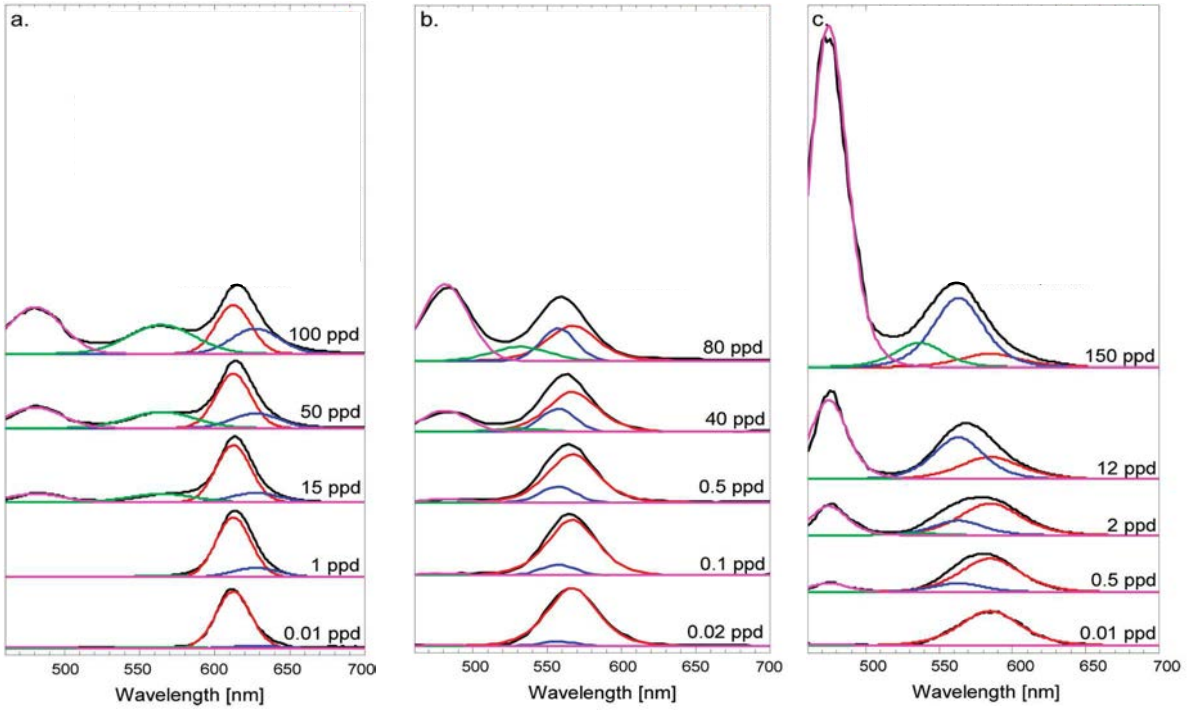

Figure I.16: CdSe/CdS dot-in-rods emission spectra at low and high excitation power. *a), b) and c) are spectra taken for different samples of dot-in-rods, the black line is the measured spectrum while the other lines are fits. Red line: X, blue line: 2X, green line: 3X and purple line: emission from the CdS rod. ppd: particle per dot, which means number of excited excitons. Figure reproduced from reference [101].*

Electron delocalization

As the band offset between CdSe and CdS is fairly small, some discrepancies are present in the literature about its measured value. The small offset implies that it might be dependent on the synthesis procedure, on the geometry of the heterostructure also. Consequently different observations for different systems lead to different conclusions about CdSe/CdSe nanocrystals. Consequently, different conclusions on electron localization inside these structures have been made. However it is widely accepted that the electron in

this kind of structure is largely spreading inside the shell, to which amount will depend on the specific structure.

The electron delocalization is confirmed by many aspects of CdSe/CdS heterostructure photoluminescence. First the lifetime of the emission is considerably longer than in CdSe/ZnS for which strong confinement of both carrier species is realized. For CdSe/ZnS, typical exciton lifetime of 20 ns are measured. For CdSe/CdS, once again it depends on the structures observed but exciton lifetime up to 100 ns have been reported [25, 86]. Also an increase of the exciton lifetime during shell growth [19,86] from 20 to 60 ns have been noticed. Spectrally, CdSe/CdS structures often exhibit a certain photoluminescence red-shift compared to the bare CdSe seeds as can be observed on Fig.I.15 for which the photoluminescence peak shift from 569 nm to 600 nm. This is a proof of a lower confinement of the charges due to the CdS shell growth. The red-shift increases with rod thickness and decreases with increasing core diameter [122]. The effect of the core diameter is also seen on the lifetime measurements for which smaller cores at a fixed rod diameter yield longer lifetimes [123].

Sitt et al. [101] measured the photoluminescence spectra of CdSe/CdS dot-in-rods at high excitation. Measuring the energy difference between the biexciton and the exciton peak, one can deduce the electron localization as already explained in paragraph I.3.1 on the different type of heterostructures. A transition from a prevalently type-II to a prevalently type-I regime for a core diameter of 2.7 nm[24] was found.

Finally, more direct measurements of the electron wavefunction localization [120,124, 125] involving pump-probe experiments suggest electron delocalization. Even if exciting only the core, a transient bleaching of the absorption in the shell is observed. This means that either the electron or the hole levels of the CdS shell are populated directly by the core absorption. In reference [125], a trend towards electron localization for larger cores with increasing dot size was noticed as in reference [101, 122].

Electric fields and dot-in-rods

Surface properties are expected to play an important role in dot-in-rods emission properties for the same reasons exposed in section I.3.3 on nanorods. In dot-in-rods the charge fluctuations can strongly influence the electronic level structure via quantum confined Stark effect (QCSE). QCSE is particularly efficient due to the possibility of large electron delocalization. By breaking the symmetry of the particle with the hole trapped in the CdSe core at one end and the elongated shell on top, a preferential direction for the redistribution of surface charge is given. The role of surface charges in dot-in-rods on the emission properties have been studied in two papers [105, 126]. In reference [126], it was

[24]However, in these measurements both the shell thickness and the length change for each core sample.

shown that if a charge is close to the core, the photoluminescence peak is red-shifted and broadened by the Stark effect, while if the charge is localized far away, photoluminescence is at higher energies and less broadened. The degree of spectral redshift, provides a measure of the spatial position and the magnitude of surface charge. The effect of an external electric field has also been studied to tailor the wavefunction distribution [105]. A longer lifetime connected with a reduction of the charge overlap is associated with a red-shift because of the band bending induced by the electric field as already depicted on Fig.I.13 for nanorods.

A permanent dipole moment exists in spherical nanocrystals and nanorods [106, 127]. This permanent ground-state dipole moment along the c crystallographic axis is due to the anistropy of the wurtzite structure as already described. It was found to scale with the nanostructure volume [127] for nanorods. The dipole moment is responsible for the dot-in-rod/dot-in-rod interactions and makes them sensitive to the electric fields. Self-assembling procedures can be based on this intrinsic property [25, 128]. Also, in heterostructures such as dot-in-rods, an extra contribution to the internal field could come from the piezoelectric polarization induced by the elastic strain due to the lattice mismatch between CdSe and CdS at the heterostructure interface [106].

Electronic structure

The uncertainties on the electron behavior in CdSe/CdS structures due to the small conduction band offset between CdSe and CdS and the number of parameters that can potentially play a role in defining its value precisely implies that no clear model of the whole electronic structure exists for dot-in-rods.

In the following part we briefly review the main ideas present in the literature on the electronic structure of dot-in-rods. Reference [101] concentrates on the effects of the geometry. They assumed a conduction band offset $\Delta = 0.3$ eV and calculated the first excited states. The second electronic level should be always delocalized in the CdS shell whatever the geometry, while the band edge level may be localized into the core or delocalized, depending on the core size. These findings are summarized on Fig.I.17. According to these calculations, it is apparent that the first energy state becomes more energetic than the CdS bandgap for cores smaller than $d = 3.2$ nm in diameter. One can also see in the inset that the electron is always centered around the core (situated at a position of -10 nm), but for the smaller core of diameter 2 nm it is largely spreading in the shell (FWHM of approximately 8 nm).

Reference [129] takes into account possible strain effects between core and shell, creating a quasi-type II conduction band offset. This leads to results similar to reference [101]. The band gap should also depend on the kind of atoms which are on the shell surface.

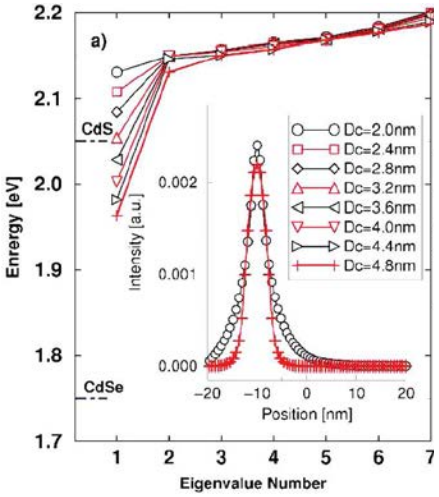

Figure I.17: CdSe/CdS dot-in-rods electronic structure. *First seven electronic levels as a function of the core diameter D_c. Inset: first electronic wave function along the main axis of the rod for $D_c = 2.0$ and 4.8 nm, the core is centered at -10 nm. Length of the rod is 40 nm and thickness 6 nm for all calculations. Figure reproduced from reference [101].*

For our purpose in the following, one should remember that the exciton photoluminescence comes only from the band-edge $1S_{3/2}1S_e$ exciton as already explained and the exact behavior of the electron wavefunction and energy remaining difficult to appreciate and very dependent on the structure geometry and synthesis.

Fine structure The fine structure exact ordering and energy shifts are also difficult to model. First for the same reason than the global electronic structure, because the fine structure level degeneracy lift depends on the electron-hole exchange interaction and so on the electron wavefunction localization. Secondly for dot-in-rods in particular, the sphericity of the CdSe core might change during the synthesis due to anisotropic strain effects imposed by the asymmetry of the shell during the growth process. This would in turn change the intrinsic crystal field of spherical particles as already seen for the prolate nanocrystals and nanorods cases described earlier in this chapter. Finally, we can also think about other potential sources of internal electric field in the structure: piezoelectric polarization due to strain [106], presence of permanent surface charges [126], that might also change the fine level splitting and ordering.

First, let us describe the situation for perfectly spherical wurtzite CdSe/CdS nanocrystals. The level ordering is the same than for bare CdSe or CdSe/ZnS nanocrystals that is described in section I.1.2. The energy shift between levels is expected to be smaller as the electron confinement is weaker, implying a smaller electron-hole exchange interaction. Reference [130] calculates the exchange interaction for CdSe/CdS with different conduction band offset. The exchange interaction defines the energy shift between the lower

dark exciton state $|\pm 2\rangle$ and the first bright exciton $|\pm 1^L\rangle$: dark-bright splitting (Δ_{db}). This was experimentally verified in reference [131], studying CdSe/CdS nanocrystals with a core radius $R = 1.5$ nm and different shell thicknesses: 4, 7, 14 and 19 CdS monolayers (corresponding to 1.6, 2.8, 5.6 and 7.6 nm of additional material). Using lifetime measurements at different temperatures, fluorescence line narrowing and measurements under magnetic field, they reported a dark-bright splitting decrease from 2 meV to 0.27 meV going from the thinner to the thicker shell (electron-hole overlap decreases from 1 to 0.2).

Concerning dot-in-rods, a recent comprehensive article [119] presents fluorescence line narrowing (FLN) measurements for CdSe/CdS dot-in-rods at cryogenic temperature. They synthesized their nanocrystals following the seeded growth methodology of Carbone et al. [25]. They obtained particles with the following geometry: a core of $d = 3.2$ nm with a shell of $l = 39.8 \pm 1.7$ nm and $t = 4.3 \pm 0.5$ nm. FLN is an ensemble measurement method for which inhomogeneous broadening is reduced thanks to the selective excitation of only a narrow subset of the ensemble. However it is still sensitive to alignment problem of the nanocrystals, especially when involving magnetic fields. In this article they ingeniously used aligned dot-in-rods ensemble and obtained very precise measurements of the spectral properties and dependencies on the magnetic fields. They came to the conclusion that the fine structure of their dot-in-rods is the same as a spherical CdSe/CdS structure, they witness a leakage of the electron wavefunction and an associated lower dark-bright splitting compared to the bare CdSe core as already described for the spherical case above. So besides the small delocalization of the electron (as for spherical shell), the growth of the rod like shell has no effects on the fine structure in this case.

The group of Rainer F. Mahrt in Gent has published various articles [122, 132, 133] on dot-in-rods emission at cryogenic temperatures. They use a model of the fine structure with the level ordering depicted for prolate nanocrystals and nanorods in section I.1.2 and I.3.3, for which a reordering of the states compared to the normal spherical ordering exists for small cores. This model was used because the core seeds they synthesize shows a slight ellipticity ($\mu = 0.15$) on electron microscope images. While previous work expect level reordering for stronger ellipticities, their calculations [132] demonstrate that it was enough to imply a level reordering. They demonstrated, as depicted above for spherical nanocrystals, that the fine structure splitting can be controlled by varying the core and/or the rod diameter [122]. In particular, samples having a small core diameter and/or a thick rod diameter exhibit a strongly reduced energy splitting because of a reduced electron-hole exchange interaction. The work by Fernée et al. [58] where the different lines are observed at 2 K and selectively excited, demonstrates experimentally the level reordering for a larger ellipticity: $\mu = 0.6$.

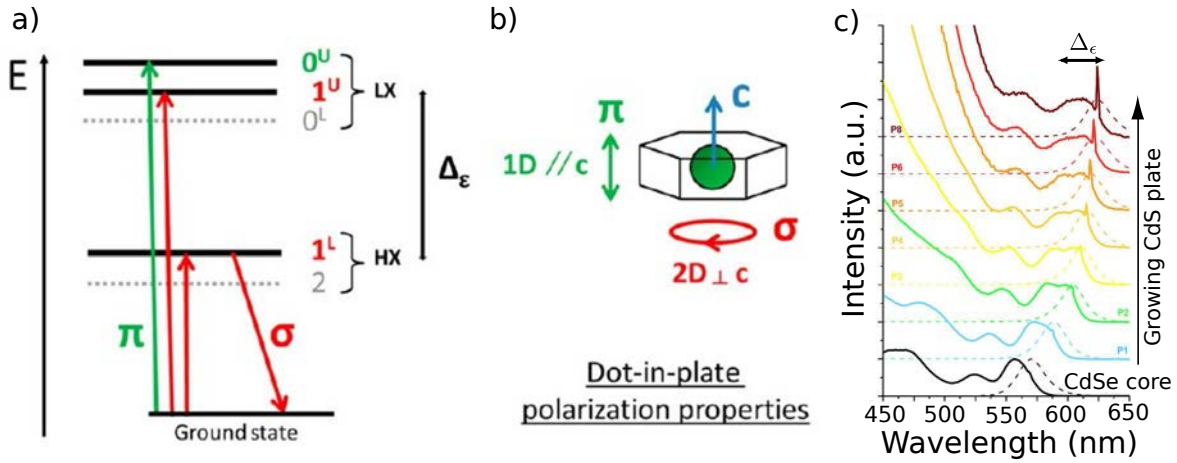

Figure I.18: CdSe/CdS dot-in-plates exciton fine structure. *a) The exciton fine structure shows the usual level ordering of spherical CdSe/CdS particles except that the splitting between the heavy hole and light hole levels called* $\Delta\epsilon$ *can reach higher values: 70 meV compared to 20 meV usually. b) Dot-in-plate schematics, the plate has its main plane perpendicular to the c axis of the core. c) Absorption from PLE (full line) and photoluminescence (dash line) spectra taken during the anisotropic shell growth. CdSe core (d = 3.2 nm) spectrum is in black and the lines from blue to brown represent the different shell sizes (1-6, 8 equivalent CdS monolayers). The sharp peaks in PLE spectra correspond to scattered light at the detection wavelength. Figure reproduced from reference [22].*

Finally, an interesting work has been conducted on the so called CdSe/CdS dot-in-plates. These particles are CdSe dots embedded inside CdS plate structures that confines the carriers only in one dimension [22, 23]. A sketch of such a particle is given in Fig.I.18b. The synthesis is such that the plate growth is quasi-two-dimensional, along directions perpendicular to the c axis. These particles spontaneously align in a controlled crystalline orientation when deposited on a substrate, such that the c axis orientation is well defined. Besides that they display a particular exciton fine structure. The exciton fine structure is split in two distinct transitions at room temperature as schematically shown on Fig.I.18a. The level ordering is the same as for spherical CdSe/CdS nanocrystals but the splitting between the levels coming from the heavy hole and light holes sub-bands Δ_ϵ is considerably enhanced as depicted on Fig.I.18a. It goes up to 70 meV (compared to 20 meV usually), such that even at room temperature, only the $|\pm 1\rangle$ and $|\pm 2\rangle$ are populated. The increase in Δ_ϵ is visible on Fig.I.18c, the bandedge exciton absorption peak is enlarged during the shell growth compared to the core only band-edge absorption. The anisotropic pressure of the shell on the spherical core is at the origin of this enhanced splitting, as demonstrated by calculation and modification of the shell parameters (addition of a ZnS layer that increases further the strain). The strain has the same effect than an oblate[25] CdSe core on the fine structure [32]. If strains play a role in

[25]Elongated in the plane perpendicular to the c axis conversely to prolate

the case of dot-in-rods, its effect should be converse to this case and lead eventually to level reordering as in the prolate/nanorod cases.

Polarization A high degree of linear polarization of dot-in-rods emission has been measured since the first synthesis of such particles [24,25]. Different factors can contribute to a measured degree of linear polarization value. Among them, factors that are not intrinsic to the emitter but rather to the measurement itself. This is detailed in chapter II for single particle measurements. It needs to be properly taken into account when discussing the results about polarization and comparing different articles found in the literature. Let us detail the intrinsic emitter properties that contribute to the polarization of the emitted photons:

- the fine structure of the band-edge exciton. As already described in section I.1.2 and I.3.3 on the fine structure of spherical and rod shape CdSe nanocrystals, the various transitions have different angular momentum that either gives linearly or circularly polarized light when radiatively relaxing. The level ordering, spacing and oscillator strengths will then impact the linear polarization measured. We emphasize one more time the fact that a small ellipticity could change the fine structure level ordering.

- Dielectric effects due to the anisotropy of the shell that favors electric fields in specific directions.

The polarization brings several questions concerning dot-in-rods exciton fine structure. If the electronic structure in dot-in-rods is such that it is exactly the same than in spherical CdSe/CdS dots as shown in reference [119], why do they show such a high degree of linear polarization compared to spherical dots? This would mean that the polarization only comes from dielectric effects. If the cores are intrinsically slightly prolate or if it is induced by the shell growth then level reordering could favor the linearly polarized $|0^U\rangle$ transition as in nanorods.

In chapter V we will review the literature on the subject and present polarization measurements on different samples of dot-in-rods.

I.4 Studied Samples

In this section, the various dot-in-rods samples studied in the manuscript are presented. They have been analyzed in details, either because they have demonstrated remarkable optical properties or because they are useful to better understand some specific properties

of dot-in-rods. They have been produced by the seeded-growth approach in the group of Luigi Carbone[26] in Lecce, Italy.

I.4.1 Samples geometry

Tab.I.1 presents the geometrical parameters of six samples. The samples name that we will use throughout this thesis follows a "certain" logic. As already foreseen in this chapter, the main geometrical parameters defining the dot-in-rods optical properties are the core diameter d and the shell thickness t rather than the length of the rod. We will therefore call the samples by increasing core diameters and shell thickness order. DR1 has the smallest shell thickness and core diameter, conversely DR4 has the largest values. There are three samples named DR3, they differ only in their shell lengths such that DR3.1 has the smallest shell and DR3.3 the longest.

	Core diameter d (nm)	Shell thickness t (nm)	Shell length l (nm)	Growth temperature (°C)	Growth time (min)
DR1 	2	3.6	51	350	8
DR2 	3.3	4	22	350	8
DR3.1 	3.3	7	22	350	20
DR3.2 	3.3	7	35	380	20
DR3.3 	3.3	7	58	350	40
DR4 	4.6	11	29	360	8

Table I.1: Samples geometry and synthesis parameters. *The shell geometrical parameters are taken from statistical analysis of TEM images. The core diameter is determined prior the addition of the shell thanks to ensemble photoluminescence spectra. Uncertainties on the geometrical parameters are of* $\pm 10\%$.

The core diameters are extracted by optical absorption and emission ensemble measurements [134] taken after their synthesis before the addition of a shell. The shell thickness and length are determined from TEM images such as in Fig.I.14, averaging on hundred nanocrystals. The shell dimensions are less than 10% dispersed. The traditional synthesis protocol [25] has been modified in order to thicken the shell size [135], for exam-

[26] http://www.nano.cnr.it/index.php?ente=globale

ple DR3.1, 3.2 and 3.3 have a total DR thickness of $t = 7$ nm against a thinner standard thickness of $t = 4$ nm obtained for DR2 using the same seed.

I.4.2 Samples spectra

Ensemble absorption and photoluminescence emission spectra are measured in solution using a spectrophotometer. They lead to curves as in Fig.I.15. Tab.I.2 resumes the spectral information about each samples: the photoluminescence peak position for the dot-in-rod and its seed, the corresponding shift and the full width at half maximum (FWHM) of the emission peak.

	Core diameter d (nm)	Core PL peak (nm)	Shell thickness t (nm)	Shell length l (nm)	DR PL peak (nm)	FWHM (nm)	Red-shift (nm)
DR1 	2	500	3.6	51	587	> 50	> 100
DR2 	3.3	580	4	22	605	33	25 (81 meV)
DR3.1 	3.3	580	7	22	605	30	25 (81 meV)
DR3.2 	3.3	580	7	35	600	27	20 (65 meV)
DR3.3 	3.3	580	7	58	595	23	15 (49 meV)
DR4 	4.6	613	11	29	665	30	52 (145 meV)

Table I.2: Samples geometry and spectral features. *The spectral features are taken from ensemble measurements such as in Fig.I.15.*

Each sample emits around 600 nm (orange), except DR4 whose emission is centered at 665 nm (red) due to its larger core. They all exhibit a certain red-shift compared to the bare seeds due to electron wavefunction delocalization during the CdS shell growth process. The photoluminescence red-shift of the dot-in-rods with respect to the core-only systems confirms the quasi-type II model for CdSe/CdS heterostructures. As the confinement energy decreases with the shell growth, the electron spreads inside the shell. A larger red-shift is therefore an indicator of a prevalent type II electron delocalization, while a smaller red-shift indicates that the electron is more localized into the core. Whereas it has the stronger confinement potential, the sample with the smallest core size DR1 ($d = 2$ nm) has the maximum red-shift (> 100 nm). This is not contradictory because the valence band offset is small, therefore the first quantized energy level

can easily spread all over the structure. The sample with the largest core $d = 4.6$ nm DR4 shows also an important red-shift, while it is minimal (15-25 nm) for the group of dot-in-rods with $d = 3.3$ nm. Moreover in samples with the same core and shell thickness but different lengths (DR3.1, DR3.2 and DR3.3), the red-shift decreases with the shell length. With respect to previous studies on dot-in-rods [101], these results suggest that the wavefunction delocalization is not determined only by the core size, but also by the shell size, providing additional degrees of freedom for wavefunction engineering in dot-in-rods with respect to spherical CdSe/CdS nanoparticles [135].

Finally, the photoluminescence FWHM reported in Tab.I.2 comes from ensemble measurements at room temperature. Typical values of 30 nm are measured. However these values include inhomogeneous broadening coming from dot to dot disparities, the photoluminescence peak dispersion originating from size and geometry differences. We also measured single dot-in-rod spectra by sending their photoluminescence to a spectrometer equipped with a high sensitivity CCD camera. Single dot-in-rods spectra are narrower than the ensemble spectra, the full-width half maximum from a Gaussian fit is in general 20 nm, typical dispersion is within ± 10 nm around the average value. This implies that the width of the ensemble spectra is only partially due to the inhomogeneous broadening. Sources of the 20 nm homogeneous broadening of single dot-in-rods photoluminescence spectra at room temperature is due to the presence of phonons and spectral diffusion induced by fluctuations of surface charges[27].

Conclusion

In this chapter we laid the foundations for the discussions of the forthcoming chapters. We started by presenting the photophysics of bare spherical CdSe nanocrystals, from their electronic levels to the various relaxation processes characteristics of these structures. We have seen that the emission is governed by the bandedge $1S_{3/2}1S_e$ exciton that possesses a fine structure. The fine structure plays a major role in the emission polarization properties of nanocrystals and this will be treated in chapter V.

Furthermore, very efficient nonradiative processes called Auger recombinations were introduced. Together with phonons, they explain the fast nonradiative relaxation of excitation towards the band edge exciton. We have briefly presented the charge trapping in nanocrystals and mentioned its connection to Auger ionization. The various species of potential emission states (exciton, trion, multiexciton) have been defined, together with the notion of quantum yield that quantifies their probability of emitting a photon. Trap-

[27]The emission line is wandering around a typical mean value on fast timescales, acquisition of a spectrum over a long period implies a broadening of the spectrum due to the line movement [136].

ping, trion and multiexciton state, Auger recombination are at the heart of nanocrystals emission intermittency and photon statistics. These topics are treated in great details in chapter III and IV. We presented the effects of the addition of a shell around a CdSe spherical core. The case of the addition of a CdS shell was presented in great details. We have seen that many aspects of CdSe/CdS dot-in-rods emission are still open questions in the literature.

Finally, the specificities of dot-in-rods compared to spherical particles (larger absorption, polarization of the emission, rod shape for positioning) were highlighted in this chapter.

Chapter II
Experimental setup and methods

Introduction

Single emitter spectroscopy is a powerful and interesting tool to study the photophysics of nanoemitters as it removes the usual ensemble average. Hidden information by ensemble measurements have been successfully revealed by single emitters spectroscopy [137]. A striking example concerning colloidal nanocrystals was the discovery that their fluorescence turns on and off intermittently [15], phenomenon that was unknown from ensemble measurements. Various experimental methods [138] have been developed to study the fluorescence of single emitters such as molecules or quantum dots during the last twenty years. Near-field scanning optical microscopy (SNOM), confocal microscopy and wide-field methods have been employed to detect single emitters fluorescence [139, 140].

First, we present the microscopy setup used to perform standard fluorescence measurements and polarization resolved measurements. The collection efficiencies expected with the different setup configurations are given.

The second part of this chapter explains the different experimental methods that we employed in order to make fruitful measurements. We first describe the sample preparation and the criteria by which we judge the quality of a sample. As we are dealing with single photon emitters, hence small signals to detect, the noise is a key parameter to control before starting the experiment. We explain the different sources of noise and typical value of signal to noise ratio for our experiments. The photoluminescence of dot-in-rods is strongly dependent on the excitation. We introduce a model to infer dot-in-rods excitation from saturation curve measurements. Finally, we explain how we register and process data to extract useful information about dot-in-rods emission properties.

II.1 Setup description

II.1.1 Standard microscopy setup

The experimental setup is depicted in Fig.II.1. Two excitation schemes can be used, either the sample is excited by a non-collimated UV lamp and a broad area of the sample is illuminated (wide-field microscopy) or a tightly focused pulsed laser is used to excite one specific dot-in-rod of the sample. These two specific schemes are described more thorough fully below. The sample is mounted on a stage with a coarse xy plane displacement possibility such that the whole sample can be investigated. The objective is screwed on a xyz piezoelectric stage (Tritor3D-102, PiezoSystem Jena) with a 100 nm displacement resolution for a precise alignment of the laser excitation on a chosen dot-in-rod. The excitation light in the blue region of the spectrum is reflected towards the sample by means of a dichroic mirror. The collected light by the objective from the sample (wavelength around 600 nm) is then sent towards the measurement apparatus. A filter is placed in the beam path to remove the excitation stray light (usually a long pass filter with a cutoff at 570 nm). The collected light can be imaged on a high quantum efficiency CCD camera, or sent to a pair of avalanche photodiodes (APDs) in a Hanbury Brown-Twiss (HBT) configuration able to record single photon events. A spectrum of the sample photoluminescence can also be realized with a spectrometer (Princeton Instrument Acton SP 2500 equipped with a high quantum efficiency CCD camera Princeton Instrument Pixis 400). The collected photoluminescence can be spatially filtered by a pinhole of tunable size that is placed in the beam path.

Wide-field microscopy

In the wide-field configuration, a large area of the sample is excited by focusing the non-collimated UV lamp (Mercury-vapor lamp) light beam through the objective. A filter spectrally selects a band between 460 nm and 490 nm out of the broad luminescence spectra of this UV lamp. The fluorescence from each nanocrystal is back-collected and spectrally isolated from residual scattered excitation light using the dichroic mirror and further the spectral filter.

The fluorescence is imaged on the CCD camera in our case, thus giving an overview of the sample. The fluorescence light could also be sent to the APDs for ensemble measurements without spatially filtering through a pinhole. In this thesis we mostly deal with single particles measurements, the wide-field microscopy has only been used to image the samples on the CCD camera.The wide-field excitation can cover the full CCD camera chip (CoolSnap ES, Roper Scientific, 1040×1392 pixels, pixels width 6.45 μm,

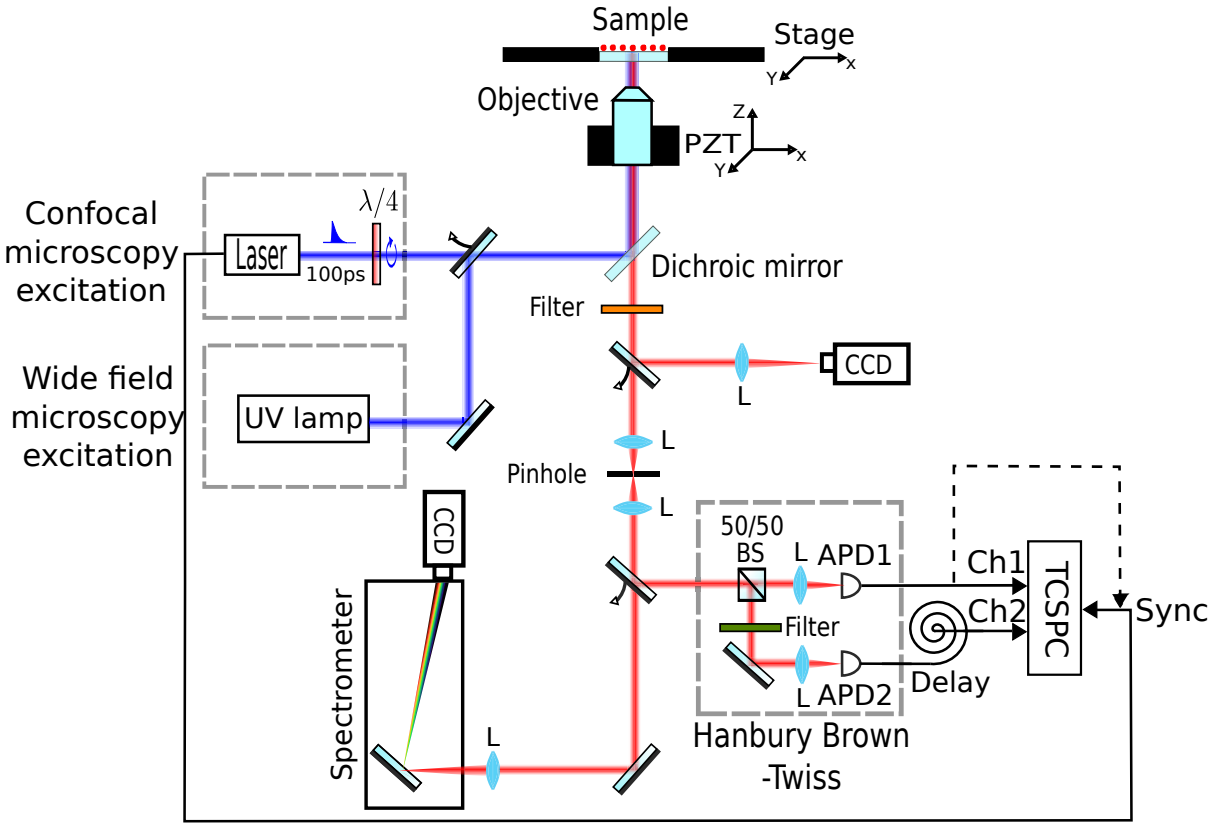

Figure II.1: Experimental setup. *Wide field microscopy can be realized by exciting the sample with a UV lamp. In this case, a CCD camera is used to image the excited area of the sample. Circularly polarized light from a picosecond-pulsed excitation laser diode with a wavelength of* 404 *nm, a pulse width of* 100 *ps and a repetition rate of* 2.5 *MHz is used to excite single dot-in-rods. A confocal microscope collects the dot-in-rods photoluminescence. A long pass filter (cutoff* 570 *nm) removes the remaining blue light from the optical path. Single photons events are recorded by two avalanche photodiodes in a Hanbury-Brown and Twiss configuration. A spectrum of the emission can also be registered by a spectrometer .λ/4: Quarter wave plate. BS: Beam Splitter. APD: Avalanche photodiode. L: Lens. TCSPC: Time-Correlated Single Photon Counting.*

quantum efficiency: 60% at 600 nm) with a 60× magnification objective, so the excitation is at least covering a 112 × 150 μm area.

A diaphragm at the output of the UV lamp can change the beam size and thus the excitation region if necessary. Having a smaller excited region can be helpful to reduce the background noise. Finally, the power of the lamp can be controlled via the integrated optics (Olympus Lamp Housing for 100 W Mercury Burner).

Confocal microscopy

Confocal microscopy can be realized with our setup. We use a picosecond pulsed diode laser (PDL 800-B, PicoQuant), emitting at 405 nm with a repetition rate of 2.5 MHz for room temperature measurements (delay between two pulses: 400 ns) and pulse width

of 100 ps. The laser beam is coupled to a single mode fiber in order to clean the beam shape. We can control the beam output coupling using an adjustable collimator, implying a tunable beam size on the sample. Fig.II.2 shows an image of the laser beam on the sample. The background scattering scales with the illumination area, a smaller spot size reducing the background noise. For standard room temperature measurements we use a high-NA immersion objective (N.A.= 1.4, 100×). The high collection efficiency of this objective (see section II.1.4) together with the high quantum efficiency of the dot-in-rods implies that a good signal to noise ratio is achieved in this setup configuration as presented afterwards in II.2.2. For a good stability of the excitation together with the ease of use we decided to work with a slightly larger laser beam than a diffraction limited one at the focal point, 1 μm of full width at half maximum as shown on Fig.II.2.

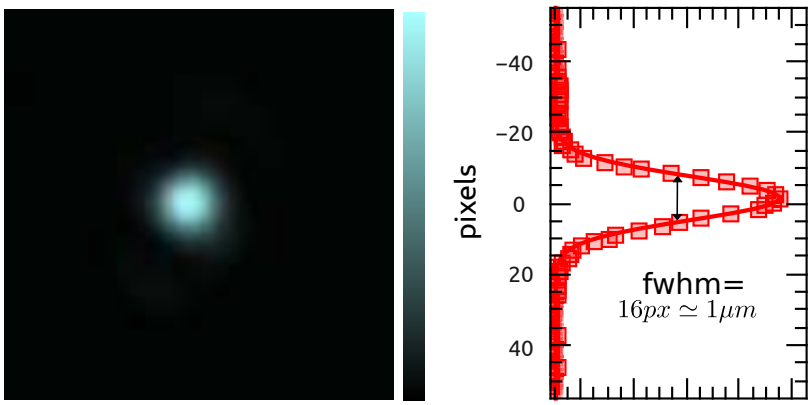

Figure II.2: CCD camera image of the laser spot on the sample. *The transverse profile of the spot can be well fitted by a Gaussian distribution, the full width at half maximum (FWHM) is of* 16 *pixels which corresponds to* 1 μm *with the* 100× *oil immersion objective used.*

The collected luminescence is then spectrally and spatially filtered with a spectral filter (long pass filter, cutoff 570 nm) and a pinhole respectively. The pinhole aperture is located at the microscope image plane. It spatially rejects out-of-focal-plane light. Small pinhole diameters reduce background noise and give better axial resolution but are more difficult to align and reduce transmission. We worked with a 150 μm pinhole diameter.

The filtered photoluminescence is then collimated by a lens and sent to the single photon detectors (APDs, Excelitas SPCM-AQRH14). Due to their typical dead time of 20 ns, period of time during which the avalanche is produced and quenched rendering photon detection impossible, a HBT configuration with two detectors is needed if one wants to record successive photons arrivals with time intervals shorter than the dead time. In this case a 50/50 beam splitter is used to divide the photoluminescence into two paths, a short pass filter (cutoff 700 nm) is placed inside one of the arms of the

HBT in order to avoid cross talk[1] between the two detectors. Two lenses are used to focus the photoluminescence onto their respective detector, the diameter of the beam is of the order of 50 μm when focused on the APD whose sensitive area is 180 μm large. Such a spot size maximizes the detection probability for these detectors. The last part of the setup concerning the electronics and the acquisition of the signal will be detailed in section II.2.4.

II.1.2 Polarization microscopy

Setup

In order to realize polarization resolved measurements a polarizer made of a half-wave plate on a motorized rotation stage together with a polarizing beam splitter cube are introduced in the confocal microscope beam path before the HBT setup as shown in Fig.II.3a. During measurements the half-wave plate is rotated from a initial position ($\theta_{\lambda/2} = 0°$) at a speed of $2°/s$ to a final position ($\theta_{\lambda/2} = 90°$). The photon count rate at the output of the polarizer follows the Malus' law for a partially polarized beam:

$$I(\theta_{\lambda/2}) = I(pcos^2(\theta_{\lambda/2} + \theta_0) + (1-p)/2) + I_{noise}, \tag{II.1}$$

where p is the degree of linear polarization of the light:

$$p = \frac{I_{max} - I_{min}}{I_{max} + I_{min} - 2I_{noise}}. \tag{II.2}$$

I_{max}, I_{min}, I_{noise} are the measured maximum, minimum and noise count rates and $I = I_{max} + I_{min}$ is the intensity of the light field. A typical measurement is presented in Fig.II.3c that introduces the various quantities of Eq.II.1 and Eq.II.2.

The degree of linear polarization measured for a specific dot-in-rod in Fig.II.3c is $p \simeq 82\%$. For these measurements we used an objective with a high numerical aperture (Olympus Mplan Apo, 100×, N.A.= 0.95) but not an oil immersion objective ($N.A. = 1.4$) as for the standard measurements described in II.1.1. In fact, in this case it is not only the photon collection that we have to take into account but also the measured polarization. The higher the numerical aperture of an objective the broader its angular collection, so the more sensitive it is to polarization distribution anisotropy as described in the next paragraph.

[1] Reemission of lower frequency photons than the excitation on a broad band by one of the detectors that are detected by the second detector.

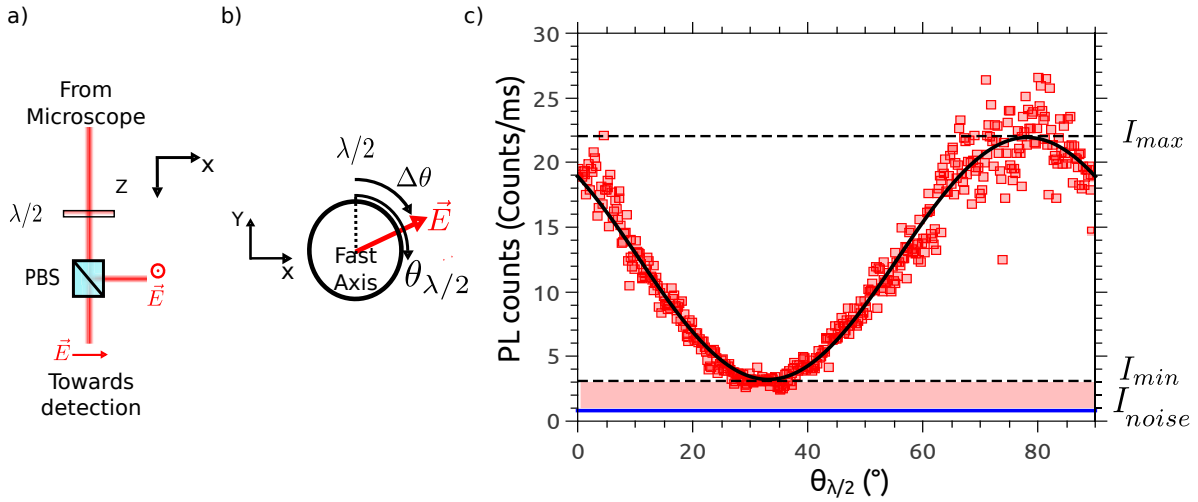

Figure II.3: Polarization setup and a measured curve. *a) Top view of the polarizer made of a half-wave plate ($\lambda/2$) and a polarizing beam-splitter (PBS). One output port of the PBS (horizontal polarization port) is sent to the detection while the other is discarded. b) Scheme of the half-wave plate with its fast axis rotating from $\theta_{\lambda/2} = 0°$ to $\theta_{\lambda/2} = 90°$ at a speed of $2°/s$. A linearly polarized incoming $\vec{E}$ making a $\Delta\theta$ angle with the fast axis will be rotated by $2\Delta\theta$. c) Red squares: typical polarization measurement on a single dot-in-rod with the avalanche photodiodes together with a fit (black line) using Eq.II.1.*

Measured degree of polarization

To give more insights to the reader we present some results obtained in reference [141] on Fig.II.5. Fig.II.5a depicts the different experimental configurations that an experimentalist might encounter. For a given emitter with its associated dipole emission (1D, 2D, degenerate ...), the measured degree of linear polarization of this emitter is highly dependent on the measurement conditions:

1. The electromagnetic environment of the emitter changes the radiation diagram and thus the collected polarization pattern (see Fig.II.4a and b),

2. A larger numerical aperture allows to collect light over a larger solid angle and thus it modifies the collected polarization pattern and measured degree of polarization,

3. The orientation of the emitter compared to the optical axis will change the collected polarization pattern.

The field radiated by a 1D dipole in a given direction of space is linearly polarized, but the polarization spatial distribution is not isotropic, the field oscillates linearly in different directions for different spatial positions. For a 2D dipole for which the charges oscillates in a plane, in a given direction the field is circularly polarized (except in a direction contained inside the dipole oscillation plane where the polarization is linear). In the limit

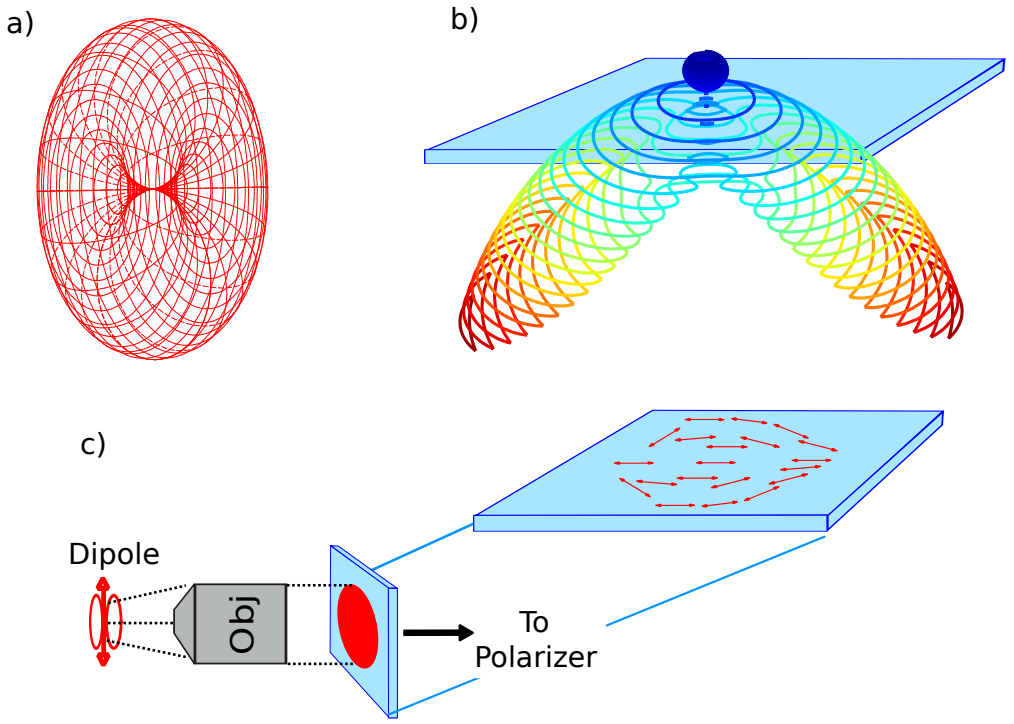

Figure II.4: Dipole radiation patterns and polarization distribution scheme. *a)1D dipole radiation pattern in a homogeneous medium. b) 1D dipole laying on a glass coverslip radiation pattern. c) Schematics of a possible polarization pattern collected by an objective from a radiating dipole. Each arrow represents a linear polarization direction for a specific position inside the light beam transverse profile. This polarization pattern is then sent to a polarizer to measure the degree of linear polarization.*

of a numerical aperture tending to zero[2], a 1D dipole gives a linear degree of polarization of one. Fig.II.4c presents a possible polarization pattern for the light emitted by a 1D dipole and collected by an objective. The polarization is locally linear but the spatial distribution of the polarization is not isotropic. The more the numerical aperture increases the more the polarization distribution will display a diversity of polarization directions as the collection solid angle will be larger. When the light is sent to the polarizer, though it is locally linearly polarized, the measured degree of linear polarization will not be unity due to the anisotropic polarization distribution. If the radiation pattern is changed, from Fig.II.4a to Fig.II.4b for example, then the collected polarization distribution is changed and with it the measured degree of linear polarization.

Fig.II.5b and c present the measured degree of linear polarization p for a 1D dipole against the dipole angle θ with the optical axis for the different experimental configurations depicted on Fig.II.5a and two numerical apertures, $N.A. = 1.4$ in b and $N.A. = 0.7$ in c.

[2]Collecting radiations coming from one specific direction

The different experimental configurations are the following ones:

- (i) The dipole is inside an homogeneous medium and an immersion objective matching the index is used.
- (ii) The dipole is deposited on a planar substrate of index n_1 and protected by a polymer layer of thickness d of same index, observed with an immersion objective, the upper medium (most likely air) being of index n_2.
- (iii) Sample with emitters at a distance d (with d tending towards 0) from a planar surface (substrate index n_2) without any protecting layer, observed with an air objective (air index n_1).
- (iv) A sample with emitters on a planar surface with a polymer protecting layer (index n_1), observed with an air objective (air index n_2).
- (v) A sample with emitters at a distance d (with d tending towards 0) from a planar surface (index n_1) without any protecting layer, observed with an immersion objective (index n_2).

In Fig.II.5b and c we can observe that the degree of linear polarization is zero for a 1D dipole aligned with the optical axis ($\theta = 0°$) for symmetry reasons. For each cases, the degree of linear polarization increases with the angle until reaching a maximum for $\theta = 90°$. One can observe that for the larger numerical aperture the curve rises slower such that it saturates only for θ close to 90°. Thus for dipole orientation determination, it is better to use a high numerical aperture [141] as it is sensitive to the dipole angle on a broader range of angles. We can also observe that the different experimental conditions gives different curves implying that one should always precisely describes the experimental conditions for such measurements. Strikingly, for the $N.A. = 1.4$ case, the maximum degree of polarization is not reaching unity no matter the experimental configuration.

In our case we used a $N.A. = 0.95$ objective for two reasons. First we wanted to measure a degree of linear polarization without being sensitive to slight dot-in-rods vertical orientation disparities with the assumption that dot-in-rods are laying on the glass coverslip with an associated 1D dipole parallel to the rod axis. So reducing the $N.A.$ compared to the standard measurements with the oil immersion objective would help as reducing the numerical aperture implies a saturation of the degree of linear polarization curve on a broader range of angles[3] below 90°. Secondly, we also performed polarization measurements for dot-in-rods embedded inside liquid crystals (see chapterV) to show

[3]In the limit of a zero numerical aperture the curve is always equal to one no matter the value of θ, except for $\theta = 0°$ as no light is collected for a 1D dipole.

that we could orientate the dot-in-rods in such structures. Using the oil immersion objective was not possible in this case as the oil often ended up destroying the sample after a couple of measurements. Working with lower numerical aperture starts to be experimentally challenging as the collection is fairly low, such that the $N.A. = 0.95$ is a good compromise.

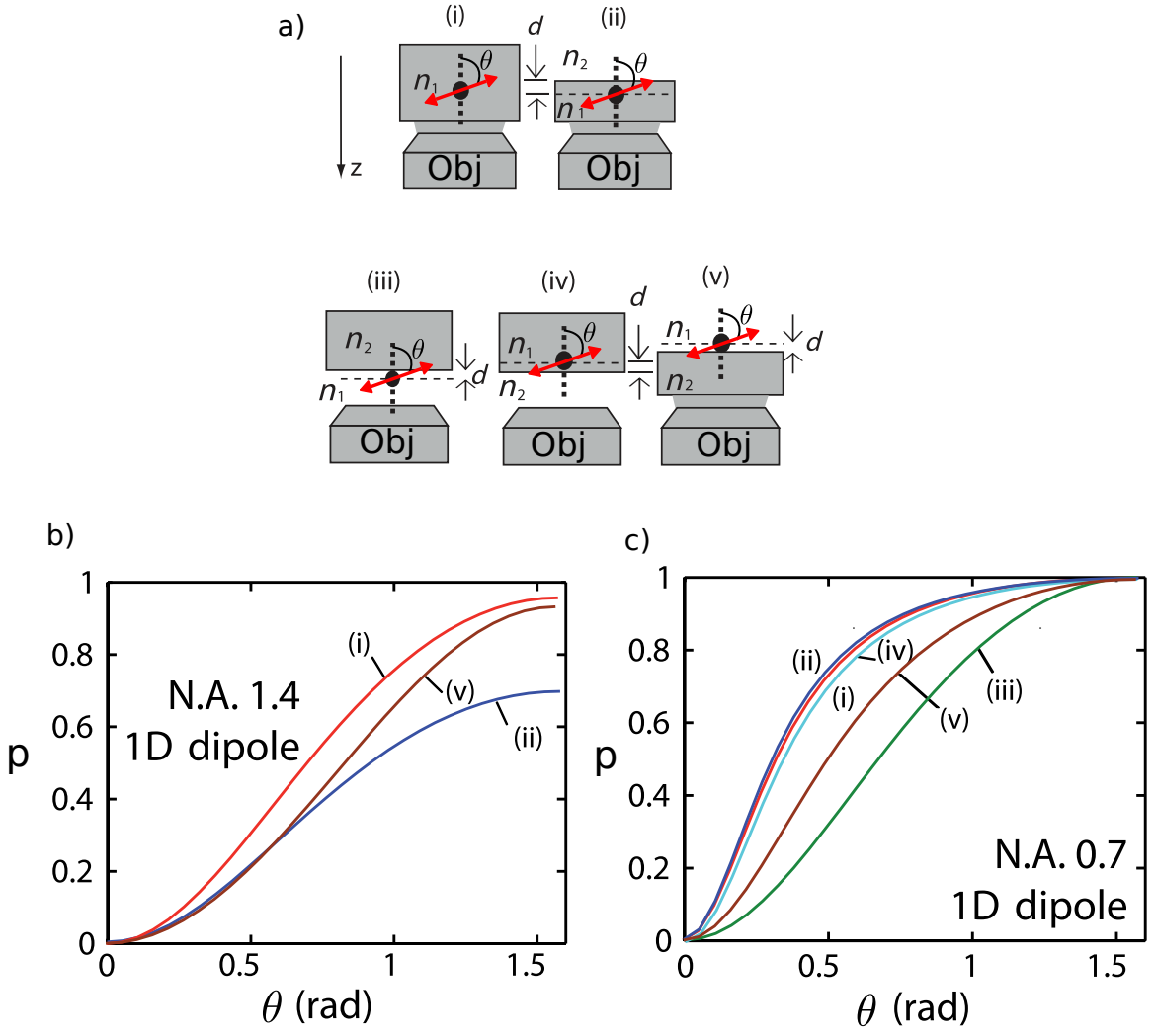

Figure II.5: Various experimental setup configurations and associated degree of linear polarization function of the dipole angle θ from the optical axis. *a)The various experimental configurations for which calculation of degree of polarization are presented in reference [141]. b) Degree of polarization p as a function of the dipole angle θ with the optical axis for an oil immersion objective ($N.A. = 1.4$). c) Degree of polarization p as a function of the dipole angle θ with the optical axis for a $N.A. = 0.7$ objective. Figures reproduced from reference [141].*

Calibration

Polarization measurements are very delicate: for example optics elements (mirrors, cubes..) often reflect differently S and P polarized light[4]. To check that our setup is maintaining polarization, a linearly polarized laser light from a HeNe laser (laser line centered at 633 nm close to the dot-in-rods emission wavelengths) is sent into the microscope from above the objective such as to follow the same path than the collected light from an emitter. The linear polarization of the input laser is then rotated in the plane perpendicular to the optical axis to verify that the different optics in the setup are insensitive to the polarization direction. Fig.II.6 shows four particular measurements with a 30° input polarization increment between each. The background noise has been subtracted. Each curve shows almost perfect extinction and the position of the different extinctions follow the 30° input polarization increment. Therefore the setup does not present any preferential direction and conserves the polarization.

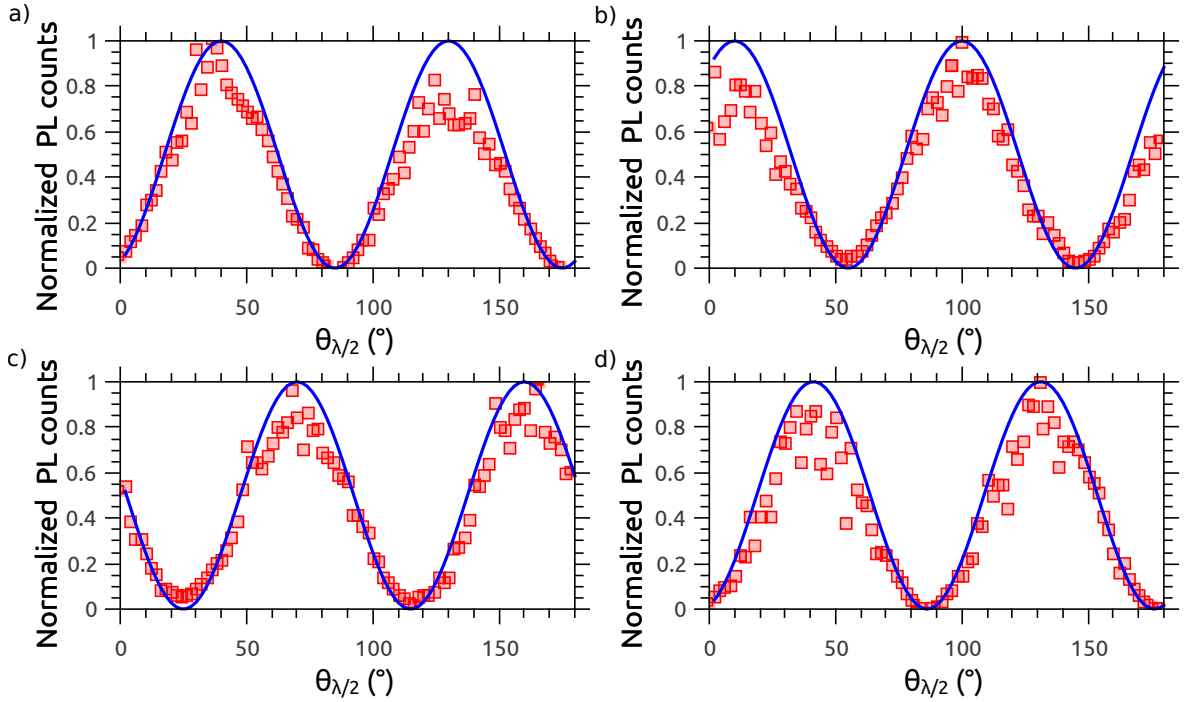

Figure II.6: polarization calibration of the setup. *Polarization curves measured as a function of the half-wave plate angle for different linear polarization input from a HeNe laser. From a) to d) the input polarization is turned by* 30° *between each measurements.*

[4]S and P polarized light refers to a coordinate system, the plane made by the propagation direction and a vector perpendicular to the plane of a reflecting surface. This is known as the plane of incidence. The component of the electric field parallel to this plane is termed P-like and the component perpendicular to this plane is termed S-like.

II.1.3 Defocused microscopy

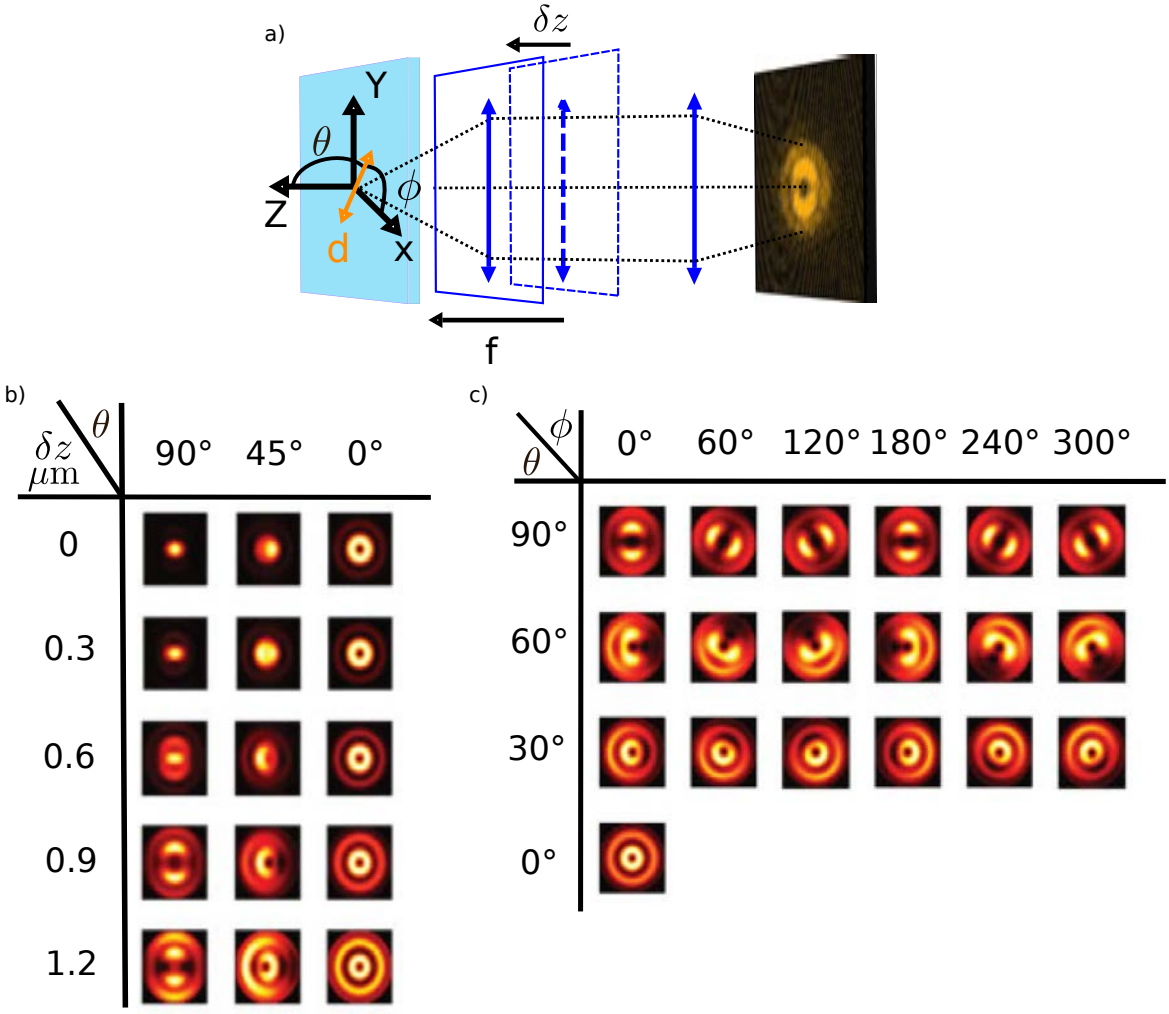

Figure II.7: Defocused microscopy scheme and patterns for a 1D dipole. *a) The objective is moved at a distance δz towards the sample compared to the focal distance f. The defocused pattern of the dipole d, in plane ϕ and out of plane θ angles with the glass coverslip, is imaged on the CCD sensor. A typical pattern found for dot-in-rods laying on a glass coverslip is shown. b) Theoretical pattern dependence on the out of plane angle and defocused distance, reproduced from [142], for a 1D dipole at an air-glass interface, objective N.A. = 1.4. c) Theoretical pattern dependence on the in plane and out of plane angles, reproduced from [142], for a 1D dipole at an air-glass interface, objective N.A. = 1.4, $\delta z = 900$ nm.*

Defocused microscopy is a powerful and simple technique for determining emission pattern of single emitters and their orientation [142–147]. As depicted on Fig.II.7a, the objective is moved towards the sample over a distance δz relative to the focal distance. The resulting defocused image on the CCD camera shows a strong dependence on the dipole in plane (ϕ) and out of plane (θ) angles as can be seen thanks to theoretical calculations reproduced from reference [142] on Fig.II.7c for an objective with $N.A. = 1.4$ at $\delta z = 900$ nm . The defocused pattern is also modified by the defocusing distance δz

as evidenced on Fig.II.7b. The calculated pattern in this specific case correspond to a 1D dipole on an air-glass interface. We will use this technique together with polarization microscopy in chapter V to determine the orientation of dot-in-rods inside liquid crystals.

II.1.4 Collection efficiency

In this section we calculate the collection efficiencies of the different setup configurations presented previously. Knowing how much photons we approximately expect from a measurement is important to assess whether or not the setup is well aligned or to estimate the emitter quantum yield.

First of all we can calculate the losses inside the common part of the various experimental configurations, it is to say everything in the setup except the objectives. Sending a collimated beam from a HeNe laser through the setup without the objective and pinhole we found that the transmission is of 50%. When looking at the signal of a single well isolated dot-in-rod, with a low excitation to minimize the fluorescence noise from the glass coverslip, the pinhole transmission is of 60%. The APDs quantum efficiency at 600 nm is of 58%. This gives a setup transmission of $T = 17\%$ when taking into account the remaining lenses, mirrors and beam-splitter of the HBT.

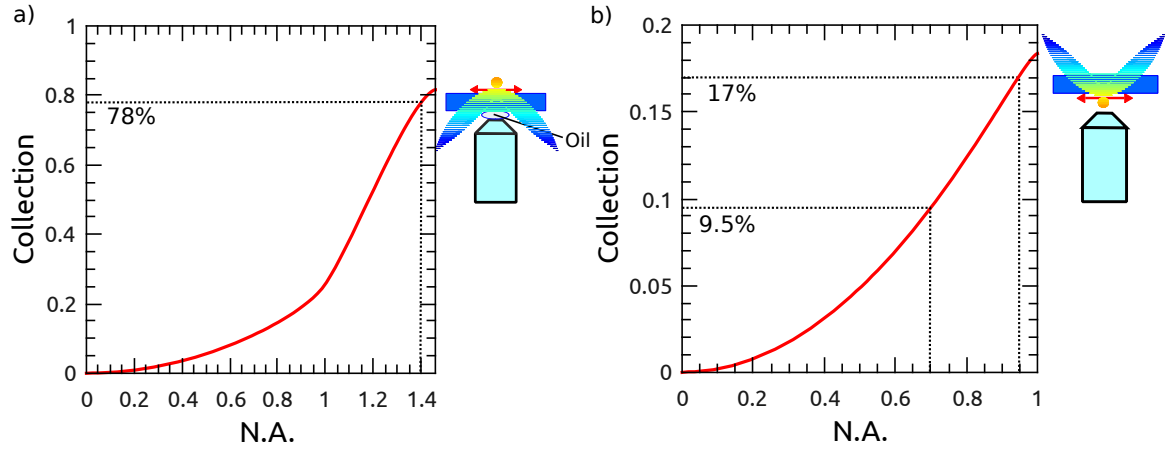

Figure II.8: Objective collection efficiencies compared to the numerical aperture for a laying 1D dipole on a glass surface. *a)Collection efficiency for an oil immersion objective. For a N.A of* 1.4 *as for our standard measurement* 78% *of the photons are collected. b)Collection efficiency for an air objective. For a N.A of* 0.95 *as for our polarization measurement* 17% *of the photons are collected while for a N.A. of* 0.7 *(cryogenic measurements) only* 9.5% *of the photons are collected. The two experimental configuration are shown next to their corresponding collection curve together with the radiation pattern of the laying dipole.*

The previously mentioned objectives have different collection efficiencies. Considering a single dot-in-rod as a 1D dipole, following reference [148] we can calculate the radiation pattern of this emitter located in a dielectric medium 1 at distance z_0 from the interface

with a different dielectric medium 2. In our case the dot-in-rods are laying ($z_0 = 0$ nm) on a glass substrate ($n = 1.46$) and are surrounded by air ($n = 1$), the radiation pattern is presented on Fig.II.8 for a laying 1D dipole on the coverslip. One can notice that the pattern is deeply modified by the presence of the interface compared to a dipole in a homogeneous medium for which a torus (donut) pattern is expected as already explained in section II.1.2. Knowing the radiation pattern in each medium and taking into account the acceptance angles for a given objective we calculated the collection efficiencies of the different experimental configuration aforementioned.

82% of the power radiated by the dipole is concentrated in the glass substrate, therefore the immersion objective (with the oil realizing index matching) with its high numerical aperture collects 78% of the emitted photons. Without an immersion objective, 17% of the photons are collected with an N.A of 0.95 and 9.5% with an N.A. of 0.7 corresponding respectively to the polarization microscopy and cryogenic configuration presented above. In the latter case without oil immersion, one should notice on Fig.II.8 that the chosen configuration is that the emitter is on the objective side, such that a maximum of 18% of the emitted photons can be collected. While 82% of the photons are radiated into the glass coverslip, the wings where the emission is exalted are near the critical angle implying that the collection is fairly low due to total internal reflection inside the coverslip if an objective is put on this side of the radiation pattern without an index matching liquid. Fig.II.8 resumes these observations.

The overall collection efficiencies $\mathcal{C}$ of the various setup configurations are summarized in Tab.II.1 below, together with the maximum count rate $\mathcal{I}_{max}$ expected for a perfect single photon emitter highly excited (one excitation pulse leads to one emitted photon) at a repetition rate $\Gamma = 2.5$ MHz.

	Standard ($N.A. = 1.4$)	Polarization ($N.A. = 0.95$)	Cryogenic ($N.A. = 0.70$)
Collection $\mathcal{C}$	13.3%	2.9%	1.6%
$\mathcal{I}_{max}$ (counts/ms)	332	72	40

Table II.1: Overall collection efficiencies of the various setup configurations and associated maximum count rates. *The count rates are calculated for a perfect single photon emitter excited at a repetition rate* $\Gamma = 2.5$ *MHz.*

II.2 Measurements and data processing

II.2.1 Sample preparation

Samples are prepared by spin coating or drop casting on a glass microscope coverslip (BK7, 180 μm thick) a diluted solution of nanocrystals. A drop of 10 μL with a concentration ranging between 10^{-13} and 10^{-15} M, i.e. moles of nanoparticles per liter, is usually drop-casted. This gives satisfactory results in terms of the number of single dot-in-rods compared to clusters on the sample. Once a sample is done, three criteria have to be fulfilled in order to go further with measurements:

1. the sample is mostly made of single nanocrystals,

2. the nanocrystals are distant enough from each other,

3. the sample exhibits a color homogeneity.

Let us detail with more precision the three criteria. Usually having at least 50% of the nanoparticles that are single and not clusters is a good situation in order not to lose time searching for single particles during measurements. It should be noted that clusters of particles on a sample are useful to align the system especially in low signal configurations as they obviously emit more photons than a single particle. As presented in section II.1.1 a laser spot of 1 μm diameter was chosen to ensure a good stability of the excitation. For this reason dot-in-rods have to be a couple of microns apart in order to be sure to excite only one dot-in-rod at a time. A density of 1 to 2 particles per 5×5 μm is typical. Finally the color of the particles has to be checked if possible: degraded samples because of aging, photo-oxidation, usually displays blueish particles [76]. With our setup, the color can be assesssed by eyes via the eyepiece of the microscope. With the oil immersion objective it is possible to see single nanocrystals by eyes. The usual wavelength dispersion of a sample is of the order of 30 to 50 nm as seen with ensemble measurements. In our case, as all samples are typically emitting around 600 nm, blueish, greenish particles should not be present in non degraded sample. Fig.II.9 shows a wide-field microscopy image of a sample that fills out the three criteria mentioned above.

II.2.2 Noise

Before starting measurements, the noise level on the APDs has to be controlled. The whole detection part of the setup is covered by a box and measurements are made in a dark room. There are four different sources of noise:

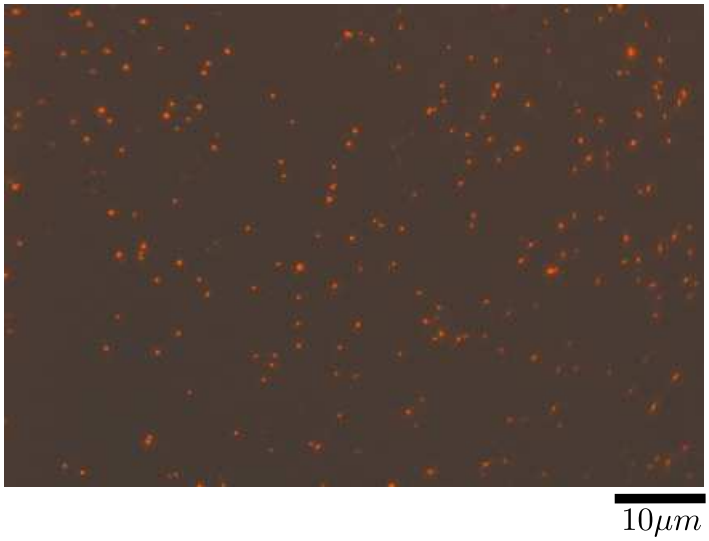

Figure II.9: Picture of a sample realized by wide-field microscopy. *This sample presents a large majority of single dot-in-rods distant enough such that one dot-in-rod can be excited at a time by the laser with intensity profile shown in Fig.II.2. Acquisition time* 200 *ms.*

1. light coming from the room (from computer screens...),
2. reflected excitation light,
3. dark counts of the APDs,
4. fluorescence noise from the sample.

Light coming from the room and reflected excitation light can be almost totally removed if the setup is well covered and a spectral filter is used. The dark counts of the APDs correspond to the intrinsic noise of the detector, thermally-generated carriers within the semiconductor can fire the avalanche process and output pulses are created even if the APD is in complete darkness. The APDs we used (Excelitas SPCM-AQRH14) have typical dark noise of 100 counts/s. The last source of noise comes from the sample itself, from the fluorescence of the coverslip that is in the same spectral domain than the dot-in-rods fluorescence and cannot be spectrally filtered. It depends on the excitation power. At low excitation, the noise count rate extends from 200 to 1000 counts/s. Measurements at room temperature are not so sensitive to noise as the collection and dot-in-rods efficiencies are high enough to ensure good signal to noise ratio (SNR), typical SNR values are ranging from 10 to 30 depending on the excitation power.

II.2.3 Excitation power and saturation curves

The dot-in-rods photoluminescence strongly depends on the excitation power. It is important to have a parameter that evaluates independently of the specific setup configuration

(laser spot diameter, excitation wavelengths ...) how the dot-in-rods are excited by the laser. The mean number of electron-hole pairs inside the crystal $\langle N_{eh} \rangle$ is a relevant parameter. A laser pulse at 405 nm excites the shell continuum of states for which the absorption of dot-in-rods is very efficient as explained in Chapter I. Laser pulses contain a random number of photons with a Poisson distribution, the number of electron-hole pairs generated by a laser pulse inside the shell continuum of states will therefore follow a Poisson distribution whose mean value will depend on the average power sent.

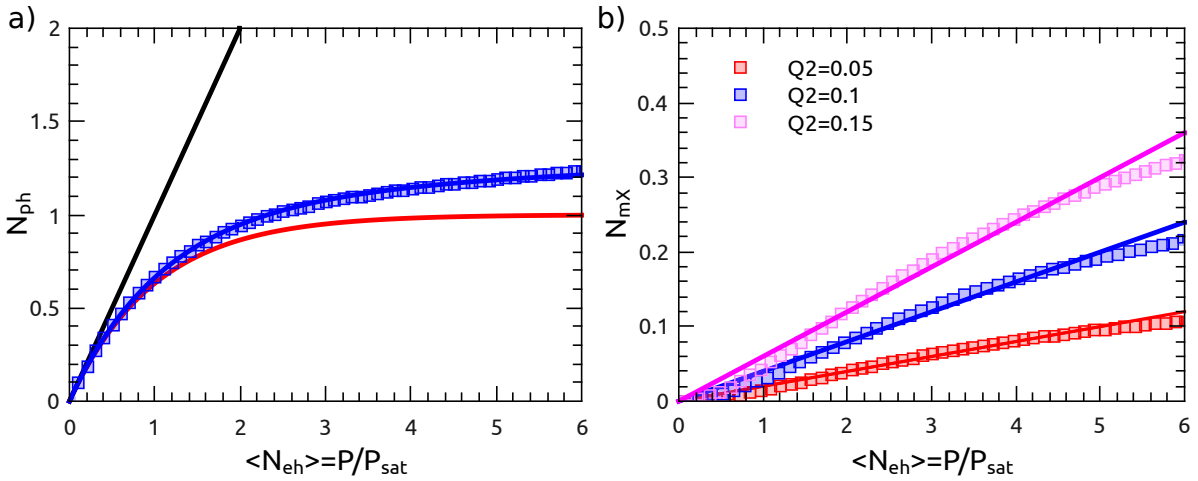

Figure II.10: Theoretical saturation curves and multiexciton emission. *a)Theoretical saturation curve from Eq.II.7. Red line: saturation curve of a nanocrystal presenting perfect saturation, no multiexciton emission. Black line: saturation curve of a nanocrystal without any multiexciton emission quenching processes ($Q_{mX} = 1\ \forall m$). Blue line: Intermediate case with $Q_{2X} = 0.1$ and $Q_{mX} = \frac{Q_{2X}}{m(1-Q_{2X})-1}$ and a simple fit of this curve (blue squares) using eq.II.10. b)N_{mX} as expected from the statistical scaling model for multiexciton quantum yields together with a linear fit using the linear approximation of eq.II.8.*

Without going into details in this chapter on the consequences of the excitation power on dot-in-rod photoluminescence, we can briefly mention and give the reader some insights why it is important to evaluate $\langle N_{eh} \rangle$. As more and more electron-hole pairs are created inside the nanocrystal the photon statistics will change because the probability to emit multiple photons will increase [135]. Also the emission intermittency (see chapter III), common to most nanoscale emitters [149], is dependent on the number of electron-hole pairs inside the crystal. Therefore controlling the excitation is fundamental to interpret the measurements. Prior to any measurements on a new sample or if the setup configuration has changed (laser spot diameter, a different objective is used...), saturation curves should be realized in order to transpose a measurable quantity such as the average laser power into a mean number of electron-hole pairs $\langle N_{eh} \rangle$.

Experimentally one usually presents a count rate measured by the photodetectors, a saturation curve is then the mean emission intensity (count rate) of a dot-in-rod plotted

against the excitation power. However, it is more straightforward to derive theoretically a photon emission probability N_{ph} for a given excitation. Taking into account the collection efficiency $\mathcal{C}$ of the setup, with a pulsed excitation of repetition rate Γ, the count rate I is defined as:

$$I = \mathcal{C}\Gamma N_{ph}. \tag{II.3}$$

I is consequently proportional to N_{ph} and the same analysis holds for analyzing a saturation curve given in terms of the photon emission probability or an intensity count rate. In the following, we present a theoretical derivation of the dot-in-rods saturation behavior; equations are therefore presented in terms of photon emission probability N_{ph}. Fig.II.10a shows theoretical examples of such saturation curves.

The mean number of photons emitted by a dot-in-rod after a given excitation pulse can be modeled [61] as follow:

$$N_{ph} = \sum_{m\geqslant 1} P_{N_{eh}=m} \sum_{m'\leqslant m} Q_{m'X}, \tag{II.4}$$

$$= \sum_{m\geqslant 1} P_{N_{eh}\geqslant m} Q_{mX}, \tag{II.5}$$

where Q_m is the quantum yields of the mth multiexciton state and $P_{N_{eh}=m}$ is the Poissonian probability to excite m electron-hole pairs:

$$P_{N_{eh}=m} = \frac{\langle N_{eh}\rangle^m}{m!} exp(-\langle N_{eh}\rangle). \tag{II.6}$$

Therefore the mean number of emitted photons is just the probability to excite m excitons times the sum of the probabilities that a photon is emitted by each $m' \leqslant m$ successive multiexcitons states. This multi-photons cascade has been experimentally observed [72]. To avoid heavy notations we do not mention in the equations that the Poissonian probabilities are functions of the mean excitation $\langle N_{eh}\rangle$. Thus $P_{N_{eh}=m}$ has to be understood as $P_{N_{eh}=m}(\langle N_{eh}\rangle)$, this is obvious when looking at Eq.II.6. Fig.II.11a and b depict the emission scheme to understand Eq.II.4 and Eq.II.5 respectively. Either one looks separately at the different excitations and counts the mean number of photons that will be emitted in each case and then makes the sum (Fig.II.11a corresponding to Eq.II.4), or one looks at each labeled excitons separately in all possible excitation scheme (Fig.II.11b corresponding to Eq.II.5). Eq.II.4 can be split into two parts, exciton and multiexciton emission, as follows:

$$N_{ph} = N_X + N_{mX} = Q_X(1 - e^{-\langle N_{eh}\rangle}) + \sum_{m>2} P_{N_{eh}=m} \sum_{m'=2}^{m} Q_{m'X}. \tag{II.7}$$

If no photon are emitted from multiexciton states (i.e $Q_{mX} = 0$ for all $m \geqslant 2$), then the saturation is perfect and a maximum of Q_X photons per excitation pulse will be emitted at high excitation as $e^{-\langle N_{eh}\rangle}$ goes to zero. This scenario is represented by the red curve on Fig.II.10a with $Q_X = 1$. Conversely, if multiexciton states are not quenched by any non-radiative relaxation process (i.e $Q_{mX} = Q_X$ for all $m \geqslant 2$), the photon emission statistics will follow the excitation linearly, this is the case of the black curve in Fig.II.10a with $Q_{mX} = Q_X = 1$ for all excited states. Dot-in-rods show an intermediate behavior between the two extreme cases presented before. Multiexciton emission are imperfectly quenched by Auger non radiative recombination and they consequently have weak but non-zero multiexciton quantum yields. The blue line in Fig.II.10a follows Eq.II.7 with a simple model, called statistical model [61], for the multiexciton quantum yields values. The higher orders multiexciton quantum yields can all be deduced from the exciton and biexciton quantum yield taking into account the different relaxation pathways for the Auger effect and radiative emission: $Q_{mX} = \frac{Q_{2X}}{m(1-Q_{2X})-Q_X}$. The statistical model consists in counting the number of relaxation pathways for a given charge, an equal probability is given for the charge to relax via any of the pathways. It is a useful simple model that roughly predicts the multiexciton quantum yields [150, 151].

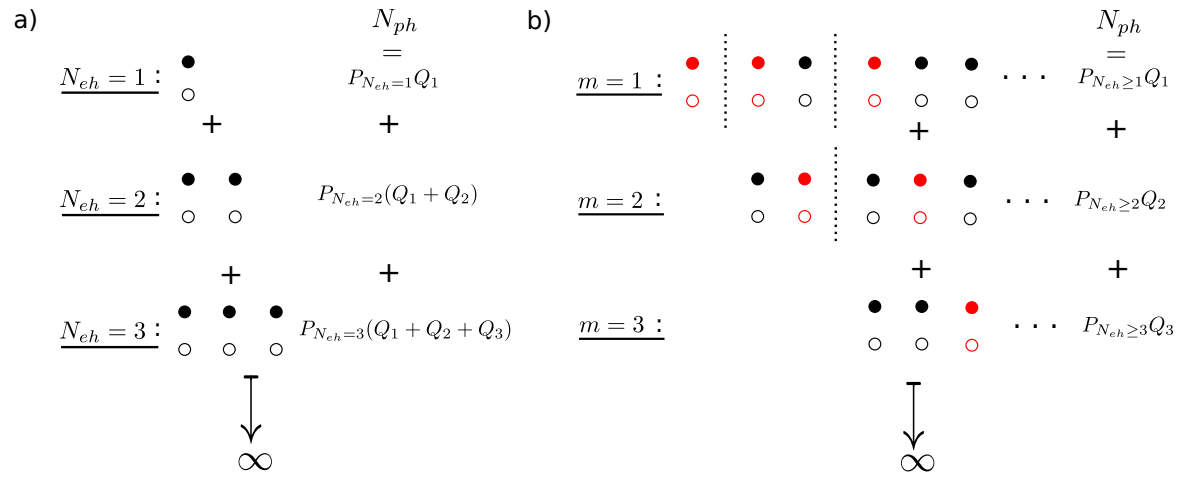

Figure II.11: Mean number of emitted photons. *a)Scheme of Eq.II.4. The excitation of the crystal is fixed and a number of emitted photons from all the electron-hole pairs is calculated. Then all the different excitation cases have to be summed. b)Scheme of Eq.II.4. One looks at each labeled exciton m (in red) in all possible associated excitations and sums over all excitons afterwards.*

By defining a saturation power P_{sat} such that $\langle N_{eh}\rangle = \frac{P}{P_{sat}}$, any power excitation can be transposed into a mean number of electron-hole pairs easily. P_{sat} is then the excitation

power that corresponds to a mean number of exciton inside the nanocrystal equal to 1. If one only considers the exciton emission in Eq.II.7, when the excitation power reaches P_{sat}, $\langle N_{eh}\rangle = 1$ and N_{ph} will be $(1 - e^{-1}) = 63\%$ of its maximum value (36% of the time the crystal is not excited when $\langle N_{eh}\rangle = 1$ according to the Poissonian probability law, explaining why maximum intensity is not reached at $\langle N_{eh}\rangle = 1$) . To accurately determine P_{sat}, multiexciton emission have to be taken into account. For $\langle N_{eh}\rangle$ up to 5, N_{mX} can be well approximated by a linear function [152] that depends only on the biexciton quantum yields:

$$N_{mX} = \sum_{m>2} P_{N_{eh}=m} \sum_{m'=2}^{m} Q_{m'X} \simeq cQ_{2X}\langle N_{eh}\rangle. \tag{II.8}$$

Fitting of different multiexciton emission curves as in Fig.II.10b has given $c = 0.4$. One should notice that the lower the biexciton quantum yield the more accurate the linear approximation is for a broad set of excitation. The biexciton quantum yield Q_{2X} is experimentally measurable via the second order autocorrelation function $g^{(2)}(0)$ at low excitation power [153]:

$$\lim_{\langle N_{eh}\rangle \to 0} g^{(2)}(0) = \frac{Q_{2X}}{Q_X}. \tag{II.9}$$

This point will be detailed in chapter IV. Q_X has been measured to be one for high-quality CdSe quantum dots with different methods, either by measuring a change in the radiative lifetime of the emitter when the electromagnetic environment is modified [71] or by measuring PL decay when the emission intensity of a dot is maximized [96]. The photon emission can then be easily fitted from measurable data by the following formula:

$$N_{ph} = N_X + N_{mX} \simeq Q_X\left[(1 - e^{-\langle N_{eh}\rangle}) + c\frac{Q_{2X}}{Q_X}\langle N_{eh}\rangle\right]. \tag{II.10}$$

The blue saturation curve in Fig.II.10a has been fitted using this model. With this procedure we are able to accurately determine the average number of excitons for a given excitation power.

II.2.4 Data acquisition and processing

In this section we will explain what happens once photons are detected by the APDs. The electronic system used to record the signal (acquisition card PicoHarp 300 together with the PHR 800 4-channel detector router from PicoQuant) is called a Time-Correlated Single Photon Counting (TCSPC) system. As depicted on Fig.II.1, the TCSPC acquires the signal from the two APDs and a synchronization signal (SYNC) coming from the laser or one of the APD is used as a reference.

Data acquisition: Time-Correlated Single Photon Counting

The APDs deliver a TTL output signal. Each output pulse is sent to the TCSPC module. A brief description of the TCSPC module working principles is proposed on Fig.II.12a. The synchronization (SYNC) input of the TCSPC device is set on the laser. When a measurement starts an absolute zero time is set. Then every incoming pulse from one of the APDs is registered and a time, called macrotime (T on fig.II.12a), is labeled to each registered pulse together with which channel (APD) the signal is coming from. Another information registered by the device is the arrival time of each pulse compared to the related synchronization pulse coming from the laser. This time is called microtime (t on fig.II.12a).

Data processing

With the measurement presented above one can easily derive quantities presented in this thesis: photoluminescence decay, photoluminescence versus time and correlation function of the signal at short time delays and long time delays as well. How to derive these quantities from the measured values of microtime, macrotime and channel of each photon is described on Fig.II.12b, c and d.

First of all, the photoluminescence decay is achieved by building a histogram of the microtime with a bin width being a multiple of the resolution. At room temperature, as long lifetimes are involved (up to 100 ns), a low resolution of 512 ps is chosen and one can bin the microtime using a bin time of 512 ps. As the SYNC signal is set by the excitation, the microtime represents the time delay between the excitation of the nanocrystal and the emission of a photon. Therefore, building a histogram over the many measured photons will give the statistical distribution of relaxation, i.e. the photoluminescence decay as in Fig.II.12b.

The derivation of the photoluminescence versus the time, the photoluminescence intensity, is obtained by building a histogram of the macrotime, thus counting the number of photons that are detected by the APDs during a given bin time. The bin time should be as small as possible in order to see fast intensity fluctuations. Nevertheless there is a limit on how small the time bin can be, a criteria should be that the lowest intensity feature should pop up out of the noise level. Therefore the bin size will be limited by the rate of emission and collection efficiency of the setup. An example of photoluminescence time trace is presented on Fig.II.12c, we indicate that a typical bin time value is 1 ms. Finally, the correlation function between the two APDs can be computed using the three registered information. To do so, the time delays between each photon of a given channel and the other channel photon ensemble need to be computed. Then a histogram of the

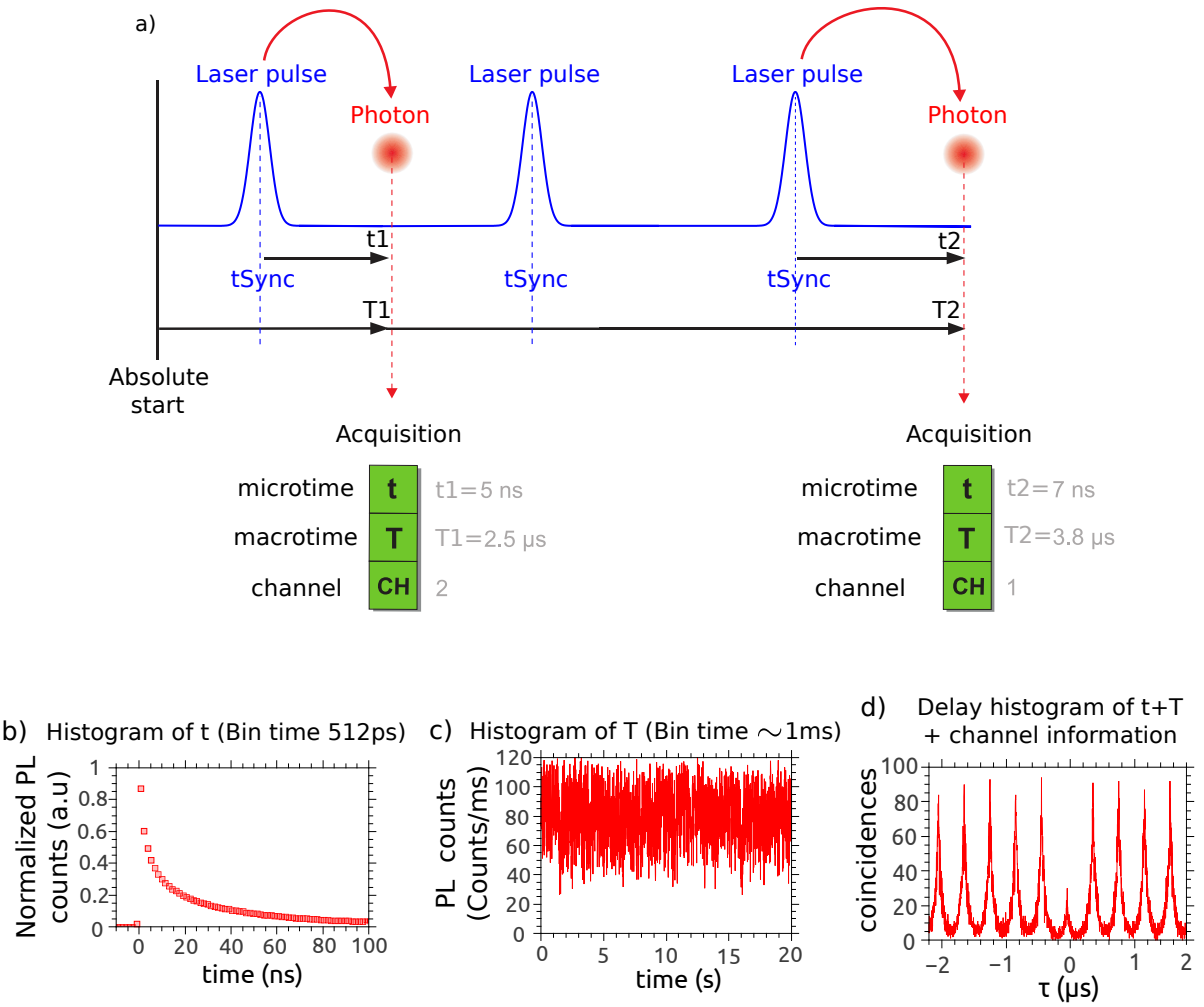

Figure II.12: TCSPC principle and example of useful data recovered from a TCSPC measurement. *a)TCSPC principle as used for acquiring data. The SYNC channel is set on the laser signal. For each detected photons, the channel (APD) on which the photon arrived is registered, together with the absolute time of arrival (T: macrotime) and a time of arrival relative to the SYNC signal. b) Photoluminescence decay curve obtained from a microtime histogram. c) Photoluminescence time trace: macrotime histogram. d) Photoluminescence correlation function at short delays.*

time delays gives the correlation function. This can be quite heavy to compute. If only information on the correlation at short time delay is needed, then one do not need to correlate each photon of a channel with the photon ensemble of the other channel but only with neighboring photons in terms of time arrival on the APDs. So a cutoff can be introduced in the computation. Conversely, if only long time delays are needed, one can realize a "classical" correlation and correlate intensity bins together instead of photons.

The software link to the TCSPC device is able to build a live histogram of the microtime. In the previously described TCSPC configuration with the laser being the SYNC signal, the software builds a photoluminescence decay curve. Before launching a measure-

ment on a specific particle spotted on the CCD camera one has to know if the particle is single or not. To do so, the SYNC signal can be set on one of the two APDs instead of the laser. So the reference signal is now a recorded photon from one of the APD and the histogram of the microtime will therefore be a histogram of delays between consecutive photons. As explained above this is the correlation function of the signal at short delays as we are only looking at consecutive photons. If the correlation function displays an antibunching behavior, correlation dip at zero delay as in Fig.II.12d, then we know we are studying a single emitter.

Conclusion

We first presented the wide field and confocal microscopy setup used to study single nanoemitters. We then showed the importance of characterizing the excitation of dot-in-rods when using confocal microscopy as the emission processes are power dependent. To do so, the saturation curves are relatively easy measurements that can be performed. Together with a simple model of dot-in-rods multiexciton emission and a linear approximation the mean number of electron-holes pair inside the nanocrystal can be accurately calculated. Coupled to a TCSPC device for signals acquisition, one can appreciate the amount of information that can be gathered from such measurements.

Chapter III
CdSe/CdS dot-in-rods blinking statistics

Introduction

The scientific community working on nanocrystals has been confronted to the emission intermittency, commonly called blinking, characteristics of these nanoscale emitters. Since the first measurements on single CdSe nanocrystals [15] reporting a switching between an ON state emitting photons and an OFF state completely dark, this phenomenon has been the focus of intense studies because it deeply undermines the possible applications foreseen for these emitters. The last years have seen considerable progresses in reducing the effects of blinking thanks to new chemical synthesis methods. However, a complete physical picture of the phenomenon has not been reached yet owing to the complexity of the processes at stake.

In this chapter we propose a study of the blinking statistics of CdSe/CdS dot-in-rods. First a review of the literature on the blinking phenomenon is presented; we expose the common models used to explain the emission intermittency and finish by a presentation of the recent progresses in order to reduce the effects of blinking. We then characterize the blinking events displayed by our CdSe/CdS dot-in-rods. First, we discuss why they mainly exhibit blinking events due to charging and nonradiative recombination via Auger relaxation. We then characterize the blinking statistics and show how it depends on the geometry of the heterostructure.

III.1 Blinking: a review

Fluorescence blinking has been observed for various types of single nanoscale emitters [149], including molecular dyes, fluorescent proteins, small nanodiamonds [154] and colloidal nanocrystals. In complex single emitters such as nanocrystals, a broad distri-

bution of blinking rates is observed, resulting in periods of high fluorescence (on-state) and low fluorescence (off-state at the noise emission level, cf Fig.III.1a) spanning from hundreds of microseconds to hundreds of seconds (cf Fig.III.1b). Since the first report of fluorescence blinking in small spherical nanocrystals [15], this behavior has been observed for many morphologies including elongated nanorods and nanowires.

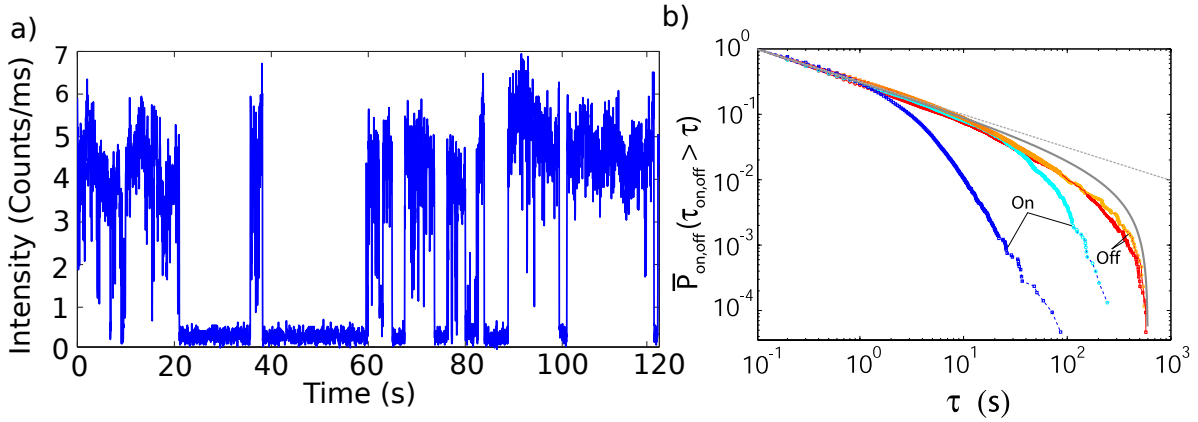

Figure III.1: Example of a CdSe/ZnS nanocrystal fluorescence time-trace and cumulative distribution of ON and OFF periods. *a)CdSe/ZnS nanocrystal fluorescence time-trace with a bin time of* 100 *ms. Succession of ON and OFF emission periods are clearly observed. b) Cumulative distributions of ON and OFF periods obtained from hundreds of single CdSe/ZnS nanocrystals at low excitation power (ON: cyan, OFF: orange) and high excitation power (ON: blue, OFF: red). The dash grey line corresponds to a power law distribution with exponent* $\mu = 0.5$ *while the full grey line takes also into account the effect of the finite measurement time by adding an exponential cut-off to the power law. Figures reproduced from reference [155].*

The first studies of blinking in nanocrystals were made using uncapped CdSe dots or CdSe/ZnS with a thin shell. They show a pronounced blinking as shown on Fig.III.1a. One way to study the blinking is to look at the distributions of ON and OFF event durations $\mathcal{P}_{on}(\tau_{on} = \tau)$ and $\mathcal{P}_{off}(\tau_{off} = \tau)$ respectively, or at the cumulative distributions $\mathcal{P}_{on}(\tau_{on} > \tau)$ and $\mathcal{P}_{off}(\tau_{off} > \tau)$ as in Fig.III.1b. The cumulative distributions tell us the probability for the emission to be ON or OFF for a time period longer than a duration τ. A non exponential distribution was found [15, 156, 157], the OFF periods following a power law distribution:

$$\begin{aligned} \mathcal{P}_{off}(\tau_{off} = \tau) &\propto 1/\tau^{\mu_{off}+1}, \\ \mathcal{P}_{off}(\tau_{off} > \tau) &\propto 1/\tau^{\mu_{off}}, \end{aligned} \tag{III.1}$$

with μ_{off} being of the order of 0.5, always between 0 and 1 independently of the experimental conditions. One should notice on Eq.III.1 that the exponent of the non cumulative distribution is also a power law but with a larger exponent; one needs to add one to the

cumulative distribution exponent[1]. We wrote Eq.III.1 only with a proportionality sign, a minimum value τ_{min} (otherwise the distribution has infinite area as τ approaches 0) and a constant are needed to normalize the distribution properly. ON periods follow power law distributions with an exponential cut-off arising usually at timescales of a couple of seconds depending on the excitation power [158]. This is summarized on Fig.III.1b, the exponential cut-off for OFF periods (red) is not due to a physical process but to the finite acquisition time. The exponential cut-off for ON periods (blue) is clearly visible as well as its dependence with the excitation power on Fig.III.1b. For strong excitations, long ON periods are less and less frequent. A physical exponential cut-off for the OFF periods [159] has been inferred from indirect measurements to be of the order of an hour. It is not accessible directly by measurements as it would require acquisition times of several days.

To compute the distributions of ON and OFF event durations, first the photoluminescence time trace is built from the measured photon detection events as in Fig.III.1a with a certain bin time. Then thresholds to discriminate between the timetrace ON and OFF events need to be defined. Determining the duration of each ON and OFF events yields the cumulative distributions as in Fig.III.1b.

Power law distributions with exponent smaller than 1, the so called Levy's distributions, have singular statistical properties: no mean value and standard deviation can be defined. Also long periods are very probable as the decay of the distribution is slow. More puzzling phenomena are associated with these distributions, such as statistical aging and non ergodicity [157]. Statistical aging implies that the fluorescence is dominated by longer and longer OFF periods while time goes by, this being not a photobleaching effect but purely statistical. Non ergodicity implies that measuring a nanocrystal fluorescence for a long period of time is not equivalent to make measurements on various nanocrystals for smaller periods of time.

In the following we briefly present the current understanding of the blinking phenomenon and the recent progresses in reducing it.

III.1.1 Two types of blinking

As attested by its unusual power law distribution, blinking is a very complex phenomenon. After 20 years of intense debate, progress have been made in reducing the effects of blinking in nanocrystals, nevertheless a common agreement on the physical origin of this phenomenon has not been reached yet. Many model coexists in the literature. We try to give an overview of the accepted facts about blinking. A recent and comprehensive

[1]In the following we present our results in terms of cumulative distributions so the exponents are given for the cumulative case.

review on the subject is given in reference [160], this work covers more aspects of blinking than this thesis.

Fluorescence blinking is a direct result of charge carrier trapping. Two types of model coexist in the literature to link the charge trapping with the non-fluorescent periods observed during blinking. Fig.III.2 resumes the main ideas for the two types of blinking.

Type A blinking The first model that we will call type A[2], in reference to an experimental article [161] on the subject, assumes that the charge trapping of one type of carrier leaves *the nanocrystal core charged by the unpaired remaining carrier*. The Auger recombination being an efficient non-radiative recombination pathway in nanocrystals, the unpaired charge in the core induces a low fluorescence quantum yield because most of the electron-hole pairs recombine nonradiatively with the extra charge by Auger effect. The low fluorescence lasts for a time dictated by the lifetime of the trapped charge. Once the trapped charge recombine with its countercharge the low fluorescence period is over.

Following Fig.III.2a, the ON emission state is a succession of absorption and radiative recombination of charges. An ON to OFF switching occurs via thermal ionization, tunneling or Auger-assisted photo-ionization [82] of a charge carrier to a trap state. The trapped charge leaves a charge of opposite sign inside the nanocrystal. The resulting charged nanocrystal remains non-fluorescent, despite the subsequent absorption cycles, because of the fast non-radiative Auger energy transfer. The OFF to ON switching occurs when the trapped charge returns into the nanocrystal and recombine with its countercharge.

Type B blinking The second model (type B model) states that the trapped charge recombines non-radiatively with its countercharge promptly after each excitation event and therefore *there is not a permanent charging of the core during low fluorescence periods*. The low fluorescence periods correspond to fast charge-trapping rates that dominate radiative recombination rate. Intermittency is caused by time-dependent fluctuations of that trapping rate. When the charge trapping rate becomes much slower than the radiative rate, the nanocrystal is in a ON fluorescence period. The durations of the off-state are dictated by the time scales of the trapping rate fluctuations and not by the lifetime of the trap state as in the type A model.

Following Fig.III.2b, a ON period occurs when the trapping rate is considerably slower than the fluorescence rate, after an absorption, an exciton is created and recombines radiatively. The switching from the ON to the OFF state occurs when the trapping rate becomes much faster than the fluorescence rate. During an OFF period the nanocrystal

[2]Also known as the charging model.

cycles between photon absorption to create an exciton, fast removal of the charge to a trap state, and non radiative recombination of the electron and trapped hole. OFF to ON switching occurs when the trapping rate becomes very slow again. This can be due to a fluctuations of the distribution of trap states on the surface. Reference [162] suggests that surface or interface atoms that exhibit light-induced hopping on the nanocrystal surface can create alternatively active traps (fast trapping rate) and inactive traps (negligible trapping rate).

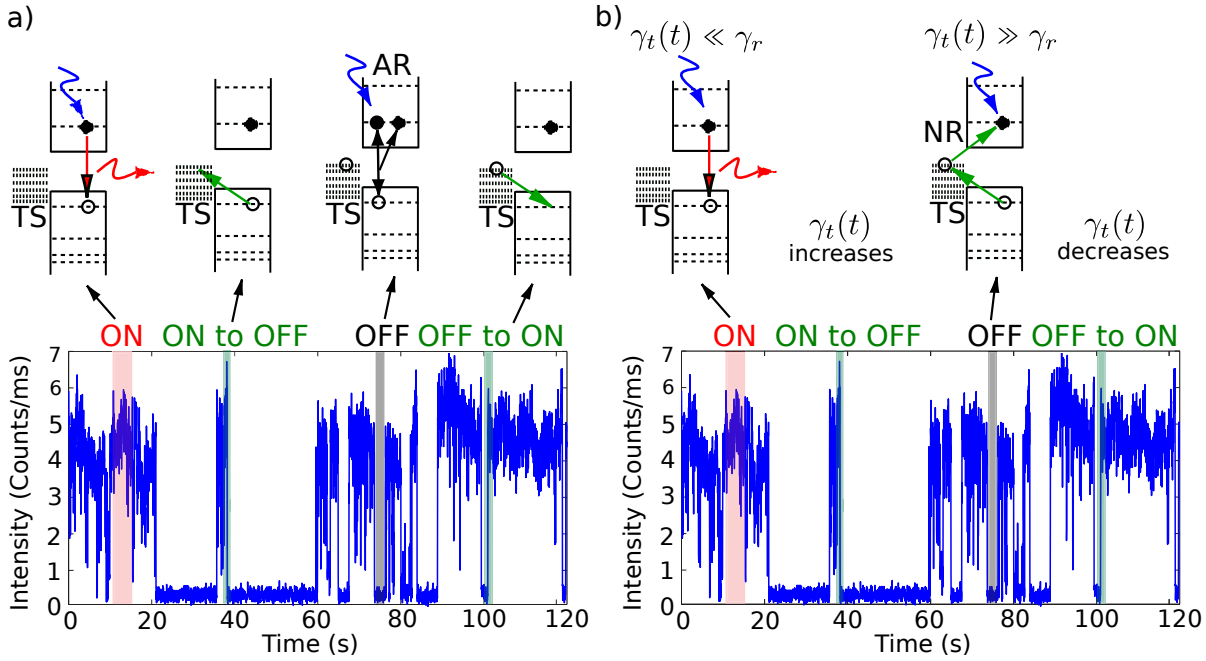

Figure III.2: Schematics of the two blinking types. *a) Type A blinking. b) Type B blinking. TS: Trap States, AR: Auger Recombination, NR: Nonradiative Recombination, $\gamma_t(t)$: trapping rate, γ_r: radiative rate, blue arrow: excitation pulse,red arrow: photon emission.*

Besides deciding which model is relevant to explain a set of measurements, there is also the problem of modeling the behavior of the trap states to explain the power law distribution of ON and OFF periods. We presented in chapter I section I.2.2 the physical nature of the trapping sites (defects inside the lattice, surface dangling bonds, ligand trapping sites). Owing to the variety of possible trapping sites, a great number of behaviors have been proposed for their physical properties [160].

Experimental evidence Different experimental evidences support one blinking model or the other. The second model (type B) is used in cases where Auger processes were shown to be irrelevant in explaining the measurements. For example, the low emission level quantum yield has been shown to be lower than expected if the Auger processes were involved [163]. Also, while the Auger processes should strongly depend on the

confinement of the charges, a lack of a systematic size dependence in the low emission state dynamics [164] has been reported.

A recent experimental article [161] has reported for the first time two types of blinking in CdSe/CdS single nanocrystals. The sample is in solution inside an electrolyte, this allows a control on the extent of nanocrystals charging. The two types of blinking are revealed by different correlations between the emission intensity and lifetime. The excitation is such that the creation of multiexcitons is fairly low, $\langle N_{eh} \rangle = 0.2$.

On Fig.III.3a are presented the intensity-lifetime correlations for a nanocrystal displaying type A blinking for a period of time under increasing negative electrolyte potential V (electron injection). At 0 V (middle), the emission switches from a high intensity emission (4 counts/ms) to a lower intensity (1 counts/ms). The lifetime is correlated to the emission intensity. For a positive potential (left), the intensity timetrace and lifetime are very stable and exhibit high values (4 counts/ms and 25 ns). Conversely, for a negative potential, the intensity timetrace and lifetime exhibit mostly low values (1 counts/ms and 5 ns). This leads to two conclusions:

- *The correlation between the intensity and lifetime suggests that it is effectively type A blinking between a neutral (denoted X^0 in Fig.III.3a) and a charged state (denoted X^- in Fig.III.3a).* When a nanocrystal is in a charged state, the three-particle Auger recombination opens a fast, nonradiative channel, resulting in a shorter lifetime and a reduced photo-luminescence quantum yield.

- *The delocalized*[3] *charge involved in the type A blinking is an electron, the trapped charge is a hole.* Indeed, for negative potential (injection of electrons), the state remains in a negative charged state because of the profusion of electrons in the surroundings of the nanocrystals, they recombine with trapped holes at the surface and prevent the delocalized negative charge inside the nanocrystal to recombine. Conversely, for a positive potential, the recombination of electrons is favored and blinking is strongly impeded. Other physical arguments are given in the next section III.1.2 to explain why holes are more likely to be trapped for CdSe/CdS nanocrystals in a type A blinking process.

Type A blinking displays a power law distribution of ON and OFF periods with an exponential cutoff on tens of millisecond timescale for both ON and OFF states as visible on Fig.III.3b. These are not the cumulative distributions of ON and OFF events that are presented on Fig.III.3b but $\mathcal{P}_{on}(\tau_{on} = \tau)$ and $\mathcal{P}_{on}(\tau_{on} = \tau)$. The authors report a fairly low ON and OFF power law exponent of $\mu = 0.37$ compared to the value of 1.5 presented in Fig.III.1. The exponential cutoff is found to be around 70 ms.

[3]Here delocalized is used again to stress that the charge is not trapped.

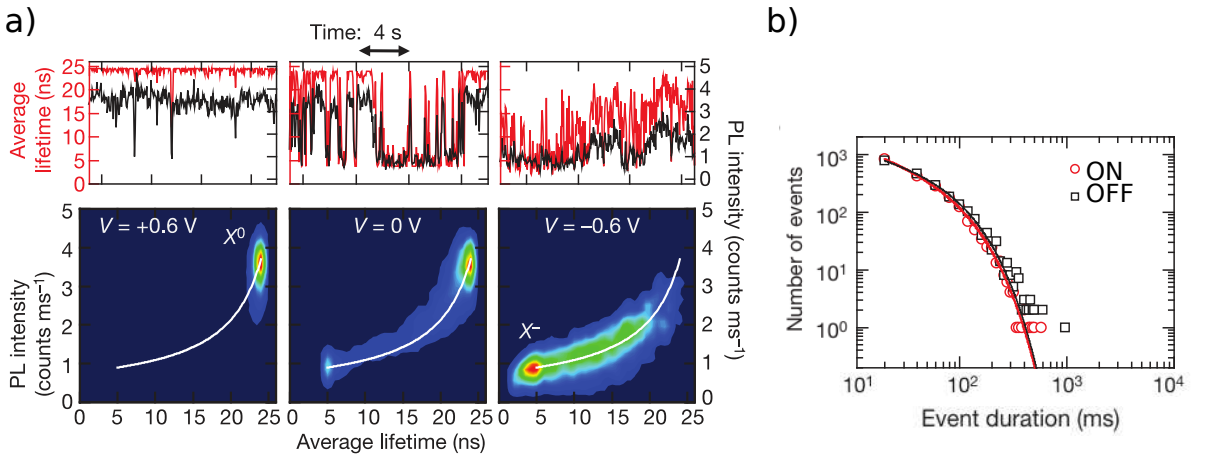

Figure III.3: Type A blinking in reference [161]. *a) Correlations between the fluorescence intensity and the lifetime of emission at different electrolyte potentials for a given nanocrystal. b) Probability distributions of the ON and OFF periods for a nanocrystal showing type A blinking. Figure reproduced from reference [161].*

In Fig.III.4a the case of a nanocrystal exhibiting a type B blinking is presented. For a positive potential (left), the intensity is fluctuating between two levels but the lifetime is remaining constant. An extra charge delocalized inside the nanocrystal cannot explain such a fluorescence because in this case the Auger recombination should induce a change in lifetime. This corresponds to a type B blinking model. At $V = -1V$ (middle), the blinking is suppressed and the nanocrystal remains in a high emission state. A further increase of the negative potential (right) shifts the photoluminescence to a lower emission and lifetime, close to the X^- state measured for this nanocrystal.

A model is proposed in Fig.III.4b, the important parameter is the trapping rate γ_D and how it compares with the intraband relaxation rate γ_B. The trapping rate γ_D can be controlled thanks to the electrolyte potential. By changing the electrolyte potential one fills in more or less the electron traps. Therefore, with the electrolyte potential, one can mimic a fluctuating trapping rate, key point of the type B blinking model. Surface traps energy states (R) can efficiently capture a "hot" electron (coming from the continuum of higher states after excitation) if $\gamma_B \ll \gamma_D$. This is the case for a positive V potential (left): trap states are empty and a high trapping rate is therefore implying a possible capture of "hot" electrons and possible blinking events. For a negative potential (middle), the trap states are filled with electrons, the rate of electron trapping becomes smaller than the relaxation of electron towards the band edge: blinking is prevented. Finally, for an even more negative potential (right) one starts to fill not just the trap states with electron but also the band edge, implying an emission from the trion state. A few questions arise about this model:

- Why do we see electron trapping and not hole trapping? *Electron are more likely*

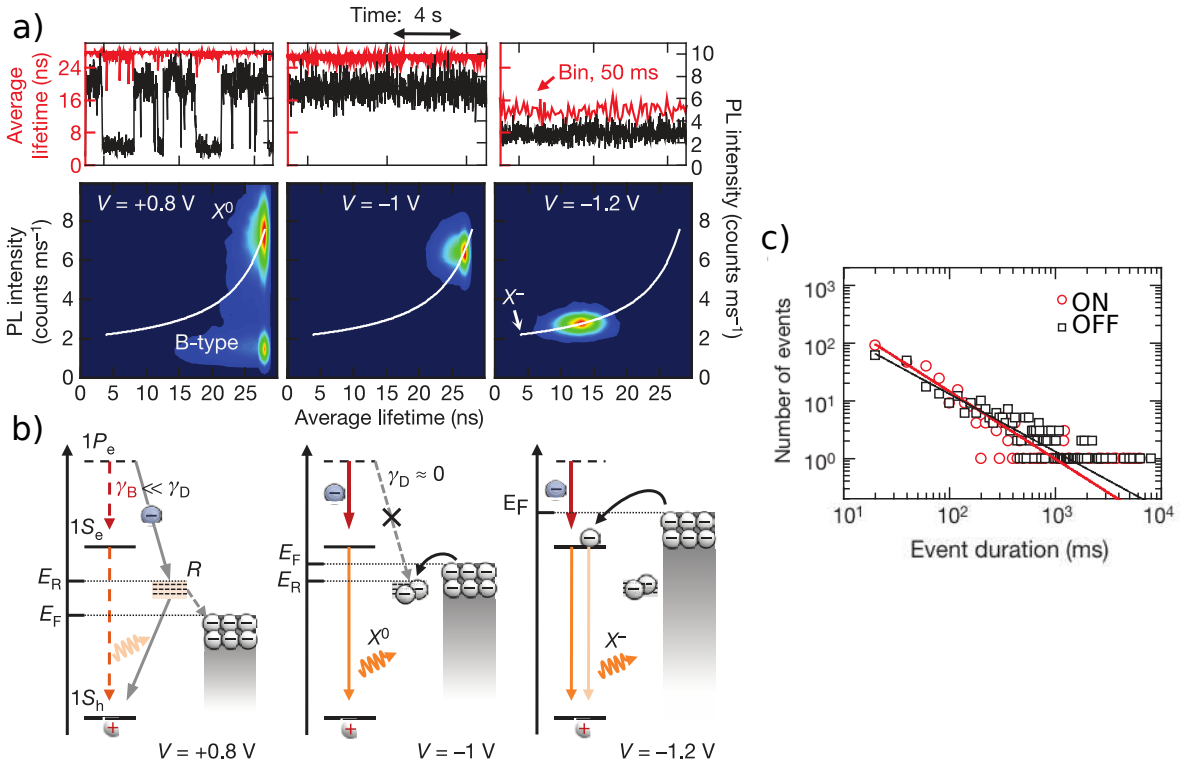

Figure III.4: Type B blinking in reference [161]. *a) Correlations between the fluorescence intensity and the lifetime of emission at different electrolyte potentials for a given nanocrystal. b) Proposed model for the B type blinking. The B-type OFF state is due to the activation of surface traps (R) that capture hot electrons (blue electrons) at a rate γ_D, that is higher than the intraband relaxation rate γ_B (the ground and the excited electron states are shown as $1S_e$ and $1P_e$ respectively; $1S_h$ is the band-edge hole state). The grey area full of electrons symbolizes an electron reservoir. The Fermi energy E_F, relative to the trap energy E_R, is determined by the electrochemical potential and controls the occupancy of the surface trap R. This allows for electrochemical control of B-type blinking. c) Probability distributions of the ON and OFF periods for a nanocrystal showing type B blinking. Figure reproduced from reference [161].*

to be captured during a type B blinking because as we have seen in Chapter I section I.2.2 their intraband relaxation is slower than for holes which benefit from a higher density of states to relax more rapidly. This explains why we observe electron trapping in this experiment.

- Why is there no lifetime decrease associated with this blinking? *The fluorescence lifetime is unchanged because the trapping process does not compete with fluorescence recombination from the band-edge as in the case of a trion recombination with Auger processes.*

- Does the electron recombine nonradiatively with the hole before the next excitation? Yes *the trapped electron recombine nonradiatively with a valence-band hole before the next photoexcitation event leaving behind a neutral dot.* Otherwise an extra hole

would be present for the next photoexcitation event, implying an Auger effect with the hole and a decrease in lifetime. However, occasionally, photon absorption might occur before reneutralization of the dot, resulting in a positive trion X^+. Indeed very short photoluminescence lifetimes within the B-type OFF periods have been observed in this article.

Finally a pure power law distribution (on the limited timescale presented, ~ 1 s) of ON and OFF events characterizes the B type blinking as shown in Fig.III.4c. The author found exponents close to unity $\mu_{on} = 1.17$ and $\mu_{off} = 1$ for the non cumulative distributions, more in accordance with the distribution shown of Fig.III.1b for CdSe/ZnS nanocrystals.

Interestingly, both types of blinking are present for medium shell (7 to 9 CdS monolayers) nanocrystals, they can both happen alternatively for a given nanocrystal. B-type is the dominant blinking process for thinner shell nanocrystals. For thicker shells (15 to 19 CdS monolayers), either the dot were not blinking at all or type A blinking was present but not type B. The fact that B type blinking is quickly suppressed as shell thickness increases is consistent with the proposed mechanism of hot-electron tunnelling outside the nanocrystal, because this process is expected to be exponentially sensitive to the thickness of the tunnelling barrier. B type blinking is likely to be the dominant blinking mechanism in standard core-only CdSe and core/shell CdSe/ZnS nanocrystals studied in earlier reports and shown on Fig.III.1. Before characterizing the blinking for our dot-in-rods, in the next section we propose a brief overview of what is called reduced blinking.

III.1.2 Reduced blinking

Very recently, several articles appeared in literature on the reduction [19, 85, 165] of blinking. Often in literature, blinking means that the nanocrystals turns its emission completely off. In that sense some articles talks about non-blinking nanocrystals when the nanocrystals do not have OFF emission periods. However large intensity fluctuations can remain. In this manuscript we prefer to talk about a reduced blinking.

Reduced blinking is linked to the new synthesis methods that allowed to grow thicker CdS shells [19, 165] or CdZnSe/ZnSe alloyed thick shells. A typical emission trace of such structures is presented in Fig.III.5a. One can notice on this zoom on a 1 s window that the low emission intensity periods are short, they never exceed 100 ms [19]. The histogram of emission in Fig.III.5b also shows that two emission states can be resolved, the lower emission state, called grey state being above the noise (noise intensity: 1.35 counts/ms while the grey state has $I_{X^-} = 10.5$ counts/ms) in contrast with a completely dark state.

The high emission state is called the bright state. The nanocrystals emission is never completely off in the sense that if the signal is binned with a long enough time bin a fluorescence signal pops up above the noise. The grey state displays a reduced lifetime compared with the bright state as presented on Fig.III.5c and d. A choice of the emission bin attributed to the grey state yields a monoexponential photoluminescence decay with a lifetime of 8.5 ns, while it yields a lifetime of 62 ns for the bright state.

Based on the previous section we can say that the reduced blinking is due to the suppression (or quasi suppression) of type B blinking. When growing thicker shells, tunneling of hot electrons towards surface traps is drastically reduced. The change in lifetime between bright and grey states is a signature of type-A blinking together with the faster switching dynamics due to the exponential cutoff on milliseconds timescales. Why is the photoluminescence emission not OFF anymore when blinking occurs? The explanation is that the Auger recombination towards electron is less efficient in thick shell CdSe/CdS nanocrystals due to the highly delocalized electron. It has been shown that increasing even more the shell thickness [151, 166] the grey state can become as bright as the bright state.

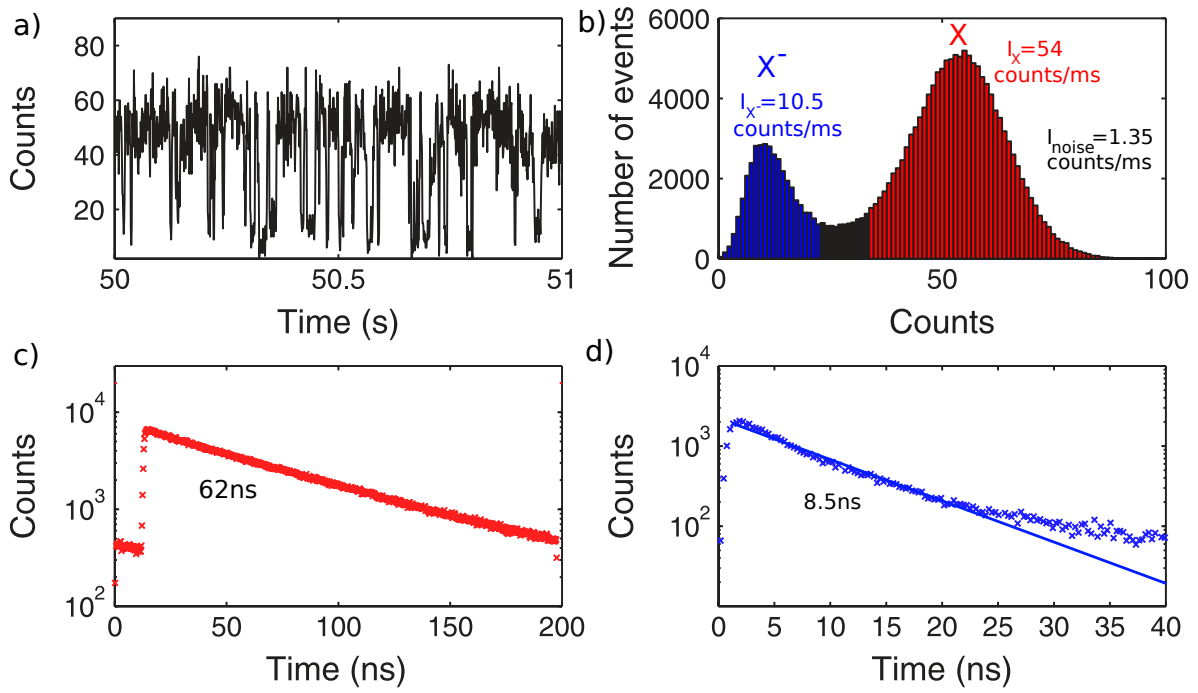

Figure III.5: Reduced blinking and grey state. *a) Photoluminescence time-trace of a CdSe/CdS nanocrystal displaying reduced blinking. b) Photoluminescence intensity histogram of the time-trace shown in a). c) Photoluminescence decay of the bright state together with a monoexponential fit. d) Photoluminescence decay of the grey state together with a monoexponential fit. Figure reproduced from reference [165].*

Negative or positive extra charge

For type A blinking, we have already shown thanks to the electrochemistry results that the extra charge remaining in the nanocrystal should be an electron, while the hole is trapped. The preferred scenario for hole trapping in this case is via photoionization [82,151]. This is suggested by pump-intensity-dependent measurements. If two electron-hole pairs are created inside the nanocrystal, one hole can be ejected via Auger effect. In fact, in CdSe/CdS the Auger relaxation towards holes is still efficient due to its high confinement inside the core and the high density of states.

Moreover, the appearance of a grey state associated with reduced blinking has been clearly observed for thin shell CdSe/CdS dot-in-rods to which is added a hole trap made of a PbS sphere grown at one tip of the dot-in-rod [167]. The addition of the hole trap leads to a negative charging of the core under photoexcitation which causes an enhanced occurrence of the grey state compared to dot-in-rods without the PbS trap and a switching dynamics between the grey and bright states with almost no long (> 100 ms) periods.

III.2 Dot-in-rods blinking statistics

The dot-in-rods are characterized by a minimum number of CdS monolayers on top of the core given in Tab.III.1. We call in the following samples DR1 and DR2 thin shell dot-in-rods while samples DR3 and DR4 are thick shell dot-in-rods. In the following we explain why a type A blinking model is well suited for our thick shell dot-in-rods. We show that the emission can be attributed to two sates: a neutral and a singly charged dot. Once this is demonstrated we focus the analysis on the blinking statistics and timescales. The case of the thin-shell dot-in-rods is briefly studied at the end of the chapter.

	Core diameter (nm)	Shell thickness (nm)	CdS monolayers
DR1	2	3.6	4
DR2	3.3	4	3
DR3.1/3.2/3.3	3.3	7	10
DR4	4.6	11	16

Table III.1: Minimum number of CdS monolayers on top of the CdSe core. *A CdS monolayer perpendicular to the c axis of a wurtzite structure corresponds to* 0.4135 *nm [168]. The number of CdS monolayers indicated is the number of monolayers on top of the core in a direction perpendicular to the c axis, it is the minimum number of monolayers on top of the core.*

III.2.1 Type A blinking

We present the photoluminescence of a typical dot-in-rod of the sample DR3.2 in Fig.III.6, for an excitation below saturation ($\langle N_{eh} \rangle = 0.3$), with a bin time $\Delta t = 250$ μs. The histogram of the photoluminescence (middle of Fig.III.6) reveals the presence of two peaks that can be fitted with the sum of two Poisson distributions (solid blue line). One emission state, for example the exciton state, corresponds to one Poisson distribution once the signal is binned. The low emission state is well above the noise level (here 1 count/ms) such that our dot-in-rods are characterized by a reduced blinking as exposed before. A striking observation is the absence of long bright and grey periods. This is clear on the zoom on a 200 ms window presented on the right of Fig.III.6. The maximum duration of each state is around 10 ms, this is discussed later on. The intensity of emission of the bright and grey states are $I_X = 69$ Counts/ms and $I_{X^-} = 20$ Counts/ms respectively. These observations points towards a dominant type A model associated with reduced blinking for our dot-in-rods.

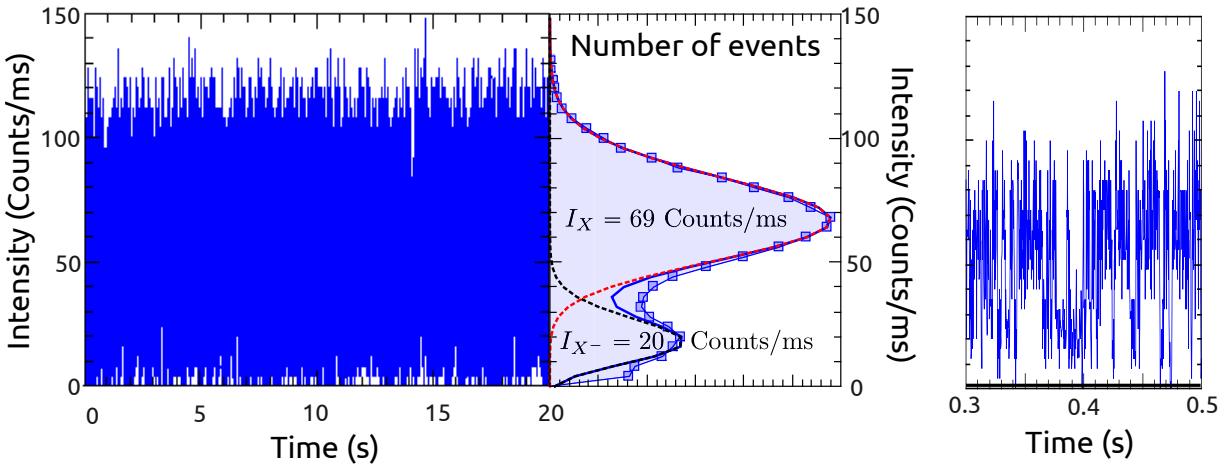

Figure III.6: Example of a typical timetrace for DR3.2 at $\langle N_{eh} \rangle = 0.3$. *Left: Photoluminescence for a 20 s duration, bin time $\Delta t = 250$ μs. The corresponding histogram is shown (middle). Two states are clearly visible, a fit with two Poisson distributions (blue line) reproduces well the measured histogram and gives $I_X = 69$ Counts/ms and $I_{X^-} = 20$ Counts/ms. Right: zoom on a 200 ms time window, the maximum duration of the two states appears to be of the order of 10 ms.*

Tools to analyze the blinking

Distribution of bright and grey states durations Let us first analyze the blinking events with the method relying on the distribution of event durations. First, let us clarify what we want to study. We would like to characterize the bright and grey states by their cumulative probability distributions $\mathcal{P}_b(\tau_b \geqslant \tau)$ and $\mathcal{P}_g(\tau_g \geqslant \tau)$. In the literature [19,135], one can typically find for nanocrystals presenting a reduced blinking as in our case, analysis taking into account only the OFF events (events very close from the noise level). We give an example on Fig.III.7, we fix a very low threshold (8 counts/ms, 8 times the noise level) as shown on Fig.III.7a with the area highlighted in black, and then compute the cumulative distribution for events below this threshold that we will call OFF events because they are close to the noise level. The result is shown on Fig.III.7b. We can fit the distribution with a power law (black straight line) with exponent $\mu_{off} = 2.4$. Such an exponent (greater than 1) tells that long OFF periods are very unlikely as the distribution decreases fast contrary to the case with an exponent smaller than one. References [19,135] use this criterion to state that their nanocrystals display a reduced blinking. However this analysis does not give information about the blinking dynamics of the grey and bright states.

In the following we want to characterize the blinking phenomenon for the bright ($\mathcal{P}_b(\tau_b \geqslant \tau)$) and grey ($\mathcal{P}_g(\tau_g \geqslant \tau)$) states. Conversely to the first studies on blinking for which the behaviors of the ON and OFF states are well detailed and studied, *the blinking statistics for nanocrystals displaying a reduced blinking is less studied in the literature.*

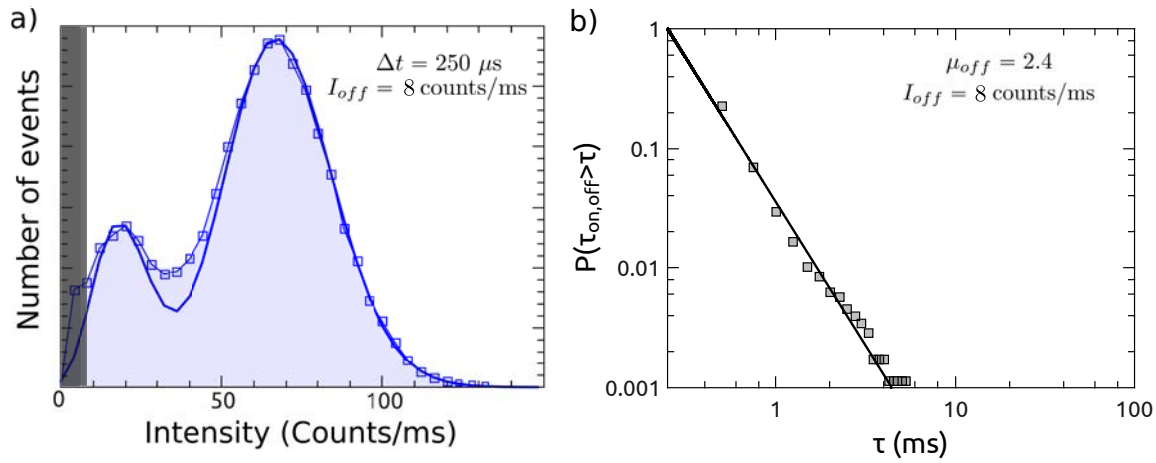

Figure III.7: Analysis of the OFF events. *a) Emission histogram for a bin time* $\Delta t =$ 250 μs*. The area in black below* 8 *counts/ms defines the OFF events. b) Cumulative distribution of OFF event durationss. A fit gives* $\mu_{off} = 2.4$*.*

On Fig.III.8a we present the cumulative distributions of the bright and grey states event durations for the same nanocrystal than on Fig.III.7, using a bin time $\Delta t = 250$ μs and thresholds I_b and I_g for the bright and grey states events fixed in between the two states at $I_b = I_g = 35$ counts/ms[4]. The distributions shows that long periods are strongly inhibited for both type of events, grey or bright, as expected from the timetrace on Fig.III.6. Fits of the distributions are presented on Fig.III.8a as dashed and full lines corresponding respectively to exponential distributions and power law with exponential cutoff distributions. The exponential distributions are defined as:

$$\mathcal{P}(\tau) \propto e^{-\tau/\tau_c}, \tag{III.2}$$

with τ_c the average event duration. The power law with exponential cutoff is written as:

$$\mathcal{P}(\tau) \propto \frac{1}{\tau^{\mu}} e^{-\tau/\tau_c}, \tag{III.3}$$

with μ the power law exponent. We can clearly observe that the experimental distributions can not be fitted by the exponential laws while a good agreement is found when considering the addition of a power law. We obtain power law exponents of 0.55 and 0.36 for the grey and bright states respectively with exponential cutoffs of 2.7 and 12.7 ms for the cumulative distributions. Exponential distributions of event duration arise from the existence of single, well defined, switching rate between the two states. A power law distribution reveals a more complex physical process. Indeed, to mathematically obtain a power law distribution of event duration, it is necessary to have switching rates that are

[4]Time bins with intensities above I_b are considered as part of the bright state and time bins with intensities below I_g are considered as part of the grey state.

exponentially distributed. For example, to explain the power law blinking in nanocrystals, carriers tunneling towards traps with different rates depending on the distance of the trap was proposed as a model, the rate k being distributed as $k \propto e^{(-d/\lambda_d)}$, with d the distance between the core and a trap and λ_d the tunneling length [169].

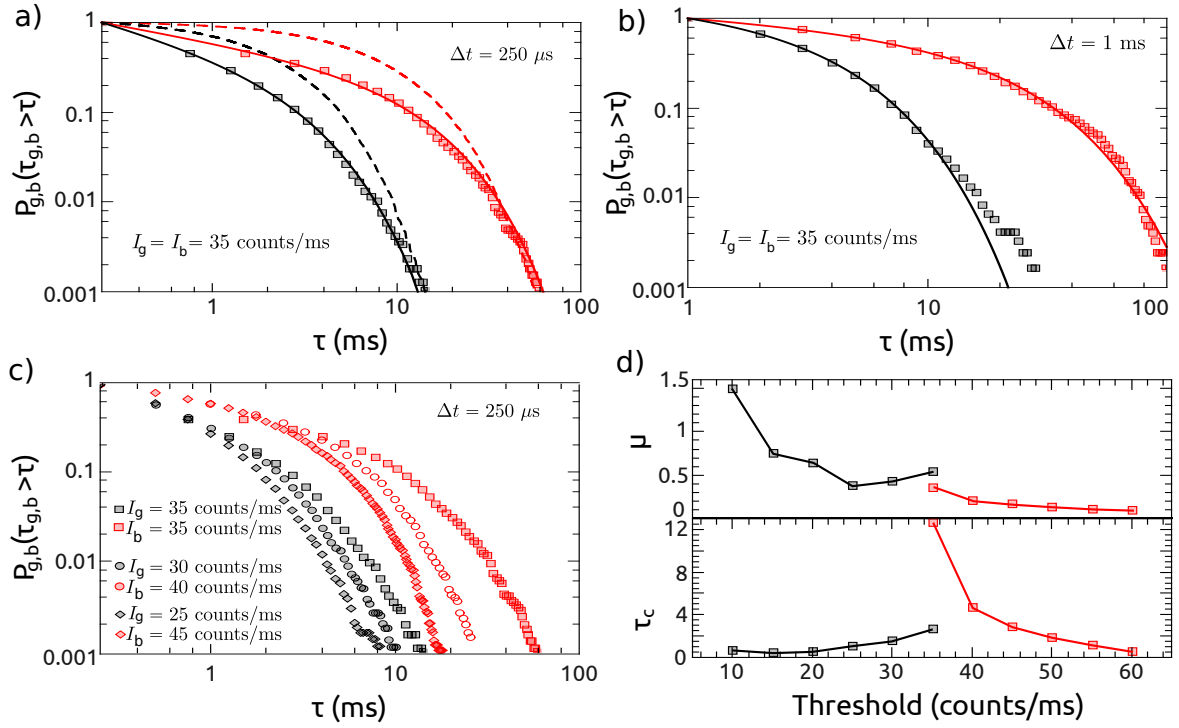

Figure III.8: Cumulative distributions of the bright and grey states event durations. *Red: bright state, black: grey state. a)Bin time Δt = 250 μs, thresholds: $I_b = I_g$ = 35 counts/ms. Dashed lines: exponential distributions (red: τ_c = 8 ms, black: τ_c = 2 ms), full lines: power law distribution with exponential cutoff (red: μ = 0.36 and τ_c = 12.7 ms, black: μ = 0.55 and τ_c = 2.7 ms). b) Bin time Δt = 1 ms, thresholds: $I_b = I_g$ = 35 counts/ms. full lines: Power law distribution with exponential cutoff (red: μ = 0.18 and τ_c = 19 ms, black: μ = 0.13 and τ_c = 3.2 ms). c) Bin time Δt = 250 μs, thresholds: $I_b = I_g$ = 35 counts/ms for □ , I_b = 30 counts/ms and I_g = 40 counts/ms for ○, I_b = 25 counts/ms and I_g = 45 counts/ms for ◇. d) Evolution of the power law with exponential cutoff fit parameters μ and τ_c with the threshold values.*

When the two states are close from each other in terms of emission rates, the analysis of event durations is not totally reliable, indeed it strongly depends on the thresholds chosen and also on the bin time Δt of the intensity timetrace as demonstrated in reference [170]. This is shown on Fig.III.8b, c and d. In Fig.III.8b we present the analysis with a bin time Δt = 1 ms and the same thresholds than in Fig.III.8a (Δt = 250 μs in Fig.III.8a). The curves have the same shapes, the fits yield power law exponents of 0.13 and 0.18 for the grey and bright states respectively with exponential cutoffs of 3.2 and 19 ms. Changing the bin time has considerably modified the distributions and the fitting values. In the next section we explain how to make a reasonable choice of bin time for a given

fluorescence timetrace. We can already say that the bin time of $\Delta t = 1$ ms is less relevant that the bin time of $\Delta t = 250$ μs for the studied timetrace. In fact, with the bin time $\Delta t = 250$ μs, the distributions of event durations present a certain dynamics, slope, between $\Delta t = 250$ μs and $\Delta t = 1$ ms on Fig.III.8a. A flat cumulative distribution means that no events at the durations considered exist. Then the slope between 250 μs and 1 ms in Fig.III.8a is due to events that have these durations. Hence all these events can not be resolved with a bin time of $\Delta t = 1$ ms.

In Fig.III.8c we show the effects of the choice of thresholds, we can clearly observe a change in the curves shapes while moving the thresholds. Fig.III.8d presents the evolution of μ and τ_c for an increasing intensity threshold for the bright state, and decreasing intensity threshold for the grey state. Both parameters are strongly affected by a change of the threshold. The choice of a threshold that gives the largest statistics for both states is more relevant, so here $I_b = I_g = 35$ counts/ms. However a minor change of threshold around the middle point between the two states changes considerably the fitting parameters. Going from $I_b = 35$ counts/ms to $I_b = 40$ counts/ms for the bright state, μ decreases from 0.36 to 0.21 and τ_c decreases from 12.7 ms to 4.7 ms.

It seems that the statistics is still distributed as a power law with exponents between 0 and 1 as for the bare CdSe or CdSe/ZnS nanocrystals ON and OFF events, except that the exponential cutoff arises on milliseconds timescales rather than seconds or minutes[5]. The analysis of bright and grey states blinking statistics by directly determining the event durations is not well suited for a quantitative study as the choices of bin time and thresholds values strongly influence the resulting distributions.

Normalized correlation function, $g^{(2)}$ function and blinking. In this section we study the blinking between the bright and grey state using a different approach: the intensity correlation function of the emission. This is not a widely used method to characterize blinking, however some articles on nanocrystals [169, 171] and molecules [172, 173] present such an analysis. Also, the power spectral density which is equal to the Fourier transform of the intensity autocorrelation function, as stated by the Wiener-Khinchin theorem, has been used in two publications [174, 175]. The autocorrelation method is less straightforward than the distribution of event durations but it does not suffer from any a priori assumptions and it yields information at short timescales not reachable when binning the signal. However it does not yield directly separate information on the bright and grey states.

The temporal intensity correlation $g^{(2)}$ of a light field is defined as follows:

[5]Here the cutoff is due to a physical phenomenon and not to the finite acquisition time of the experiment. We usually register the photoluminescence for 20 to 60s, the cutoff due to the acquisition time arises in this case around a couple of hundreds of milliseconds as shown later on in this chapter.

$$g^{(2)}(t_0, t_0+\tau) = \frac{\langle I(t_0)I(t_0+\tau)\rangle}{\langle I(t_0)\rangle\langle I(t_0+\tau)\rangle}, \tag{III.4}$$

with t_0, $t_0+\tau$ time instants, $\langle\rangle$ denotes a statistical (ensemble) average. For stationary light fields, the average intensity is constant in time, $\langle I(t_0)\rangle = \langle I(t_0+\tau)\rangle$, and $g^{(2)}(t, t+\tau) = g^{(2)}(\tau) = \langle I(t)I(t+\tau)\rangle/\langle I(t)\rangle^2$. We briefly discuss the physical meaning of the $g^{(2)}$ function necessary for the understanding of the discussion in this chapter, some more details and physical insights on the $g^{(2)}$ function are given in the next chapter. For a Poisson emission process, one can show that the $g^{(2)}$ function has a value of one. In a Poisson process, the time between each consecutive emission events has an exponential distribution and each of these arrival times is assumed to be independent of other arrival times. So it is a random emission with a given rate defined by the exponential law of the arrival times. This leads to a Poisson distribution of the intensity of emission.

If the statistics of the emission does not follow a Poissonian process but rather a super-Poissonian statistics (a probability distribution with a larger variance than a Poisson distribution with the same mean value) then the $g^{(2)}$ function is greater than one. The emission is said to be bunched. The emission from a given state of a nanocrystal follows a Poissonian process, however blinking between two states leads to a super-Poissonian statistics because two emission rates coexist. The super-Poissonian statistics is clearly visible in the histogram of Fig.III.6 where two Poisson distributions are necessary to fit the histogram.

At this stage of the discussion it is important to say that we are interested in the nanocrystals as emitters of "classical light". Therefore, in the following we are not approaching timescales of the order of the emitter lifetime (nanoseconds timescales) as will be the case in the next chapter. Even when we talk about short timescales, they are even longer than the emission lifetime. We deal with binned signals from the avalanche photodiodes, a photocurrent, and not discrete single photon detection events. Hence, Eq.III.4 is a classical autocorrelation calculated from the photocurrent $I(t)$. In this case the light source is either Poissonian or super-Poissonian as described above, it is a classical light source. Previously we said that we are not limited by a bin time to calculate the $g^{(2)}$ function. This is true if one truly computes the $g^{(2)}$ function detection events by detection events, so not by dealing with photocurrents. This is possible but computationally heavy and it cannot be extended to timetraces longer than a couple of seconds otherwise too many detection events need to be computed. In this chapter we binned the signal to compute the $g^{(2)}$ function but we are not limited to milliseconds or hundreds of microseconds as in the case of intensity distributions or cumulative distributions of bright and grey duration events but rather to 1 μs to be computationally efficient. Therefore

the timescales investigated in this chapter are limited to an inferior bound of 1 μs. The fact that the $g^{(2)}$ function is a statistical average with a normalization implies that the bin time can be taken as small as one wants contrary to methods relying on the intensity distribution.

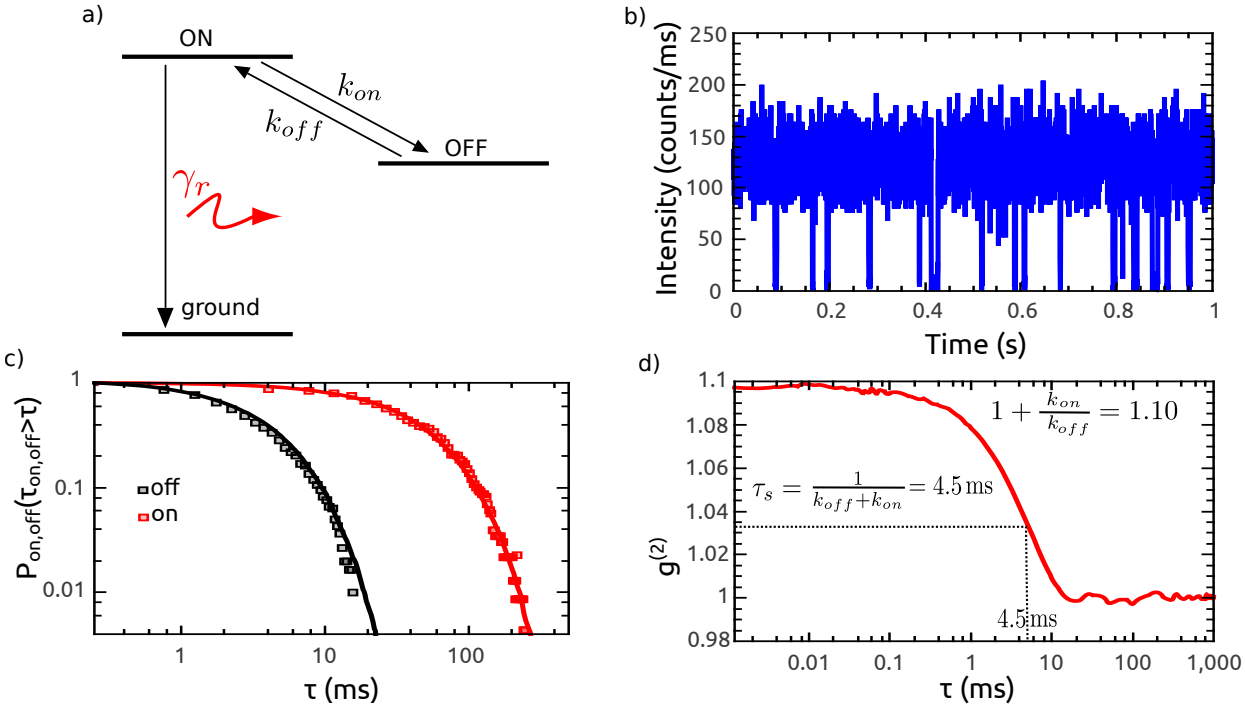

Figure III.9: Blinking between ON and OFF states with simple exponential laws. *a) Model for the photoluminescence. A ON state emits photons with a rate γ_r. The emitter can switch to a dark state (OFF state) that does not emit photons with a rate k_{on} and switch back to the ON state with a rate k_{off}. b) Simulation of the emission from an emitter following the model depicted in a with $1/k_{on} = 50$ ms and $1/k_{off} = 5$ ms. c) Cumulative distributions $\mathcal{P}_{off}(\tau_{off} > \tau) \propto 1/\tau^{\mu_{off}}$, $\mathcal{P}_{on}(\tau_{on} > \tau) \propto 1/\tau^{\mu_{on}}$ found from the emission simulation. The straight lines are fits with the expected exponential distributions with rates $1/k_{on} = 50$ ms and $1/k_{off} = 5$ ms. d) $g^{(2)}$ function found from the emission simulation. The bunching value agrees with the proposed value from Eq.III.5 as well as the exponential decay value.*

Looking at the literature we can find that for molecules displaying emission intermittency, the case of a blinking with a single rate k_{on} for a transition from ON state to OFF state and another rate k_{off} for a transition from OFF state to ON state, has been studied [172,173]. We propose to detail this case to grasp the physics before tackling the more complex case of nanocrystals. The model is presented on Fig.III.9a, one level of emission (ON) emits photons with a certain rate γ_r. The emitter eventually falls in a dark state (OFF) with a given rate k_{on}, no photons are emitted until the emitter switches back to the ON state with a given rate k_{off}. We present on Fig.III.9 simulations of such an emission process considering a random telegraph whose ON and OFF periods deterministically succeed one another, but without any memory of previous ON and OFF times.

We thus generate a series of detected counts similar to the experiment and analyze this simulated detected events.

The resulting time trace is presented on Fig.III.9b for $1/k_{on} = 50$ ms and $1/k_{off} = 5$ ms with a bin time $\Delta t = 250$ μs. The ON periods are longer than the OFF periods as expected from the chosen rates. The existence of a single switching rate for the transition from one state to another lead to exponential distributions of the ON and OFF duration events. In Fig.III.9c we can see that the cumulative distributions of ON and OFF periods are very well fitted by the expected exponential distributions (full lines). In this case, this analysis works fine because the two states are very well separated in terms of emission rates and the blinking dynamics is slow compared to the bin time. The $g^{(2)}$ function also shows an exponential dependency[6] according to references [172, 173]:

$$g^{(2)}(\tau) = 1 + \frac{k_{on}}{k_{off}} \exp(-\tau/\tau_s), \tag{III.5}$$

with $\tau_s = 1/(k_{on} + k_{off})$ and a bunching value of $1 + k_{on}/k_{off}$. This function looks flat on a log scale before falling for timescales corresponding to the cutoff τ_s. Physically, the switches between the two states happen at timescales shorter than three times the cutoff (for longer times the exponential distribution is close to zero). When the $g^{(2)}$ function is unity, it means that virtually no switching happens between the two states. As we can see on Fig.III.9d, the $g^{(2)}$ function found from the simulation of the emission follows Eq.III.5, the bunching value is close to the expected one $1 + k_{on}/k_{off} = 1.10$. The exponential falls down with a time of 4.5 ms, as attested by the value at 37% of the bunching, which is in agreement with the theoretical formula: $\tau_s = 1/(k_{on} + k_{off}) = 4.5$ ms.

The $g^{(2)}$ is therefore a powerful tool to analyze the blinking as it gives directly the timescales on which the switching between the states happens without limitations for the fast dynamics due to a bin time.

[6] The expression in Eq.III.5 and the given value of bunching and τ_s are valid in the limit of a fast pumping rate compared to the relaxation rates of the emitter and $k_{on} \ll k_{off}$.

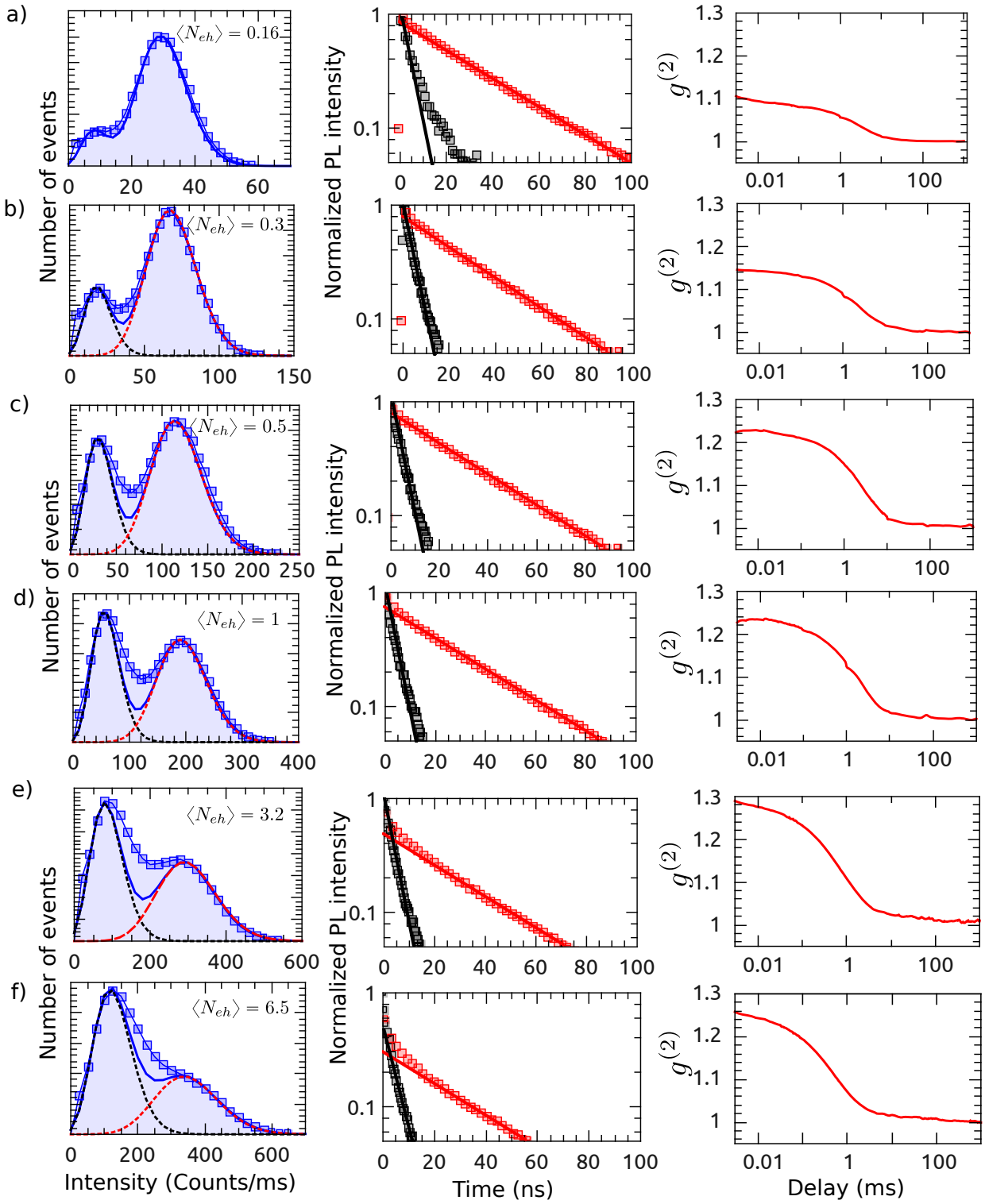

Figure III.10: Blinking for a dot-in-rod of sample DR3.2 at different excitation power. *Left: Histogram of emission together with a fit with two Poisson distributions (solid blue line). Middle: Photoluminescence decay for the grey (black) and bright state (red) with monoexponential fits: $\tau_X \simeq 34$ ns and $\tau_{X^-} \simeq 5$ ns. Right: $g^{(2)}$ function for delays from 1 μs up to 1 s. a) $\langle N_{eh}\rangle = 0.16$, Histogram: Bin time $\Delta t = 500$ μs, bright state mean intensity: $I_X = 30$ counts/ms, grey state mean intensity: $I_{X^-} = 9$ counts/ms. b) $\langle N_{eh}\rangle = 0.3$, $\Delta t = 250$ μs, $I_X = 69$ counts/ms, $I_{X^-} = 20$ counts/ms. c) $\langle N_{eh}\rangle = 0.5$, $\Delta t = 150$ μs, $I_X = 117$ counts/ms, $I_{X^-} = 33$ counts/ms. d) $\langle N_{eh}\rangle = 1$, $\Delta t = 100$ μs, $I_X = 195$ counts/ms, $I_{X^-} = 60$ counts/ms. e) $\langle N_{eh}\rangle = 3.2$, $\Delta t = 50$ μs, $I_X = 300$ counts/ms, $I_{X^-} = 90$ counts/ms. f) $\langle N_{eh}\rangle = 6.5$, $\Delta t = 40$ μs, $I_X = 350$ counts/ms, $I_{X^-} = 130$ counts/ms.*

Analysis of the blinking at various excitation powers.

Let us now present the case of our dot-in-rods. Fig.III.10 shows the emission of the same nanocrystal than in fig.III.6 but at various excitation power. We present the main ideas that can be extracted from such data; a discussion on some specific points of interests is developed in the next sections. It is straightforward to notice that the emission is characterized by two Poisson distributions. The average intensity of the low emission state is positioned at 30% $\pm$ 3% of the bright emission state (the average intensities are given in the caption of Fig.III.10).

The photoluminescence decay of the intensity bin falling in the black and red windows of the intensity histograms are plotted on the middle figures. The decay curves are well fitted by monoexponential decay functions with $\tau_X \simeq 34$ ns and $\tau_{X^-} \simeq 5$ ns. For Fig.III.10a, the grey state decay fit is not relevant as the number of photons is fairly low with consequently a low signal to noise ratio. Above saturation in Fig.III.10e and f, a fast decay component is present that can be attributed to multiexciton emission. The presence of this two decay constants implies that a type A blinking model is well suited to describe the emission of our dot-in-rod. The grey state is associated to the negative trion and the bright state to the exciton. The decay constants fit very well with the value of the grey state quantum yield of 30% found with the histograms (assuming a quantum yield of 1 for the exciton [94,96]). In fact, by definition $Q_{X^-} = \gamma_r^{X^-}/\gamma^{X^-} = \gamma_r^{X^-}\tau_{X^-}$, with τ_{X^-} the measured decay constant of the trion state and $\gamma_r^{X^-}$ its radiative recombination rate. Assuming a scaling of the recombination rate with the number of charges, we expect that $\gamma_r^{X^-} = 2\gamma_r^X$ because of the presence of the extra electron that offers an additional relaxation path. This approximation is expected to be valid for modeling room-temperature photoluminescence dynamics, when the bright-dark exciton splitting is small compared with the thermal energy [150, 151, 161]. Then it comes that $Q_{X^-} = 2\gamma_r^X\tau_{X^-} = 2\tau_{X^-}/\tau_X$ as the exciton recombination is purely radiative[7]. The measured values gives $Q_{X^-} = 2 \times 5/34 \simeq 29\%$ in good agreement with the intensity ratio obtained with the emission histograms.

Finally, on the right side of Fig.III.10 we present the $g^{(2)}$ function. The emission is characterized by a bunching for delays between 1 μs and roughly 10 ms. For delays longer than 10 ms the $g^{(2)}$ function drops down to one. As explained previously this reflects the fact that the blinking periods rarely last more than 10 ms as already envisioned on the photoluminescence time trace in Fig.III.6.

The previously described emission characteristics with the two well defined states is the common emission scenario for thick shells dot-in-rods.

[7] $Q_X = 1$ implies $\gamma_r^X = 1/\tau_X$.

The absence of additional charged states at the high excitation values in Fig.III.10 is puzzling. One could expect that at higher excitation a doubly charged exciton state with a lower emission rate than the trion state can appear due to the possible ejection of a second hole. Such a state has been observed for nanocrystals under electrochemical control with a large potential bias [151, 161], the authors suggest that a doubly charged state is less stable than a singly charged state under zero applied potential. They calculate with a relaxation model and their collected data that such a state should relax nonradiatively 20 times faster than a trion state. Also, experiments performed in reference [176] have shown that individual nanocrystals accommodate at most one or two positive charges (holes) upon photoexcitation. Verberk et al. [169] proposed that Coulomb blockade prevents further ionization of the charged dot, another ionization would cost more electrostatic energy than the exciting photon can provide.

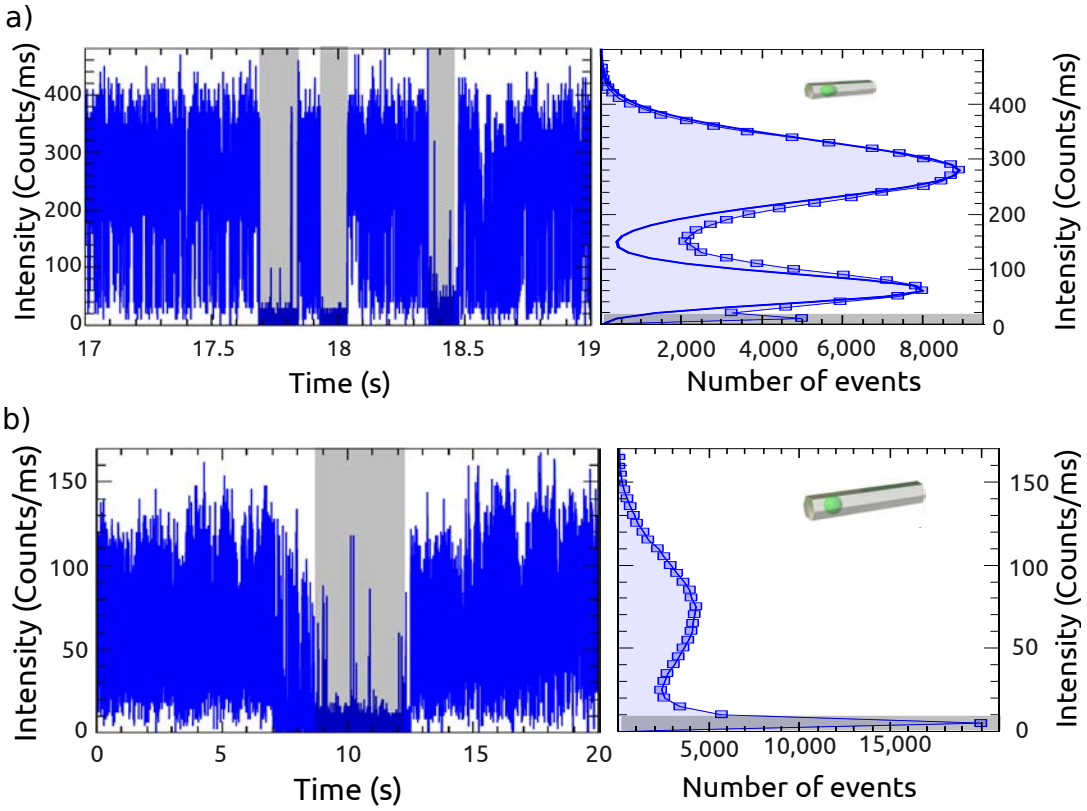

Figure III.11: Example of long blinking events corresponding to a dark state for thin shell DR2 and thick shell DR3.3 samples. *a) DR2, Bin time $\Delta t = 100$ μs. b) DR3.3, Bin time $\Delta t = 500$ μs. The long dark states events are highlighted in black and corresponds to the sharp peak events on the lower part of the histogram on the left hand side.*

A completely dark state of emission is sometimes visible in our measurements that could be associated with a doubly charged exciton. An example of such blinking events for thin shell sample DR2 is presented on Fig.III.11 and highlighted in black on the photoluminescence timetrace. The case of the thick and long shell DR3.3 is also presented.

Let us argue why this dark state of emission is most probably associated with a Type B blinking that would occasionally happen rather than with a doubly charged exciton in a charging model (Type A blinking):

- it occurs mostly for the thinner shells dot-in-rods. We have seen that as the traps are located at the surface of the shell, type B blinking affects more the emission of thinner shells nanocrystals as the electron can tunnel more easily towards the traps.
- The thick shell samples DR3.3 is the exception among the four thick shell samples. It displays this type of blinking more often than the other thick shells samples. It has the biggest surface of all the samples, implying more surface traps compared to the other thick shells samples.
- These blinking events can last for long periods of time (up to a couple of seconds such as on Fig.III.11b) conversely to the above mentioned blinking process characterized by a cutoff on milliseconds timescales.

The conclusion of this section is that *a dominant type A (charging) blinking model with two states of emission* characterizes the emission of our thick shell dot-in-rods. The three points that lead to this conclusion are:

- The histogram of the emission if built with a proper bin time shows two distinct Poisson distributions.
- Each Poisson distribution is characterized by a well defined decay constant.
- The statistics of blinking duration shows a cutoff at the milliseconds timescale.

In the following we are focusing our analysis mainly on the type A blinking.

III.2.2 Blinking timescales and statistics

Blinking timescales

The histograms in Fig.III.10 were realized with different time bins. When using a technique of analysis of the signal relying on binning the photon detection events together, it is important to optimize the value of the time bin. In fact, when at least two states of emission exist with different emission rates, an "unoptimized" bin time can lead to a wrong appreciation of the emission processes. In the literature about nanocrystals most of the publications present data with bin times of 10 ms or more even when they have

high collection rates [166]. Such bin times are not suited for nanocrystals presenting a reduced blinking.

In Fig.III.12, we show the histogram of the emission corresponding to the nanocrystal of Fig.III.10 at the excitation $\langle N_{eh} \rangle = 0.3$ for different time bin. The intensity scale is renormalized in counts/ms in each case as it is a convenient scaling value. We can clearly see that for $\Delta t = 5$ ms (left) and $\Delta t = 1$ ms (middle) the fit with 2 Poisson distributions does not reproduced the measured distribution properly. One could think that a continuous distribution of emission state is present [166], but this is only due to the fact that the bin width is too large compared to the typical blinking event duration such that the two states are mixed. Fig.III.12 right shows that with a bin time $\Delta t = 250$ μs, a fit with two Poisson distributions is far more accurate than with larger bin times. Therefore the question of finding an "optimized" bin time is intrinsically linked to the timescales at which the blinking process occurs.

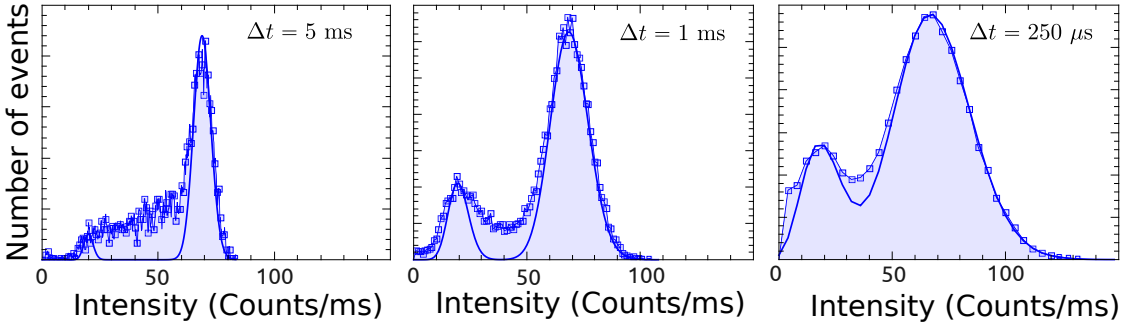

Figure III.12: Bin time effect on the intensity histogram. *Histogram of Fig.III.10b for different time bin Δt. Each histogram is renormalized in counts/ms. Left: $\Delta t = 5$ ms, middle: $\Delta t = 1$ ms, right: $\Delta t = 250$ μs. A fit with two Poisson distributions is given for each case.*

As described earlier, the $g^{(2)}$ function is a powerful tool to determine the blinking timescales. Fig.III.13a presents the $g^{(2)}$ function corresponding to the intensity histograms in Fig.III.12. For this dot-in-rod that is typical of the dot-in-rods displaying a reduced blinking, the blinking events happen on timescales smaller than 10 ms for which the $g^{(2)}$ function is greater than one. Therefore a bin value of 10 ms is a superior bound to consider when binning the signal. In Fig.III.12c we can see that even a histogram built with a bin time of $\Delta t = 250$ μs is not perfectly fitted by the sum of two Poisson distributions because events with duration shorter than 250 μs exist.

In Fig.III.13b, for comparison, we show the $g^{(2)}$ function measured for a CdSe/ZnS nanocrystal [171] with blinking events between ON and OFF states up to seconds or minutes timescales as in Fig.III.1. In this case the blinking dynamics is distributed on 5 orders of magnitude, there is no cutoff on millisecond delays. The three curves comes from the same measurement, the $g^{(2)}$ function is computed for different acquisition times

T: 18, 180, and 1800 s for curves (i), (ii) and (iii) respectively. The existence of ON and OFF times that are comparable to T explains why the decay of the $g^{(2)}$ function always occurs on a timescale of the order of the measurement time. So, for this measurement, the cutoff is imposed by the acquisition time rather than by a physical process.

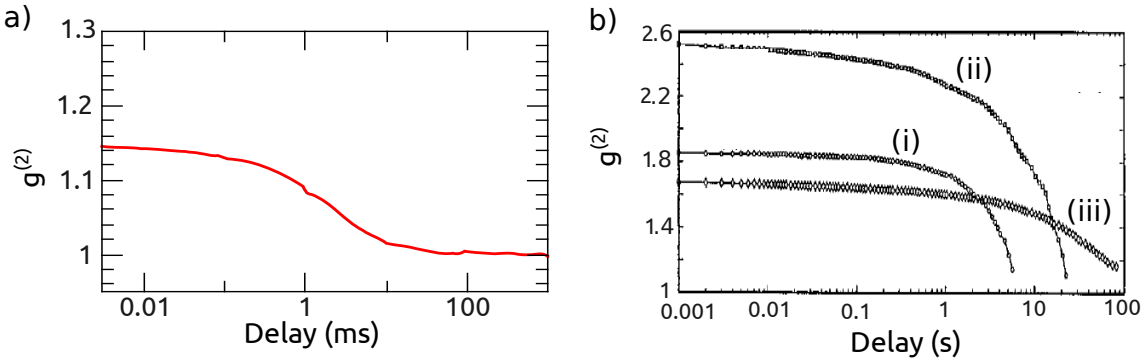

Figure III.13: Blinking timescales for our CdSe/CdS dot-in-rods and CdSe/ZnS dots. *a) Typical $g^{(2)}$ function for dot-in-rods characterized by a reduced blinking. The acquisition time is of $T = 20$ s. b) $g^{(2)}$ functions for a CdSe/ZnS nanocrystal computed for the same measurement. Curves (i), (ii), and (iii) correspond to time intervals T of 18, 180, and 1800 s for computing the corresponding $g^{(2)}$ functions. Figure b is reproduced from reference [171].*

The conclusion of this paragraph is that for our dot-in-rods displaying a reduced blinking the switching between the bright and grey states happens on timescales from microseconds up to 10 ms. This implies that bin time of the order of hundred microseconds and not a couple of milliseconds have to be used in order to correctly resolve the emission processes.

Sorting photons We will now add a few words on how to sort photons, i.e. how to determine for each measured photons from which states it is emitted from. The method we use throughout this thesis is to discriminate the photons using the histogram of intensity as in Fig.III.10. In the next chapter we determine the photon statistics of our dot-in-rods in the presence of blinking by sorting photons with this method. It is therefore important to understand the conditions in which this method is relevant. The conditions are the following ones:

- first of all the bin time has to be carefully chosen as described above to accurately discriminate the detection events. The obtained histogram needs to be accurately fitted by two Poisson distributions.

- The two states need to have emission rates (quantum yields) different enough such that the Poisson distributions do not overlap too much. DR3.1 and DR3.2 usually

fulfills this criterion. In this case intensity windows such as the red and black intensity windows in the histograms of Fig.III.10 can be chosen for each state. If the associated photoluminescence decay curves are monoexponentials then the photon sorting is relevant.

More sophisticated statistical methods to sort photons emitted by a single particle displaying intensity jumps have been recently proposed [177].

Blinking statistics

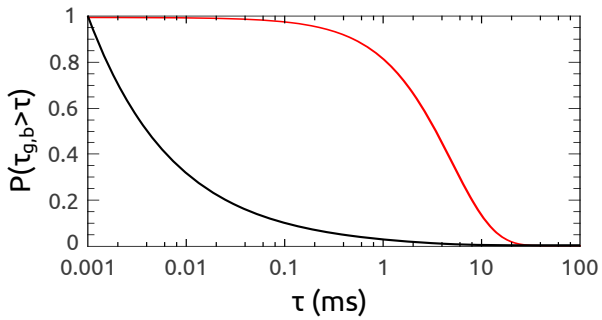

Figure III.14: Examples of cumulative distributions. *Red line: exponential distribution with cutoff of* 5 *ms, black line: truncated power law with exponent* $\mu = 0.5$ *and cutoff of* 5 *ms.*

In this section we want to focus the study on the statistics of blinking. The analysis in terms of cumulative distributions of event durations points towards truncated power laws (power laws with an exponential cutoff) for the statistics of blinking. Compared to an exponential distribution, the power law with truncation confers a higher statistical weight to fast switching events as shown on Fig.III.14. We can observe that an exponential distribution of cumulative event durations (in red on Fig.III.14) is characterized by a higher probability for longer events than a truncated power law (in black on Fig.III.14) with the same cutoff value.

The fact that fast blinking dynamics are favored by truncated power laws is directly visible on our measurements. Fig.III.15a shows the intensity histogram of a measurement already presented on Fig.III.10c with an excitation of $\langle N_{eh} \rangle = 0.5$. The corresponding cumulative distributions of event duration are presented on Fig.III.15b for intensity thresholds $I_b = I_g = 58$ counts/ms in between the two states. A fit with truncated power laws gives exponential cutoffs of 6 ms and 2.5 ms for the bright and grey state respectively.

We simulated the emission of a nanocrystal with exponential distributions of bright and grey states. The simulation generates photon detection events and takes into account the quantum yields of the exciton and trion as well as the losses of the system. For the exponential distributions of bright and grey state events we chose to simulate the emission

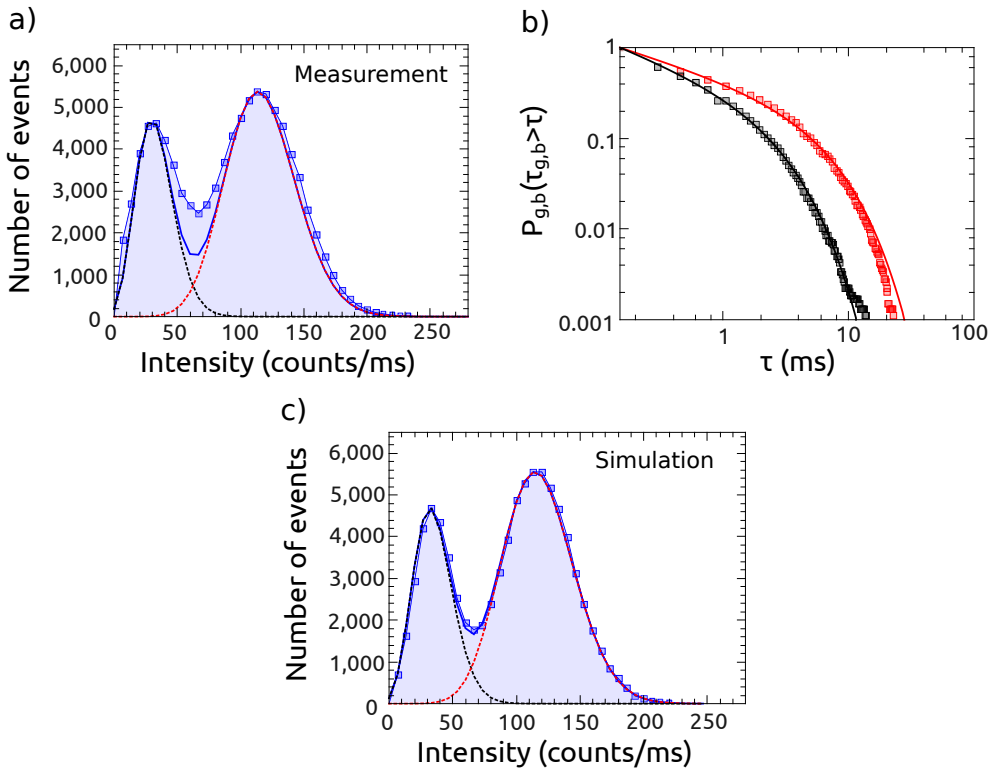

Figure III.15: Measurement and simulation of the emission of a nanocrystal with exponential distributions of blinking events. *a) Measurement: histogram of emission of a measurement on a dot-in-rod of sample DR3.2 for* $\langle N_{eh} \rangle = 0.5$. *Bin time* $\Delta t = 150$ μs. *b) Cumulative distributions of bright (red) and grey states (black). Intensity thresholds:* $I_b = I_g =$ 58 *counts/ms. Truncated power law fits yield* $\mu_b = 0.42$, $\mu_g = 0.53$ *and exponential cutoffs of* 6 *and* 2.5 *ms. c) Simulation: histogram of emission obtained from the simulation of the emission of a nanocrystal with exponential distributions of blinking events, grey state cutoff:* 4.5 *ms, bright state cutoff:* 9.2 *ms. Bin time* $\Delta t = 150$ μs.

processes with exponential cutoffs in the range 1 to 10 ms as suggested by the measured distributions of event duration in Fig.III.15b. The simulated histogram of emission on Fig.III.15c is therefore obtained for pure exponential distributions with a grey state cutoff of 4.5 ms and bright state cutoff of 9.2 ms. The general shape of the obtained histogram is very close to the measurement and with such a distribution of events the histogram is perfectly resolved with a bin time of $\Delta t = 150$ μs, the fit with two Poisson distributions matches the obtained histogram. This is not the case for the measurement because fast switching events favored by the power law are not correctly resolved with the bin time of $\Delta t = 150$ μs.

The imperfect fit of the measured intensity distributions with the sum of two Poisson distributions is therefore a direct consequence of the fast switching dynamics imposed by the power law.

Let us now develop a quantitative description of the blinking statistics. As we have

seen in the previous section the cumulative distributions of event durations obtained from the binned signal cannot yield precise information on the blinking statistics because of their dependence on the chosen bin time and thresholds. References [169, 178] derive a formula for the $g^{(2)}$ function in the case of an emitter switching between ON and OFF emission states, both emission states following power law distributions of event durations:

$$g^{(2)}(\tau) = B(1 - A\tau^{1-\mu}), \tag{III.6}$$

with A and B constants. μ is the largest power law exponent, either μ_{OFF} or μ_{ON}. This formula is only valid for timescales smaller than the exponential cutoffs. B is equal to the bunching value at very low timescales for which $\lim_{\tau \to 0} \tau^{1-\mu} = 0$ as μ is smaller than unity. The parameter A is equal to:

$$A = \frac{1}{\langle \tau_b \rangle} \frac{\tau_{min}^{\mu}}{\Gamma(2-\mu)}, \tag{III.7}$$

with $\langle \tau_b \rangle$ the average duration of the bright state events, τ_{min} the minimum duration of an event and Γ the usual Γ function. For our experiment, the minimum duration of an emission event τ_{min} is equal to 400 ns, the delay between two excitation pulses[8]. The factor A is inversely proportional to the average duration of the bright state. Long average duration of bright state yields $g^{(2)}$ curves that looks flat on a log scale as it gives small A values that counterbalance the decrease imposed by the $\tau^{1-\mu}$ factor. Indeed, the $A\tau^{1-\mu}$ term starts to have a visible effect on the $g^{(2)}$ function on timescales for which it is of the order of 0.1, before it is negligible compared to unity. Hence $\langle \tau_b \rangle$, together with μ, define on which timescales the $g^{(2)}$ starts to fall towards unity. Even though the exponential cutoff is not included in the model, the shape of the $g^{(2)}$ function at short timescales directly depends on the average time duration and therefore on the cutoff.

We first look at the case of the thinner shell dot-in-rods displaying long blinking periods and switching between a bright state and an OFF state. Fig.III.16a shows the photoluminescence of such a dot-in-rod with a bin time of $\Delta t = 250$ μs. The corresponding $g^{(2)}$ has the same characteristics than the previous dot-in-rods $g^{(2)}$ functions at small timescales due to the last part of the photoluminescence timetrace. It nevertheless displays an additional bunching tail at larger timescales (> 10 ms) due to the long blinking events present in the first seconds of the recording. The effect of the finite acquisition time is highlighted by an arrow at 500 ms. The decrease of the $g^{(2)}$ function below 10 ms is therefore due to a physical phenomenon as already stated before.

We make the hypothesis that exponential cutoffs are of the order of 5 ms. We fit the

[8]Assuming that a nanocrytsal is charged only upon a photoexcitation event, then the minimum duration of an event, being ON or OFF, is defined by the delay between two excitation pulses.

curve by Eq.III.6 for $\tau < 500$ μs[9]. The fit of the lower part of the $g^{(2)}$ function by Eq.III.6 gives $A = 0.13$ and $\mu = 0.52$. This leads to $\langle \tau_b \rangle = 0.15$ ms.

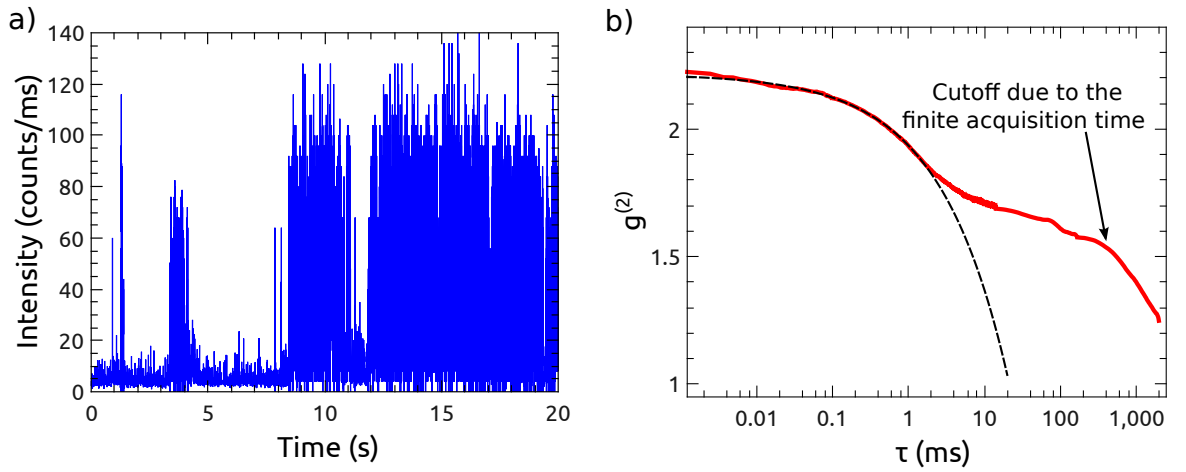

Figure III.16: Photoluminescence and $g^{(2)}$ function for DR2 displaying long blinking events. *a) Photoluminescence timetrace. Bin time $\Delta_t = 250$ μs. b) $g^{(2)}$ function corresponding to the photoluminescence timetrace in a. The fit of the lower part of the curve yields $\mu = 0.52$ and $A = 0.13 \Longrightarrow \langle \tau_b \rangle = 0.15$ ms. The cutoff due to the finite acquisition time is highlighted by the arrow at 500 ms.*

We extend the use of Eq.III.6 to the case of the thick shell dot-in-rods that presents a blinking between a bright and a grey state. Fig.III.17 presents the $g^{(2)}$ function for three dot-in-rods of sample DR3.2, DR3.3 and DR4. We obtain the following parameter values:

	μ	A (ms$^{\mu-1}$)	$\langle \tau_b \rangle$ (ms)
DR2	0.52	0.13	0.15 ms
DR3.2	0.32	$6.4.10^{-2}$	1.36 ms
DR3.3	0.68	0.12	0.46 ms
DR4	0.4	$5.5.10^{-2}$	0.89 ms

Table III.2: Fitting parameters from Fig.III.17

The $g^{(2)}$ curves for DR3.2 and DR4 appears to be almost flat for $\tau < 500$ μs on Fig.III.17a and c because their average bright periods duration are long, of the order of 1 ms. They also have lower power law exponents than DR3.3. Their switching dynamics is therefore slower explaining why we can correctly resolve the histograms with two Poisson distributions. Conversely DR3.3 is characterized by a faster switching dynamics between the states with an average bright period duration of 0.46 ms and a larger power law exponent. This fast dynamics is poorly resolved with the bin time $\Delta t = 150$ μs as visible on the histogram in Fig.III.17b.

[9]The fit gives the same parameter values for τ up to 1 ms.

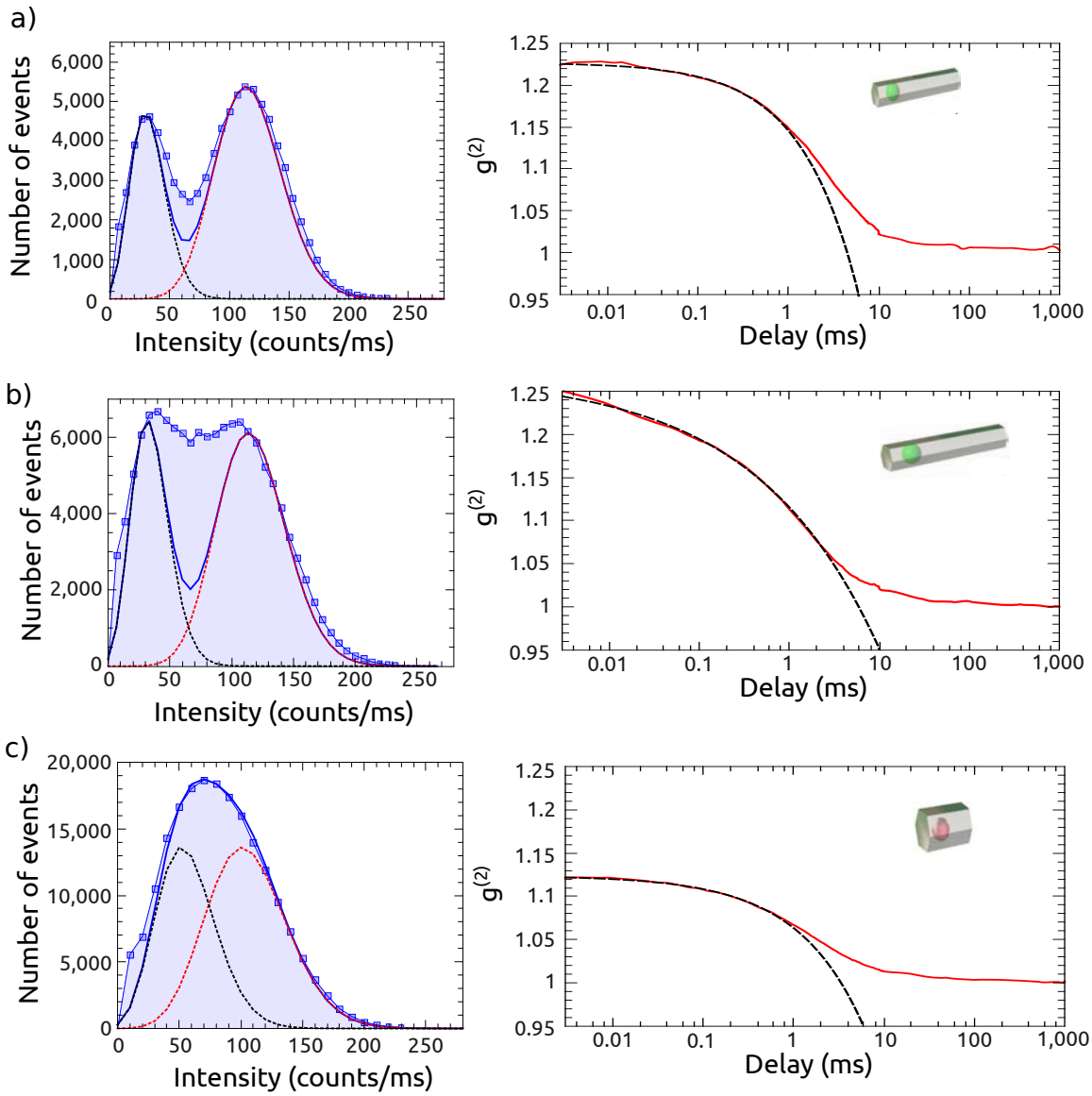

Figure III.17: Histograms and $g^{(2)}$ function for DR3.2, DR3.3 and DR4 excited at $\langle \mathbf{N_{eh}} \rangle = \mathbf{0.5}$. *Red curve: $g^{(2)}$ function, black dashed curve: fit with eq.III.6 for $\tau < 500$ μs. a) DR3.2, bin time $\Delta t = 150$ μs, fit parameters: $A = 0.064$ and $\mu = 0.32$. b) DR3.3, bin time $\Delta t = 150$ μs, fit parameters: $A = 0.12$ and $\mu = 0.68$. c) DR4, bin time $\Delta t = 100$ μs, fit parameters: $A = 0.055$ and $\mu = 0.4$.*

It is to be noted that the cumulative distribution of ON events for DR3.2 presented in Fig.III.15b yields $\langle \tau_b \rangle = 1.7$ ms. The value is slightly larger than the one found with the $g^{(2)}$ function: $\langle \tau_b \rangle = 1.36$ ms. The fact that it is larger for the cumulative distribution seems logical as the cumulative distribution does not take into account the fast events (faster than the bin time of $\Delta t = 150$ μs). We do not compute the cumulative distributions for DR3.3 and DR4 as we expect them to be irrelevant. For DR4 because the two states of emission strongly overlap (see the histogram on Fig.III.17c), for DR3.3 because the blinking is too fast (see the histogram on Fig.III.17b that is poorly fitted).

Conclusion

In this chapter we studied the photoluminescence blinking of our dot-in-rods. We demonstrated that the blinking, even at high excitation power, is characterized by two states of emission that we attribute to the exciton and negatively charged exciton, as attested by the photoluminescence decay of each state of emission.

We have shown that the blinking statistics is power law distributed with the same exponents as for bare CdSe or CdSe/ZnS nanocrystals. Nevertheless, the blinking statistics does not extend to long times but is truncated in the millisecond regime. Owing to this fast blinking dynamics, we can conclude that a bin time of the order of hundreds microseconds has to be chosen for studying such photoluminescence timetraces.

Finally, we have shown that the power law distribution of events gives an important statistical weight to fast blinking events. This implies that the histogram of emission intensity is often poorly fitted by a sum of two Poisson distributions. By studying various samples of dot-in-rods we highlighted that the fast blinking dynamics is strongly dependent on the geometrical parameters.

Chapter IV
CdSe/CdS dot-in-rods photon statistics

Introduction

In this chapter we want to characterize the photon statistics of our dot-in-rods nanocrystals. For a given excitation, we want to know how many photons on average a nanocrystal will emit. As already addressed in chapter II section II.2.3, we need to quantify the probability to emit one photon, two photons, ..., m photons for a given excitation. To do so, a measure of the quantum yields of the various states involved in the emission process is necessary. The task is more complex than foreseen in chapter II because we need to take into account the emission intermittency inherent to such nanometer scale emitters as presented in the previous chapter.

We first present a theoretical part on the photon statistics and the second order autocorrelation function that we use for the analysis of the photon statistics. Once this is settled, we derive the first element of the photon statistics: the single photon emission probability. We consider the blinking effects on the probability to emit a single photon and compare the various dot-in-rods samples. Finally, we present the second part of our analysis on the photon statistics, we derive the higher order photon emission probabilities in presence of blinking. A last section is devoted to an outlook on a different method we used to determine the photon statistics. Beyond the photon statistics, this chapter shows the existence of two different non-radiative relaxation channels in dot-in-rods, namely the Auger relaxations for which the energy is given to holes or electrons.

IV.1 Photon statistics theory

In this part of the chapter we present the theoretical background on the photon statistics. First a very general overview on the notion of light sources photon statistics and how it

can be measured is given. Then we focus on nanocrystals photon statistics and show how it can be modeled and what can be precisely determined with our measurements.

IV.1.1 A general approach to the photon statistics

Let us first explain more precisely what do we mean with the photon statistics of a light source. First, we are interested in the particle nature of the light emitted by the source under study. This description is chosen because it is the best suited for our light source. When relaxing radiatively from an excited state a nanocrystal emits a photon, such that a description in terms of photon is intrinsically linked to the emission mechanisms and thus very convenient. Secondly, we want to count the emitted photons and make a statistics of the probabilities that the source emits a single photon, two photons, three photons, ... and higher order number states. If we characterize the probabilities of emission of every number state then we get physical insights into the behavior of how our light source.

Single photons are now widely studied and used in laboratories. We can cite the first experimental demonstration by Kimble, Dagenais and Mandel that showed that the fluorescence light emitted by an isolated atom displayed intensity anti-correlation that could not be explained by a wave model of the electromagnetic field [179]. This is indeed the same approach that we are going to use in the following to characterize the photon statistics of our dot-in-rods: measuring the intensity correlations using a Hanbury-Brown and Twiss setup.

Photon statistics measurements: $g^{(2)}$ function

Most single photon detectors produce an electronic signal upon absorption of one or more photons, without discriminating between the number of photons. This is the case of the avalanche photodiodes that we use to detect single photon events. Under this experimental configuration, the normalized intensity correlation of the emitted light field is a powerful tool to characterize the photon statistics. The following derivation of the normalized correlation function can be found in great details in the literature [180], for this reason only the main lines are given here.

Normalized correlation function for a classical field As already briefly presented in chapter III, the temporal intensity correlation $g^{(2)}$ of the light field E is defined as follows:

$$g^{(2)}(t_0, t_0+\tau) = \frac{\langle E^*(t_0)E^*(t_0+\tau)E(t_0+\tau)E(t_0)\rangle}{\langle |E(t_0)|^2\rangle\langle |E(t_0+\tau)|^2\rangle} = \frac{\langle I(t_0)I(t_0+\tau)\rangle}{\langle I(t_0)\rangle\langle I(t_0+\tau)\rangle}, \qquad \text{(IV.1)}$$

with $I(t_i) = E^*(t_i)E(t_i)$ the intensity of the light field at time t_i, $\langle\rangle$ denotes a statistical (ensemble) average. For stationary light fields, the average intensity is constant in time, $\langle I(t_0)\rangle = \langle I(t_0+\tau)\rangle$, and $g^{(2)}(t, t+\tau) = g^{(2)}(\tau) = \langle I(t)I(t+\tau)\rangle / \langle I(t)\rangle^2$. The Cauchy-Schwartz inequality imposes that $\langle I(t_0)I(t_0+\tau)\rangle^2 \leqslant \langle I(t_0)^2\rangle\langle I(t_0+\tau)^2\rangle$. For a stationary field, this simplifies into $\langle I(t_0)I(t_0+\tau)\rangle \leqslant \langle I(t_0)^2\rangle$:

$$g^{(2)}(\tau) \leqslant g^{(2)}(0). \tag{IV.2}$$

Moreover, the variance $\sigma^2 = \langle (I(t_0) - \langle I(t_0)\rangle)^2\rangle \geqslant 0$ by definition, such that $\langle I(t_0)^2\rangle \geqslant \langle I(t_0)\rangle^2$ and:

$$g^{(2)}(0) \geqslant 1. \tag{IV.3}$$

We comment the previous equations in the next paragraph after having defined the situation for a quantum field and compare both cases.

Normalized correlation function for a quantum field The quantized electromagnetic field [180] is represented by the electric field operator $E = E^{(+)} + E^{(-)}$ with $E^{(-)}$ the hermitian conjugated of $E^{(+)}$. The difference with the classical case is that the conjugate fields do not commute. For a quantized field, the intensity $I(t)$ is a flux of photons. Eq.IV.1 is written in the quantum case as:

$$g^{(2)}(t_0, t_0+\tau) = \frac{\langle E^{(-)}(t_0)E^{(-)}(t_0+\tau)E^{(+)}(t_0+\tau)E^{(+)}(t_0)\rangle}{\langle E^{(-)}(t_0)E^{(+)}(t_0)\rangle\langle E^{(-)}(t_0+\tau)E^{(+)}(t_0+\tau)\rangle}, \tag{IV.4}$$

with $\langle\rangle$ being the expectation value of an operator for a given quantum state. A photon detection corresponds to the annihilation of a photon by the operator $E^{(+)}$. The probability $P(t_0, t_0+\tau)$ to detect photons at a time t_0 and later on at $t_0+\tau$ for a state $|\Psi\rangle$ is then:

$$\begin{aligned} P(t_0, t_0+\tau) &= \eta^2 |E^{(+)}(t_0+\tau)E^{(+)}(t_0)|\Psi\rangle|^2, \\ &= \eta^2 \langle\Psi|E^{(-)}(t_0)E^{(-)}(t_0+\tau)E^{(+)}(t_0+\tau)E^{(+)}(t_0)|\Psi\rangle, \end{aligned} \tag{IV.5}$$

with η the detection efficiency. For a stationary field it appears that:

$$g^{(2)}(\tau) = \frac{P(t_0, t_0+\tau)}{P(t_0)^2} = \frac{P(t_0+\tau|t_0)}{P(t_0)}, \tag{IV.6}$$

with $P(t_0)$ the probability to detect photons at time t_0. We simplified the equation by introducing the conditional probability $P(t_0+\tau|t_0) = P(t_0+\tau, t_0)P(t_0)$ to detect photons at $t_0+\tau$ knowing at least one photon was detected at t_0. We can notice that *the* $g^{(2)}$

function is independent of the detection efficiency [181]. We can already see that the $g^{(2)}$ is not minimally bounded to one with this definition as the conditional probability $P(t_0+\tau|t_0)$ can freely change with τ. The previous derivation is for a continuous excitation of the emitter, a pulsed excitation scheme gives a similar result except that the time is discretized at the laser pulses[1].

The previous description of the $g^{(2)}$ function is very convenient because in strong connection with the experiment for which one typically looks at coincidences between two single photon detectors of a HBT setup. Going on a more quantum description, for a single mode of the field, the usual bosonic creation and annihilation operators of the quantized electromagnetic field can be defined: a and $a^\dagger$, together with the number state operator $n = a^\dagger a$, its eigenstates corresponding to the number of photons in the considered mode. Then, for a stationary field, Eq.IV.4 can be rewritten [180]:

$$g^{(2)}(\tau) = \frac{\langle a^\dagger a^\dagger a a\rangle}{\langle a^\dagger a\rangle^2} = \frac{\langle n(n-1)\rangle}{\langle n\rangle^2}, \tag{IV.7}$$

The appearance of the -1 in the formula is due to the non commuting operators and is not present in the classical case. The $g^{(2)}$ function can be further developed into: $g^{(2)}(\tau) = (\langle n^2\rangle - \langle n\rangle)/\langle n\rangle^2 = 1 + ((\Delta n)^2 - \langle n\rangle)/\langle n\rangle^2$ with $(\Delta n)^2$ the photon number variance. As $(\Delta n)^2 = \langle n^2\rangle - \langle n\rangle^2 \geqslant 0$, it follows that the second order correlation function is now minimally bounded as follows:

$$1 - \frac{1}{\langle n\rangle} \leqslant g^{(2)}(\tau) \qquad for\ \ \langle n\rangle \geqslant 1. \tag{IV.8}$$

The correlation function is not anymore bounded to a minimum value of 1. In the specific case of a single photon emitter the $g^{(2)}$ function will be 0 as $\langle n\rangle = 1$.

Let us now give a physical meaning to the light belonging to the different domains of $g^{(2)}$ values:

- *Poisson fluctuations:* $g^{(2)} = 1$. Light fields with a Poisson photon number distribution are such that $\langle n\rangle = (\Delta n)^2$ by definition, implying $g^{(2)} = 1$ in Eq.IV.6. In the classical formula, a Poisson distribution of the field intensity also leads to $g^{(2)} = 1$ for high intensities because if one takes $\langle I\rangle = (\Delta I)^2$ in Eq.IV.1, it leads to $g^{(2)} = 1 + 1/\langle I\rangle$. It marks the limit between classical and quantum fields. Light fields that exhibit such a photon distributions are typically generated by lasers and called coherent states in quantum optics. These states reach the standard quantum limit in terms of phase and photon number fluctuations [180] and thus mark the

[1]To be precise in this case, instead of t_0 one should use the index i for example to refer to a pulse i and $i+j$ for the pulse $i+j$ instead of $t_0+\tau$. In the following we keep on using the t_0 and $t_0+\tau$ even for the pulse excitation case as it is more convenient.

limit between the fluctuations of a classical and a quantum field that can reach lower fluctuations, a so called squeezed state.
In terms of photon flux, the Poisson distribution by definition expresses the probability of a given number of events occurring in a fixed interval of time if these events occur with a known average rate and independently of the time interval since the last event. It basically describes a random arrival of photons for a given rate; there are therefore no correlations between the different photon detection events. In terms of detection probability of consecutive photon events defined in Eq.IV.5 and Eq.IV.6, $P(t_0+\tau|t_0) = P(t_0)$ because of the events independence. Eq.IV.6 can be interpreted as the conditional probability of detection $P(t_0+\tau|t_0)$ for a given source normalized by its value for a Poisson light flux of the same average emission rate.

- *Super-poissonian fluctuations:* $g^{(2)} > 1$. In this case the photon statistics is said to be super-poissonian, the fluctuations of the photon number are larger than in the Poisson case, there is an excess of noise. In terms of photon flux, it means that $P(t_0+\tau|t_0)$ is higher that for a Poisson source of the same rate, then there are extra correlations in time. Photons arising from such a source are therefore said to be bunched, they arrive in bunch on the detector because the probability to detect one photon after another is higher than in the Poisson random case. A black body radiation is typically super-poissonian.

- *Sub-Poisson fluctuations:* $g^{(2)} < 1$. Conversely to the super-poissonian statistics, the fluctuations in the photon number are smaller than in the Poisson case, there is less uncertainty on the number of photons arriving on the detector than for the Poisson distribution. The photon flux is therefore very well defined, $P(t_0+\tau|t_0)$ is smaller that for a Poisson source, there are strong anti-correlations in time. For some specific values of τ after the detection of a photon, the probability to detect a photon is lower than in the Poisson case. The photons are said to be antibunched. This is the case of our dot-in-rods.

Fig.IV.1 proposes a summary of the discussion. We present the photon flux and $g^{(2)}$ function of three sources belonging to the photon statistics presented above, a black-body radiation, a coherent state with a Poisson distribution and a perfect single photon source from a CdSe dot for example. We will not derive the formula for the $g^{(2)}$ functions, that can be found in many textbooks [180]. For the super-poissonian source (Gaussian thermal source) the photon are bunched and this gives extra correlations at delays of the order of the source lifetime, while it is the contrary for the sub-poissonian light. After some delay, the $g^{(2)}$ eventually goes towards 1 and a Poisson statistics is retrieved because the field

loses its memory of previous times and can thus have no correlation with its past self. Therefore, for acquiring knowledge about the photon statistics, only the $g^{(2)}$ function at short delays (of the order of the lifetime of the photon source) is useful.

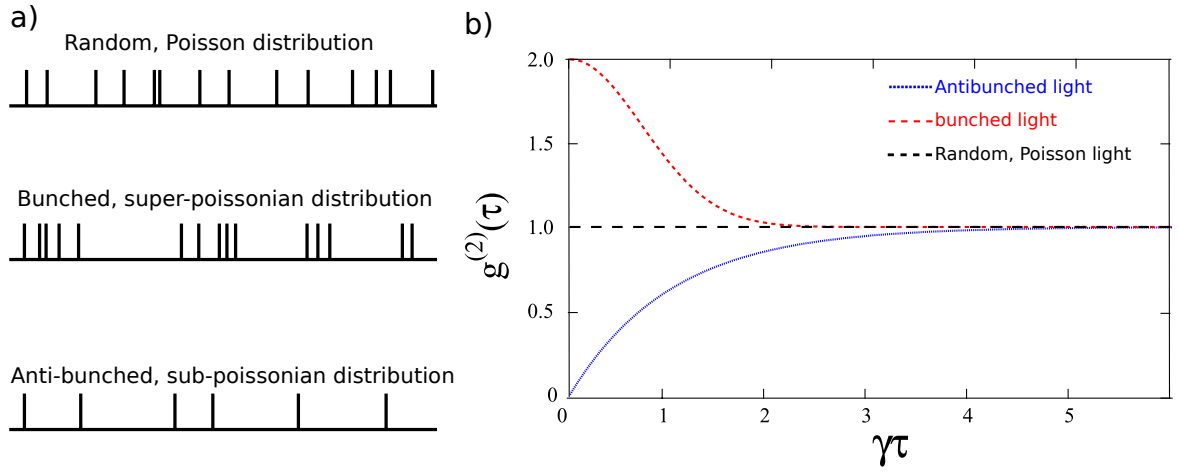

Figure IV.1: Schematics of the photon arrival time and autocorrelation function for super-poissonian, poissonian and sub-poissonian light sources. *a) Schematics of the photon arrival on a detector for the different types of sources. b) $g^{(2)}$ of the sources as a function of a normalized delay $\gamma\tau$, τ being the time delay and γ the decay rate of the sources, the inverse of the lifetime.*

IV.1.2 Photon statistics and nanocrystals

A model for the $g^{(2)}$ function

Let us now apply the knowledge we gathered in the previous section to the case of nanocrystals. We have already seen in chapter I section I.2.3 that nanocrystals are not simple two level systems, various emission states exist. Apart from the exciton, there is the possibility of multiexcitons emission and emission from charged states. As we have seen, what is interesting in the $g^{(2)}$ function in order to gather knowledge on the photon statistics are the correlations at short delays. In the following we model the $g^{(2)}$ function of a nanocrystal excited by a laser pulse. The time is discretized by the laser pulses repetition rate Γ. In this case short delays means a delay shorter than the inverse of the repetition rate of the laser, so the delay τ between photons is taken such that $|\tau| < 1/\Gamma$ in the following derivation. Therefore, we look at correlations just after each laser pulse to find the value of $g^{(2)}$ at zero delay.

It has been demonstrated in reference [153] that the autocorrelation function at zero delay can be expressed as a function of the quantum yields of the different multiexcitonic states Q_{mX} and the Poisson excitation probability, assuming the independence of the

different multiexcitonic fluorescence processes. Below, we show a different derivation of such a formula.

First we consider a stationary emission from the nanocrystals, meaning we consider no blinking. We write the different quantum yields as Q_m, to say that we are considering a neutral or charged nanocrystal separately[2]. From Eq.IV.6, we can write that:

$$g^{(2)}(0) = \frac{P(t_0, t_0+\tau)}{P(t_0)^2} = \frac{2P_{2+}}{P_{1+}^2}. \tag{IV.9}$$

$P(t_0, t_0+\tau)$ is twice the probability to detect at least two photons P_{2+}, while the denominator P_{1+}^2 is the probability to detect at least one photon squared. It is now fairly easy to express the $g^{(2)}(0)$ with the quantum yields of the different emission states. These quantities were actually already derived in chapter II section II.2.3, P_{1+} is what we called N_{ph}, the mean number of photons emitted by a DR after a given pulse and P_{2+} is N_{mX} the multiexciton part of N_{ph}. Therefore:

$$g^{(2)}(0) = \frac{2\sum_{m>1} P_{Neh\geqslant m} \sum_{m'<m} Q_m Q_{m'}}{(\sum_{m\geqslant 1} P_{Neh\geqslant m} Q_m)^2}. \tag{IV.10}$$

We can see that we can not separate the quantum yields in the previous formula. However, considering an emitter displaying antibunching, therefore having low multiexciton quantum yields, the previous equation simplifies to:

$$g^{(2)}(0) = \frac{2\sum_{m>1} P_{Neh\geqslant m} Q_m Q_1}{(P_{Neh\geqslant 1} Q_1)^2}, \tag{IV.11}$$

where we assume that $P_{1+} \simeq P_1$ and that if two photons are emitted one comes from the exciton. We can see now that the knowledge of the exciton quantum yields implies that with a $g^{(2)}(0)$ measurement we can quantify the multiexciton processes. If a low excitation power is used, which will be the case in the following of this chapter, the formula can be further simplified as the probability to excite multiexcitons is low. Let us take an excitation such that $P_{Neh\geqslant 3} \ll P_{Neh\geqslant 1}$:

$$g^{(2)}(0) = \frac{2P_{Neh\geqslant 2}}{P_{Neh\geqslant 1}^2}\frac{Q_2 Q_1}{Q_1^2} = \frac{2P_{Neh\geqslant 2}}{P_{Neh\geqslant 1}^2}\frac{Q_2}{Q_1}, \tag{IV.12}$$

which means that for low pumping $g^{(2)}(0) = 2P_2/P_1^2$, with P_2 and P_1 the probabilities to emit exactly 2 and 1 photon. In extremely weak pumping regime such that the number of electron hole pairs inside the nanocrystals tends to zero, $\langle N_{eh}\rangle \to 0$, Eq.(IV.12) simplifies

[2] $Q_m = Q_{mX}$ or Q_{mX^-} depending if the nanocrystal is charged or not.

to:

$$g^{(2)}(0, \langle N_{eh} \rangle \to 0) = \frac{Q_2}{Q_1}, \tag{IV.13}$$

as $\lim_{\langle N_{eh} \rangle \to 0} (2P_{Neh \geqslant 2})/(P^2_{Neh \geqslant 1}) = 1$. This formula has been used in [61, 153, 182] to derive the biexciton quantum yield from a $g^{(2)}(0)$ measurement. This implies that an emitter having a non zero biexciton quantum yield Q_2 will not show complete antibunching even at extremely low pumping regime due to the Poisson character of the excitation.

Measurement of coincidence histograms and normalization

With the HBT setup, we measure a histogram of photon coincidences between the two detectors, $h(\tau)$, an example is shown on Fig.IV.2. The central peak corresponds to coincidences originating from the same excitation pulse, thus to the emission of multiple photons by the nanocrystal. On the other hand, the coincidences registered at delays equal or multiple of the laser temporal pulse spacing correspond to photons generated by different pulses. Fig.IV.2 is a raw autocorrelation function (ACF) of the signal.

This quantity is proportional to the conditional probability $P(t_0+\tau|t_0)$ defined earlier in Eq.IV.6. To get $P(t_0+\tau|t_0)$, one needs to renormalize by the total number of realization of the coincidence experiment, this corresponds to the number of events on one of the channels, let us say channel 1. Then, APD1 in Fig.IV.2 is taken as the reference (often called Start channel) for the coincidences. We call N_1 the number of photons detected on channel 1. As $h(\tau)$ is a histogram (a number of coincidence per histogram bin), we can not just divide by N_1 but we need to take into account the bin width of the histogram Δ_τ. Last, the losses induced by the beam splitter in the HBT setup affect the histogram $h(\tau)$. If T is the transmission of the beam-splitter for channel 1, then the losses are $1-T$. $P(t_0 + \tau|t_0)$ is then:

$$P(t_0 + \tau|t_0) = \frac{1}{1-T}\frac{h(\tau)}{\Delta_\tau N_1}. \tag{IV.14}$$

Then the $g^{(2)}$ function is calculated after normalizing $P(t_0 + \tau|t_0)$ by $P(t_0)$ according to Eq.IV.6. $P(t_0)$, the probability to detect at least one photon, is the number of detected events $N = N_1/T$ over the number of laser pulses[3] N_l, and:

$$g^{(2)}(\tau) = \frac{T}{1-T}\frac{N_l h(\tau)}{\Delta_\tau N_1^2}. \tag{IV.15}$$

We did not mention in the formula above that in this case, considering a pulse excitation, the probability $P(t_0+\tau|t_0)$ and the $g^{(2)}$ function are defined relatively to each excitation

[3]Or the total acquisition time for a continuous wave excitation.

pulse such that one should integrate the coincidence events over each correlation peak.

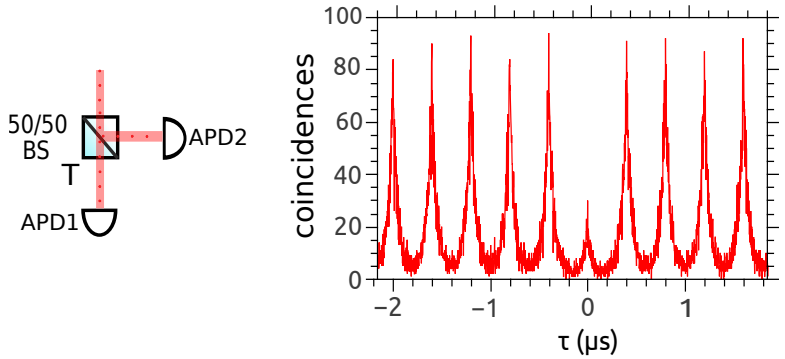

Figure IV.2: Example of a coincidence histogram measured with the HBT setup. *The coincidences are counted with the HBT setup, one APD (let us say APD1) is chosen as a reference and the counts with the photons from the other channel are listed and gathered in a histogram $h(\tau)$ (right) realized with a certain bin time Δ_τ.*

Outlook

We can see that our analysis suffers from some limitations. We can only derive a ratio between the multi photon emission and the single photon emission in the case of our nanocrystals (cf Eq.IV.11). Furthermore it is not possible to separate the different multi photon processes. By going to low excitation power we can restrain the multi photon emission to the two photon emission (cf Eq.IV.12), so we can eventually characterize the two photon and single photon emission with this analysis.

This is what is done in the following. We first look at the single photon emission, we quantify the exciton and trion emission efficiencies. Once a comprehensive understanding of the single photon emission is settled, the two photon emission from the biexciton and charged biexciton is derived using measurements of the $g^{(2)}$ function at low excitation power.

IV.2 Single photon emission: exciton and negative trion

In this first part, we study the emission characteristics of the exciton and trion state. We explain the role played by the electron delocalization in determining the trion state quantum yield.

IV.2.1 Saturation and exciton quantum yield

It was shown for CdSe/ZnS nanocrystals that the exciton quantum yield is equal to one for high quality synthesis [94, 96]. This means that if an exciton relaxes to the band-edge, no mechanism competes with a radiative recombination and a photon is emitted. Throughout this thesis we will assume the validity of this result for our dot-in-rods. Nevertheless, we propose a simple experiment to test it. We calculated in the chapter II the maximum rate expected for a perfect single photon emitter (no multiphoton emission and $Q_X = 1$) knowing the losses of the system. On Fig.IV.3b we present the results of saturation measurements on 20 single dot-in-rods from sample DR3.1. We chose this sample because it is very resistant to the photobleaching, it can be excited at high power and it presents a relatively low multiphoton emission[4].

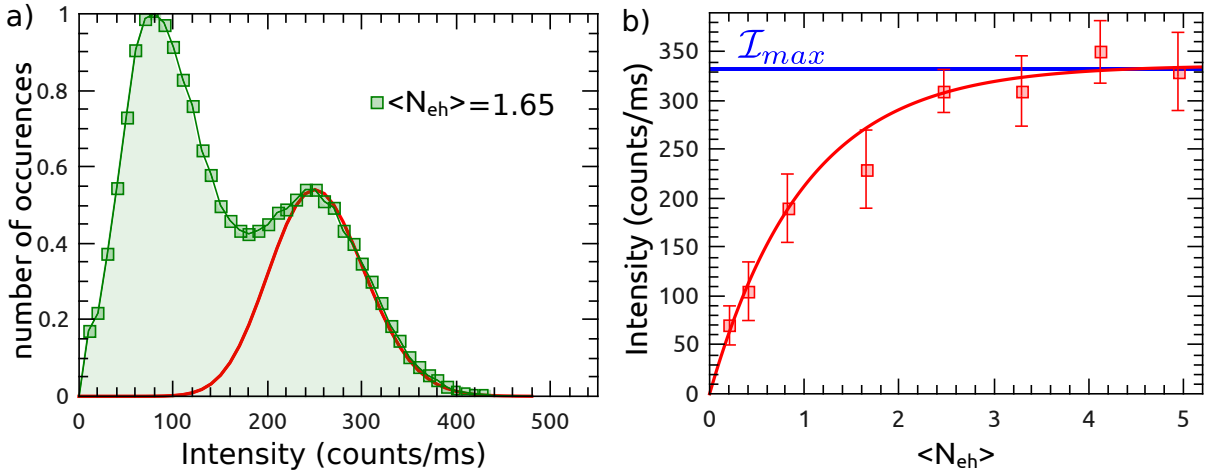

Figure IV.3: Saturation curve for DR3.1. *a) Example of emission intensity histogram for one dot-in-rod of the sample at an excitation power* $\langle N_{eh} \rangle = 1.65$*. A Poisson distribution fit of the upper part of the emission distribution yields the exciton emission intensity. b) The experimental points are the results of measurements over* 20 *single dot-in-rods. The fit is based on Eq.II.10, the biexciton quantum yield of the sample is* $Q_{2X} = 0.1$*.* $\mathcal{I}_{max} = 332$ *counts/ms is the maximum emission intensity expected for a perfect single photon emitter (no multiphoton emission and* $Q_X = 1$*) knowing the losses of the system, see Tab.II.1.*

[4]For this sample, $Q_{2X} = 0.1$ as evaluated on many emitters by measurements of $g^{(2)}(0)$.

For each registered dot-in-rod emission, an intensity histogram is computed as in Fig.IV.3a at different excitation powers. A Poisson distribution fit (red line on Fig.IV.3a) of the upper part of the distribution yields the exciton emission rate at the given excitation. This is realized on 20 dot-in rods for different excitations and yields the saturation curve of Fig.IV.3b. We can see that a good agreement of the saturation curve with the maximum value expected for a perfect single photon emitter ($\mathcal{I}_{max}$ = 332 counts/ms) is achieved. This confirms that the exciton quantum yield is close to one for our heterostructure.

IV.2.2 Trion quantum yield and electron delocalization

Let us now look at the trion emission rate for our various dot-in-rod samples. We work with a low excitation, typically $\langle N_{eh} \rangle \leqslant 0.5$, to ensure a small probability to excite three or more electron-hole pairs. Exciting at $\langle N_{eh} \rangle = 0.5$ yields: $P_{N_{eh}\geqslant 2}/P_{N_{eh}\geqslant 1} \simeq 20\%$ and $P_{N_{eh}\geqslant 3}/P_{N_{eh}\geqslant 1} \simeq 3.4\%$. At this power the trion emission is clearly visible meaning that photoionization events can occur when two electron-hole pairs are present inside the structure.

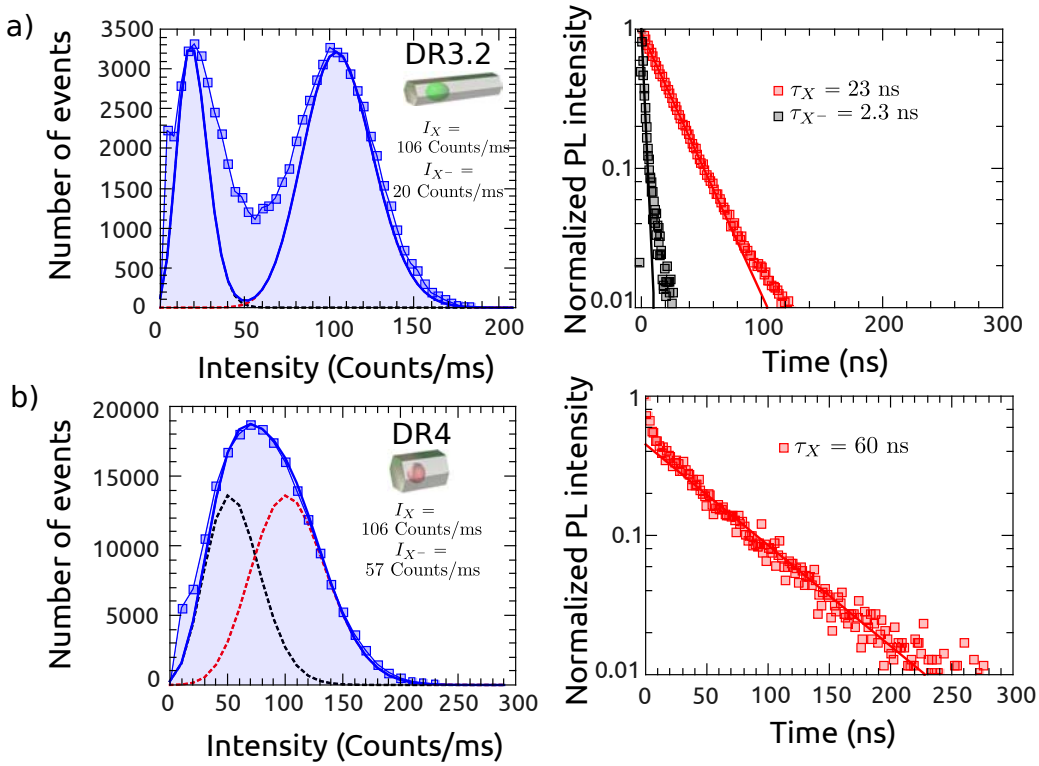

Figure IV.4: Histograms of emission and decay curves for representative dot-in-rods of sample DR3 and DR4. *a)DR3.2 emission histogram and photoluminescence decay for the trion (black) and exciton (red) states: $\tau_X = 23$ ns and $\tau_{X^-} = 2.3$ ns. b) DR4 emission histogram and photoluminescence decay for the exciton (red) states: $\tau_X = 60$ ns.*

We observe on Fig.IV.4 that the sample DR4, that on average displays an exciton lifetime larger than the other samples, has a larger trion quantum yield. This is illustrated on Fig.IV.4a and b which shows typical emission histograms from sample DR3.2 and DR4. The dot-in-rod from the sample DR3.2 has an exciton lifetime of $\tau_X = 23$ ns and a trion quantum yield of $Q_{X^-} = I_{X^-}/I_X = 20/106 = 19\%$ while the dot-in-rod from sample DR4 has an exciton lifetime of $\tau_X = 60$ ns and a trion quantum yield of $Q_{X^-} = I_{X^-}/I_X = 57/106 = 54\%$. We do not show on IV.4b the decay curve for the trion state of the dot-in-rod from the sample DR4 as it is not possible to discriminate between the two states. Taking only the lower part of the histogram yields decay curve spoiled by the noise. However the exciton decay curve can always easily be computed by taking the high emission intensity part of the histogram. The fast dynamics that is present in the first nanosecond of the photoluminescence decay of DR4 is attributed to multiexcitons as this sample has an efficient multiexciton emission as we will see in the following. The fact that on average DR4 presents a large exciton lifetime and consequently a highly delocalized electron can be rationalized by the fact that it is the sample with the thickest shell.

In the framework of the two states model, we can explain the trion quantum yield value by the electron delocalization: a high trion quantum yield value is explained by a large electron delocalization. CdSe/CdS dot-in-rods are quasi-type II heterostructures, the hole is confined inside the core while the electron spreads inside the shell. A large electron delocalization leads to a lower Auger efficiency transfer to the extra electron as Auger efficiency scales with the confinement. Therefore a lower nonradiative relaxation probability for the trion state is associated with highly delocalized electrons.

IV.3 Two photon emission: biexciton and charged biexciton

We now focus our analysis of the photon statistics on the biexciton and charged biexciton emission. First we show that nonradiative relaxations of multiexciton are driven by Auger energy transfers towards the hole. We then arrive at the heart of this chapter, we explain why dot-in-rods displaying the same photon statistics at low excitation power often display very different statistics at higher excitation power. The answer to this question is that one should take into account the effects of blinking on the overall photon statistics.

IV.3.1 Dot-in-rod geometry and biexciton quantum yield

We study the emission at very low excitation ($\langle N_{eh} \rangle < 0.2$) to reduce the probability of photoionization and blinking. We present on Fig.IV.5 the emission properties for samples DR1, DR2, DR3 and DR4. We obtain for all the samples a well defined single photoluminescence decay (left) and single Poisson distribution (middle). The emission is therefore attributed to the exciton state. The photoluminescence decay of DR4 presents a fast component that is attributed to the multiexciton emission as the $g^{(2)}(0)$ value is large in this case. The $g^{(2)}(0)$ value is directly a measure of the biexciton quantum yield as can be seen from Eq.IV.13 with the exciton quantum yield being equal to unity.

The measurements presented Fig.IV.5 are representative of the different samples. The geometrical parameter that explains the differences of biexciton quantum yields is the core diameter. DR1 has the smaller core diameter ($d = 2$ nm), DR2 and DR3 have the same core diameters ($d = 3.3$ nm) and DR4 has the largest core diameter ($d = 4.6$ nm). A larger core implies a smaller confinement of the hole and consequently less efficient Auger energy transfers towards this carrier. The delocalization of electrons inside the shell for CdSe/CdS dot-in-rods implies that holes constitute the most efficient channel of Auger nonradiative relaxation for multiexcitons. By changing the size of the core we can therefore tune the multiexcitons quantum yields.

IV.3.2 Blinking and charged biexciton emission

The previous section presented the major role played by the sample geometry in the photon emission processes and consequently on the photon statistics. Each sample has its own typical average photon statistics that can be explained by the geometry. Measurements at higher excitation power brings much more dispersion on $g^{(2)}(0)$ values for

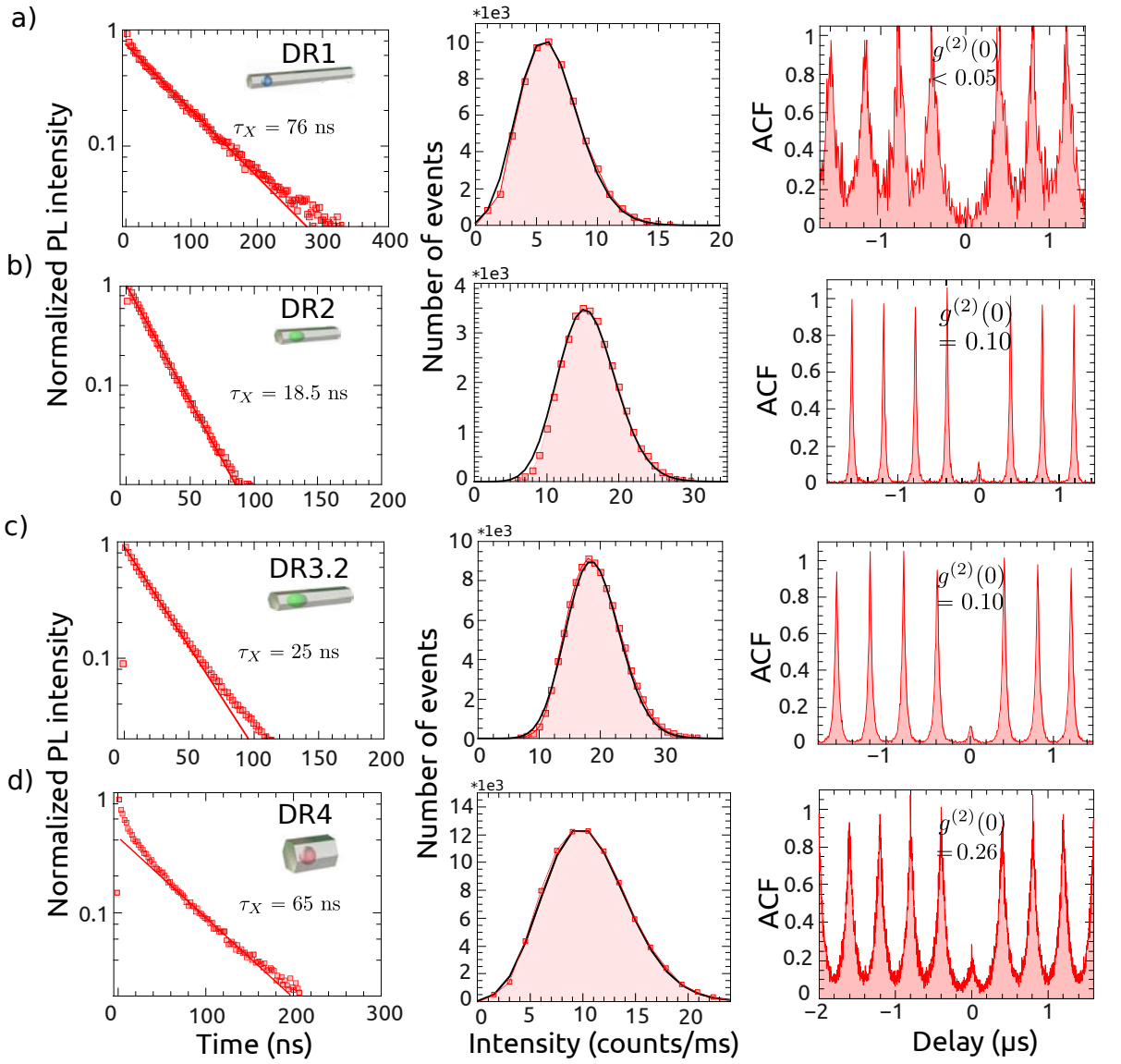

Figure IV.5: Photon statistics at low excitation power for DR1, DR2, DR3 and DR4. *Photoluminescence decay (left), histogram of emission (middle) and coincidence (right) for a) DR1, b) DR2, c) DR3.2 and d) DR4. Monoexponential fits of the photoluminescence decay yields the exciton lifetime τ_X. The histogram of emission are well fitted by single Poisson distributions (black line). The excitation power is maximum for DR3.2 $\langle N_{eh}\rangle = 0.12$, $\langle N_{eh}\rangle = 0.05$ for DR1, $\langle N_{eh}\rangle = 0.11$ for DR2 and $\langle N_{eh}\rangle = 0.05$ for DR4.*

a given sample. Besides the sample geometry, an extra parameter that we have to take into account at higher excitation is the blinking.

A first observation when exciting at higher energies is that dot-in-rods displaying shorter photoluminescence decay have higher $g^{(2)}(0)$ values. This is highlighted on Fig.IV.6, the autocorrelation of two specific dot-in-rods of sample DR3.2, namely DRa and DRb, are presented. It appears that at very low excitation power ($\langle N_{eh}\rangle = 0.05$), the two dots have similar $g^{(2)}(0)$ values in Fig.IV.6a and b: $g^{(2)}(0) = 0.11$ and $g^{(2)}(0) = 0.12$.

We can notice that DRa has a slower luminescence decay as its autocorrelation peaks span a larger area than DRb. At an excitation of $\langle N_{eh} \rangle = 0.4$, the photon statistics of DRb has considerably changed in Fig.IV.6d, its $g^{(2)}(0)$ value has doubled while for DRa it has only slightly increased (Fig.IV.6c). An increase of $g^{(2)}(0)$ value with the excitation power is normal as the Poisson probability to excite 2 excitons increases and with it the occurrence of 2 photon events. However both DRs should show the same evolution with the excitation power if the Poisson probability to excite 2 excitons was the only parameter at stake. When increasing the excitation power we also trigger the possibility to create trion state and therefore blinking. This needs to be taken into account to fully understand the photon statistics at high excitation power.

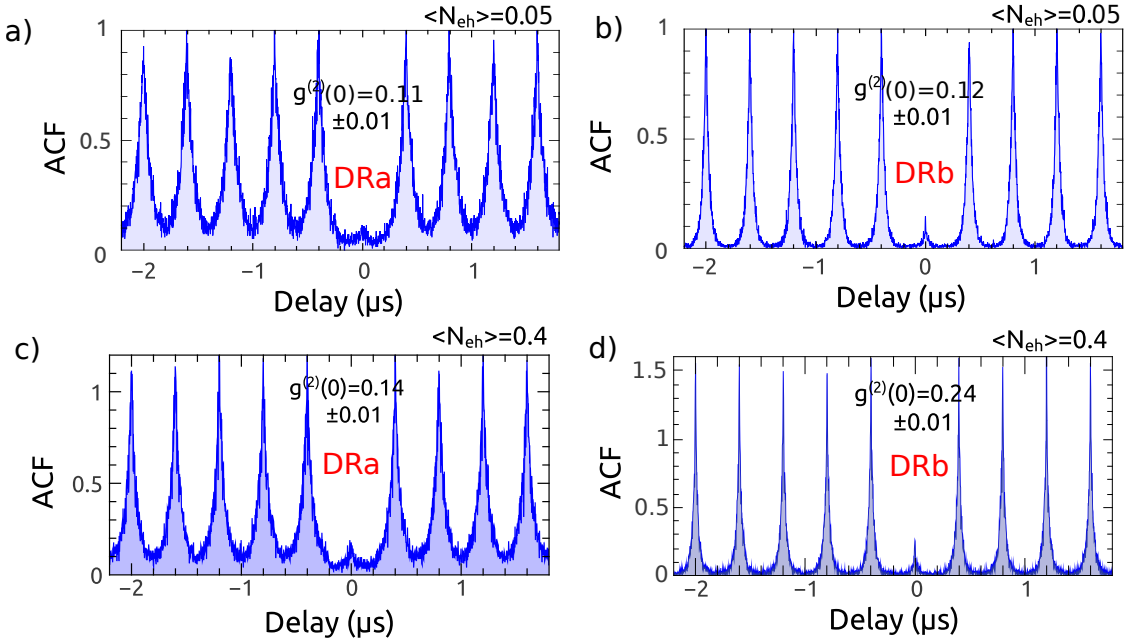

Figure IV.6: Autocorrelation of DRa and DRb, 2 dot-in rods of sample DR3.2. *a) Autocorrelation of DRa for an excitation of $\langle N_{eh} \rangle = 0.05$. b) Autocorrelation of DRb for an excitation of $\langle N_{eh} \rangle = 0.05$. c) Autocorrelation of DRa for an excitation of $\langle N_{eh} \rangle = 0.4$. d) Autocorrelation of DRb for an excitation of $\langle N_{eh} \rangle = 0.4$.*

In the following we will concentrate on the two dot-in-rods of sample DR3.2 presented on Fig.IV.6 to show the effects of a binary blinking on the photon statistics. Beyond the problematic of single photon emission, this study brings some new insights on the emission processes and confirms the effects of the electron delocalization on blinking.

DRa and DRb binary blinking

We consider an excitation power of $\langle N_{eh} \rangle \sim 0.4$. This excitation power has been chosen such that the grey state generated by photoionization could be clearly observed. This is typically realized when the probability to excite at least two electron-hole pairs is

high enough, here $P_{N_{eh}\geqslant 2}/P_{N_{eh}\geqslant 1} \simeq 17\%$. Also, the probability to create more than 2 electron-hole pairs at this excitation power is low: $P_{N_{eh}\geqslant 3}/P_{N_{eh}\geqslant 1} \simeq 2\%$, implying that we can neglect multiexciton emission coming from more than two electron-hole pairs. In this case, ionization events through Auger processes are frequent enough to observe the grey state in the photoluminescence intensity distribution, which is not the case at lower excitation. Under this condition, the dot-in-rods emission is well described by a fast switching (flickering) between two states of emission: a bright state with a high emission efficiency and a grey state with a low emission efficiency [135,165] corresponding respectively to the exciton and the negative trion emission as described in the previous chapter. Fig.IV.7a presents the DRa photoluminescence intensity recorded during 15 seconds with a bin time of 250 μs. A zoom on a 100 ms time window is also shown. The switching between the two states is clear on the shorter time window of 100 ms.

In Fig.IV.7b and c top, DRa and DRb photoluminescence intensity histograms confirm the presence of two states. A fit of these histograms with two Poisson distributions reproduce the intensity distributions properly, except in the intermediate regions. We consider the exciton quantum yield to be unity in the following [71, 96]. The intensity ratio between the two Poisson distributions mean values gives the trion quantum yield. The poissonian mean values I_X and I_{X^-} are given on Fig.IV.7b and c top, they are the mean emission rate for the exciton and trion state respectively. It appears that DRb is characterized by a lower grey state quantum yield (15%) compared to DRa (35%). This is precisely what is interesting in this comparison as we are aiming at quantifying the effect of the trion emission on the overall photon statistics.

Fig.IV.7b and c bottom show the normalized second order autocorrelation functions for long timescales. Concerning DRa, a super-Poissonian statistics with a bunching value of 1.2 is observed on timescales ranging from 1 μs to 10 ms due to the flickering between the two states. For DRb, the $g^{(2)}$ is characterized by a bunching on the same timescales as DRa, from microseconds delays to tens of milliseconds. The bunching value of 1.6 is higher than DRa owing to a higher quantum yield discrepancy between the two states together with an increased grey state photon proportion compared to DRa as it can be seen from the two intensity histograms. We quantify the photon proportions in the next paragraph.

For DRa, in Fig.IV.7a and b, the red part of the graphs above 70 counts/ms is associated to the bright state while the green part below 40 counts/ms can be attributed to the grey state. The photons associated with the intensities between 40 counts/ms and 70 counts/ms inside the central region of the intensity histogram in Fig.IV.7b cannot be attributed to a specific state and have therefore been discarded. They represent 17% of the photon events recorded for this specific measurement, while the grey and

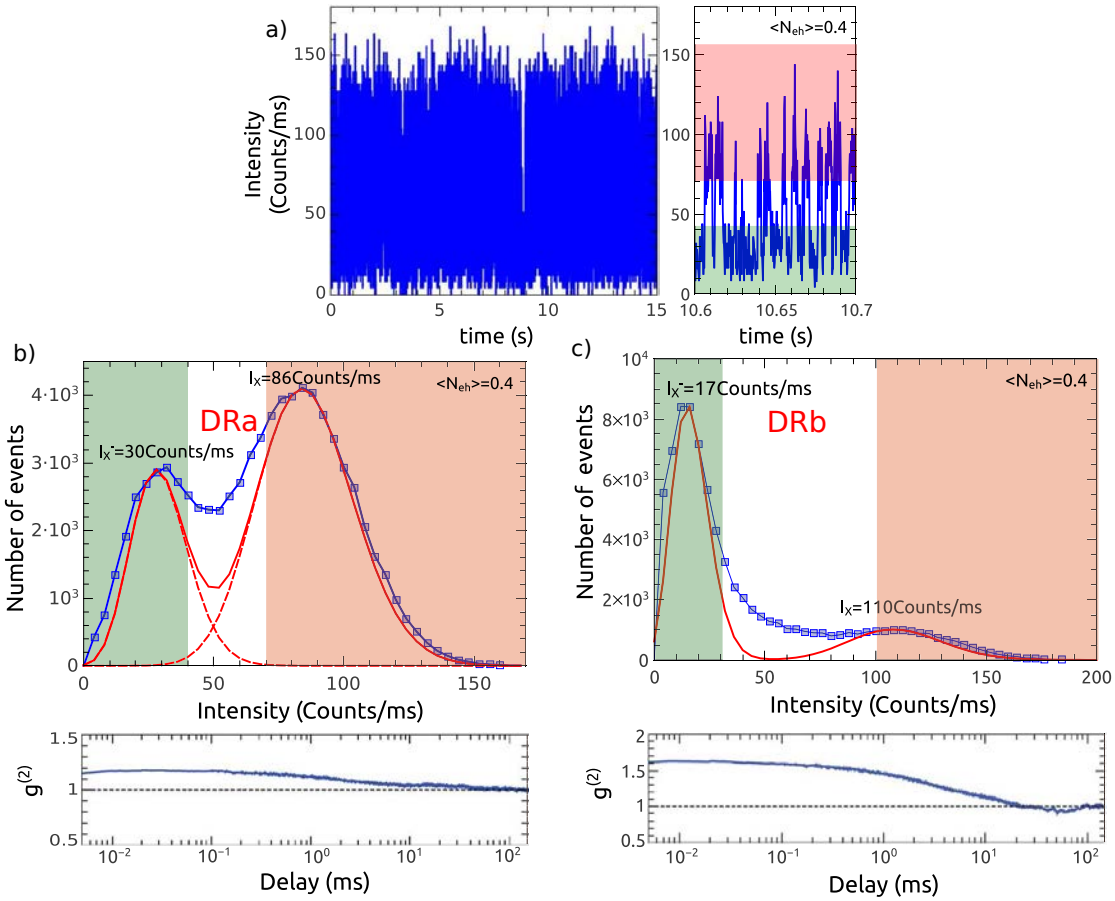

Figure IV.7: Blinking characteristics of DRa and DRb. *a) Photoluminescence intensity of DRa on second (left) and millisecond (right) timescales for an average number of excitons in the nanocrystal of* $\langle Neh \rangle = 0.4$ *and a bin time of* 250 μs. *b) Top: Histogram of DRa photoluminescence intensity together with a fit with two Poisson distributions. The bright state in red has a mean emission intensity* $I_X = 86$ *counts/ms, the grey state in green has a mean emission intensity* $I_{X^-} = 30$ *counts/ms. Bottom:* $g^{(2)}$ *of DRa photoluminescence intensity on several decades of delays between photons. c) Top: Histogram of DRb photoluminescence intensity together with a fit with two Poisson distributions. The bright state in red has a mean emission intensity* $I_X = 110$ *counts/ms, the grey state in green has a mean emission intensity* $I_{X^-} = 17$ *counts/ms. Bottom:* $g^{(2)}$ *of DRb photoluminescence intensity on several decades of delays between photons of the whole photoluminescence intensity.*

bright state photons represent 6.5% and 76.5% of the recorded photons respectively. For DRb, photon events with count rates below 30 counts/ms and above 100 counts/ms are attributed to the grey and bright states respectively in Fig.IV.7c. The proportions are the following ones: 42% of the registered photons are discarded, 18% belongs to the grey state and 40% to the bright state. The photoluminescence decay curves of the post-selected photons are plotted on Fig.IV.8 for DRa and DRb. Monoexponential behaviors are found demonstrating the accurate photon sorting.

To summarize, the important points for the following analysis on the trion state

impact on the photon statistics are:

- DRa has a higher trion quantum yield than DRb, 35% against 15%,
- DRa spends less time in the trion state, it has a smaller number of trion state photons: 6.5% against 18% for DRb.

DRa and DRb electron delocalization and photon statistics

Electron delocalization The photoluminescence decay curves of the bright and grey state on Fig.IV.8 confirm the difference of emission rates between DRa and DRb already noticed on the the autocorrelation function in Fig.IV.6. The exciton decay curve (in red) for DRa gives $\tau_X = 65$ ns, while for DRb we find $\tau_X = 28$ ns. Concerning the trion state, fits give $\tau_{X^-} = 11.6$ ns and $\tau_{X^-} = 2.6$ ns for DRa and DRb respectively. These numbers are in good agreement with the trion quantum yield derived from the emission rates. Indeed, the trion quantum yield obtained from the lifetime ratio are $Q_{X^-} = 2\tau_{X^-}/\tau_X = 2 * 11.6/65 = 36\%$ for DRa and $Q_{X^-} = 2\tau_{X^-}/\tau_X = 2 * 2.6/28 = 18.6\%$ for DRb.

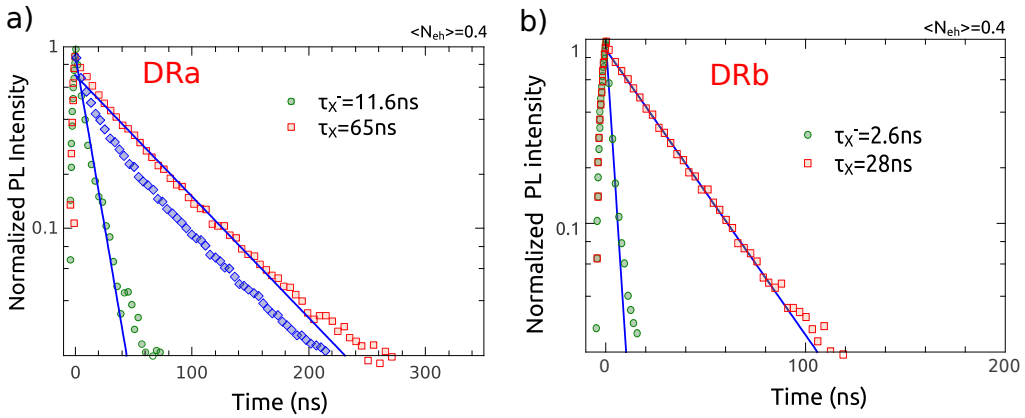

Figure IV.8: DRa and DRb photoluminescence decay. *a) Photoluminescence decay of DRa. Blue diamonds: photoluminescence decay of the whole intensity distribution. Red squares: photoluminescence decay for the photons in the red intensity window in Fig.IV.7b, a monoexponential decay fit gives $\tau_X = 65$ ns. Green circles: photoluminescence decay for the photons in the green intensity window in Fig.IV.7b, a monoexponential decay fit gives $\tau_{X^-} = 11.6$ns. b) Photoluminescence decay of DRb for the grey state photons (green circles) and bright state photons (red squares) corresponding to the selected regions in Fig.IV.7c.*

The DRb has a shorter exciton lifetime because of a less delocalized electron compared to DRa. Owing to this smaller electron delocalization, the trion state of DRb is characterized by a smaller quantum yield compared to DRa because Auger nonradiative recombination towards an electron is more efficient in the case of DRb.

Biexciton emission On Fig.IV.9 we computed the post selected bright state photons autocorrelation functions for DRa and DRb. Using Eq.IV.12, we can define the exciton $g^{(2)}(0)$ as such:

$$g_X^{(2)}(0) = \frac{2P_{Neh\geqslant 2}}{P_{Neh\geqslant 1}^2}\frac{Q_{2X}}{Q_X} \tag{IV.16}$$

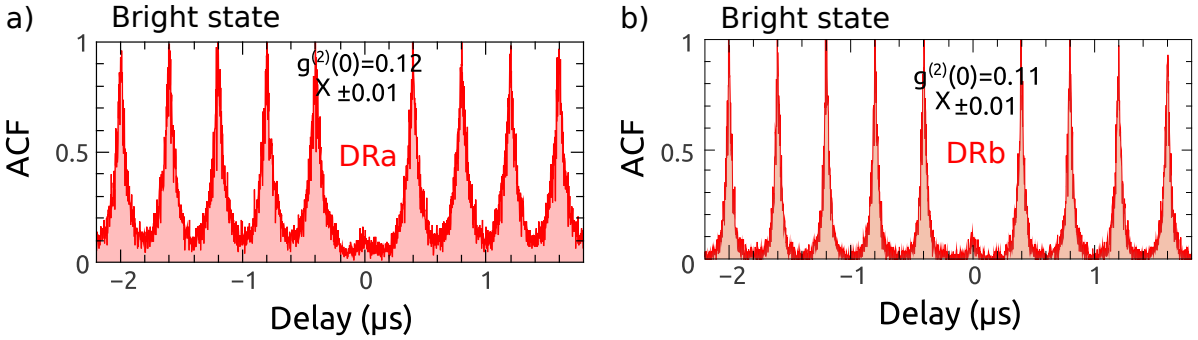

Figure IV.9: DRa and DRb bright state autocorrelation. *a) DRa bright state autocorrelation,* $g_X^{(2)}(0) = 0.12$. *b) DRb bright state autocorrelation,* $g_X^{(2)}(0) = 0.11$.

From the measurements, we find very similar $g_X^{(2)}(0)$ values for the two dot-in-rods. The accuracy of these values is confirmed by the autocorrelation measurements at very low excitation on Fig.IV.6a and b for which trion emission is not present. For the excitation power such that $\langle N_{eh}\rangle \sim 0.4$, the Poisson weighting term in Eq.IV.16 is $(2P_{Neh\geqslant 2})/({P_{Neh\geqslant 1}}^2) = 1.13$. This leads to $Q_{2X} = 10.6\%$ for DRa and 9.7% for DRb.

Charged biexciton emission On Fig.IV.10, the post selected grey state photons autocorrelation functions for DRa and DRb are presented. We can define the trion $g^{(2)}(0)$:

$$g_{X^-}^{(2)}(0) = \frac{2P_{Neh\geqslant 2}}{P_{Neh\geqslant 1}^2}\frac{Q_{2X^-}}{Q_{X^-}} \tag{IV.17}$$

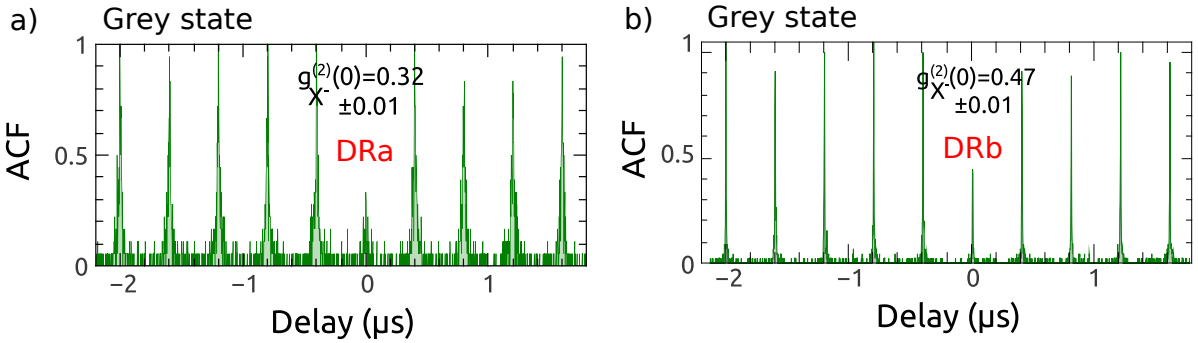

Figure IV.10: DRa and DRb grey state autocorrelation. *a) DRa grey state autocorrelation,* $g_{X^-}^{(2)}(0) = 0.32$. *b) DRb grey state autocorrelation,* $g_{X^-}^{(2)}(0) = 0.47$.

Conversely to the bright state case, we find a significant difference between DRa and DRb for the trion $g^{(2)}$ function. Calculations using Eq.IV.17 and the trion quantum yield previously found give $Q_{2X^-} = 10.1\%$ and $Q_{2X^-} = 6.2\%$ for DRa and DRb respectively.

Discussion A first observation is that *a degradation of the single photon emission properties is associated with a dot-in-rod in a charged state.* The degradation of the single photon emission with charging is related to the increase of the ratio between the biexciton and exciton quantum yields. A higher $g^{(2)}(0)$ value is not necessarily due to an increase of the two photon emission but can also be the result of a decrease in the single photon emission which is the case here. The degradation of the single photon emission is more important for DRb with $g^{(2)}_{X^-}(0) = 0.47$, versus $g^{(2)}_{X^-}(0) = 0.32$ for DRa. For DRb the $g^{(2)}(0)$ value corresponding to all the photons is equal to 0.24, it is almost twice the value found for DRa. This difference can be explained by the proportion of photons of each state in the overall measurement. The grey state photon proportion being three times larger for DRb than for DRa, $g^{(2)}(0)$ is therefore increasing towards the charged exciton photon statistics. The $g^{(2)}$ at zero delay of the entire photon events detection reflects therefore the interplay between the two states characterized by different photon statistics.

We can go further into this analysis by looking at the different quantum yields involved and deduce the Auger rates. This is summarized in Tab.IV.1. We follow the statistical scaling analysis [150, 151, 161]. The non radiative relaxation process is the Auger effect. The Auger relaxation rate γ_{A^-} of an electron hole pair to a neighboring electron can be derived from the negative trion state quantum yield:

$$Q_{X^-} = \frac{2\gamma_r}{2\gamma_r + \gamma_{A^-}}. \tag{IV.18}$$

In the case of a biexciton, the energy of an electron-hole pair can be transferred to a negative or a positive charge (electron or hole) by an Auger process. Assuming again that the non radiative decay channels are only due to the Auger effect, the biexciton quantum yield can be written as:

$$Q_{2X} = \frac{4\gamma_r}{4\gamma_r + 2\gamma_{A^+} + 2\gamma_{A^-}}. \tag{IV.19}$$

This formula allows to deduce the Auger relaxation rate to a positive charge γ_{A^+} from the quantum yield of the biexciton. To help understanding the following analysis, Fig.IV.11 presents the different relaxation possibilities for an excitation of $\langle N_{eh} \rangle \sim 0.4$. First possibility, the dot-in-rod is in a neutral state. Starting from two excitons in the structure, the dot-in-rod will emit one photon with probability $P_{Neh \geqslant 1} Q_X$ after Auger non-radiative

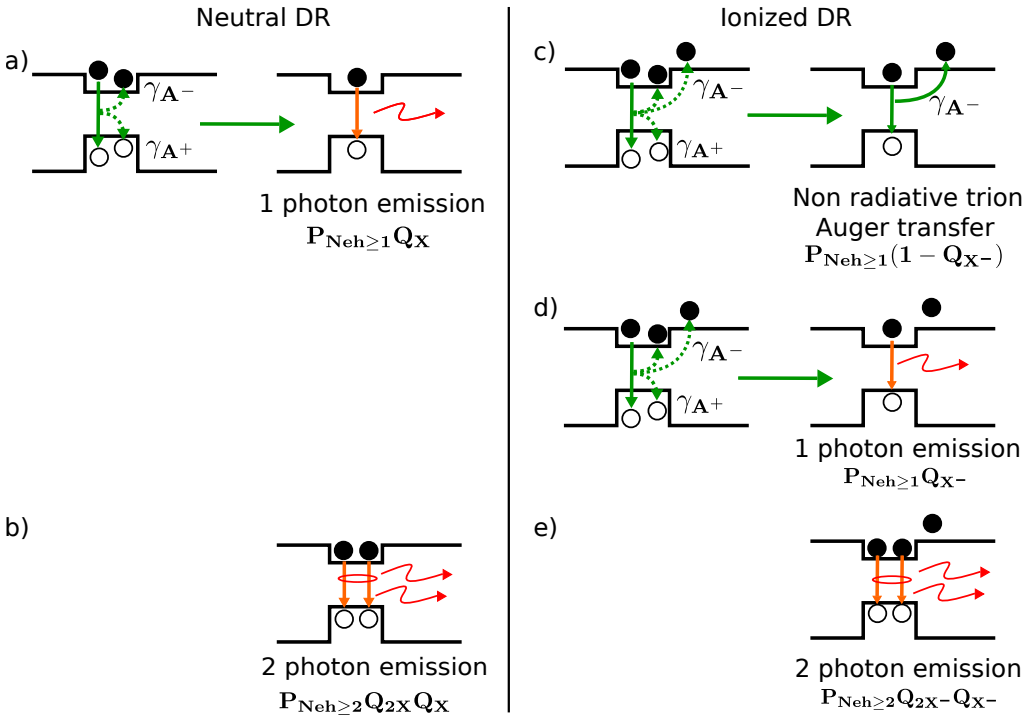

Figure IV.11: *Schematic of the different relaxation pathways after a pulsed excitation of the shell state continuum. Green arows symbolizes the possible Auger relaxation with their associated rates γ_{A^+} if the relaxation energy is given to a hole or γ_{A^-} if it is given to an electron. Dashed green arrows means that different Auger relaxation possibilities are in competition. Orange arrows symbolise radiative recombinations. For the low power excitation considered: $\langle Neh \rangle = 0.4$, five relaxation cases are possible. For a neutral DR, a) single photon emission after an Auger non radiative decay of the biexciton, b) biexciton binding and two photon emission with the given probabilities. For an ionized DR, c) non radiative relaxation of the biexciton and exciton, d) single photon emission after Auger non radiative decay of the biexciton, e) biexciton binding and two photon emission.*

relaxation of the biexciton with rate γ_{A^+} or γ_{A^-} depending to which charge the energy is given to (a hole or an electron as depicted on Fig.IV.11a). Or it will emit two photons with probability $P_{Neh\geqslant 2}Q_{2X}Q_X$ if no Auger relaxation takes place (Fig.IV.11b). Second possibility, the dot-in-rod is in a negative charged state. It will either emit one (Fig.IV.11d) or two photons (Fig.IV.11e) with probabilities $P_{Neh\geqslant 1}Q_{X^-}$ and $P_{Neh\geqslant 2}Q_{2X^-}Q_{X^-}$ respectively, with Q_{2X^-} the charged biexciton quantum yield. Non radiative Auger transfer to the extra electron with rate γ_{A^-} can also quench the emission and no photon will be emitted (Fig.IV.11c).

For DRa, $\tau_{A^-} = 1/\gamma_{A^-}$ is found to be 18.3 ns while the Auger relaxation to positive charges $\tau_{A^+} = 1/\gamma_{A^+} = 4.9$ ns is almost four times faster. The long Auger relaxation lifetime for electrons can be explained by a highly delocalized electron inside the shell as expected from the long exciton lifetime $\tau_X = 65$ ns. Auger relaxation to an electron is less efficient than to a hole because of electron delocalization in quasi type-II heterostructure

	τ_X (ns)	Q_X	Q_{X^-}	Q_{2X}	Q_{2X^-}	τ_{A^-} (ns)	τ_{A^+} (ns)
DRa	65	100%	36%	10.6%	10.1%	18.3	4.9
DRb	28	100%	18%	9.7%	6.2%	3.1	2.9

Table IV.1: Exciton lifetime τ_X, Q_X , Q_{X^-}, Q_{2X}, Q_{2X^-} quantum yields and Auger relaxation time constants for negative (τ_{A^-}) and positive (τ_{A^+}) charges for the different DRs.

like CdSe/CdS dot-in-rods. In this case, positive charges constitute a preferred decay channel and the extra negative charge does not increase the number of non radiative relaxation paths as it is an inefficient relaxation solution. The biexciton mainly relaxes giving its energy to a well confined hole whether the dot-in-rod is charged or not, thus in Fig.IV.11 the scenari c and d are similar to the scenario a. This explains that for DRa the negatively charged biexciton quantum yield is similar to the neutral biexciton quantum yield.

In contrast, for DRb characterized by a shorter exciton lifetime of $\tau_X = 28$ ns and consequently a less delocalized electron compared to DRa, using the same calculations, $\tau_{A^-} = 3.1$ ns and $\tau_{A^+} = 2.9$ ns are similar. It implies in this case a decrease of the charged biexciton quantum yield compared to the neutral biexciton quantum yield. No decay channel for the biexciton is favored in this case, so when a DR is charged, the extra negative charge offers an additional non radiative decay channel, as can be seen on Fig.IV.11c and d, which decreases the charged biexciton quantum yield compared to the neutral biexciton quantum yield. These different behaviors probably come from a slightly different structure of DRb as compared to DRa, implying a different localization of the electrons and the holes in the two DRs as expected from the different exciton lifetimes.

With our measurements and analysis, we were able to explain the differences between the overall photon statistics of different dot-in-rods by quantifying the bright and grey state photons proportions and statistics. At very low excitation power the photon statistics is only characterized by the exciton and biexciton. However, this gives only a partial information on the photon statistics at higher excitation power as the appearance of the grey states needs to be taken into account. Dot-in-rods having the same photon statistics at low excitation power can have very different emission statistics at higher power because of a distinct grey state emission. The role of the electron delocalization in defining a charged dot-in-rod radiative recombination properties can be summarized as follows: *the more the electrons are delocalized into the shell the less the charging affects the emission probability (quantum yield) of the different species.* This is exemplified above by the comparison between the two dot-in-rods: DRa, showing a strong electron delocalization, has its quantum yields that diminishes less when charged than DRb. Another important conclusion of this analysis is the following one: *as the number of relaxation pathways*

increases, higher order excited states are less affected by the charging process. The last statement is illustrated in our measurements by the fact that the biexciton quantum yield decreases less than the exciton quantum yield while the dot-in-rod is charged.

IV.4 Measuring the photon statistics with an ICCD camera

In this section we present an experiment realized in collaboration with the QuaRad[5] group of the Max Planck institute for the science of light in Erlangen where single photon detection is combined together with spatial resolution. Having the possibility to make single emitter measurements as presented in the previous sections on many emitters at the same time is an obvious experimental breakthrough. To realize such measurements we used an intensified CCD (ICCD) camera: Princeton Instruments PI-MAX3:1024i. This device can be used as an array of single-photon detectors for spatially resolved measurements of the second order correlation function. In the following we show that we can correctly measure the correlation function with such a device and we apply it to single dot-in-rods and clusters. The correlation function measurement is confirmed by the brightness of the measured objects as well as with a measure obtained with a standard HBT setup.

ICCD camera

Fig.IV.12 shows a simplified schematics of the ICCD camera. In intensified mode, the ICCD camera works as follow[6]:

- an input image is focused onto a photocathode. Incident photons strike the photocathode and create electrons.
- If the intensifier is gated ON, the photocathode is more negative than the microchannel plate (MCP) input thanks to an applied voltage, the electrons will be attracted towards the MCP. Gating acts like a shutter in that gating the intensifier on allows the CCD to collect light.
- The voltage at the MCP output is much more positive, most of the electrons accelerates into the MCP channels. When they hit the channel walls, they generate

[5]Website link: http://www.mpl.mpg.de/de/leuchs/forschung/quarad.html

[6]The instrument manual can be found at: ftp://ftp.princetoninstruments.com/public/Manuals/PrincetonInstruments/PI-MAX3SystemManual.pdf.

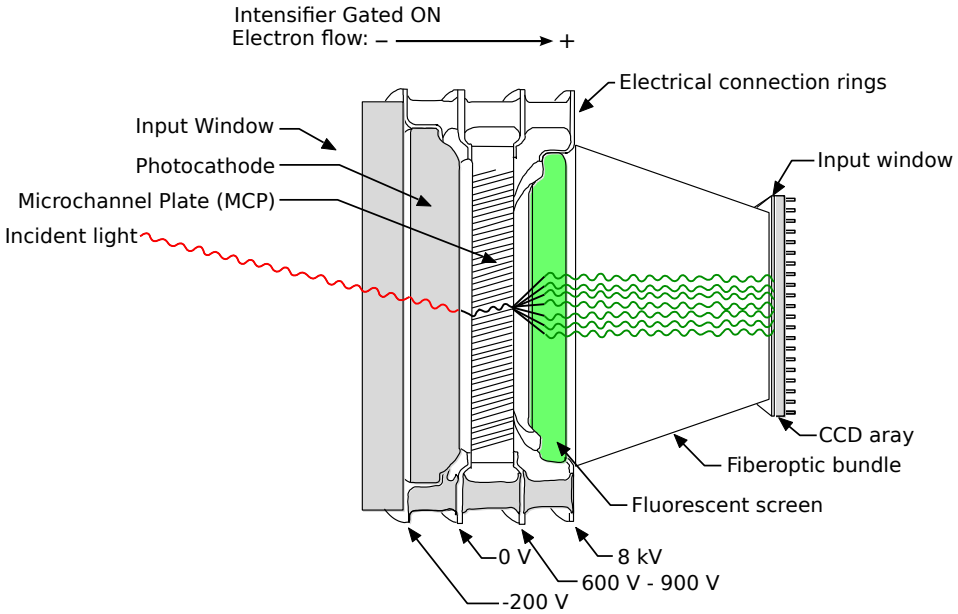

Figure IV.12: Schematics of the major Components of the ICCD. *Reproduced from the instrument manual.*

additional electrons, resulting in amplification. The gain can be adjusted by increasing or decreasing the voltage at the MCP output.

- When the electrons exit the MCP they are further accelerated by a constant high voltage ($5 - 6$ kV) before striking a fluorescent screen. The excited fluorescent screen releases photons. For each photon incident on the photocathode there are now many corresponding photons at the output of fluorescent screen thanks to the electron avalanche in the MCP.

- The photons released by the fluorescence screen are transferred to the the CCD array and produce charge at the pixels they strike.

Setup

The setup of the experiment is presented on Fig.IV.13. A continuous wave laser at 405 nm is used to excite the sample in a wide-field configuration using an out of focus objective (O). The luminescence of the sample is collected with an immersion oil objective ($N.A = 1.3$) ensuring a high collection efficiency. The collected light is then sent to a 50/50 beam-splitter via a dichroic mirror. Each output path of the beam-splitter is imaged on the ICCD camera. The remaining excitation light is spectrally filtered by an interference filter placed in front of the camera. This setup is analog to the Hanbury Brown-Twiss setup described in section II.1.1 except that the two avalanche photodiodes

are replaced by a single ICCD camera on which two images (A and B) of the sample are made.

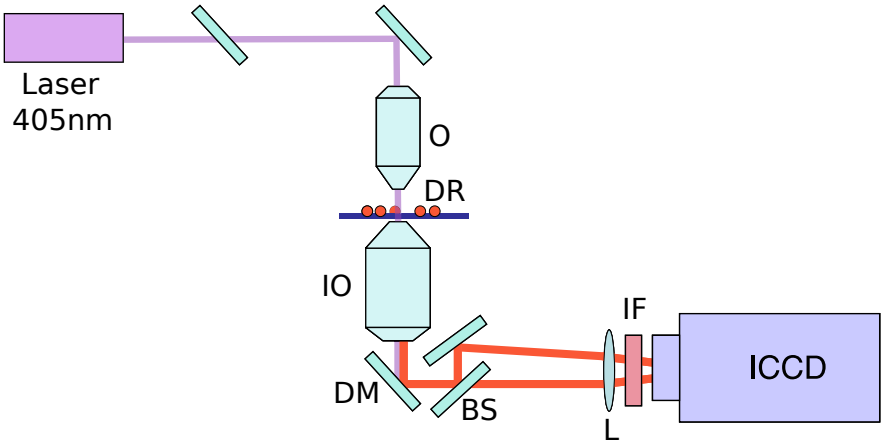

Figure IV.13: Setup. *Wide-field microscopy is realized using an out of focus objective (O) shining continuous wave laser light on a broad area of the sample. Photoluminescence is collected by an oil immersion objective (IO). It is separated from the excitation light by a dichroic mirror (DM) and sent on a HBT like setup made of a beam splitter (BS) and two detection areas on the ICCD camera. A lens (L) is used to image the collected light on the CCD camera and an interference filter (IF, bandwidth* 40 *nm) removes the remaining excitation light.*

Fig.IV.14a presents a typical image registered by the ICCD camera when working as a conventional CCD camera (without gain). In the following we will show that we can measure the second order correlation function of each object detected on the image. The accuracy of this measurement is strongly confirmed by the brightness associated to each object of the image.

Measurements

For a measurement of the second-order correlation function, a set of 10^6 frames is acquired. The long lifetime (3 ms) of the fluorescence screen imposes to work with a slow rate (30 Hz), thus the whole data acquisition takes many hours. The unavoidable small displacements of the images during this time (due to small temperature variations and mechanical vibrations) were taken into account by taking a long frame after every 10^4 standard frames. These control frames allow to trace the displacement of the dot-in-rod images and to make appropriate corrections to the coordinates of pixels chosen in each frame. The excitation is performed by irradiating with a continuous wave diode laser light at 405 nm. To slow down the bleaching of the dot-in-rods, the laser beam is modulated with a frequency of 30 Hz and a pulse duration of 550 μs[7]. Given the long

[7]Minimum pulse duration achievable with the material.

measurement duration, we performed the measurement with the thicker shell dot-in-rods (DR4) of 4.6 nm core diameter, 29 nm shell length, and 11 nm shell width as they are the more resistant to photobleaching.

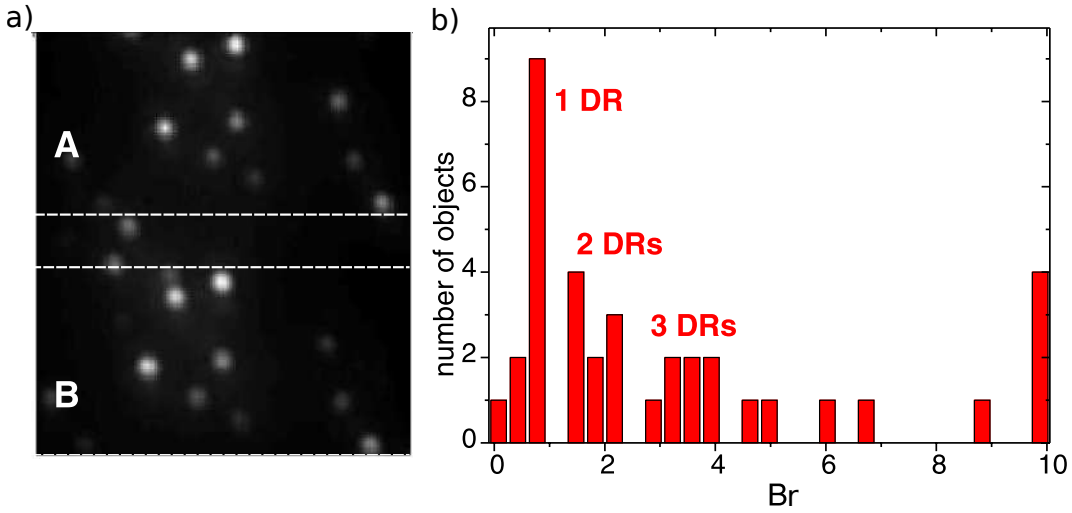

Figure IV.14: ICCD camera image and typical object brightness histogram. *a) A and B images of the sample obtained by splitting the collected luminescence with a* 50/50 *beam-splitter. b) Histogram of the brightness of the different objects recorded on the ICCD camera. The first three groups of bars are associated with single dot-in-rods and two-dot-in-rod and three-dot-in-rod clusters, respectively.*

To optimize the single-photon detection, every group of 4×4 pixels are binned together into a single superpixel. An object on the image is defined by an area of a given number of pixels and the number of single photon counts over this area defines the signal associated to an object. The ICCD camera is gated synchronously with the laser pulses, the gate width can be tuned between 10 and 40 ns, the signal is acquired during this gate duration. We work with the shortest gate time of 10 ns.

Processing

A level of the dimensionless readout signal S of a superpixel (proportional to the electric charge acquired in a superpixel) is chosen as a threshold, and *any signal exceeding this value is interpreted as a single photon event for a corresponding superpixel*[8]. For each object in the image of Fig.IV.14a, the dimensionless brightness Br is calculated taking into account the average number of counts $\langle N_A \rangle$ per gate in image A[9], the gate time T_g of 10 ns, and the intensity I of the excitation beam at the object position:

[8] A pixel is therefore taken as equivalent to an APD detector, an output pulse equals a photon.
[9] $\langle\rangle$ denotes averaging over all frames, $N_A = 0$ or 1 for a given gate, frame.

$$Br = \frac{\langle N_A \rangle}{T_g \tilde{I}}, \tag{IV.20}$$

with $\tilde{I} = \alpha I$. Here α is a normalization factor, the same for all measurements, which has been chosen in such a way that the dimmest objects have a value of Br close to 1. The distribution of the objects, with respect to the brightness value Br, is shown in Fig.IV.14b. One can see that, despite the low total number of objects in the image, several groups can be seen: roughly, with $Br < 1.25$, $1.25 < Br < 2.5$ and $2.5 < Br < 4$. We make the hypothesis that these groups correspond to single dot-in-rods, clusters of 2 dot-in-rods and clusters of 3 dot-in-rods respectively. The second-order correlation function at zero delay $g^{(2)}(0)$ is calculated as:

$$g^{(2)}(0) = \frac{\langle N_A N_b \rangle}{\langle N_A \rangle \langle N_B \rangle}, \tag{IV.21}$$

with N_B the number of single-photon events for an area associated with a given object in the image B for a given gate, analogous to N_A for image A defined previously. Due to the mechanical vibrations in the system, as well as to the bleaching and blinking of the dot-in-rods, the brightness of each object can change during the data acquisition time. This was taken into account by normalizing the resulting correlation function of each object to its value at a time delay of $T = 30$ ms, $g^{(2)}(T)$. The latter was calculated by taking frames separated by 30 ms, which is much longer than the lifetime.

If the threshold S_{th} is chosen too high, the resulting quantum efficiency becomes low, but this does not affect the normalized correlation function [181]. On the other hand, if the threshold is too low, the noise is increased. The results of $g^{(2)}(0)$ measurements of 3 objects with the gate time $T_g = 10$ ns are shown in Fig.IV.15b, c and d. The correlation is plotted against the threshold signal S_{th}. The measurement error is estimated from the number of registered single-photon events, therefore it increases with increasing threshold signal S_{th}. For all objects, no anti-bunching is observed for low threshold values. This is because at low threshold, the noise is high and its Poisson statistics masks the anti-bunching. At higher threshold values, an object that most probably is a single dot-in-rod ($Br = 0.74$) in Fig.IV.15b manifests significant anti-bunching: $g^{(2)}(0) = 0.35 \pm 0.1$. This value is relatively high for two reasons:

- first, the $g^{(2)}(0)$ value of these emitters is high. We found that on average these dot-in-rods display $g^{(2)}(0) = 0.22$ at low excitation (below saturation). Fig.IV.15a shows a typical antibunching curve under continuous wave excitation measured with a pair of APDs in a HBT configuration, here $g^{(2)}(0) = 0.25$ without noise correction.

- The gating implies that our measurement is actually an average of $g^{(2)}(\tau)$ for τ

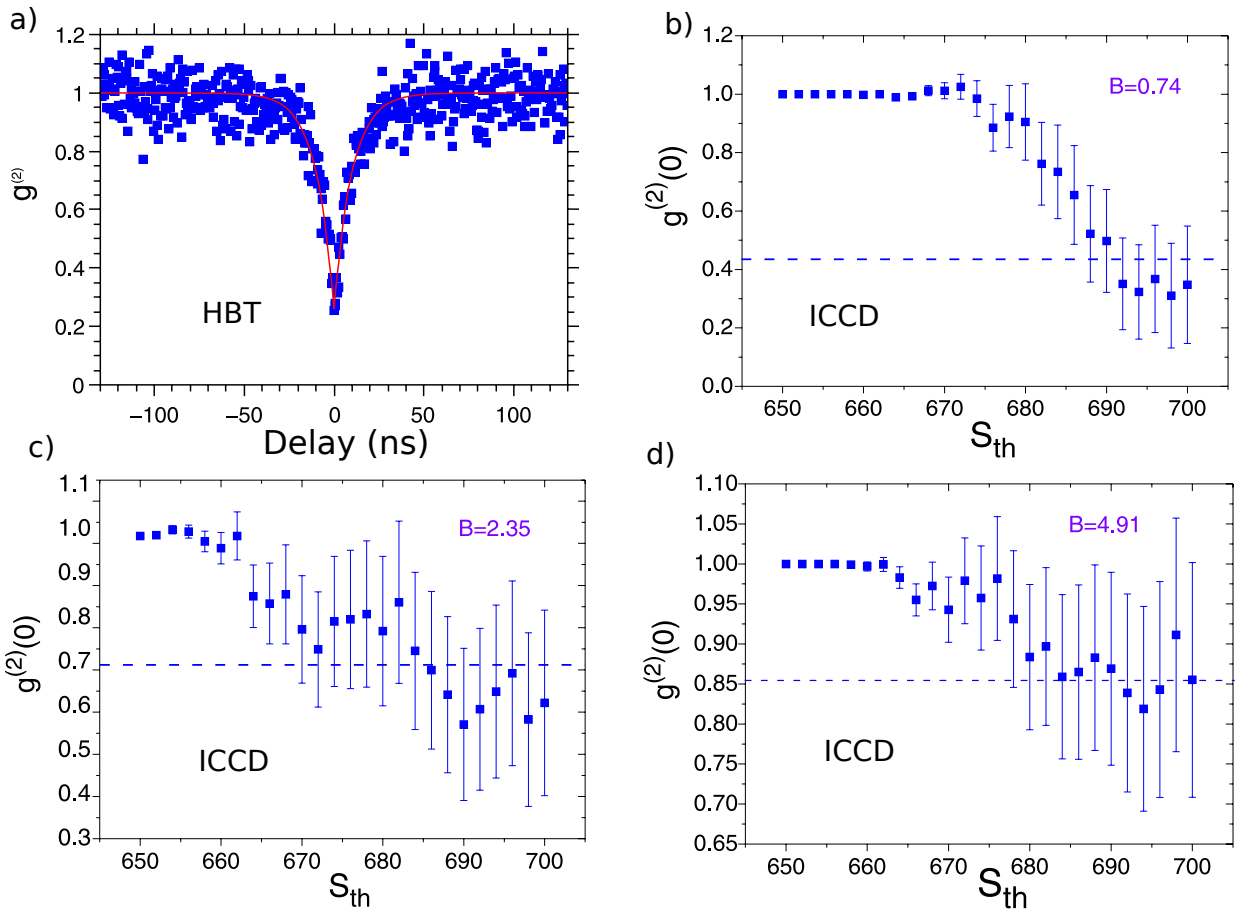

Figure IV.15: $g^{(2)}$ ***measurement from standard HBT setup and ICCD camera in continuous wave excitation.*** *a)* $g^{(2)}$ *measurement on a dot-in-rod from sample DR4 with the standard HBT setup and a continuous wave excitation. b)* $g^{(2)}$ *measurement with the ICCD camera as a function of the signal threshold value* S_{th} *on an object displaying a brightness* $Br = 0.74$*. c)* $g^{(2)}$ *measurement with the ICCD camera as a function of the signal threshold value* S_{th} *on an object displaying a brightness* $Br = 2.35$*. d)* $g^{(2)}$ *measurement with the ICCD camera as a function of the signal threshold value* S_{th} *on an object displaying a brightness* $Br = 4.91$*.*

between 0 and 10 ns. Averaging [183] a $g^{(2)}(0)$ of 0.22 for a gate time of 10 ns gives $g^{(2)}(0) = 0.43$.

The expected value of the bunching parameter measured for a single dot-in-rod, with the gate time 10 ns, is 0.43. It is reported in Fig.IV.15b as a dashed line and is in agreement with the measured value by the ICCD.

For a brighter object ($Br = 2.35$), which we associate with a cluster of two dot-in-rods, the value of $g^{(2)}(0)$ measured at optimal threshold values is 0.65 ± 0.2 in Fig.IV.15c. The existence of two single-photon emitters in a cluster can be taken into account by using the general formula describing $g^{(2)}(0)$ in the presence of m identical contributions (modes) [184]:

$$g_m^{(2)} = 1 + \frac{g_1^{(2)} - 1}{m}, \tag{IV.22}$$

where $g_1^{(2)}$ is the value for a single emitter. For $m = 2$ and $g_1^{(2)} = 0.43$, we get $g_1^{(2)} = 0.72$, which is in agreement with the data in Fig.IV.15c. Finally, Fig.IV.15d shows the bunching parameter for an object with $Br = 4.91$, for which we assume $m = 4$. This gives the theoretical prediction $g_1^{(2)} = 0.86$, again in good agreement with the measurement (0.85 ± 0.1). The hypothesis about the number of dot-in-rods in clusters, based on their brightness, agrees very well with the $g^{(2)}(0)$ measurements. This confirms the accuracy of our measurement with the ICCD camera.

Outlook

The previous measurements show the feasibility of single and few particles measurements with an ICCD camera, especially for demonstrating the nonclassicality of such emitters. It is to be noted that these measurements are completely equivalent to what can be measured with two APDs in a HBT configuration, except that they are spatially extended such that multiple emitters can be measured simultaneously. Beyond the measurement of the $g^{(2)}$ function, one could realize measurements of higher order correlation functions with the ICCD camera to unambiguously determine the number of single-photon emitters in a cluster. This would overcome what can be done with a simple HBT setup. To measure the $g^{(3)}$ function one needs 3 APDs and two 50/50 beam splitters, the number of detectors scales with the correlation function number. With the ICCD camera, each pixels could be used as a single photon detector and correlations between different pixels of the same image would yield higher order correlation functions; correlations between different images as presented above would also be possible but would require to scale the number of beam splitters and images.

Conclusion

In this chapter we have measured the photon statistics of different dot-in-rods samples. The trion emission rate is governed by the electron delocalization, a delocalized electron implies a lower Auger recombination rate and therefore a higher quantum yield for the trion. This gives a complete description of the single photon emission events for dot-in-rods. The emission of two photons by these nanoemitters is mostly governed by the hole localization. Samples with smaller cores display lower two photon emission due to a high efficiency of biexciton nonradiative recombination via energy transfer to a hole. We also quantified the effects of charging on the two photon emission. Our analysis has shown

that the more the electrons are delocalized the less the two photon emission is affected by the charging as it is the case for the single photon emission. The characterization of the photon statistics is strongly limited by the measurement apparatus that up to now limits us to single and two photon emission events for a single emitter at a time. We presented an original measurement of the photon statistics with an ICCD camera that can give the second order correlation function of many emitters at the same time.

Chapter V
CdSe/CdS dot-in-rods emission polarization

Introduction

This chapter is devoted to the analysis of the polarization properties of the emission of dot-in-rods. Conversely to spherical CdSe/CdS nanocrystals, dot-in-rods have high degrees of linear polarization as reported in literature [13, 24, 25], typically around 70%. There are two potential sources of electric field polarization for dot-in-rods: a classical origin coming from dielectric effects due to the shape anisotropy of the shell and a quantum origin associated with the transition dipoles. As seen in chapter I, the band edge exciton fine structure is not completely clarified for dot-in-rods. It should strongly depend on the electron localization and therefore be very dependent on the sample geometry. The effect of the shape anisotropy on the polarization has been first studied for nanowires [185] and should also play a role in dot-in-rods emission polarization.

First, we give a brief overview of the recent studies on dot-in-rods and nanorods emission polarization. Most of the articles in the literature are based on ensemble measurements and study only one sample geometry. To understand better how linear polarization can arise from such emitters, we propose a comparative study of single dot-in-rods emission polarization for various samples. We finish the chapter by a discussion on the results and their relationship with the already existing studies.

V.1 Dot-in-rods polarization: an overview

In this section we describe the interesting ideas and experimental methods that we can find in literature on the polarization of dot-in-rods or nanorods. The different points presented will be used at the end of this chapter when discussing the results of our measurements.

V.1.1 Ensemble measurement methods

Various articles [111, 186–190] published recently present ensemble polarization measurements of dot-in-rods, nanorods or rod-in-rods in solution. The measurement is either called polarized excitation spectroscopy or photoselection method and is based on the same method than the photoluminescence excitation (PLE) spectroscopy presented in chapter I section I.1 except that it is resolved in polarization.

This measurement procedure is interesting because it yields information on the polarization of the transitions over the whole spectrum while the single particle measurement presented in Chapter II yields only information on the emission polarization originating from the band-edge exciton. Moreover a single measurement is needed to characterize the average behavior of a sample, however no information on the deviation from this average value is obtained.

We are only interested in studying the polarization of the emission, single particle measurements are in this case a more straightforward way to obtain information on the polarization. We leave the reader with the references aforementioned for more details on ensemble measurements.

V.1.2 Dielectric effects

Dielectric effects were theoretically calculated in various articles on colloidal particles [22, 110, 186] with shape anisotropy. The calculations presented in these articles are derived from a broad area of research in electromagnetism that is the modeling of the effective properties of heterogeneous materials made of a collection of small light scatterers. The modeling is usually based on the calculation of the response of individual scatterers to an incoming field which is then generalized to the macroscopic properties of a material made of a collection of such scatterers. For our study, we are just interested in the first step, the electromagnetic response of a dielectric rod excited by an incoming field.

Dot-in-rods or a nanorods are geometrically close to ellipsoids, they are therefore modeled as homogeneous dielectric ellipsoids [22, 110, 186] with axes $a = b < c$. Moreover, the ellipsoid is one of the few geometrical shape for which an analytical solution [191, 192] to the problem exists. A schematics of the ellipsoid is proposed on Fig.V.1. The eccentricity e of the ellipsoid is defined as:

$$e = \sqrt{1 - \frac{a^2}{c^2}}. \tag{V.1}$$

An ellipsoid with axes $a = b < c$ has an anisotropic response to an excitation field. A dot-in-rod or nanorod can therefore be seen as a directional antenna which is preferentially

excited in a particular direction. Let us call $f_c = E_c(in)/E_c(out)$ and $f_a = E_a(in)/E_a(out)$ the ratios of electric field amplitudes inside the rod over the electric field amplitude outside the rod along and perpendicularly to the c axis respectively, also called local field factors [186]. They are expressed as [191, 192]:

$$\begin{aligned} f_c &= \frac{E_c(in)}{E_c(out)} = \frac{\epsilon_{medium}}{\epsilon_{medium} + (\epsilon_{rod} - \epsilon_{medium})\alpha_c}, \\ f_a &= \frac{E_a(in)}{E_a(out)} = \frac{\epsilon_{medium}}{\epsilon_{medium} + (\epsilon_{rod} - \epsilon_{medium})\alpha_a}, \end{aligned} \tag{V.2}$$

with ϵ_{medium} and ϵ_{rod} the relative permittivities of the surrounding medium and rod material respectively. α_a and α_c are called the depolarization factors for the minor axes and major axis respectively.

The depolarization factor is a term that takes into account the geometry of the scatterer. For a spherical scatterer α is independent of the direction [192]. Hence for spherical shell nanocrystals no shape effect is expected to enhance or attenuate the electric field in a given direction compared to the others and therefore modify the polarization properties. Spherical shell nanocrystals would be omni-directional antennas as opposed to the directional antenna formed by rod shape particles. For a prolate ellipsoid one finds [193] that:

$$\begin{aligned} \alpha_c &= \frac{1-e^2}{2e^3}\left(ln(\frac{1+e}{1-e}) - 2e\right), \\ \alpha_a &= \frac{1}{2}(1-\alpha_c) \end{aligned} \tag{V.3}$$

The ratio of electric field strength between the major and minor axis R_e is then:

$$R_e = \frac{f_c}{f_a} = \frac{\epsilon_{medium} + (\epsilon_{rod} - \epsilon_{medium})\alpha_a}{\epsilon_{medium} + (\epsilon_{rod} - \epsilon_{medium})\alpha_c}, \tag{V.4}$$

In our case $\epsilon_{rod} > \epsilon_{medium}$[1] and $\alpha_c < \alpha_a$, this gives $f_c > f_a$ and consequently $R_e > 1$. As shown on Fig.V.1, this implies a stronger attenuation of the electric field in the directions perpendicular to the c axis. An incoming field with a given amplitude impinging the nanorod will be $1/R_e$ times weaker inside the shell material if it is along one of the minor axis direction compared to the case for which the field is directed along the long axis of the rod. Concerning the emission, a dipole inside the ellipsoid shell will be affected by the dielectric shape effect. The oscillator strength of a transition along the c axis should

[1] $\epsilon_{rod} = \epsilon_{CdS} = 5.7$ and $\epsilon_{medium} = \epsilon_{air} = 1$.

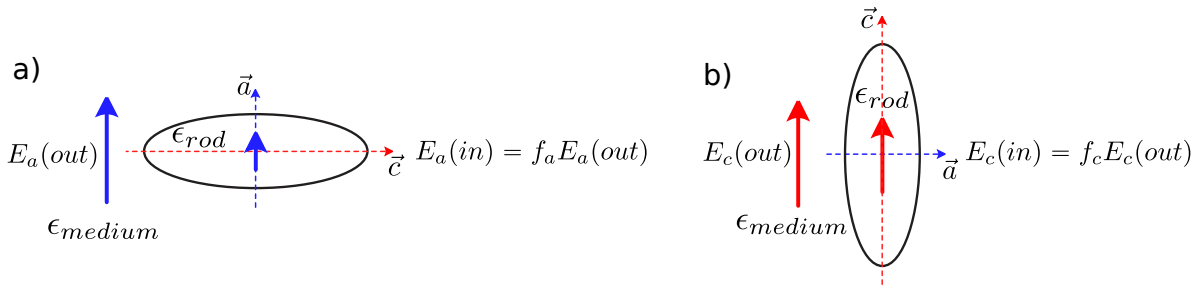

Figure V.1: Schematics of the dielectric effects for an electric field impinging a prolate spheroid. *a) An electric field $E_a(out)$ aligned perpendicularly to the c axis is attenuated by a factor f_a. b) An electric field $E_c(out)$ aligned along the c axis is attenuated by a factor f_c. In the case $\epsilon_{rod} > \epsilon_{medium}$, $f_c > f_a$. This implies a stronger attenuation of the electric field inside the rod material in the directions perpendicular to the c axis.*

be multiplied by R_e[2] to account for the dielectric shape effect [22, 110]. In Tab.V.1 we give the values of eccentricities, depolarization factors and ratio of electric field strength between the major and minor axis R_e for the dot-in-rods studied in this chapter. We can observe that R_e ranges from 1.9 to 3.2. We therefore expect the dielectric effect to play a major role in defining the polarization of our dot-in-rods.

	Thickness (nm)	Length (nm)	Aspect ratio	Eccentricity	α_c	α_a	R_e
DR1	3.6	51	14.2	0.998	7.10^{-3}	0.5	3.2
DR2	4	22	5.5	0.98	$3.6.10^{-2}$	0.48	2.8
DR3.1	7	22	3.1	0.95	$9.4.10^{-2}$	0.45	2.2
DR3.3	7	58	8.3	0.99	$1.8.10^{-2}$	0.49	3
DR4	11	29	2.6	0.92	0.13	0.44	1.9

Table V.1: Geometrical parameters of the investigated samples, depolarization factors α_c, α_a along the major and minor axis respectively and ratio of electric field strength between the major and minor axis R_e. .

This effect has been clearly evidenced when exciting dot-in-rods in the UV. In fact, at high energies the states are not quantized and the continuum of electronic transitions shows no preferential directionality, thus removing any quantum mechanical mechanisms as potential source of polarization of the absorption. The polarization of absorption of dot-in-rods is therefore constant with the wavelength of excitation at high energies because no underlying quantum mechanical process brings any particular feature in the absorption polarization. Nevertheless, it is non-zero [186, 188, 190] because of the shape anisotropy, a preferential direction of absorption exists. The measured anisotropy at high energies matches particularly well with the expected anisotropy [186, 190] from the

[2]Or conversely the oscillator strength of a transition perpendicular to the c axis should be multiplied by $1/R_e$.

dielectric geometrical model above described. Reference [190] even checked the model for particles in different solvant (changing ϵ_{medium}) and showed that the ligands should also play a role in precisely defining the anisotropy due to the rod shape.

V.1.3 Fine structure

We briefly summarize the role of the fine structure in defining the polarization properties of CdSe nanocrystals as exposed in chapter I.

The exciton fine structure of the lowest excited state of CdSe consists of eight states: $|\pm 2\rangle$, $|\pm 1^L\rangle$, $|\pm 1^U\rangle$, $|0^L\rangle$ and $|0^U\rangle$. The $|\pm 2\rangle$ and $|0^L\rangle$ states are optically forbidden and not expected to contribute to room temperature emission. The photoluminescence comes from the radiative relaxation of the exciton fine structure level according to their oscillator strength weighted by the excited state populations at a given temperature. Room temperature emission is a mixture of recombinations from the $|0^U\rangle$ state, with photons linearly polarized along the wurtzite c-axis, and from the $|\pm 1^L\rangle$, $|\pm 1^U\rangle$ states, with photons circularly polarized. Conversely to CdSe spherical dots, the photoluminescence polarized along the wurtzite c-axis dominates the transitions relaxation for CdSe nanorods. Theory and experiments suggest that both the oscillator strength and the population of the $|0^U\rangle$ excitonic state explain this phenomenon. The oscillator strength of the linearly polarized transition increases with the aspect ratio of the nanorod and the anisotropic dielectric environment further increases the dominance of the linearly polarized emission [110].

V.1.4 Polarization and c axis

As described in chapter II for the single particle polarization measurements, the orientation of a dipole compared to the optical axis (axis of the microscope) is a fundamental parameter to control in order to correctly interpret the results. A 1D dipole emitting linearly polarized light will show a high degree of polarization if oscillating perpendicularly to the optical axis. However the measured degree of polarization will decrease if the angle between the optical axis and the dipole decreases (the trend with which it decreases depends on the setup configuration: interfaces, objective numerical aperture ...). This is very well summarized in reference [141].

First, concerning dot-in-rods, transmission electron microscope images suggests that they lie flat when drop-casted on a substrate as evidenced by the size homogeneity. If the CdS shell grows without stacking faults then the c-axis of the CdSe core and CdS shell

are aligned and correspond to the long axis of the rod shell[3]. Assuming that dot-in-rods are lying flat on the coverslip, *the c axis is also lying flat on the coverslip and is therefore perpendicular to the optical axis of our microscope.* This is a common assumption in literature.

From single particle measurements, reference [194], assuming that dot-in-rods are 1D dipole emitters, concludes that the optical dipole is on average not aligned with the c-axis of the particles. The angle between the c axis and the 1D dipole would range from 15° and 60°, being on average around 30°. However reference [187] shows, using polarization single particle measurement together with an atomic force microscope, that dot-in-rods and nanorods have their long axis (c-axis) aligned with the measured polarization direction. We actually show the same result in chapter VI when aligning dot-in-rods inside liquid crystal defects. These two experiments prove that the linear polarization is aligned with the c-axis. The conclusion in reference [194] of a tilted dipole compared to the c axis is driven by the fact that they model the emission of dot-in-rods as a 1D dipole. The average polarization of the sample being lower than what expected for a lying 1D dipole they conclude that the 1D dipole should not lie flat on the microscope coverslip and so not be aligned with the rod axis. However at room temperature, the whole fine structure is populated such that the emission comes from different dipoles, some of them being 2D and another 1D given the fine structure depicted in chapter I.

On the other hand, as proposed in reference [190], stacking faults, dangling bonds and perturbation of morphology might imply deviations from the theoretical model as witnessed for higher states absorption. Nevertheless, the direct correlation between the atomic force microscope images and polarization directions demonstrated in reference [187] is a strong argument in favor of the linear polarization being aligned with the c-axis. This is the assumption we take to interpret our experimental results.

[3]The c-axis of the CdSe core is aligned with the c-axis of the CdS shell because it is precisely the anisotropy of the CdSe core along the c-axis that induces the growth process of the shell along the same axis. So a misalignment of the c-axis of the core with the rod long axis is not possible except if stacking faults [114, 115] exist for example.

V.2 Polarization of the emission and geometrical parameters

We present now our measurement on various samples of dot-in-rods. We recall in Tab.V.2 the geometrical parameters of the investigated samples.

	Core diameter (nm)	Thickness (nm)	Length (nm)	Core diameter (% of thickness)	Aspect ratio
DR1	2	3.6	51	61%	14.2
DR2	3.3	4	22	82.5%	5.5
DR3.1	3.3	7	22	47%	3.1
DR3.3	3.3	7	58	47%	8.3
DR4	4.6	11	29	42%	2.6

Table V.2: Geometrical parameters of the investigated samples. *Core diameter (% of thickness) is the core diameter over shell thickness ratio.*

V.2.1 Measurements procedure

Preliminary to any polarization measurements we check if the chosen particle is single or not with an antibunching measurement. The measurement procedure was described in chapter II section II.1.2: a rotating half wave plate is placed in the nanocrystal fluorescence path together with a polarizing beam splitter. A fit of the obtained fluorescence time-trace with the Malus law gives the degree of linear polarization. Fluorescence time-traces exhibiting strong blinking are systematically removed from the analysis as the fitting can not be accurately determined.

In our polarization-resolved single particle measurements, dot-in-rods lie on glass and are observed through air by means of a $NA = 0.95$ air objective.

V.2.2 Measurements

Fig.V.2 shows the degree of polarization histograms obtained after measurements of 35 to 40 nanocrystals per sample. While Fig.V.2a presents samples with different core sizes, samples with the same core size but different lengths and different thicknesses are shown on Fig.V.2b and c respectively. Fig.V.2d is a table giving the polarization mean values and standard deviations obtained by fitting the histograms with a Gaussian distribution.

A first observation is that different samples have different mean values of polarization. It appears that for a given core size, the shell length and thickness are playing a role in defining the degree of linear polarization as it is clear on Fig.V.2b and c: a longer

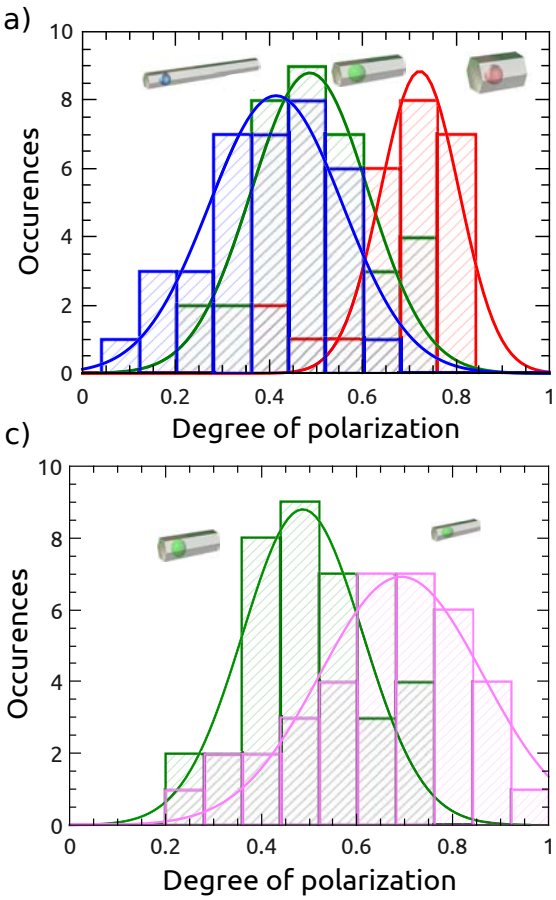

d)

	DR2	DR3.1	DR3.3
$\langle p \rangle$	0.69	0.50	0.65
σ	0.17	0.12	0.16

	DR1	DR4
$\langle p \rangle$	0.42	0.68
σ	0.13	0.12

Figure V.2: Histogram of the degree of linear polarization. *a) Blue: DR1, green: DR3.1, red: DR4. Different core diameters, lengths and thicknesses. b) Green: DR3.1, violet: DR3.3. Same cores, same thicknesses, different lengths. c) Green: DR3.1, pink: DR2. Same cores, same lengths, different thicknesses. d) Table of the polarization mean values $\langle p \rangle$ and standard deviation σ obtained for a Gaussian fit of the histograms.*

shell increases the degree of polarization while a thicker shell decreases the degree of polarization. The effect of the core size is also clear on Fig.V.2a: in this case all the geometrical parameters are changing, nevertheless we can see that bigger cores show a higher polarization degree even though the aspect ratio of the shell is decreasing.

A second observation is that our measurements shows large dispersions that we should try to explain in the following.

Considering the information given in the previous section V.1, let us summarize the points we should try to clarify in the discussion of the results:

- the role of the core size in defining the fine structure energy levels,
- the role of the shell geometry in defining the fine structure energy levels,
- the role of the shell geometry in the dielectric shape effect,
- the origin of the measurements dispersion.

V.3 Discussion

V.3.1 Comparison with the literature

For ensemble measurements in solution presented in section V.1.1, we can find in literature average values of emission polarization p of dot-in-rod samples in the same range of values than for our measurements:

- in reference [111], $p = 0.65$ for $d = 3.7$ nm, $l = 20$ nm and $t = 4.8$ nm and $p = 0.71$ for $d = 3.9$ nm, $l = 65$ nm and $t = 5$ nm,
- In reference [189], $p \simeq 0.5$ up to $p \simeq 0.7$ for different samples.

Reference [187] presents single particle measurements. They report measurements for 2 samples without mentioning the geometrical parameters, they found $p = 0.75 \pm 0.07$ and $p = 0.74 \pm 0.10$. We can see that our measurements give the same range of degree of polarization. The dispersions are slightly lower in reference [187] than for our measurements but confirm that for a given sample the degree of polarization fluctuates strongly from dot to dot.

Finally reference [189] studied different samples of dot-in-rods, its conclusion is that the degree of polarization depends on the ratio of the core diameter over the shell thickness. Our measurements is compatible with this statement when comparing DR2 and DR3.1 that have the same geometrical parameters except their thicknesses. However, the core diameter itself seems to play a major role in defining the polarization. We can see in Tab.V.2 that DR4 has a small core diameter over shell thickness ratio compared to DR1 but has a higher average polarization degree.

V.3.2 A model for the emission polarization

In this last part of the chapter we build a model to explain the measured degree of polarization that takes into account:

- the fine structure energy levels,
- the dielectric shape effect,
- the measurement configuration.

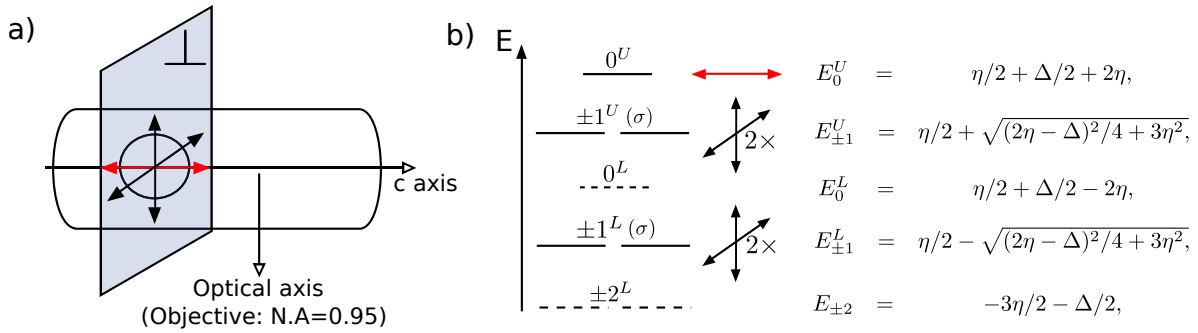

Figure V.3: Emission characteristics of dot-in-rods and polarization. *a) Experimental configuration: a single dot-in-rod is lying with its c axis perpendicular to the optical axis.* $\longleftrightarrow$ *represents the* $|0^U\rangle$ *transition along the c axis, while* $\perp$ *represents the* $|\pm 1^L\rangle$ *and* $|\pm 1^U\rangle$ *transitions oscillating in a plane perpendicular to the c axis. b) Fine structure energy level, the dashed transitions have zero oscillator strengths. The energy level splitting depends on the net splitting* Δ *between the heavy-hole and light-hole sub-bands, it depends also on* η *which represents the electron-hole exchange interaction. The level ordering presented can change depending on the values of* η *and* Δ*.*

Dipoles and polarization

Based on the elements given in section V.1, we assume for our model of the emission that the dot-in-rods are lying horizontally on the glass substrate and therefore the c axis is perpendicular to the optical axis as depicted on Fig.V.3a. There are 5 transitions that have non zero oscillator strengths:

- the $|0^U\rangle$ oscillating along the c axis and represented as $\longleftrightarrow$ on Fig.V.3a and b,
- the degenerate $|\pm 1^L\rangle$ oscillating in the plane ($\perp$) perpendicular to the c axis and represented as $\perp$ on Fig.V.3a and b. Each one is a 2D dipole corresponding to two perpendicular 1D dipoles, thus the representation as $\perp$,
- the degenerate $|\pm 1^U\rangle$ oscillating in the plane ($\perp$) perpendicular to the c axis and represented as $\perp$ on Fig.V.3a and b. Each one is a 2D dipole corresponding to two perpendicular 1D dipoles, thus the representation as $\perp$.

Let us start from a ideal experimental case. In the configuration shown on Fig.V.3a (c axis perpendicular to the optical axis) and in the limit of an objective with a numerical aperture $N.A. \to 0$, the objective collects from the 2D transitions a field that is strictly perpendicular to the c axis (the horizontal contribution of the 2D dipole), while it collects from the 1D transition a field strictly aligned along the c axis. If we assume that the 1D transition has the strongest intensity of emission, then it defines the maximum of intensity while rotating the half wave plate placed in the photoluminescence path and:

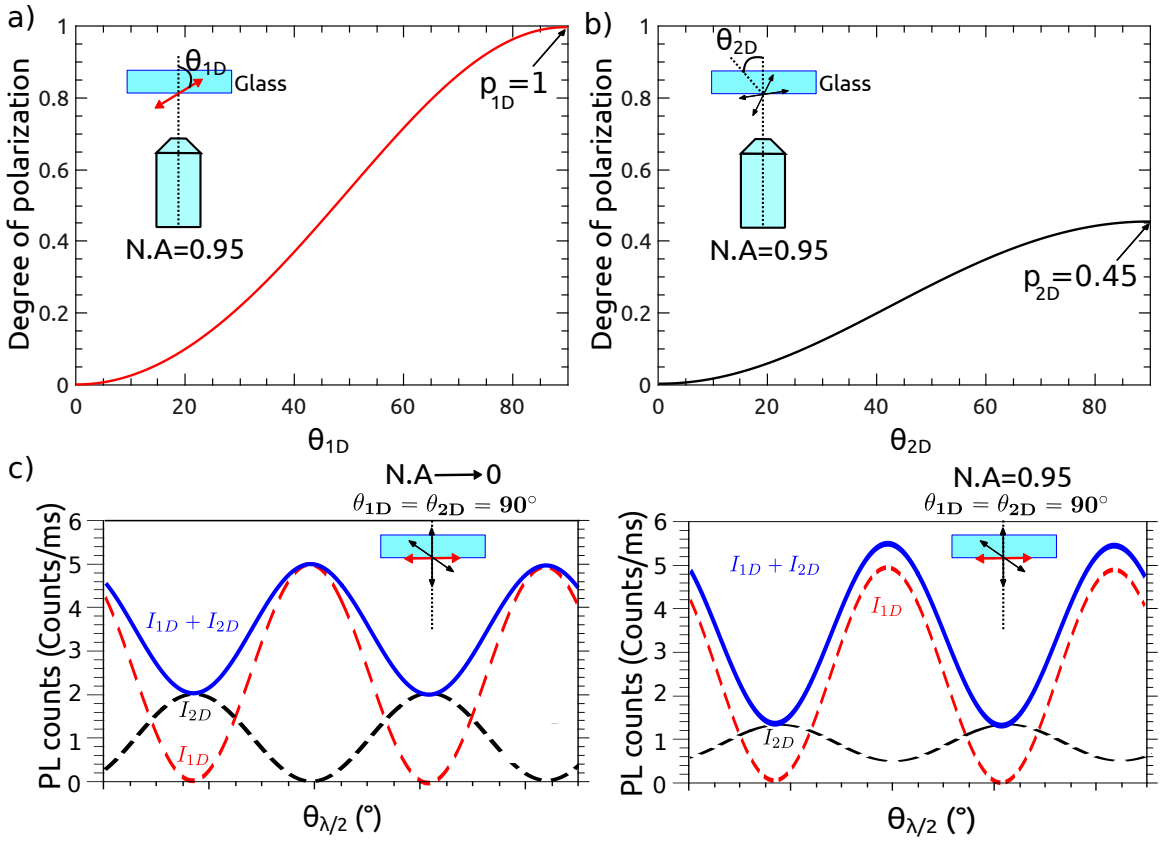

Figure V.4: Calculations of the polarization degree versus the angle of a 1D and 2D dipoles with the optical axis for an objective with N.A. = 0.95 and schematic examples of polarization curves. *a) 1D dipole lying on glass with an angle θ_{1D} compared to the optical axis. b) 2D dipole lying on glass with an angle θ_{2D} between its axis and the optical axis. We consider only dot-in-rods lying horizontally on the glass substrate, therefore $\theta_{1D} = \theta_{2D} = 90°$ and $p_{1D} = 1$ while $p_{2D} = 0.45$. c) Schematic example of polarization curves function of the half wave plate angle $\theta_{\lambda/2}$ for and objective with a zero numeriacal aperture (left) and $N.A. = 0.95$ (right).*

$$p_{N.A\to 0} = \frac{I_{max} - I_{min}}{I_{max} + I_{min}} = \left|\frac{I_{1D} - I_{2D}}{I_{1D} + I_{2D}}\right| \tag{V.5}$$

with I_{1D} the intensity of the 1D transition and I_{2D} the intensity of the 2D transitions. According to reference [187] the 1D transition is the strongest because a polarization aligned with the dot-in-rod long axis direction is measured in polarization resolved measurement combined with AFM images. We nevertheless add absolute values to Eq.V.5 to generalize it to the cases for which the 1D transition has not the strongest intensity. We present a limiting case on Fig.V.4c with $N.A. \to 0$ (left) for the configuration presented in Fig.V.3a: $\theta_{1D} = \theta_{2D} = 90°$. Both types of transitions have perfect degree of polarization $p = 1$ in this case, it gives a total polarization curve in blue with $p_{N.A=0} = 3/7 \simeq 0.43$.

Let us now consider the effect of the real experimental configuration, the non zero numerical aperture of the objective and the fact that the dipole is lying on a glass plate. For $N.A. = 0.95$ and dipoles on a glass substrate ($n = 1.46$) surrounded by air ($n = 1$), we performed calculations following references [141, 195] to obtain the degree of polarization for 1D and 2D transitions. The results are presented on Fig.V.4a and b. We can see on Fig.V.4a that a 1D transition perpendicular to the optical axis ($\theta_{1D} = 90°$) has a measured degree of polarization of $p_{1D} = 1$. A non zero numerical aperture decreases the contrast of the polarization curve because it mixes different directions of emission as explained in chapter II. However, for a 1D dipole, a $N.A$ of 0.95 is not enough to reduce the contrast of the polarization curve as $p_{1D} = 1$. Therefore, our setup scheme has no limitation for the degree of polarization: a 1D dipole perpendicular to the optical axis will show a perfect degree of linear polarization. This is not the case for 2D transitions. A 2D transition has a maximum value of polarization of $p_{2D} = 0.45$ for $\theta_{2D} = 90°$. The measured degree of polarization for dot-in-rods are often above 0.45. This means that the 1D dipole must be the strongest transition. The limiting case presented on Fig.V.4c left with $N.A. \to 0$, becomes slightly different for $N.A. = 0.95$ and is presented on Fig.V.4c right. The polarization degree of the 2D emission is now $p_{2D} = 0.45$, while the polarization degree of the 1D emission is unchanged because $p_{1D} = 1$. We keep the same intensities for the 1D and 2D dipoles, so $I_{1D} = 5$ counts/ms and $I_{2D} = 2$ counts/ms, it gives $p_{N.A=0.95} \simeq 0.59$. This value is higher than in the $N.A = 0$ case because the degree of polarization of the 2D transition has been heavily reduced.

We can then generalize Eq.V.5 by including the experimental configuration. Knowing that the minimum intensity I_{min} and maximum intensity I_{max} of a polarization curve with a degree of polarization p are linked to the intensity of the source $I = I_{min} + I_{max}$ by $I_{min} = \frac{1-p}{2} I$ and $I_{max} = \frac{1+p}{2} I$, we have that:

$$\begin{aligned}
p_{N.A} &= \frac{I_{max} - I_{min}}{I_{max} + I_{min}}, \\
&= \left| \frac{(I_{max,1D} + I_{min,2D}) - (I_{min,1D} + I_{max,2D})}{(I_{max,1D} + I_{min,2D}) + (I_{min,1D} + I_{max,2D})} \right|, \\
&= \left| \frac{(\frac{1+p_{1D}}{2} I_{1D} + \frac{1-p_{2D}}{2} I_{2D}) - (\frac{1-p_{1D}}{2} I_{1D} + \frac{1+p_{2D}}{2} I_{2D})}{(\frac{1+p_{1D}}{2} I_{1D} + \frac{1-p_{2D}}{2} I_{2D}) + (\frac{1-p_{1D}}{2} I_{1D} + \frac{1+p_{2D}}{2} I_{2D})} \right|, \\
&= \left| \frac{p_{1D} I_{1D} - p_{2D} I_{2D}}{I_{1D} + I_{2D}} \right|,
\end{aligned} \tag{V.6}$$

p_{1D} and p_{2D} depend on the experimental configuration and are equals to 1 and 0.45 respectively in our case. Eq.V.6 is valid only for 2D transitions oscillating in a plane orthogonal to the 1D transition axis. Nevertheless the orientations θ_{1D} and θ_{2D} of the dipoles compared to the optical axis do not necessarily have to be fixed as in Fig.V.3a: $\theta_{1D} = \theta_{2D} = 90°$, but a change in θ_{1D} and θ_{2D} values has to be taken into account because p_{1D} and p_{2D} are depending on these angles.

Fig.V.5 presents the evolution of p_{1D} and p_{2D} with the objective numerical aperture. We observe that a high numerical aperture gives a larger discrepancy between p_{1D} and p_{2D}. Given our experimental configuration, it is then more suitable to use a high numerical aperture in order to probe the strength of the 1D transition compared to the 2D transitions.

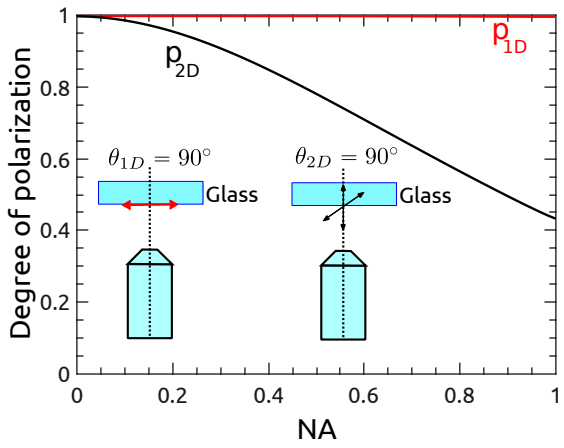

Figure V.5: Degree of polarization versus numerical aperture for a 1D dipole and a 2D dipole with $\theta_{1D} = \theta_{2D} = 90°$.

Fine structure and polarization

To complete our model, we have now to determine the emission intensities of the 1D dipole and 2D dipoles, I_{1D} and I_{2D}. The fine structure energy levels are recalled on Fig.V.3b, their energy and ordering depend on the factor η that comes from the electron-hole exchange interaction and on the net-splitting Δ.

The term η that describes the Coulombian interaction between holes and electrons is inversely proportional to the volume of the nanocrystal for uncapped CdSe nanocrystals [32].

The net-splitting Δ is the heavy-hole/light-hole sub-bands energy splitting. There are commonly two contributions to the net-splitting, the intrinsic splitting Δ_{int} and the shape splitting Δ_{sh} [32]. We consider an additional contribution that we will call the strain splitting Δ_{strain} [22].

The net splitting Δ is then expressed as:

$$\Delta = \Delta_{int} + \Delta_{sh} + \Delta_{strain},$$

with:

- Δ_{int} = 23 meV [32] for CdSe nanocrystals. It is the splitting due to the crystal field induced by the hexagonal lattice structure that lifts the degeneracy of the heavy-holes and light-holes sub-bands (see Fig.I.2).
- If the nanocrystal is slightly elongated along the c axis for example (prolate nanocrystal), then the heavy-holes and light-holes subbands splitting needs to be corrected by adding a factor Δ_{sh} that depends on the ellipticity of the nanocrystal.
- Strain forces [22, 196] can modify the band structure of a crystal. Reference [22] reports a strain contribution to the net-splitting in CdSe/CdS dot-in-plates (see chapter I) of Δ_{strain} = +40 meV because of the growth of the anisotropic CdS shell upon the CdSe core.

The net-splitting Δ and electron hole interaction η define the fine structure states, their energy and their oscillator strength. Let N be the occupancy of a state at a given temperature, and f its relative oscillator strength[4], then $I = Nf$ is the normalized intensity of a state, its emission probability. For the 1D emission we have:

$$I_{1D} = I_{0^U} = N_{0^U} f_{0^U}, \tag{V.7}$$

and for the 2D emission:

$$I_{2D} = I_{\pm 1^U} + I_{\pm 1^L} = 2 \times \frac{1}{R_e}(N_{\pm 1^U} f_{\pm 1^U} + N_{\pm 1^L} f_{\pm 1^L}), \tag{V.8}$$

with a factor of 2 because of the degeneracy of the 2D emission states and $\frac{1}{R_e}$ to take into account the dielectric shape effect that inhibits the transitions in the plane perpendicular to the c axis.

Depending on the value of the parameters η and Δ, the oscillator strengths [32] of the different energy levels will be modified as well as their energy and so occupancies. Therefore I_{1D}, I_{2D} and consequently the measured polarization are functions of the energy parameters η and Δ. We propose in the following to study the polarization as a function of these unknown energy parameters η and Δ following the model presented above.

[4]Oscillator strength of the state normalized by the sum of the oscillator strengths of all the states involved in the emission process.

V.3.3 Simulations of the emission polarization

Range of energy parameters

In this section we define in which range of values η and Δ are physically bounded.

Following reference [32] we computed the value of η as a function of the core diameter for uncapped CdSe nanocrystals on Fig.V.6a. η is proportional to $1/d^3$, with d the CdSe nanocrystals diameter [32]. The electron-hole interaction is directly connected to the confinement and overlap of the charges wavefunctions. For CdS capped nanocrystals, as the electron wavefunction spreads inside the shell owing to the small valence band offset between CdSe and CdS, we expect smaller values of η than in the uncapped CdSe case. This has been experimentally demonstrated for spherical CdSe/CdS nanocrystals [131] and CdSe/CdS dot-in-rods [119, 122, 197] by changing the CdS shell thickness and determining the fine structure energy splitting at cryogenic temperatures. Therefore, for a given core radius, we can search for η values between 0 meV and η_b the value for bare CdSe nanocrystals, this corresponds to the blue area under the curve on Fig.V.6a.

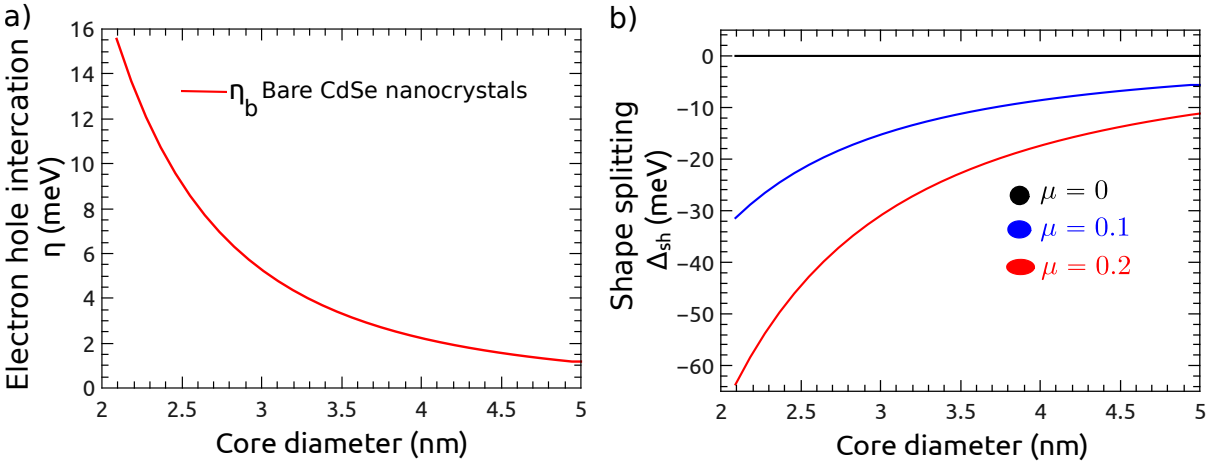

Figure V.6: Evolution of the electron hole interaction η and shape splitting Δ_{sh} with the CdSe core diameter. *a) Red line: electron hole interaction η versus the core diameter for uncapped CdSe nanocrystals calculated from reference [32]. For CdS capped nanocrystals (blue area) the parameter η is smaller and has consequently an upper bound corresponding to the uncapped case and a lower bound that is nil. b) Shape splitting Δ_{sh} against the core diameter for various ellipticities μ, black line $\mu = 0$, blue line $\mu = 0.1$ and red line $\mu = 0.2$.*

On fig.V.6b, we computed the dependency of the shape splitting Δ_{sh} on the core diameter for different values of the ellipticity μ of the core according to reference [32]. The ellipticity is defined in reference [32] as $\mu = c/a - 1$ with c the c axis length and a the perpendicular axis length. $\mu = 0$ (black line) corresponds to spherical dots ($\Delta_{sh} = 0$), $\mu = 0.1$ (blue line) and $\mu = 0.2$ (red line) correspond to prolate dots (elongated along the c axis). For prolate particles, Δ_{sh} has a superior bound that corresponds to the spherical

CdSe case: $\Delta_{sh} = 0$. Also we can see that if there is an ellipticity, Δ_{sh} decreases with decreasing core diameters.

The net-splitting is $\Delta = \Delta_{int} + \Delta_{sh} + \Delta_{strain}$. $\Delta_{int} = 23$ meV for CdSe particles. The strain induced by the anisotropic growth of the CdS shell adds a negative contribution to the net-splitting as we are in the converse situation[5] with respect to dot-in-plates [22] for which a positive Δ_{strain} is observed of 40 meV. A negative value of the net-splitting Δ can therefore be reached, this implies a reordering of the energy levels compared to what is presented on Fig.V.3b as it is the case for CdSe nanorods.

The uncapped spherical CdSe dots case

We briefly describe what we expect for uncapped spherical CdSe dots with $\Delta = \Delta_{int} = 23$ meV on Fig.V.7. The parameter η evolves with the core diameter as described on Fig.V.6a, red line $\eta = \eta_b$. The energy levels as a function of the core diameter are presented on Fig.V.7a. This leads to flat emission probabilities with the core diameter for the 2D dipoles and 1D dipole, with the following values: $I_{2D} \simeq 80\%$ and $I_{1D} \simeq 20\%$. A poor degree of polarization $p \simeq 20\%$ is found according to Eq.V.6 with $p_{1D} = 1$ and $p_{2D} = 0.45$.

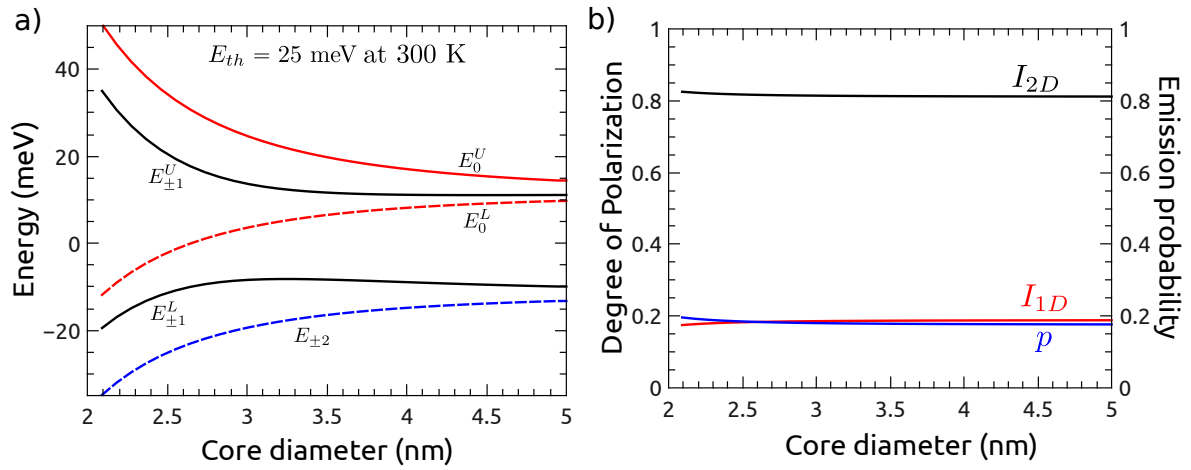

Figure V.7: Energy levels and degree of polarization for a bare spherical CdSe core. *$\Delta = \Delta_{int} = 23$ meV, $\eta = \eta_b$ follows the curve in Fig.V.6a. a) Energy levels versus core diameter. b) Degree of polarization p (blue line) and radiative probabilities I_{1D} (red line) and I_{2D} (black line) versus the core diameter.*

[5]CdSe/CdS dot-in-plates have their shell that grows in the plane perpendicular to the c-axis, while dot-in-rods have their shell that grows in the c-axis direction.

The spherical core/shell case

To model the spherical core/shell nanocrystals, we consider a broader range of possible values for η and Δ independently of the core diameter value. We take $\eta \in [0; 16]$ meV according to the range of values we determined on Fig.V.6a. We also add the possibility of having prolate CdSe core, $\Delta = \Delta_{int} + \Delta_{sh}$ is expected to be in $[-40; 23]$ meV according to the values of Δ_{sh} found in Fig.V.6b and $\Delta_{int} = 23$ meV. No contribution from the strain is expected as the shell grows isotropically.

We recall on Fig.V.8a and c respectively the level ordering for a negative and a positive net-splitting Δ. When the whole parameter space is spanned, we can see that the degree of polarization evolves from 0 to 0.4 in Fig.V.6b. For a fixed η, it starts from a value of roughly 0.2 at $\Delta = \Delta_{int} = 23$ meV, with $p_{2D}I_{2D} > p_{1D}I_{1D}$ in Eq.V.6 due to the position of the energy levels (see Fig.V.8c). Then it decreases towards $p = 0$ for $\Delta \simeq 4$ meV as the 2D dipoles emission gets weaker and the 1D dipole emission stronger due to a smaller energy gap between the levels. Finally, for negative values of Δ, p increases as the 1D emission gets stronger because of the swapping of level order (see Fig.V.8a) .

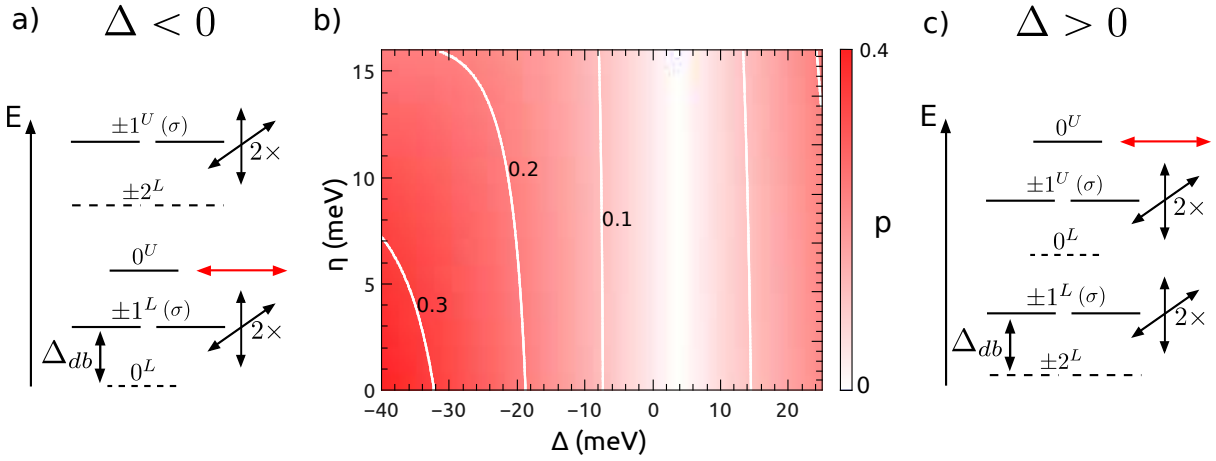

Figure V.8: Degree of polarization versus η and Δ for a spherical CdS shell and fine structure level ordering as a function of the net-splitting Δ. *a) Fine structure level ordering for a negative net-splitting. b) Degree of polarization versus η and Δ for a spherical CdS shell. c) Fine structure level ordering for a positive net-splitting. Δ_{db} is the dark-bright exciton splitting energy, difference of energy between the optically inactive lowest state and the first optically active state.*

A polarization degree that evolves from 0 to 0.4 is in good agreement with spherical CdSe/ZnS single particle polarization measurements [17,49]. In our calculation we do not consider a random orientation of the dipole transitions compared to the optical axis, this is however typically the case when dealing with spherical shell particles. Nevertheless, as one can notice on Fig.V.4, no orientation of the dipoles compared to the optical axis can yield a higher degree of polarization than in the configuration $\theta_{1D} = \theta_{2D} = 90°$ because in

this case the ratio p_{1D}/p_{2D} is maximized. High degree of polarization cannot be observed with CdSe dots embedded inside spherical shells.

The dot-in-rod case

Now let us consider a rod-like shell around a spherical core. One difference with the previous case of spherical shell is that the oscillator strengths of the 2D dipoles are inhibited by the dielectric shape effect by a factor $1/R_e$ implying an enhanced emission of the 1D dipole with respect to the previous case. The values of R_e calculated thanks to Eq.V.4 for the different samples are given in Tab.V.3.

	DR1	DR2	DR3.1	DR3.3	DR4
R_e	3.2	2.8	2.2	3	1.9

Table V.3: Dielectric factor $\mathbf{R_e}$***.***

A second difference with the spherical case is that the anisotropy of the shell could induce an anisotropic strain on the core. Reference [22] reports $\Delta_{strain} = +40$ meV of extra net-splitting because of strain effects in dot-in-plates. As explained earlier, we expect the converse effect (negative values of Δ_{strain}) in our case as the growth of the shell is along the c axis for dot-in-rods and not perpendicularly to the c axis as in dot-in-plates. Therefore we allow Δ to span a broader range of negative values than in the spherical shell case: $\Delta \in [-100; 23]$ meV.

Fig.V.9 presents the polarization curve as a function of η and Δ for the different dot-in-rods studied. On each graph, the solid black line represent the mean value of p measured for each sample while the blue area represent the range of possible p values (standard deviation of the measured distribution) limited by $\eta < \eta_b$, η_b being the electron hole interaction in the case of an uncapped CdSe core as derived in Fig.V.6a.

Mean values We first comment the results focusing on the mean values of polarization (black lines in Fig.V.9). According to the mean value of polarization, given the limitation for each sample of η to η_b, we see that we can narrow the range of the allowed values of Δ. However, the uncertainty on η is still too large to obtain any information on the energy levels of each sample.

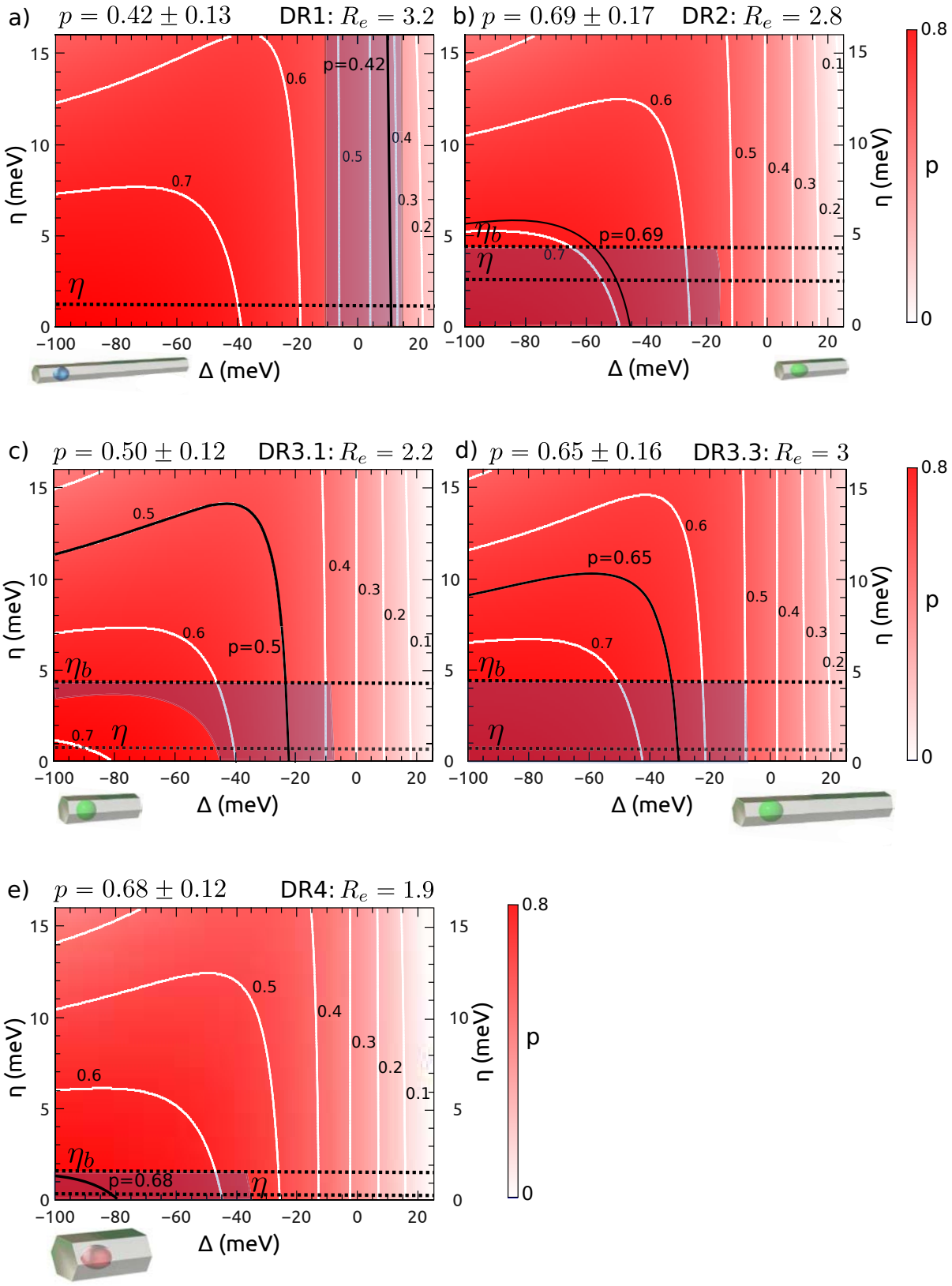

Figure V.9: Degree of polarization versus η and Δ for a rod-like CdS shell. *a) DR1. b)DR2. c)DR3.1. d)DR3.3. e)DR4. The areas in blue correspond to the measured value of polarization with its dispersion for each sample together with a limitation for η to its maximum value η_b calculated for core only particles and shown on Fig.V.6a. We also report the value of η expected from calculations according to reference [197] and shown in Tab.V.4.*

We can further reduce the parameter space. Indeed, according to the literature, we should have $\eta << \eta_b$ because of the electron delocalization in the CdS shell. To estimate the value of η we can use the value of the dark-bright exciton splitting Δ_{db}. The dark-bright exciton splitting is the difference of energy between the lowest fine structure level that is always optically inactive ($|\pm 2\rangle$ or $|0^L\rangle$) and the first optically active level ($|\pm 1^L\rangle$): see Fig.V.8a and c. It can be measured at cryogenic temperature. For a normal level ordering ($\Delta > 0$):

$$\Delta_{db} = E^L_{\pm 1} - E_{\pm 2} = 2\eta + \Delta/2 - \sqrt{(2\eta - \Delta)^2/4 + 3\eta^2}, \tag{V.9}$$

while for a level ordering with $\Delta < 0$:

$$\Delta_{db} = E^L_{\pm 1} - E^L_0 = 2\eta - \Delta/2 - \sqrt{(2\eta - \Delta)^2/4 + 3\eta^2}. \tag{V.10}$$

According to Fig.V.9, we have that $|\Delta| \gg \eta$, except for DR1. If $|\Delta| \gg \eta$, Δ_{db} can be approximated as η:

$$|\Delta| \gg \eta \Longrightarrow \Delta_{db} \simeq \eta. \tag{V.11}$$

For CdSe/CdS, spherical particles, reference [131] reports Δ_{db} ranging from 0.1 meV to 2 meV for a core diameter of 3 nm and different shell thicknesses while the bare CdSe model in Fig.V.6a gives $\eta \simeq 6$ meV. More interestingly, for CdSe/CdS dot-in-rods, Biadala et al. [197] measured Δ_{db} for various samples of dot-in-rods. The authors demonstrate that Δ_{db} does not depend on the core radius[6] or the shell length[7] but rather on the shell thickness[8]. They demonstrate a quadratic dependence of the bright-dark exciton energy splitting on the inverse CdS rod thickness t:

$$\Delta_{db} \propto 1/t^2 \tag{V.12}$$

This results can be explained by the fact that the electron is delocalized inside the shell, the long axis of the rod does not confine the electron wavefunction because its dimension is typically greater than the Bohr radius of the exciton. Consequently, the dark-bright splitting and electron hole interaction η do not depend on the volume anymore, but rather on the transverse area of the rod that realizes the confinement.

According to Eq.V.12 we can calculate the expected Δ_{db} for our dot-in-rods, reference [197] gives the proportionality constant in Eq.V.12 with its measurement. We can then deduce the value of η expected using $\Delta_{db} \simeq \eta$, except for DR1. Given that we have η we

[6]Measurements with core diameters ranging from 2.5 nm to 3.7 nm were realized in reference [197].
[7]Measurements with shell lengths ranging from 20 nm to 60 nm were realized in reference [197].
[8]Measurements with shell thicknesses ranging from 3 nm to 6 nm were realized in reference [197].

obtain Δ according to the mean polarization value using Fig.V.9. The values of η and Δ are reported in Tab.V.4.

For the case of DR1, we already have $\Delta_{DR1} \simeq 11$ meV using the average value of polarization in Fig.V.9a. We can also calculate Δ_{db} according to Eq.V.12, and from that calculate η using Eq.V.9. We found $\eta_{DR1} = 1.3$ meV.

	DR ref. [197]	DR1	DR2	DR3.1	DR3.3	DR4
t (nm)	5.3	3.6	4	7	7	11
Δ_{db} (meV)	1.5	3.3	2.6	0.9	0.9	0.3
η (meV)		1.3	2.6	0.9	0.9	0.3
Δ (meV)		11	−49	−22	−30	−82

Table V.4: Energy parameters η (meV) and Δ (meV). *Δ_{db} is calculated according to reference [197]: $\Delta_{db} \propto 1/t^2$.*

DR1 has a small core diameter ($d = 2$ nm), ellipticity should have a strong impact on the value of Δ according to Fig.V.6b. However, taking into account the fact that Δ_{DR1} is not so far from $\delta_{int} = 23$ meV, we can conclude that neither ellipticity nor strain should play a major role in defining the fine structure of this sample. Also, Δ_{DR1} is positive implying a regular level ordering.

DR2, DR3.1, and DR3.3 have the same core, they were synthesized from the same seeds. They should have the same ellipticity. Then Δ_{DR2}, $\Delta_{DR3.1}$ and $\Delta_{DR3.2}$ should only differ because of the strain effects. From Tab.V.4, we find $\Delta_{DR2} = -49$ meV, $\Delta_{DR3.1} = -22$ meV and $\Delta_{DR3.2} = -30$ meV. These values are compatible with a strain effect as we expect that:

- the strain induced by the shell should increase when increasing the length of the shell for a given thickness. This is the case when going from DR3.1 to DR3.3, the strain increases and Δ increases in absolute value.
- The strain induced by the shell should increase when decreasing the thickness of the shell for a given length. This is the case when going from DR3.1 to DR2, the strain increases and Δ increases in absolute value.

Finally DR4 shows the largest value of net-splitting: $\Delta_{DR4} = -82$ meV. One explanation could be that the core of this sample has a strong ellipticity. Large cores usually have strong ellipticities [3, 189]. Also, we have seen that DR1 with a very small core, despite its large aspect ratio, has a net-splitting value indicating a negligible effect of strain. This suggests that the strain effects might depend on the core diameter, strain increasing when increasing the core diameter such that DR1 shows no signs of strain induced energy splitting while DR4 energy splitting is strongly impacted by strain.

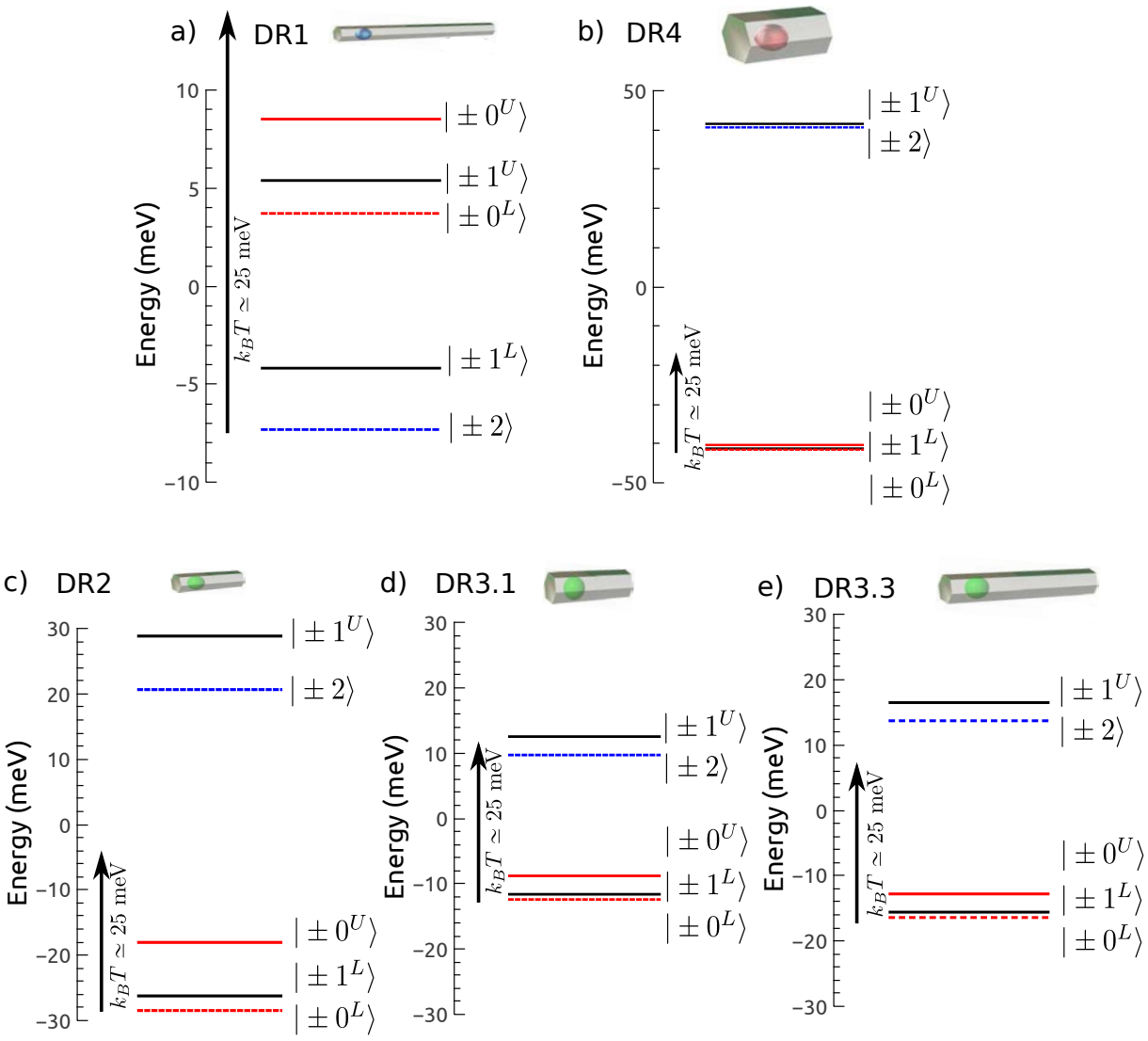

Figure V.10: Band edge exciton fine structure deduced from the polarization measurements. *a) DR1. b) DR4. c) DR2. d) DR3.1. e) DR3.3. Thermal energy at* 290 *K is* 25 *meV. The careful reader should notice that the scale is the same for c, d and e but different scales are used for a and b.*

Fig.V.10 shows the calculated energy levels for the different samples using the values of η and Δ from Tab.V.4. Only DR1 displays a spherical-like (normal) level ordering with the lowest state being $|\pm 2\rangle$. This suggests that there should be a transition between a spherical-like bandedge exciton symmetry to a rod-like (prolate) bandedge exciton symmetry for dot-in-rods when increasing the core size. Reference [119] reports a spherical-like bandedge exciton symmetry for dot-in-rods with core diameter of $d = 3.2$ nm, shell length $l = 39.8 \pm 1.7$ nm and thickness $t = 4.3 \pm 0.5$ nm. These dot-in-rods are very similar to DR2. The transition might depend on the core seeds and synthesis parameters.

The case of DR2, DR3.1 and DR3.3 is interesting because it reveals how one can tune

the fine structure energy level by engineering the shell geometry. We can see that increasing the shell thickness (DR2↦DR3.1) leads to a smaller splitting of the fine structure because of a reduced electron hole interaction and net-splitting (in absolute value). The converse effect arises when increasing the shell length (DR3.1↦DR3.3).

Finally, DR4 displays a significant splitting of its fine structure that explains its high degree of polarization, one of the 2D dipole ($|\pm 1^U\rangle$) is poorly populated at room temperature and does not contribute to the 2D emission.

Dispersion of the measurements Finally, let us comment the dispersion of the polarization measurements.

A first explanation of the dispersion of the measurements is the size inhomogeneity of the samples. We have seen in the previous chapters that for a given sample different particles exhibit different lifetime and consequently different electronic structures. Also, defects in the crystal structure might induce a deviation of the electronic properties from the theoretical model, stacking faults occurring along the growth direction of nanorods have been reported to modify the optical anisotropy [188, 190] for example.

One could think also about the angles between the optical axis and the c-axis. In our model, we supposed that the c-axis was perpendicular to the optical axis based on TEM images. The glass coverslip has a certain roughness such that small angles between the c axis and the optical axis might be present. As the ratio p_{1D}/p_{2D} decreases when the angle between the c axis and the optical axis gets different from 90° as visible on Fig.V.4a and b, this should lower the measured degree of polarization. However it should not play a major role as p_{1D} and p_{2D} are almost insensitive to small deviations around 90° (cf Fig.V.4a and b).

Conclusion

In this chapter we have presented single particle polarization measurements on various samples of dot-in-rods. We proposed a model to explain the measurements that takes into account the fine structure of the particles, the dielectric shape effect of the shell as well as the setup configuration. As demonstrated, the setup configuration plays a major role in defining the measured values of polarization and has to be included in the model. Conversely to spherical CdSe/CdS particles, the fixed orientation of the c-axis compared to the optical axis renders the analysis of the polarization easier for dot-in-rods.

Compared to purely spherical particles, the possibility to reach a high degree of polarization for dot-in-rods is primarily given by the dielectric shape effect, due to the anisotropy of the shell, that confers to the 1D transition a stronger oscillator strength.

Moreover, the fine structure is of the utmost importance. An inversion of the bandedge exciton symmetry from a spherical-like behavior to a rod-like symmetry is necessary to reach high polarization degrees. This inversion of symmetry is certainly a combination of two factors, one being the prolate nature of the core and the other the strain anisotropy applied by the anisotropic shell growth on the core.

Chapter VI
Coupling nanocrystals to devices: towards integrated nanophotonics

Introduction

In this chapter we describe experiments in which we couple CdSe/CdS dot-in-rods with various systems. The systems we present try to tackle the difficult problem of efficiently orientating/positioning a single light emitter, and exciting it with nanodevices. These are common subjects of interest for all single nanoscale light emitters.

Here we first present the realization of a hybrid system composed of a ZnO nanowire coupled to a single CdSe/CdS dot-in-rod. We show that using the nanowire as a waveguide or as an active material emitting and guiding its own fluorescence light we can efficiently excite a dot-in-rod. In the second part of the chapter we present another experiment and demonstrate the successful alignment of dot-in-rods inside controlled linear defects of a liquid crystal.

VI.1 Coupling nanocrystals to ZnO nanowires

In this section we are addressing a key point of integrated photonics [198, 199]: the integration of nanoemitters with all-optical buses towards the efficient generation and transfer of single photons. Semiconductor nanowires, synthesized by top-down or bottom-up methods, have been applied in nanophotonics as linking blocks for optical circuits due to their high-quality sub-wavelength waveguiding features [200–202]. The integration of quantum dots and nanowires systems has attracted increasing interests in the new field of quantum photonics, as a 1D nanowire can favour the excitation, extraction and transfer of single photons emitted by a quantum dot nanostructure [93, 203–205]. The so-called photonic wire is a good example of such system [206]. Most works emphasizes on the collection of light, while the issue of effectively addressing a nanoscale emitter is often not

discussed. In the following we present a new strategy to realize a localized excitation of a dot-in-rod with a nanowaveguide made of a ZnO nanowire. ZnO nanowires have a wide bandgap of 3.3 eV, larger than our dot-in-rods; together with the large absorption cross section of CdSe/CdS dot-in-rods they constitute a good system to study such a localized excitation.

This experiment was realized in collaboration with the Laboratoire de Nanotechnologie et d'Instrumentation Optique[1] of the Université de technologie de Troyes.

VI.1.1 System description

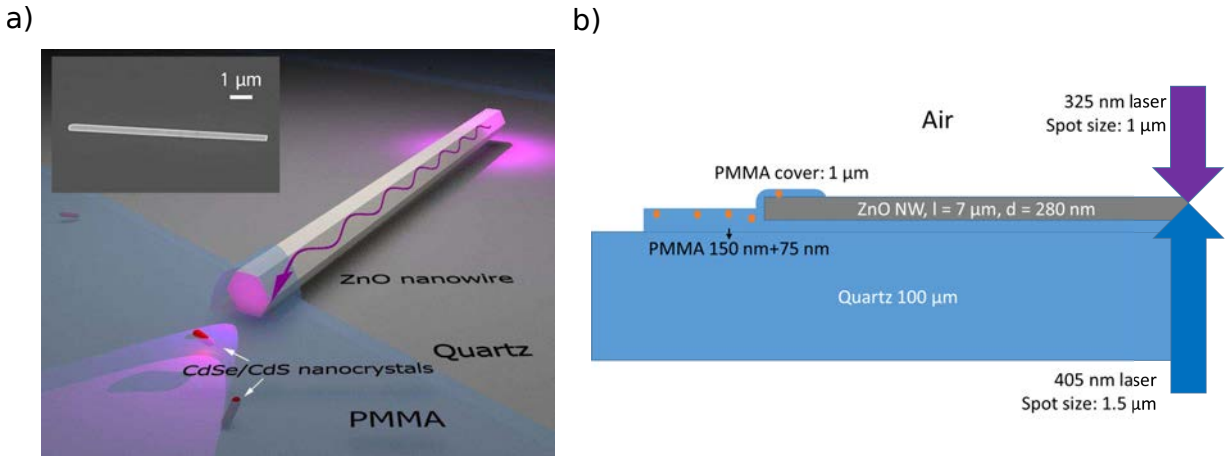

Figure VI.1: Schematics of the ZnO nanowire CdSe/CdS dot-in-rod coupled system. *a) Sketch of the system with in inset a scanning electron microscope image of a ZnO nanowire (7 − 8 µm in length and 260 − 300 nm in diameter). The nanowire is lying on a quartz substrate, one of its tip in a region without dot-in-rods for the excitation by a laser, the other tip in a region containing dot-in-rods. b) Sketch of the two possible excitation schemes. Either we excite the nanowire from the bottom of the sample with a 405 nm laser (below its bangap) or we excite from above the sample with a 325 nm laser (above the ZnO bandgap).*

Fig.VI.1a presents a schematic of the system where a ZnO nanowaveguide excited at one of its tip guides light towards a dot-in-rod situated at the other nanowire tip. The ZnO nanowires are grown by metal organic chemical vapor deposition (MOCVD) [207]. Using this technique, ZnO nanowires with a high crystallinity, fairly uniform diameters and almost defect-free surfaces [207] can be fabricated. Due to their high refractive index[2] [208], these ZnO nanowires are ideal for light confinement and guiding in a wide wavelength range [209], which includes its own near-UV photoluminescence around 380 nm. Their dimensions can be controlled during the fabrication process and the nanowires used in this experiment are 7−8 μm in length and 260−300 nm in diameter,

[1] http://lnio.utt.fr/fr/index.html
[2] $n_{ZnO} = 2.2$ to 2.5 for the 370 to 410 nm range.

as observed under a scanning electron microscope (inset of Fig.VI.1a). Concerning the dot-in-rods, we decided to use the sample DR3.3 with a shell of 58 nm long and 7 nm thick. They display the highest absorption cross section (together with DR4) with a fairly good single photon emission statistics. This way, we maximize the chance of exciting the emitter and we can also measure a high degree of antibunching to prove that we are exciting a single emitter.

PMMA[3] stripes with and without nanocrystals are fabricated using electron beam lithography on top of dispersed individual nanowires deposited on a quartz plate as depicted on Fig.VI.3a. The sample is placed on top of the confocal microscope and two excitation schemes can be employed: the ZnO nanowire can be excited either below its bandgap at 405 nm or above its bandgap at 325 nm. In the following we call this two excitation schemes passive and active excitation respectively. In the first case the nanowire passively excites the nanocrystal by guiding the 405 nm light while in the second case the nanowire excites the nanocrystals with its own photoluminescence.

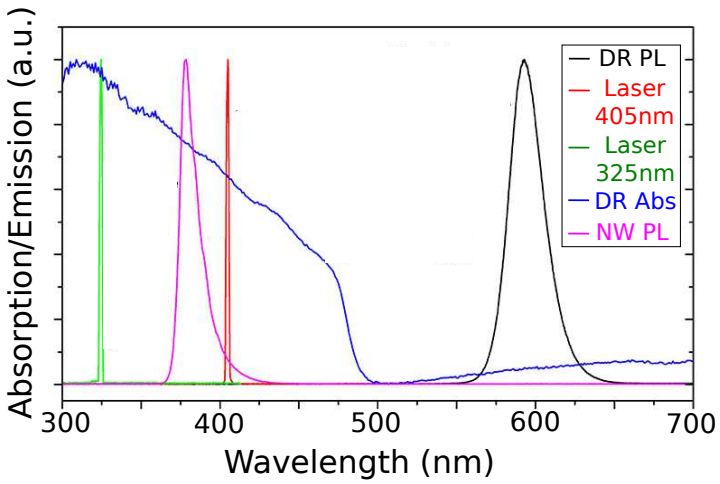

Figure VI.2: Spectra of the different elements of the coupled system. *The nanowire emission spectrum (pink) covers the wavelength from* 370 *to* 400 *nm. The broad DR absorption (blue) implies that it is easy to excite with the different sources.*

Fig.VI.2 presents the spectra of the different elements involved in the experiment. The ZnO nanowire emission spectrum (pink curve), the absorption/emission spectrum of the CdSe/CdS nanocrystals (blue/black curve) together with the excitation laser line are displayed. The broad absorption spectrum of the dot-in-rod ensures that it can be excited by the lasers and also by the nanowire photoluminescence.

Fig.VI.3a top shows a wide field reflection image of a single ZnO nanowire crossing the border between a stripe containing nanocrystals and one without nanocrystals. By filter-

[3]PMMA: Poly(methylmethacrylate) is a transparent polymer often used to cover nanocrystals samples.

ing out the illumination light, the photoluminescence of a single CdSe/CdS nanocrystal at the extremity of the nanowire (Fig.VI.3a bottom) is visible. A $g^{(2)}(0)$ measurement presented on Fig.VI.3b confirms the unicity of the dot-in-rod. The coupling between this specific nanowire and the single nanocrystal is studied in the following.

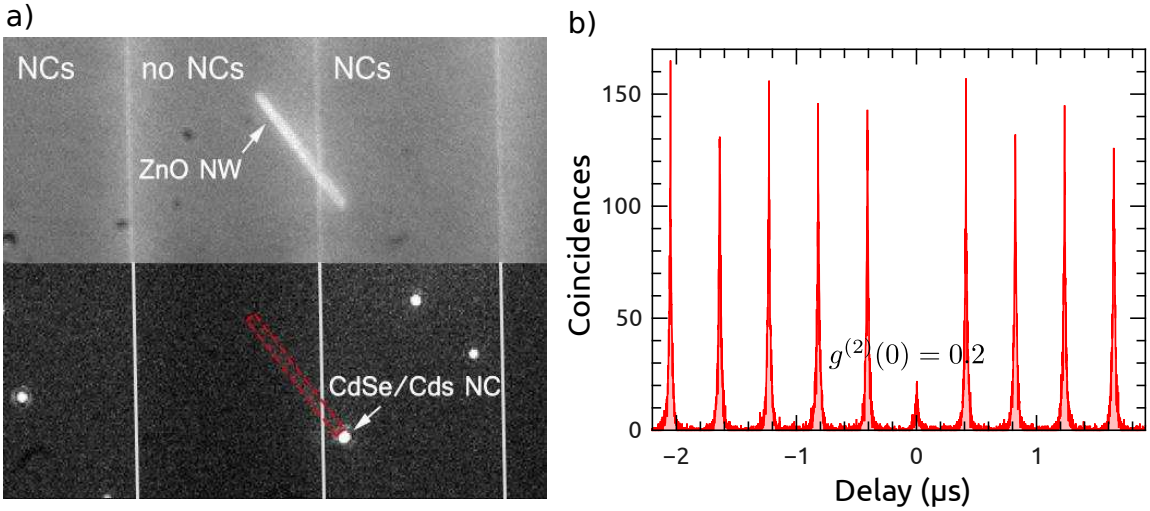

Figure VI.3: Wide field images of the specific nanowire/nanocrystal couple and antibunching curve of the nanocrystal. *a) Top: Wide field reflection image of the sample showing a nanowire at the border between a zone with and without nanocrystals. Bottom: Filtering the excitation light reveals the presence of a dot-in-rod at one extremity of the nanowire. b) Antibunching curve of the studied dot-in-rod.*

VI.1.2 Passive/Active excitation

We first present the passive case with excitation of the ZnO nanowire below its bandgap with a 405 nm laser. ZnO nanowires have been proven to be efficient nanowaveguides for light with energy below bandgap [209,210]. By focusing a 405 nm laser on one end of the nanowire we can observe light guiding along the nanowire in Fig.VI.4a: the guided light couples out at the tip of the nanowire. When filtering the excitation, we can see that the single nanocrystal is excited by the outcoupled light on Fig.VI.4b (inset). We measure the spectrum of the light collected in the white circle area in inset of Fig.VI.4b while exciting with the laser the tip of the nanowire (blue disk in inset) or out of the nanowire (red disk in inset). These data show clearly that the nanocrystal is selectively excited only when the laser spot is on the nanowire, as the spectrum of the single nanocrystal appears at 585 nm (blue excitation spot on the nanowire) and disappears (red excitation spot off the nanowire).

The second case uses the nanowire as an active waveguide. When the same nanowire as in Fig.VI.4 is under the excitation of a 325 nm laser on one end, a strong photoluminescence at 377 nm from the ZnO can be observed on the excitation spot as seen on

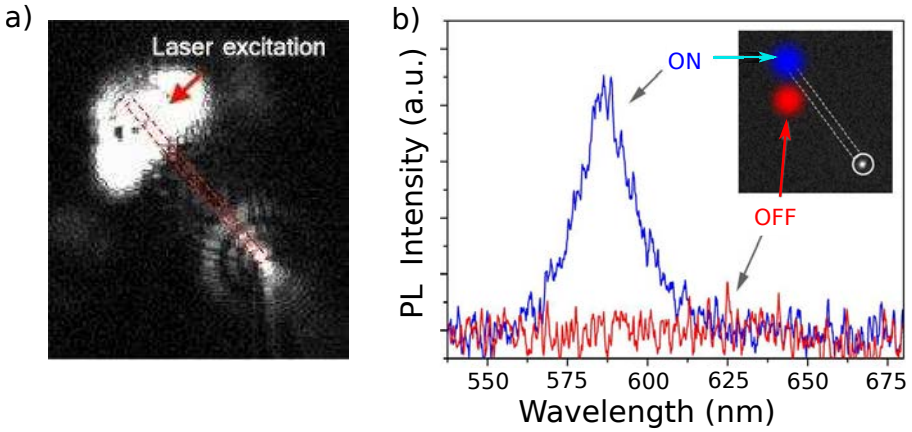

Figure VI.4: Passive excitation spectrum of the nanocrystal. *a) Waveguiding image of the 405 nm excitation laser. b) Dot-in-rod excited through the passive nanowire. A long pass filter (cut off 550 nm) is used to filter the 405 nm laser. The shape of the nanowire is drawn in white dashed line in inset. When the laser is placed on and off the end of the nanowire (blue and red spot in inset, respectively), the emission of the nanocrystal appears (blue line) and disappears (red line) in the spectra.*

the green spectrum on Fig.VI.5a taken at the excitation tip (0 μm). On the opposite facet, due to waveguiding, the light is outcoupled as seen in the inset of Fig.VI.5a. The spectrum associated to the outcoupled light is shown in blue on Fig.VI.5a. It is slightly redshifted compared to the ZnO nanowire intrinsic fluorescence. This shift is due to a higher linear attenuation coefficient for the high energy side of the spectrum as seen on CdS nanowires [211]. The nanowire is an active waveguide because the local ZnO photoluminescence at the excitation spot acts as a light source inside the nanowire and is itself waveguided. In fact, in Fig.VI.5b, as previously we can switch ON and OFF the dot-in-rod excitation by exciting the nanowire at its tip or just next to it. In the inset of Fig.VI.5b we can hardly see the nanocrystals photoluminescence inside the white circle because a part of the visible photoluminescence of the ZnO nanowire is unable to be filtered by the long pass filter as it spectrally overlaps with the emission of the nanocrystal. In Fig.VI.5c we present a zoom of the ZnO spectrum at long wavelengths. Luminescence from a surface defect of the nanowire is clearly present between 520 and 700 nm. This is however not what we measure in Fig.VI.5b as the spectral lineshape is different. In Fig.VI.5b the lineshape is Gaussian with a full width at half maximum of 15 nm, this is characteristic of single dot-in-rod. Moreover it is the same spectrum than in Fig.VI.4b, ensuring that it comes from the nanocrystal under investigation.

VI.1.3 Losses and excitation efficiency

By comparing the photoluminescence intensity of the nanocrystal when directly excited by the laser or through the nanowire, we measure that the passive nanowaveguide con-

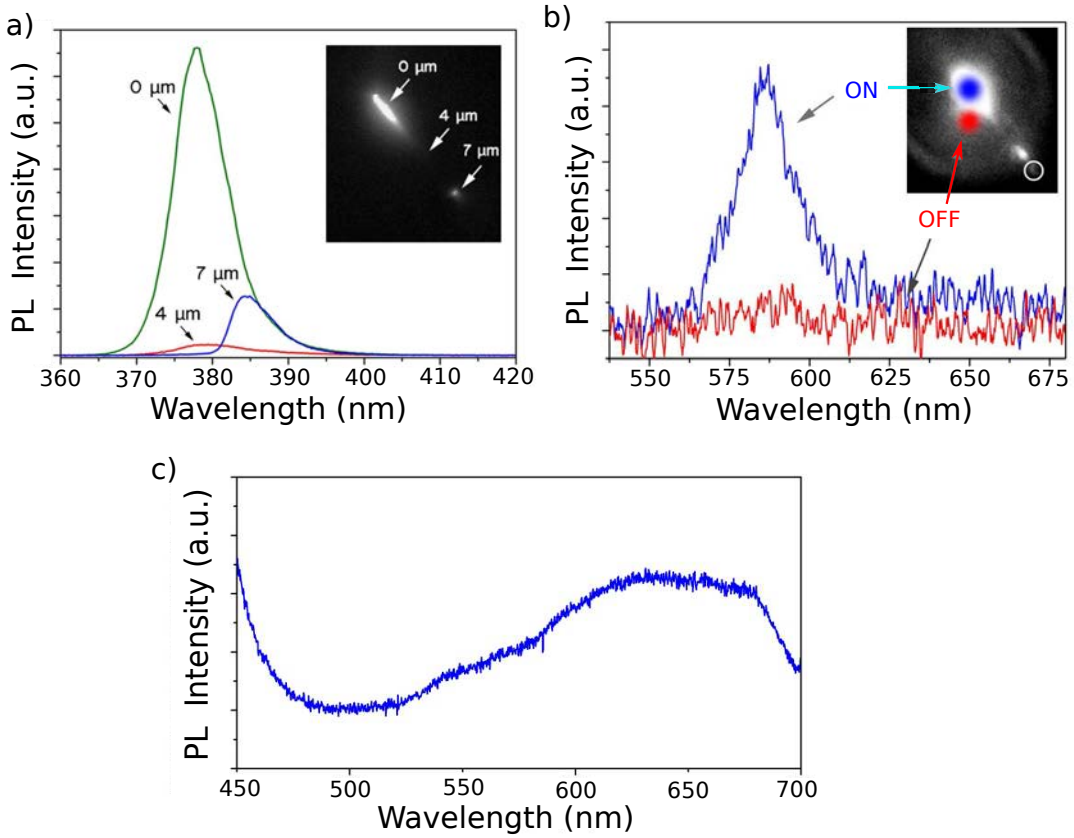

Figure VI.5: Active excitation of the nanocrystal. *a) Waveguiding image of the* 325 *nm excitation laser. b) Single CdSe/CdS nanocrystal excited through the active nanowire, in blue when the laser is on the nanowire and in red when it is away from the nanowire. Part of the visible photoluminescence of the ZnO nanowire is unable to be filtered by the long pass filter in the image as it spectrally overlaps with the emission of the nanocrystal. c) Zoom on the ZnO nanowire spectrum (*200× *magnification compared to Fig.VI.2) at long wavelengths: broad spectrum emission from a surface defect of the nanowire.*

figuration has an uncorrected excitation efficiency of 0.7%. However, we measured by a transmission experiment that only 7% of the incoming 405 nm laser is coupled into the nanowire. Correcting for the coupling losses, an addressing efficiency of 10% compared with the direct excitation scheme is found. The lost power compared to the direct excitation scheme is due to propagation losses along the nanowire.

For the active waveguide excitation, as in the passive case, less emission is observed through waveguided excitation than with direct excitation leading to a ratio of 1.1%. If we assume that the excitation losses originate only from the imperfect geometrical overlap between the nanowire diameter (280 nm) and the Gaussian laser beam spot (1 μm), only 35% of the incident light at 325 nm is absorbed by the nanowire. An addressing efficiency of 3.1% is therefore reached after correction of the coupling losses.

VI.1.4 Outlook

To conclude, we have proposed and shown a proof of principle of a simple method for photonic integration of a single photon emitter with a passive and/or active sub-wavelength nanowaveguide based on a semiconductor nanowire. The integration of the two nanostructures is demonstrated by successfully exciting the single photon emitter through the nanowaveguide. An excitation efficiency of 10% in the passive case has been achieved. We expect that this photonic integration can be extended to various applications and also further improved for a more efficient addressing. For instance, instead of relatively weak PL at output facet, strong lasing effect can be generated with nanowires which will greatly increase the excitation efficiency on the single photon emitters [212, 213]. Moreover, by contacting the nanowire with metallic electrodes, we can generate electron-hole pairs without incoming light, such that the single photon emitter next to the nanowire might be electrically excited [214].

VI.2 Orientation of CdSe/CdS dot-in-rods using liquid crystals

In this section, taking advantage of the high linear polarization of dot-in-rods, we demonstrate that arrays of liquid crystal defects behave as matrix to govern the positional and directional ordering of single dot-in-rods embedded within and parallel to the defects. This work is realized in collaboration with the "Physico-Chimie et dynamique des surfaces"[4] group at Institut des Nanosciences de Paris.

VI.2.1 Orientation and positioning of nanoparticles

Various system have demonstrated accurate nanoparticle positioning. Aligned nanoparticles have been obtained through mechanical rubbing [215], short-range interactions [127] or patterned substrates [116]. Materials composed of a large number of aligned elongated nanocrystals assembled in multi-layers have also been evidenced on both solid substrates [216] and water films [25, 117].

Orientation and positional ordering of wurtzite nanorods has been obtained through the utilization of a local electric field, exploiting their intrinsic electric dipole moments [25, 217]. However, this procedure ends up in closely packed nanorods ensembles and does not allow single particle orientation. Concerning liquid crystals, several works have been devoted to composite materials realized by dispersing nanoemitters into liquid crystals

[4] http://www.insp.upmc.fr/-Physico-chimie-des-surfaces-.html?lang=fr

in the literature [218]. However, only ensemble anisotropic emission properties [219–221] have been studied either due to the aggregation of the embedded particles or to the device configuration.

VI.2.2 The liquid crystal samples

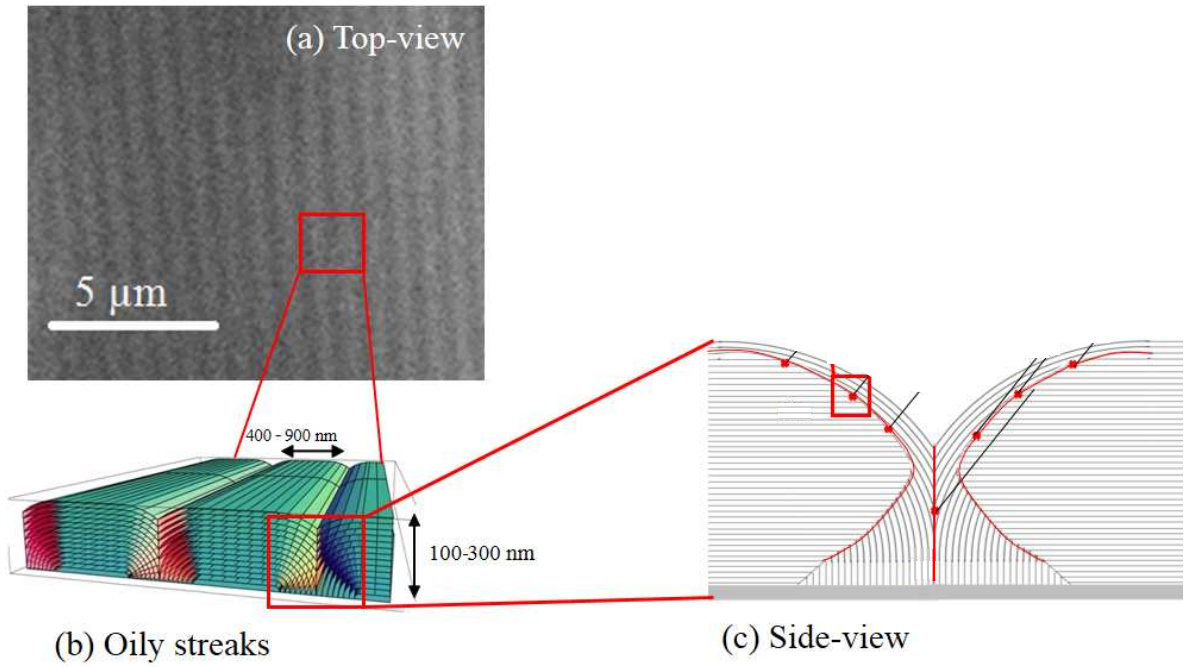

Figure VI.6: Liquid crystal structure. *a) Oily streaks observed by optical microscopy, viewed from the top. b) Oily streaks structure schematically shown in 3D. c) A zoom on the most distorted areas of the sample in side view.*

In this section we present the system. Glass with spin-coated and rubbed polyvinyl alcohol polymer (PVA) of thickness 10 nm is used as substrate to realize films of a liquid crystal composed of elongated molecules of 4-n-octyl-4'-cyanobiphenyl (8CB). A rubbing machine is used to rub the PVA. Hand rubbing with cotton sticks is also possible but results in sample of lower quality in terms of creating liquid crystal defects on large scales. 40 μL drops of a 2.10^{-1} M 8CB solution in toluene, containing 10^{-13} moles of dot-in-rods are spin-coated on top of rubbed PVA-coated substrates at $4,000$ rpm during 30 seconds with an acceleration of 300 rpm/s. This results in a 100 nm-thick 8CB film where arrays of parallel stripes are visualized on our microscope in Fig.VI.6a when shining the mercury lamp and imaging the light reflected at the interface between the liquid crystal (average optical index 1.57) and glass. On the PVA rubbed surfaces, a planar anchoring of the liquid crystalline molecules is induced, while a perpendicular alignment is produced at the air interface. Such an anchoring antagonism leads to distortions of the liquid crystal

films as shown on Fig.VI.6b and c, commonly named oily streaks for film thicknesses in the range of 100 to 300 nm [222]. The layers are curved between the air and PVA interfaces, stacking on top of each other to form flattened hemicylinders of axis parallel to the substrate and perpendicular to the anchoring orientation, defined by the PVA rubbing direction, Fig.VI.6a and b. The corresponding hemicylinders periodicity and orientation can be determined by optical microscopy since they are associated with straight linear stripes on Fig.VI.6a.

VI.2.3 Polarization microscopy of dot-in-rods inside a liquid crystal

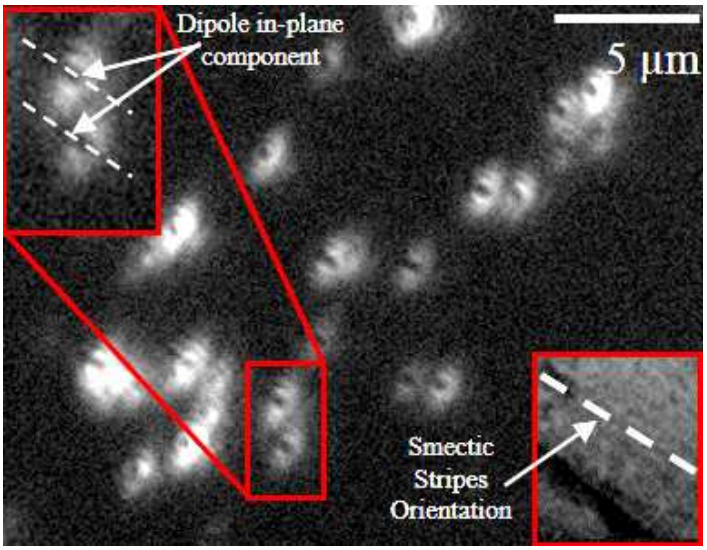

Figure VI.7: Defocus image of dot-in-rods inside the liquid crystal. *The bottom left corner shows the oily streaks in this area of the sample. The defocused pattern dark axis is aligned with the oily streaks.*

The circularly polarized picosecond pulsed laser diode is used to excite dot-in-rods embedded in the liquid crystal through the high numerical aperture air objective (NA= 0.95). The oil immersion objective could not be used because it invariably destroys the liquid crystal with oil ending on the sample. Low excitation power below the dot-in-rod absorption saturation level was used in order to limit multi exciton emission and blinking. In a first step, the unicity of dot-in-rods was tested, the dilution previously described gives satisfactory results with at least 50% of the particles being single dot-in-rods. So the system does not lead to an unusual formation of aggregates as it is the same kind of percentages we can see when dot-in-rods are dropcasted on glass. The measurements presented in the following where all realized on single dot-in-rods, prior to any photoluminescence measurement, the $g^{(2)}$ function was measured to ensure the

particles are singles.

A first observation of the dot-in-rods in a region displaying well defined oily streaks by defocused microscopy shows nicely aligned defocused patterns on Fig.VI.7. The dark axis of the defocused pattern are aligned with the oily streaks direction shown in inset in the bottom right corner of Fig.VI.7.

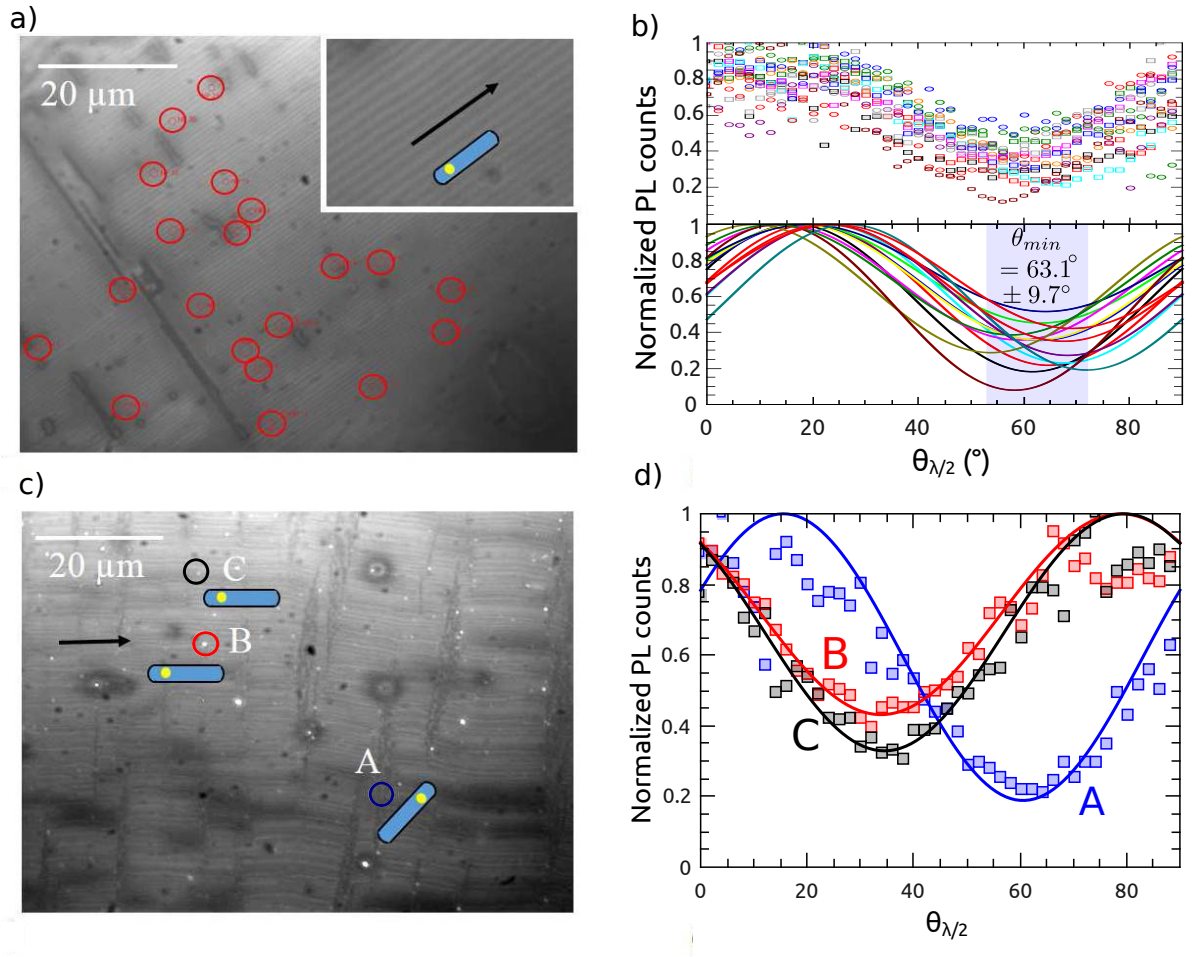

Figure VI.8: Defocus image of dot-in-rods inside the liquid crystal. *a) Oily streaks observed through optical microscopy. The position of the dot-in-rods is found in the oily streaks, via fluorescence microscopy and is highlighted by red circles on the picture - the arrow indicates the axis of the oily streaks, the dot-in-rods being shown with the blue icon. The inset shows a zoom of size* $13,5\ \mu m \times 9\ \mu m$ *. b) Up: photoluminescence intensity obtained from dot-in-rods shown in a). Bottom: photoluminescence intensity fits obtained from dot-in-rods shown in a) as a function of the half wave plate angle. c) Superposition of the pictures obtained in optical microscopy (oily streaks) and fluorescence microscopy (dot-in-rods) on a sample with imperfect PVA polymer rubbing. Three specific dot-in-rods are chosen for observation, DRA, DRB and DRC. The arrow indicates the axis of the oily streaks, the orientation of the dot-in-rods being shown with the blue icon. d) Photoluminescence intensity emitted by the three dot-in-rods shown in c) as a function of the half wave plate angle. Fits to the three curves are shown as solid lines.*

The dot-in-rods alignment in oily streaks is further confirmed by polarization mea-

surements. Fig.VI.8a presents a large area of the samples with well organized oily streaks; the dot-in-rods positions are marked by red circular pattern. The fit with Eq.II.1 of the photoluminescence intensity registered for the different particles while rotating the half wave plate[5] are plotted on Fig.VI.8b bottom, the normalized data are shown above. The minimum of the photoluminescence is on average positioned at $\theta_{min} = 63.1° \pm 9.7°$. A standard deviation of $\pm 10°$ is typical, it is found for dot-in-rods positioned inside oily streaks on different part of the sample. This is comparable with the $\pm 12.5°$ of standard deviation reported in reference [215] for CdSe/Cds nanorods deposited on a mechanically rubbed glass substrate. The alignment has been tested for the different types of dot-in-rods samples with similar results.

Fig.VI.8c shows a sample with more disordered areas. This samples was realized by hand rubbing the substrate while the previous sample was rubbed using the rubbing machine. The hand rubbing leads to smaller organized areas for the liquid crystals. The disordered areas are visible on the image as discontinuities inside the oily streak pattern. For example DRA inside the blue circle is positioned in a disordered area while DRB and DRC are inside oily streaks of same directions. The detected photoluminescence of the three dot-in-rods while rotating the half wave plate are plotted in Fig.VI.8d. While DRB and DRC show alignment of their luminescence polarization, DRA displays a different alignment as expected from its position inside a disordered area.

VI.2.4 Outlook

We showed that the oily streak structure created by a liquid crystal deposited on a rubbed polymer induces an alignment along a unique direction of the dot-in-rods diluted in the liquid crystal matrix due to the trapping within the oily streaks. This has been shown at the single particle level. This work shows the feasibility of a large-scale orientation of anisotropic emitters without the stringent requirements shown in previous studies (control of the ligands nature, continuity of the sample, particles in direct contact with each other or external electric fields). The experiment demonstrates the trapping efficiency of oily streaks which not only trap but also align elongated nano-objects, along a single direction for a given sample.

These results open the way for orienting dot-in-rods before eventually couple them to other devices. The creation of chains of oriented dot-in-rods could also be used to study collective emission effects [223, 224].

[5] See section II.1.2 for the setup used to the measure polarization degree.

Conclusion

We have shown that we can successfully excite a single dot-in-rod positioned at one tip of a ZnO nanowire via the guiding of light or the excitation of the nanowire. We can also position and orientate dot-in-rods along lines using crystal liquid defects.

The group is also investigating the problem of light collection. A single emitter in free space typically emits its photon in a 4π solid angle which renders the efficient collection of the emitted light a difficult task. However, as we have already seen throughout this manuscript, fluorescence properties such as the lifetime of emission or the radiation pattern are not intrinsic properties of the emitter. They depend on its coupling with the electromagnetic field in the surrounding medium. By controlling the environment of the emitter the emission lifetime and radiation pattern can be engineered. The motivations associated with the problematic of light harvesting for nanoemitters are multiple. As highlighted in chapter III of this manuscript, as soon as the need to bin photon detection events together is necessary, the problem of the losses has to be carefully addressed. Information on fast timescales phenomena are lost or need to be retrieved through indirect means, such as looking at the correlations of the emission. Even more critical is the collection efficiency for emitters not as efficient as nanocrystals, for example in biology for the detection of weak traces of chromophores fluorescence with low quantum yields or imaging of fast dynamical phenomena [225]. The majority of the works around single nanoemitters light collection is linked to the quantum optics field with applications in sub-shot-noise detection [226], quantum communication [227], and quantum computation [228]. In these applications, the losses quickly undermine the performance. The group is now working on coupling dot-in-rods with a parabolic mirror, this is very briefly presented in appendix B. Also a system of tapered fiber is investigated. Both these systems should allow collecting the light more efficiently, increasing the overall detection efficiency compared to our current working scheme.

Conclusion and outlooks

This work analyzed different aspects of the photoluminescence of CdSe/CdS dot-in-rods at room temperature, from the photoluminescence blinking to the photon statistics and polarization properties. Examples of coupling of these emitters with nanophotonics devices was also presented.

First we studied the blinking statistics of CdSe/CdS dot-in-rods. We have shown that dot-in-rods with thick shells are characterized by a reduced blinking. We demonstrated that two states of emission are involved in this blinking process, namely the exciton and the negatively charged exciton. The reduced blinking statistics follows a power law distribution with the same exponents as for bare CdSe or CdSe/ZnS nanocrystals. Nevertheless, an exponential cutoff arises at milliseconds timescales. We have seen that the correlation function is an appropriate tool to analyze such fast blinking statistics. We have seen that even with a careful choice of bin time, the histogram of emission intensity can be poorly fitted by a sum of two Poisson distributions because of the large statistical weight attributed to fast switching events by the power law distribution. By studying various samples of dot-in-rods we highlighted the fact that the fast blinking dynamics is strongly dependent on the geometrical parameters.

We then focused our analysis on the photon statistics of dot-in-rods. We derived a formula to link the normalized intensity correlation function with the quantum yields of the emission states. At low excitation power the photon statistics is dominated by the emission of the exciton and biexciton. We have shown that the biexciton emission can be tuned by changing the size of the core. Indeed, the non radiative relaxation of multiexcitons is dominated by the Auger relaxation of electron-hole pairs with the strongly confined hole inside the core for CdSe/CdS heterostructures. By changing the size of the CdSe core, the confinement of the hole is modified and consequently the multiexciton emission. At higher excitation powers, the blinking of dot-in-rods needs to be taken into account in order to understand the photon statistics. The radiative relaxation of a negatively charged exciton or biexciton is governed by the electron delocalization. Delocalization of electrons is primarily determined by the thickness of the shell. The

overall photon statistics is a mixture of the photon statistics of a neutral nanocrystal and the photon statistics of a charged nanocrystal. A charged nanocrystal displays a photon statistics that is characterized by a larger proportion of multiphoton emission compared to a neutral nanocrystal because the single photon emission decreases in a larger proportion than the multiphoton emission when a nanocrystal is charged.

In chapter V the polarization of the emission of dot-in-rods was investigated. We have shown with our measurements that CdSe/CdS dot-in-rods, conversely to spherical CdSe/CdS nanocrystals, have large degrees of polarization. The degree of polarization is strongly dependent on the geometry of the dot-in-rods. We have built a model of the experiment that takes into account the experimental configuration, the CdSe bandedge exciton fine structure and the anisotropy of the CdS shell. We show that the anisotropy of the rod shell enhances the emission of the linear dipole constituted by the $|\pm\rangle 0^U$ state of the bandedge exciton fine structure. From our measurements of polarization we are able to recover the fine structure of the CdSe bandedge exciton. Samples displaying a high degree of polarization have necessarily a rod-like bandege exciton symmetry due to a negative net-splitting between the heavy-holes and light-holes subbands.

Finally, we also presented experiments where we coupled dot-in-rods with various photonic devices. We have demonstrated the possibility of excitation of a single emitter using a Zinc Oxyde (ZnO) nanowire. Guiding laser light or exciting the nanowire can efficiently trigger the emission of single photons by a dot-in-rod placed at one end of the nanowire. Using defects in liquid crystals, we also show that we are able to efficiently orientate single nanoemitters.

Outlooks The group is now working on cryogenic temperature measurements. A first part of the work would be to acquire knowledge on the fine structure of the bandedge exciton. This can be realized by performing lifetime measurements at various temperature such as in reference [197]. Also, a setup of photon correlation Fourier spectroscopy has been built (see appendix A). Measurements of coherence of the emission can be realized as well as characterization of spectral diffusion using this correlation spectroscopy method.

We are also trying to integrate dot-in-rods in cavities. As demonstrated in chapter V, owing to their high degree of polarization dot-in-rods have a dominant 1D dipole-like emission. Therefore, they are emitters well suited for integration inside a parabolic mirror (see appendix B). Integration of dot-in-rods on tapered nanofibers is also a system investigated in the group. Both these systems should help in collecting more photons from the emitter. A higher collection efficiency would help for example in understanding the fast dynamics of blinking as smaller bin time would be required.

Appendix A
CdSe/CdS dot-in-rods emission at cryogenic temperature

CdSe/CdS particles are suitable fluorescent particles at room temperature for many research and application fields. In biology as robust fluorescent markers easy to functionalize, in optics they are integrated into light emitting or light harvesting devices. Even in quantum optics as we have seen in chapter IV where their single and multiphoton emission was conveniently used for testing an ICCD camera. However there is still an interest in making studies at cryogenic temperatures. Cryogenic temperatures are useful to acquire knowledge about emission processes of such particles. At room temperature there are no possibilities to carry on any detailed spectral studies as the thermal noise broadens every line.

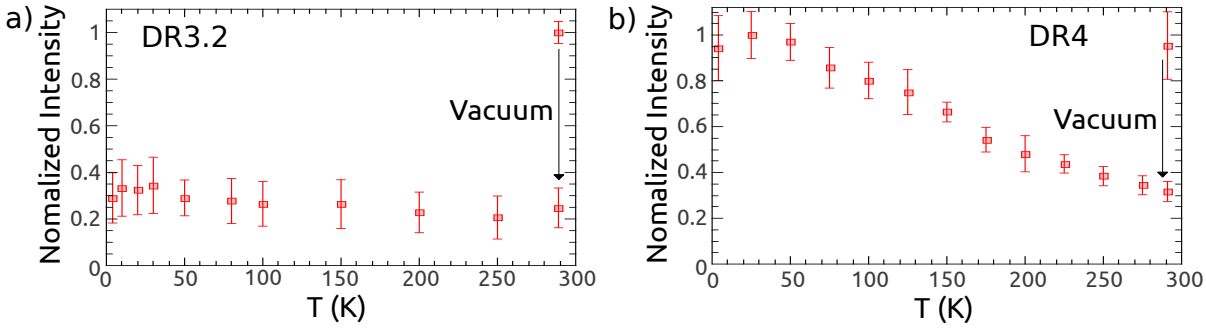

Figure A.1: Normalized emission intensity of nanocrystals ensembles versus the temperature for samples DR3.2 and DR4. *The intensity is normalized by its value at* 290 *K before vacuum conditions are applied inside the cryostat. a) Sample DR3.2, the emission intensity is constant throughout the whole temperature range studied. b) Sample DR4, the intensity increases with decreasing temperatures until reaching its value at* 290 *K before vacuum conditions.*

Here we show the results of preliminary cryogenic measurements on dot-in-rods ensembles and then briefly present future studies the group wants to develop on the coherence of the emission of dot-in-rods.

We excite dot-in-rods ensembles below the saturation. The intensity of the emission

decreases when vacuum is made inside the cryostat. Given that the intensity falls at a level characteristics of the trion emission this might indicate that dot-in-rods stays charged under vacuum conditions as observed for thick shells nanocrystals [88]. All the samples show a constant intensity [123] while the temperature decreased as in Fig.A.1a for DR3.2, except the sample DR4 which shows an increase of the emission intensity when the temperature is decreased. This suggests a temperature activation of the Auger recombination for DR4, as reported in reference [88] for spherical nanocrystals.

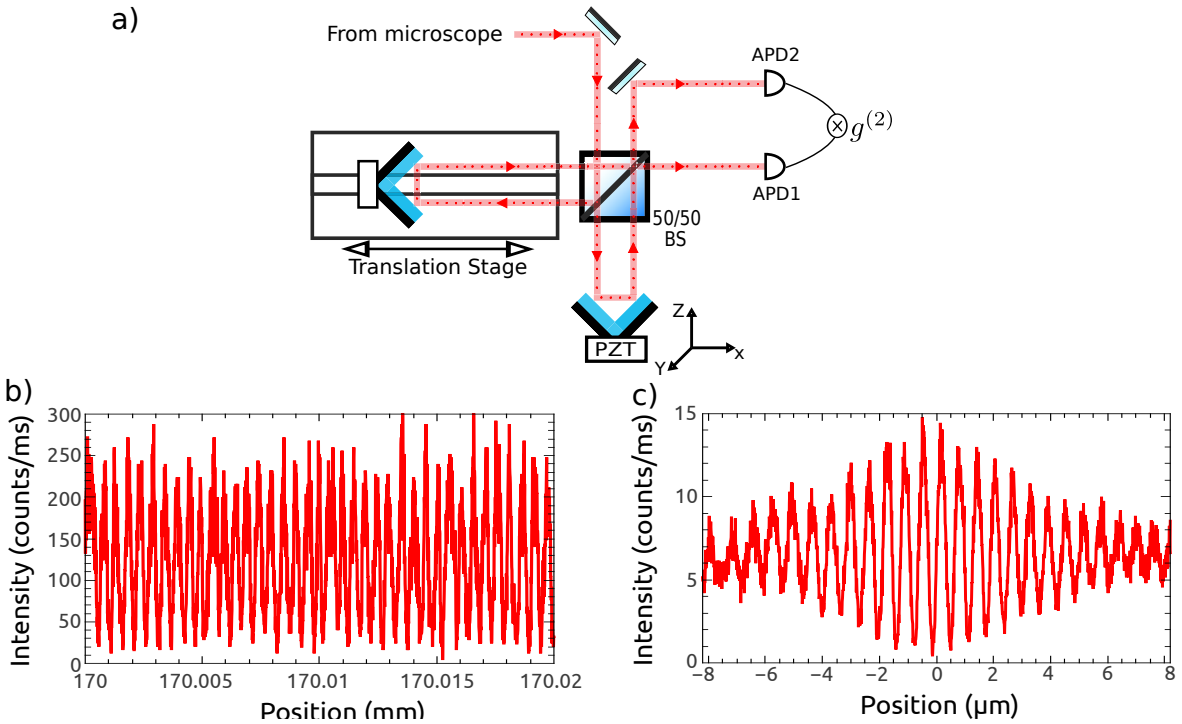

Figure A.2: Interferometer for photon correlation Fourier spectroscopy and first measurements. *a) Interferometer composed of two retroflectors. Combining discrete steps of the mirror mounted on the linear stage together with the addition of a piezoeclectric (PZT) stage on the other mirror implies that an unlimited amount of photons can be collected for each interferometer position. b) HeNe laser interference fringes, visibility is above* 95%*. c) Single nanocrystal interference fringes.*

Measurements on single nanocrystals need to be conducted. Lifetime measurements can yield several informations of the nanocrystal fine structure [229]. The next step is to characterize the temporal coherence of the emission of dot-in-rods. To avoid the inherent line broadening due to spectral diffusion [16], photon correlation Fourier spectroscopy is a possible measurement procedure we can implement with the material already existing in the laboratory. This measurement consists in an interferometry measurement (see Fig.A.2 for the setup) but the analysis is then based on the $g^{(2)}$ function rather than the simple intensity envelop of the classical interferometry [230, 231]. By selecting the delay between photons, it is possible to retrieve the emission linewidth at different timescales

and thus have information on the coherence of the emission [232] at short timescales without the broadening due to spectral diffusion. Looking at a wide range of delays, the dynamics of spectral diffusion can also be studied [233].

Up to now, nanocrystals have been shown to be far from Fourier limited (coherence time of 200 ps [232]), the short coherence time explains that no 2 photon interferometry has been demonstrated with these single photon sources contrary to other sources such as epitaxial quantum dots. The setup for photon correlation Fourier spectroscopy has been built and optimized, a good visibility is already obtained as shown on Fig.A.2b and c.

Appendix B
Coupling CdSe/CdS dot-in-rods to a parabolic mirror

During my thesis I have also been involved in a project in collaboration with the 4piPAC[1] group of the Max Planck Institute for the Science of Light in Erlangen, Germany. The goal of this project is to couple a single dot-in-rod to a parabolic mirror. The parabolic mirror constitutes a half cavity especially suited for the excitation and collection of the emission of a dipole [234, 235] as depicted on Fig.B.1a. Experiments are carried out in the 4piPAC group at the Max Planck Institute on single ions [236, 237], theoretical investigations of the coupling of dipoles with light in free space with such a parabolic mirror are also carried out [238–240]. Such a system has also been investigated for exciting and collecting the light emitted by molecules [241, 242].

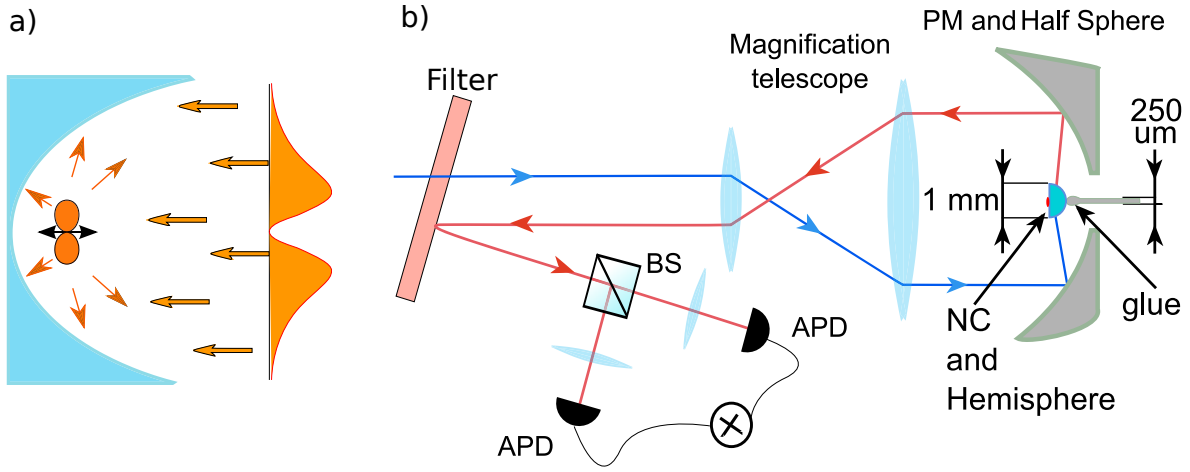

Figure B.1: Experiment principle and preliminary setup. *a) A dipole wave impinging the parabolic mirror excites efficiently a dipole placed at the focus of the parabolic mirror. The emitted light is efficiently collected by the parabolic mirror. b) Preliminary setup to test the possibility of exciting a dot-in-rod. A dot in rod sample is realized on a small (1mm) half-sphere and inserted inside the parabolic mirror. Light is collected by the parabolic mirror and sent to a Hanbury Brown and Twiss setup.*

[1] http.//www.mpl.mpg.de/en/leuchs/research/4pipac/

Preliminary experiments on dot-in-rods with the setup depicted on Fig.B.1b were successful in collecting the emission of a single dot-in-rod as shown by the antibunching curve in Fig.B.2a. Up to now the parabolic mirror are made by mechanical means and are millimeters scale, we are investigating the possibility of fabrication of micrometer scale parabolic mirrors [243, 244] by means of 2 photon lithography with an already embedded dot-in-rod at the focus of the parabolic mirror. A picture of such a device realized at the National Nanotechnology laboratory in Lecce is shown on Fig.B.2b.

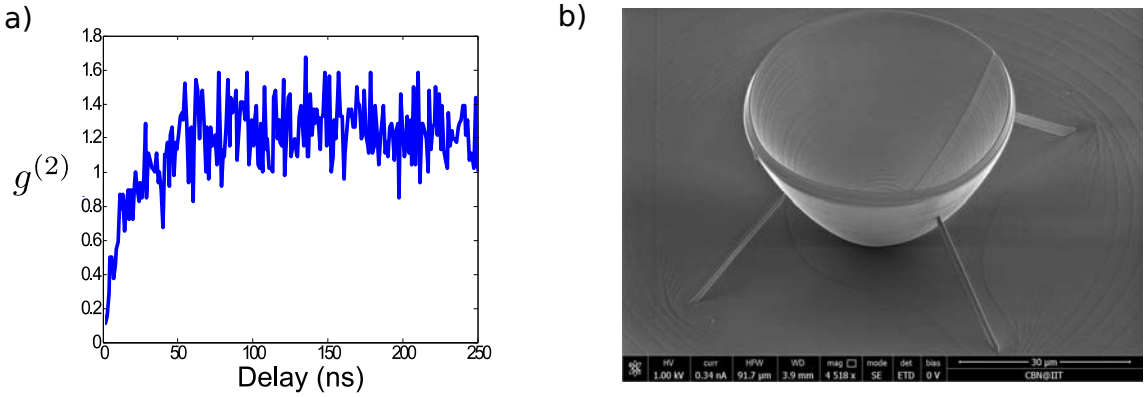

Figure B.2: Experiment principle and preliminary setup. *. a) Antibunching from a single dot-in-rod inside the parabolic mirror in the configuration depicted in Fig.B.1b. b) parabolic mirror realized in IIT Lecce by two photon lithography.*

Bibliography

[1] A. Ekimov, A. L. Efros, and A. Onushchenko, "Quantum size effect in semiconductor microcrystals," *Solid State Communications*, vol. 56, no. 11, pp. 921–924, 1985.

[2] R. Rossetti, J. Ellison, J. Gibson, and L. Brus, "Size effects in the excited electronic states of small colloidal CdS crystallites," *The Journal of chemical physics*, vol. 80, no. 9, pp. 4464–4469, 1984.

[3] C. Murray, D. J. Norris, and M. G. Bawendi, "Synthesis and characterization of nearly monodisperse CdE (E= sulfur, selenium, tellurium) semiconductor nanocrystallites," *Journal of the American Chemical Society*, vol. 115, no. 19, pp. 8706–8715, 1993.

[4] B. Dabbousi, J. Rodriguez-Viejo, F. V. Mikulec, J. Heine, H. Mattoussi, R. Ober, K. Jensen, and M. Bawendi, "(CdSe) ZnS core-shell quantum dots: synthesis and characterization of a size series of highly luminescent nanocrystallites," *The Journal of Physical Chemistry B*, vol. 101, no. 46, pp. 9463–9475, 1997.

[5] X. Wu, H. Liu, J. Liu, K. N. Haley, J. A. Treadway, J. P. Larson, N. Ge, F. Peale, and M. P. Bruchez, "Immunofluorescent labeling of cancer marker Her2 and other cellular targets with semiconductor quantum dots," *Nature biotechnology*, vol. 21, no. 1, pp. 41–46, 2002.

[6] I. L. Medintz, H. T. Uyeda, E. R. Goldman, and H. Mattoussi, "Quantum dot bioconjugates for imaging, labelling and sensing," *Nature materials*, vol. 4, no. 6, pp. 435–446, 2005.

[7] R. Freeman and I. Willner, "Optical molecular sensing with semiconductor quantum dots (QDs)," *Chemical Society Reviews*, vol. 41, no. 10, pp. 4067–4085, 2012.

[8] S. Coe, W.-K. Woo, M. Bawendi, and V. Bulović, "Electroluminescence from single monolayers of nanocrystals in molecular organic devices," *Nature*, vol. 420, no. 6917, pp. 800–803, 2002.

[9] D. C. Oertel, M. G. Bawendi, A. C. Arango, and V. Bulović, "Photodetectors based on treated CdSe quantum-dot films," *Applied Physics Letters*, vol. 87, no. 21, p. 213505, 2005.

[10] G. I. Koleilat, L. Levina, H. Shukla, S. H. Myrskog, S. Hinds, A. G. Pattantyus-Abraham, and E. H. Sargent, "Efficient, stable infrared photovoltaics based on solution-cast colloidal quantum dots," *ACS nano*, vol. 2, no. 5, pp. 833–840, 2008.

[11] V. Klimov, A. Mikhailovsky, S. Xu, A. Malko, J. Hollingsworth, C. Leatherdale, H.-J. Eisler, and M. Bawendi, "Optical gain and stimulated emission in nanocrystal quantum dots," *Science*, vol. 290, no. 5490, pp. 314–317, 2000.

[12] B. Lounis, H. Bechtel, D. Gerion, P. Alivisatos, and W. Moerner, "Photon antibunching in single CdSe/ZnS quantum dot fluorescence," *Chemical Physics Letters*, vol. 329, no. 5, pp. 399–404, 2000.

[13] F. Pisanello, L. Martiradonna, G. Leménager, P. Spinicelli, A. Fiore, L. Manna, J.-P. Hermier, R. Cingolani, E. Giacobino, M. De Vittorio, *et al.*, "Room temperature-dipolelike single photon source with a colloidal dot-in-rod," *Applied Physics Letters*, vol. 96, no. 3, p. 033101, 2010.

[14] C. H. Bennett and D. P. DiVincenzo, "Quantum information and computation," *Nature*, vol. 404, no. 6775, pp. 247–255, 2000.

[15] M. Nirmal, B. Dabbousi, M. Bawendi, J. Macklin, J. Trautman, T. Harris, and L. Brus, "Fluorescence intermittency in single cadmium selenide nanocrystals," *Nature*, vol. 383, no. 6603, pp. 802–804, 1996.

[16] S. Empedocles and M. Bawendi, "Influence of spectral diffusion on the line shapes of single CdSe nanocrystallite quantum dots," *The Journal of Physical Chemistry B*, vol. 103, no. 11, pp. 1826–1830, 1999.

[17] S. Empedocles, R. Neuhauser, and M. Bawendi, "Three-dimensional orientation measurements of symmetric single chromophores using polarization microscopy," *Nature*, vol. 399, no. 6732, pp. 126–130, 1999.

[18] M. A. Hines and P. Guyot-Sionnest, "Synthesis and characterization of strongly luminescing ZnS-capped CdSe nanocrystals," *The Journal of Physical Chemistry*, vol. 100, no. 2, pp. 468–471, 1996.

[19] B. Mahler, P. Spinicelli, S. Buil, X. Quelin, J.-P. Hermier, and B. Dubertret, "Towards non-blinking colloidal quantum dots," *Nature materials*, vol. 7, no. 8, pp. 659–664, 2008.

[20] J. Hu, L. shi Li, W. Yang, L. Manna, L. wang Wang, and A. P. Alivisatos, "Linearly polarized emission from colloidal semiconductor quantum rods," *Science*, vol. 292, no. 5524, pp. 2060–2063, 2001.

[21] C. Galland, S. Brovelli, W. K. Bae, L. A. Padilha, F. Meinardi, and V. I. Klimov, "Dynamic hole blockade yields two-color quantum and classical light from dot-in-bulk nanocrystals," *Nano letters*, vol. 13, no. 1, pp. 321–328, 2012.

[22] E. Cassette, B. Mahler, J.-M. Guigner, G. Patriarche, B. Dubertret, and T. Pons, "Colloidal CdSe/CdS dot-in-plate nanocrystals with 2D-polarized emission," *ACS nano*, vol. 6, no. 8, pp. 6741–6750, 2012.

[23] B. Mahler, B. Nadal, C. Bouet, G. Patriarche, and B. Dubertret, "Core/Shell colloidal semiconductor nanoplatelets," *Journal of the American Chemical Society*, vol. 134, no. 45, pp. 18591–18598, 2012.

[24] D. V. Talapin, R. Koeppe, S. Götzinger, A. Kornowski, J. M. Lupton, A. L. Rogach, O. Benson, J. Feldmann, and H. Weller, "Highly emissive colloidal CdSe/CdS heterostructures of mixed dimensionality," *Nano Letters*, vol. 3, no. 12, pp. 1677–1681, 2003.

[25] L. Carbone, C. Nobile, M. De Giorgi, F. D. Sala, G. Morello, P. Pompa, M. Hytch, E. Snoeck, A. Fiore, I. R. Franchini, *et al.*, "Synthesis and micrometer-scale assembly of colloidal CdSe/CdS nanorods prepared by a seeded growth approach," *Nano letters*, vol. 7, no. 10, pp. 2942–2950, 2007.

[26] Z. Alfassi, D. Bahnemann, and A. Henglein, "Photochemistry of colloidal metal sulfides. 3. Photoelectron emission from cadmium sulfide and cadmium sulfide-zinc sulfide cocolloids," *The Journal of Physical Chemistry*, vol. 86, no. 24, pp. 4656–4657, 1982.

[27] X. Peng, L. Manna, W. Yang, J. Wickham, E. Scher, A. Kadavanich, and A. P. Alivisatos, "Shape control of CdSe nanocrystals," *Nature*, vol. 404, no. 6773, pp. 59–61, 2000.

[28] R. Bandaranayake, G. Wen, J. Lin, H. Jiang, and C. Sorensen, "Structural phase behavior in II–VI semiconductor nanoparticles," *Applied physics letters*, vol. 67, no. 6, pp. 831–833, 1995.

[29] Z. Deng, L. Cao, F. Tang, and B. Zou, "A new route to zinc-blende CdSe nanocrystals: mechanism and synthesis," *The Journal of Physical Chemistry B*, vol. 109, no. 35, pp. 16671–16675, 2005.

[30] B. Mahler, N. Lequeux, and B. Dubertret, "Ligand-controlled polytypism of thick-shell CdSe/CdS nanocrystals," *Journal of the American Chemical Society*, vol. 132, no. 3, pp. 953–959, 2009.

[31] S. Kumar and T. Nann, "Shape control of II–VI semiconductor nanomaterials," *Small*, vol. 2, no. 3, pp. 316–329, 2006.

[32] A. L. Efros, M. Rosen, M. Kuno, M. Nirmal, D. Norris, and M. Bawendi, "Band-edge exciton in quantum dots of semiconductors with a degenerate valence band: Dark and bright exciton states," *Physical Review B*, vol. 54, no. 7, p. 4843, 1996.

[33] V. I. Klimov, *Semiconductor and metal nanocrystals: synthesis and electronic and optical properties*. CRC Press, 2003.

[34] L.-W. Wang and A. Zunger, "Pseudopotential calculations of nanoscale CdSe quantum dots," *Physical Review B*, vol. 53, no. 15, p. 9579, 1996.

[35] M. Califano, A. Franceschetti, and A. Zunger, "Temperature dependence of excitonic radiative decay in CdSe quantum dots: the role of surface hole traps," *Nano letters*, vol. 5, no. 12, pp. 2360–2364, 2005.

[36] M. Califano, A. Franceschetti, and A. Zunger, "Lifetime and polarization of the radiative decay of excitons, biexcitons, and trions in CdSe nanocrystal quantum dots," *Physical Review B*, vol. 75, no. 11, p. 115401, 2007.

[37] D. Norris, A. L. Efros, M. Rosen, and M. Bawendi, "Size dependence of exciton fine structure in CdSe quantum dots," *Physical Review B*, vol. 53, no. 24, p. 16347, 1996.

[38] A. Ekimov, F. Hache, M. Schanne-Klein, D. Ricard, C. Flytzanis, I. Kudryavtsev, T. Yazeva, A. Rodina, and A. L. Efros, "Absorption and intensity-dependent photoluminescence measurements on CdSe quantum dots: assignment of the first electronic transitions," *JOSA B*, vol. 10, no. 1, pp. 100–107, 1993.

[39] A. L. Efros and M. Rosen, "The Electronic Structure of Semiconductor Nanocrystals 1," *Annual Review of Materials Science*, vol. 30, no. 1, pp. 475–521, 2000.

[40] D. Norris and M. Bawendi, "Measurement and assignment of the size-dependent optical spectrum in CdSe quantum dots," *Physical Review B*, vol. 53, no. 24, p. 16338, 1996.

[41] M. Nirmal, D. Norris, M. Kuno, M. Bawendi, A. L. Efros, and M. Rosen, "Observation of the" dark exciton" in CdSe quantum dots," *Physical review letters*, vol. 75, no. 20, p. 3728, 1995.

[42] H. Htoon, P. J. Cox, and V. I. Klimov, "Structure of excited-state transitions of individual semiconductor nanocrystals probed by photoluminescence excitation spectroscopy," *Physical review letters*, vol. 93, no. 18, p. 187402, 2004.

[43] P. Guyot-Sionnest, M. Shim, C. Matranga, and M. Hines, "Intraband relaxation in CdSe quantum dots," *Physical Review B*, vol. 60, no. 4, p. R2181, 1999.

[44] D. Norris and M. Bawendi, "Structure in the lowest absorption feature of CdSe quantum dots," *The Journal of chemical physics*, vol. 103, no. 13, pp. 5260–5268, 1995.

[45] M. Bawendi, W. Wilson, L. Rothberg, P. Carroll, T. M. Jedju, M. Steigerwald, and L. Brus, "Electronic structure and photoexcited-carrier dynamics in nanometer-size CdSe clusters," *Physical Review Letters*, vol. 65, no. 13, p. 1623, 1990.

[46] A. L. Efros, "Luminescence polarization of CdSe microcrystals," *Physical Review B*, vol. 46, no. 12, p. 7448, 1992.

[47] M. Chamarro, C. Gourdon, P. Lavallard, O. Lublinskaya, and A. Ekimov, "Enhancement of electron-hole exchange interaction in CdSe nanocrystals: A quantum confinement effect," *Physical review B*, vol. 53, no. 3, p. 1336, 1996.

[48] B. Cagnac, *Physique atomique-Tome 1.* Dunod Université, 1982.

[49] I. Chung, K. T. Shimizu, and M. G. Bawendi, "Room temperature measurements of the 3D orientation of single CdSe quantum dots using polarization microscopy," *Proceedings of the National Academy of Sciences*, vol. 100, no. 2, pp. 405–408, 2003.

[50] H. Htoon, M. Furis, S. Crooker, S. Jeong, and V. Klimov, "Linearly polarized 'fine structure'of the bright exciton state in individual CdSe nanocrystal quantum dots," *Physical Review B*, vol. 77, no. 3, p. 035328, 2008.

[51] D. Oron, A. Aharoni, C. de Mello Donega, J. van Rijssel, A. Meijerink, and U. Banin, "Universal role of discrete acoustic phonons in the low-temperature optical emission of colloidal quantum dots," *Physical review letters*, vol. 102, no. 17, p. 177402, 2009.

[52] M. J. Fernée, P. Tamarat, and B. Lounis, "Cryogenic single-nanocrystal spectroscopy: reading the spectral fingerprint of individual CdSe quantum dots," *The Journal of Physical Chemistry Letters*, vol. 4, no. 4, pp. 609–618, 2013.

[53] O. Labeau, P. Tamarat, and B. Lounis, "Temperature Dependence of the Luminescence Lifetime of Single CdSe/ZnS Quantum Dots," *Physical review letters*, vol. 90, no. 25, p. 257404, 2003.

[54] N. Le Thomas, E. Herz, O. Schöps, U. Woggon, and M. Artemyev, "Exciton fine structure in single CdSe nanorods," *Physical review letters*, vol. 94, no. 1, p. 016803, 2005.

[55] L. Biadala, Y. Louyer, P. Tamarat, and B. Lounis, "Band-edge exciton fine structure of single CdSe/ZnS nanocrystals in external magnetic fields," *Physical review letters*, vol. 105, no. 15, p. 157402, 2010.

[56] Y. Louyer, L. Biadala, P. Tamarat, and B. Lounis, "Spectroscopy of neutral and charged exciton states in single CdSe/ZnS nanocrystals," *Applied Physics Letters*, vol. 96, no. 20, p. 203111, 2010.

[57] Y. Louyer, L. Biadala, J.-B. Trebbia, M. Fernée, P. Tamarat, and B. Lounis, "Efficient biexciton emission in elongated CdSe/ZnS nanocrystals," *Nano letters*, vol. 11, no. 10, pp. 4370–4375, 2011.

[58] M. J. Fernee, C. Sinito, P. Tamarat, and B. Lounis, "State selective pumping reveals spin-relaxation pathways in CdSe quantum dots," *Nano letters*, 2014.

[59] M. J. Fernée, C. Sinito, Y. Louyer, C. Potzner, T.-L. Nguyen, P. Mulvaney, P. Tamarat, and B. Lounis, "Magneto-optical properties of trions in non-blinking charged nanocrystals reveal an acoustic phonon bottleneck," *Nature communications*, vol. 3, p. 1287, 2012.

[60] C. Leatherdale, W.-K. Woo, F. Mikulec, and M. Bawendi, "On the absorption cross section of CdSe nanocrystal quantum dots," *The Journal of Physical Chemistry B*, vol. 106, no. 31, pp. 7619–7622, 2002.

[61] Y.-S. Park, A. V. Malko, J. Vela, Y. Chen, Y. Ghosh, F. Garcia-Santamaria, J. A. Hollingsworth, V. I. Klimov, and H. Htoon, "Near-unity quantum yields of biexciton emission from CdSe/CdS nanocrystals measured using single-particle spectroscopy," *Physical review letters*, vol. 106, no. 18, p. 187401, 2011.

[62] U. Bockelmann and G. Bastard, "Phonon scattering and energy relaxation in two-, one-, and zero-dimensional electron gases," *Physical Review B*, vol. 42, no. 14, p. 8947, 1990.

[63] U. Woggon, H. Giessen, F. Gindele, O. Wind, B. Fluegel, and N. Peyghambarian, "Ultrafast energy relaxation in quantum dots," *Physical Review B*, vol. 54, no. 24, p. 17681, 1996.

[64] V. I. Klimov and D. W. McBranch, "Femtosecond 1 P-to-1 S electron relaxation in strongly confined semiconductor nanocrystals," *Physical Review Letters*, vol. 80, no. 18, p. 4028, 1998.

[65] V. Klimov, D. McBranch, C. Leatherdale, and M. Bawendi, "Electron and hole relaxation pathways in semiconductor quantum dots," *Physical Review B*, vol. 60, no. 19, p. 13740, 1999.

[66] A. L. Efros, V. Kharchenko, and M. Rosen, "Breaking the phonon bottleneck in nanometer quantum dots: Role of Auger-like processes," *Solid State Communications*, vol. 93, no. 4, pp. 281–284, 1995.

[67] E. Hendry, M. Koeberg, F. Wang, H. Zhang, C. de Mello Donega, D. Vanmaekelbergh, and M. Bonn, "Direct observation of electron-to-hole energy transfer in CdSe quantum dots," *Physical review letters*, vol. 96, no. 5, p. 057408, 2006.

[68] S. Xu, A. Mikhailovsky, J. Hollingsworth, and V. Klimov, "Hole intraband relaxation in strongly confined quantum dots: Revisiting the "phonon bottleneck" problem," *Physical Review B*, vol. 65, no. 4, p. 045319, 2002.

[69] U. Woggon, S. Gaponenko, W. Langbein, A. Uhrig, and C. Klingshirn, "Homogeneous linewidth of confined electron-hole-pair states in II-VI quantum dots," *Physical Review B*, vol. 47, no. 7, p. 3684, 1993.

[70] A. I. P Michler *et al.*, "Quantum correlation among photons from a single quantum dot at room temperature," *Nature*, vol. 406, no. 6799, pp. 968–970, 2000.

[71] X. Brokmann, G. Messin, P. Desbiolles, E. Giacobino, M. Dahan, and J. Hermier, "Colloidal CdSe/ZnS quantum dots as single-photon sources," *New Journal of Physics*, vol. 6, no. 1, p. 99, 2004.

[72] B. Fisher, J. M. Caruge, D. Zehnder, and M. Bawendi, "Room-temperature ordered photon emission from multiexciton states in single CdSe core-shell nanocrystals.," *Physical review letters*, vol. 94, no. 8, pp. 087403–087403, 2005.

[73] S. Ulrich, S. Strauf, P. Michler, G. Bacher, and A. Forchel, "Triggered polarization-correlated photon pairs from a single CdSe quantum dot," *Applied physics letters*, vol. 83, no. 9, pp. 1848–1850, 2003.

[74] T. Aichele, V. Zwiller, O. Benson, I. Akimov, and F. Henneberger, "Single CdSe quantum dots for high-bandwidth single-photon generation," *Journal of the optical society of America B*, vol. 20, no. 10, pp. 2189–2192, 2003.

[75] K. Tvrdy and P. V. Kamat, "Substrate driven photochemistry of CdSe quantum dot films: charge injection and irreversible transformations on oxide surfacesâ ," *The Journal of Physical Chemistry A*, vol. 113, no. 16, pp. 3765–3772, 2009.

[76] W. G. van Sark, P. L. Frederix, A. A. Bol, H. C. Gerritsen, and A. Meijerink, "Blueing, bleaching, and blinking of single CdSe/ZnS quantum dots," *Physical chemistry and chemical physics*, vol. 3, no. 10, pp. 871–879, 2002.

[77] X. Wen, A. Sitt, P. Yu, H. chen Ko, Y.-R. Toh, and J. Tang, "Studies of the photostability of CdSe/CdS dot-in-rod nanoparticles," *Journal of Nanoparticle Research*, vol. 14, no. 12, pp. 1–13, 2012.

[78] A. Mikhailovsky, A. Malko, J. Hollingsworth, M. Bawendi, and V. Klimov, "Multiparticle interactions and stimulated emission in chemically synthesized quantum dots," *Applied physics letters*, vol. 80, no. 13, pp. 2380–2382, 2002.

[79] A. Efros, "Auger processes in nanosize semiconductor crystals," in *Semiconductor nanocrystals*, pp. 52–72, Springer, 2003.

[80] V. Klimov, A. Mikhailovsky, D. McBranch, C. Leatherdale, and M. Bawendi, "Quantization of multiparticle Auger rates in semiconductor quantum dots," *Science*, vol. 287, no. 5455, pp. 1011–1013, 2000.

[81] M. Achermann, J. Hollingsworth, and V. Klimov, "Multiexcitons confined within a subexcitonic volume: Spectroscopic and dynamical signatures of neutral and charged biexcitons in ultrasmall semiconductor nanocrystals," *Physical Review B*, vol. 68, no. 24, p. 245302, 2003.

[82] J. J. Peterson and D. J. Nesbitt, "Modified power law behavior in quantum dot blinking: a novel role for biexcitons and auger ionization," *Nano letters*, vol. 9, no. 1, pp. 338–345, 2008.

[83] I. Robel, R. Gresback, U. Kortshagen, R. D. Schaller, and V. I. Klimov, "Universal size-dependent trend in Auger recombination in direct-gap and indirect-gap semiconductor nanocrystals," *Physical review letters*, vol. 102, no. 17, p. 177404, 2009.

[84] G. E. Cragg and A. L. Efros, "Suppression of Auger processes in confined structures," *Nano letters*, vol. 10, no. 1, pp. 313–317, 2009.

[85] X. Wang, X. Ren, K. Kahen, M. A. Hahn, M. Rajeswaran, S. Maccagnano-Zacher, J. Silcox, G. E. Cragg, A. L. Efros, and T. D. Krauss, "Non-blinking semiconductor nanocrystals," *Nature*, vol. 459, no. 7247, pp. 686–689, 2009.

[86] F. García-Santamaría, S. Brovelli, R. Viswanatha, J. A. Hollingsworth, H. Htoon, S. A. Crooker, and V. I. Klimov, "Breakdown of volume scaling in Auger recombination in CdSe/CdS heteronanocrystals: the role of the core- shell interface," *Nano letters*, vol. 11, no. 2, pp. 687–693, 2011.

[87] Y.-S. Park, W. K. Bae, L. A. Padilha, J. M. Pietryga, and V. I. Klimov, "Effect of the Core/Shell Interface on Auger Recombination Evaluated by Single-Quantum-Dot Spectroscopy," *Nano letters*, vol. 14, no. 2, pp. 396–402, 2014.

[88] C. Javaux, B. Mahler, B. Dubertret, A. Shabaev, A. Rodina, A. L. Efros, D. Yakovlev, F. Liu, M. Bayer, G. Camps, *et al.*, "Thermal activation of non-radiative Auger recombination in charged colloidal nanocrystals," *Nature nanotechnology*, vol. 8, no. 3, pp. 206–212, 2013.

[89] S. Jeong, M. Achermann, J. Nanda, S. Ivanov, V. I. Klimov, and J. A. Hollingsworth, "Effect of the thiol-thiolate equilibrium on the photophysical properties of aqueous CdSe/ZnS nanocrystal quantum dots," *Journal of the American Chemical Society*, vol. 127, no. 29, pp. 10126–10127, 2005.

[90] Y. Kim, N. W. Song, H. Yu, D. W. Moon, S. J. Lim, W. Kim, H.-J. Yoon, and S. K. Shin, "Ligand-dependent blinking of zinc-blende CdSe/ZnS core/shell nanocrystals," *Physical Chemistry Chemical Physics*, vol. 11, no. 18, pp. 3497–3502, 2009.

[91] C. Burda, S. Link, M. Mohamed, and M. El-Sayed, "The relaxation pathways of CdSe nanoparticles monitored with femtosecond time-resolution from the visible to the IR: Assignment of the transient features by carrier quenching," *The Journal of Physical Chemistry B*, vol. 105, no. 49, pp. 12286–12292, 2001.

[92] P. Lodahl, A. F. Van Driel, I. S. Nikolaev, A. Irman, K. Overgaag, D. Vanmaekelbergh, and W. L. Vos, "Controlling the dynamics of spontaneous emission from quantum dots by photonic crystals," *Nature*, vol. 430, no. 7000, pp. 654–657, 2004.

[93] A. Akimov, A. Mukherjee, C. Yu, D. Chang, A. Zibrov, P. Hemmer, H. Park, and M. Lukin, "Generation of single optical plasmons in metallic nanowires coupled to quantum dots," *Nature*, vol. 450, no. 7168, pp. 402–406, 2007.

[94] X. Brokmann, L. Coolen, M. Dahan, and J. Hermier, "Measurement of the radiative and nonradiative decay rates of single CdSe nanocrystals through a controlled modification of their spontaneous emission," *Physical review letters*, vol. 93, no. 10, p. 107403, 2004.

[95] X. Brokmann, L. Coolen, J.-P. Hermier, and M. Dahan, "Emission properties of single CdSe/ZnS quantum dots close to a dielectric interface," *Chemical physics*, vol. 318, no. 1, pp. 91–98, 2005.

[96] B. R. Fisher, H.-J. Eisler, N. E. Stott, and M. G. Bawendi, "Emission intensity dependence and single-exponential behavior in single colloidal quantum dot fluorescence lifetimes," *The Journal of Physical Chemistry B*, vol. 108, no. 1, pp. 143–148, 2004.

[97] S. A. Ivanov, A. Piryatinski, J. Nanda, S. Tretiak, K. R. Zavadil, W. O. Wallace, D. Werder, and V. I. Klimov, "Type-II core/shell CdS/ZnSe nanocrystals: synthesis, electronic structures, and spectroscopic properties," *Journal of the American Chemical Society*, vol. 129, no. 38, pp. 11708–11719, 2007.

[98] S. Kim, Y. T. Lim, E. G. Soltesz, A. M. De Grand, J. Lee, A. Nakayama, J. A. Parker, T. Mihaljevic, R. G. Laurence, D. M. Dor, *et al.*, "Near-infrared fluorescent type II quantum dots for sentinel lymph node mapping," *Nature biotechnology*, vol. 22, no. 1, pp. 93–97, 2003.

[99] J. Nanda, S. A. Ivanov, M. Achermann, I. Bezel, A. Piryatinski, and V. I. Klimov, "Light amplification in the single-exciton regime using exciton-exciton repulsion in type-II nanocrystal quantum dots," *The Journal of Physical Chemistry C*, vol. 111, no. 42, pp. 15382–15390, 2007.

[100] A. Piryatinski, S. A. Ivanov, S. Tretiak, and V. I. Klimov, "Effect of quantum and dielectric confinement on the exciton-exciton interaction energy in type II core/shell semiconductor nanocrystals," *Nano letters*, vol. 7, no. 1, pp. 108–115, 2007.

[101] A. Sitt, F. D. Sala, G. Menagen, and U. Banin, "Multiexciton engineering in seeded core/shell nanorods: Transfer from type-I to quasi-type-II regimes," *Nano letters*, vol. 9, no. 10, pp. 3470–3476, 2009.

[102] J. Li and L.-W. Wang, "First principle study of core/shell structure quantum dots," *Applied physics letters*, vol. 84, no. 18, pp. 3648–3650, 2004.

[103] F. García-Santamaría, Y. Chen, J. Vela, R. D. Schaller, J. A. Hollingsworth, and V. I. Klimov, "Suppressed auger recombination in "giant" nanocrystals boosts optical gain performance," *Nano letters*, vol. 9, no. 10, pp. 3482–3488, 2009.

[104] H. Eshet, M. GruÌnwald, and E. Rabani, "The electronic structure of CdSe/CdS core/shell seeded nanorods: type-I or quasi-type-II?," *Nano letters*, vol. 13, no. 12, pp. 5880–5885, 2013.

[105] J. Müller, J. Lupton, P. Lagoudakis, F. Schindler, R. Koeppe, A. Rogach, J. Feldmann, D. Talapin, and H. Weller, "Wave function engineering in elongated semiconductor nanocrystals with heterogeneous carrier confinement," *Nano letters*, vol. 5, no. 10, pp. 2044–2049, 2005.

[106] G. Morello, F. Della Sala, L. Carbone, L. Manna, G. Maruccio, R. Cingolani, and M. De Giorgi, "Intrinsic optical nonlinearity in colloidal seeded grown CdSe/CdS nanostructures: Photoinduced screening of the internal electric field," *Physical Review B*, vol. 78, no. 19, p. 195313, 2008.

[107] N. J. Borys, M. J. Walter, J. Huang, D. V. Talapin, and J. M. Lupton, "The role of particle morphology in interfacial energy transfer in CdSe/CdS heterostructure nanocrystals," *Science*, vol. 330, no. 6009, pp. 1371–1374, 2010.

[108] R. Krahne, G. Morello, A. Figuerola, C. George, S. Deka, and L. Manna, "Physical properties of elongated inorganic nanoparticles," *Physics Reports*, vol. 501, no. 3, pp. 75–221, 2011.

[109] D. Katz, T. Wizansky, O. Millo, E. Rothenberg, T. Mokari, and U. Banin, "Size-dependent tunneling and optical spectroscopy of CdSe quantum rods," *Physical review letters*, vol. 89, no. 8, p. 086801, 2002.

[110] A. Shabaev and A. L. Efros, "1D exciton spectroscopy of semiconductor nanorods," *Nano letters*, vol. 4, no. 10, pp. 1821–1825, 2004.

[111] A. Sitt, A. Salant, G. Menagen, and U. Banin, "Highly emissive nano rod-in-rod heterostructures with strong linear polarization," *Nano letters*, vol. 11, no. 5, pp. 2054–2060, 2011.

[112] H. Htoon, J. Hollingworth, A. Malko, R. Dickerson, and V. Klimov, "Light amplification in semiconductor nanocrystals: Quantum rods versus quantum dots," *Applied physics letters*, vol. 82, no. 26, pp. 4776–4778, 2003.

[113] E. Rothenberg, M. Kazes, E. Shaviv, and U. Banin, "Electric field induced switching of the fluorescence of single semiconductor quantum rods," *Nano letters*, vol. 5, no. 8, pp. 1581–1586, 2005.

[114] R. Krishnan, M. A. Hahn, Z. Yu, J. Silcox, P. M. Fauchet, and T. D. Krauss, "Polarization surface-charge density of single semiconductor quantum rods," *Physical review letters*, vol. 92, no. 21, p. 216803, 2004.

[115] Z. Yu, M. A. Hahn, S. E. Maccagnano-Zacher, J. Calcines, T. D. Krauss, E. S. Alldredge, and J. Silcox, "Small-angle rotation in individual colloidal CdSe quantum rods," *ACS nano*, vol. 2, no. 6, pp. 1179–1188, 2008.

[116] M. Artemyev, B. Möller, and U. Woggon, "Unidirectional alignment of CdSe nanorods," *Nano Letters*, vol. 3, no. 4, pp. 509–512, 2003.

[117] A. Rizzo, C. Nobile, M. Mazzeo, M. D. Giorgi, A. Fiore, L. Carbone, R. Cingolani, L. Manna, and G. Gigli, "Polarized light emitting diode by long-range nanorod self-assembling on a water surface," *ACS nano*, vol. 3, no. 6, pp. 1506–1512, 2009.

[118] T. Wang, J. Zhuang, J. Lynch, O. Chen, Z. Wang, X. Wang, D. LaMontagne, H. Wu, Z. Wang, and Y. C. Cao, "Self-assembled colloidal superparticles from nanorods," *Science*, vol. 338, no. 6105, pp. 358–363, 2012.

[119] A. Granados del Aguila, B. Jha, F. Pietra, E. Groeneveld, C. de Mello Donegá, J. C. Maan, D. Vanmaekelbergh, and P. C. Christianen, "Observation of the Full Exciton and Phonon Fine-Structure in CdSe/CdS Dot-in-Rod Heteronanocrystals," *ACS nano*, 2014.

[120] M. G. Lupo, F. Della Sala, L. Carbone, M. Zavelani-Rossi, A. Fiore, L. LuÌer, D. Polli, R. Cingolani, L. Manna, and G. Lanzani, "Ultrafast Electron- Hole Dynamics in Core/Shell CdSe/CdS Dot/Rod Nanocrystals," *Nano letters*, vol. 8, no. 12, pp. 4582–4587, 2008.

[121] D. V. Talapin, J. H. Nelson, E. V. Shevchenko, S. Aloni, B. Sadtler, and A. P. Alivisatos, "Seeded growth of highly luminescent CdSe/CdS nanoheterostructures with rod and tetrapod morphologies," *Nano letters*, vol. 7, no. 10, pp. 2951–2959, 2007.

[122] G. Rainò, T. Stöferle, I. Moreels, R. Gomes, Z. Hens, and R. F. Mahrt, "Controlling the Exciton Fine Structure Splitting in CdSe/CdS Dot-in-Rod Nanojunctions," *ACS nano*, vol. 6, no. 3, pp. 1979–1987, 2012.

[123] G. Rainò, T. Stöferle, I. Moreels, R. Gomes, J. S. Kamal, Z. Hens, and R. F. Mahrt, "Probing the wave function delocalization in CdSe/CdS dot-in-rod nanocrystals by time-and temperature-resolved spectroscopy," *ACS nano*, vol. 5, no. 5, pp. 4031–4036, 2011.

[124] M. G. Lupo, M. Zavelani-Rossi, A. Fiore, D. Polli, L. Carbone, R. Cingolani, L. Manna, and G. Lanzani, "Evidence of electron wave function delocalization in CdSe/CdS asymmetric nanocrystals," *Superlattices and Microstructures*, vol. 47, no. 1, pp. 170–173, 2010.

[125] M. Lupo *et al.*, "Band-edge ultrafast pump–probe spectroscopy of core/shell CdSe/CdS rods: assessing electron delocalization by effective mass calculations," *Physical Chemistry Chemical Physics*, vol. 14, no. 20, pp. 7420–7426, 2012.

[126] J. Müller, J. Lupton, A. Rogach, J. Feldmann, D. Talapin, and H. Weller, "Monitoring surface charge migration in the spectral dynamics of single Cd Se/ Cd S nanodot/nanorod heterostructures," *Physical Review B*, vol. 72, no. 20, p. 205339, 2005.

[127] L. shi Li and A. P. Alivisatos, "Origin and scaling of the permanent dipole moment in CdSe nanorods," *Physical review letters*, vol. 90, no. 9, p. 097402, 2003.

[128] K. M. Ryan, A. Mastroianni, K. A. Stancil, H. Liu, and A. Alivisatos, "Electric-field-assisted assembly of perpendicularly oriented nanorod superlattices," *Nano letters*, vol. 6, no. 7, pp. 1479–1482, 2006.

[129] Y. Luo and L.-W. Wang, "Electronic Structures of the CdSe/CdS Core- Shell Nanorods," *ACS nano*, vol. 4, no. 1, pp. 91–98, 2009.

[130] A. Shabaev, A. Rodina, and A. L. Efros, "Fine structure of the band-edge excitons and trions in CdSe/CdS core/shell nanocrystals," *Physical Review B*, vol. 86, no. 20, p. 205311, 2012.

[131] S. Brovelli, R. Schaller, S. Crooker, F. Garcia-Santamaria, Y. Chen, R. Viswanatha, J. Hollingsworth, H. Htoon, and V. Klimov, "Nano-engineered electron–hole exchange interaction controls exciton dynamics in core–shell semiconductor nanocrystals," *Nature communications*, vol. 2, p. 280, 2011.

[132] I. Moreels, G. Raino, R. Gomes, Z. Hens, T. Stoferle, and R. F. Mahrt, "Band-edge exciton fine structure of small, nearly spherical colloidal CdSe/ZnS quantum dots," *ACS nano*, vol. 5, no. 10, pp. 8033–8039, 2011.

[133] G. Rainò, I. Moreels, A. Hassinen, T. Stoferle, Z. Hens, and R. F. Mahrt, "Exciton dynamics within the band-edge manifold states: the onset of an acoustic phonon bottleneck," *Nano letters*, vol. 12, no. 10, pp. 5224–5229, 2012.

[134] W. W. Yu, L. Qu, W. Guo, and X. Peng, "Experimental determination of the extinction coefficient of CdTe, CdSe, and CdS nanocrystals," *Chemistry of Materials*, vol. 15, no. 14, pp. 2854–2860, 2003.

[135] F. Pisanello, G. Leménager, L. Martiradonna, L. Carbone, S. Vezzoli, P. Desfonds, P. D. Cozzoli, J.-P. Hermier, E. Giacobino, R. Cingolani, M. D. Vittorio, and A. Bramati, "Non-blinking single-photon generation with anisotropic colloidal nanocrystals: towards room-temperature, efficient, colloidal quantum sources.," *Adv. Mater. Weinheim*, vol. 25, pp. 1974–80, Apr. 2013.

[136] S. Empedocles and M. Bawendi, "Quantum-confined stark effect in single CdSe nanocrystallite quantum dots," *Science*, vol. 278, no. 5346, pp. 2114–2117, 1997.

[137] W. Moerner and M. Orrit, "Illuminating single molecules in condensed matter," *Science*, vol. 283, no. 5408, pp. 1670–1676, 1999.

[138] W. Moerner and D. P. Fromm, "Methods of single-molecule fluorescence spectroscopy and microscopy," *Review of Scientific Instruments*, vol. 74, no. 8, pp. 3597–3619, 2003.

[139] E. Betzig and R. J. Chichester, "Single molecules observed by near-field scanning optical microscopy," *Science*, vol. 262, no. 5138, pp. 1422–1425, 1993.

[140] Ü. Mets and R. Rigler, "Submillisecond detection of single rhodamine molecules in water," *Journal of fluorescence*, vol. 4, no. 3, pp. 259–264, 1994.

[141] C. Lethiec, J. Laverdant, H. Vallon, C. Javaux, B. Dubertret, J.-M. Frigerio, C. Schwob, L. Coolen, and A. Maître, "Measurement of Three-Dimensional Dipole Orientation of a Single Fluorescent Nanoemitter by Emission Polarization Analysis," *Physical Review X*, vol. 4, no. 2, p. 021037, 2014.

[142] P. Dedecker, B. Muls, A. Deres, H. Uji-i, J. ichi Hotta, M. Sliwa, J.-P. Soumillion, K. Müllen, J. Enderlein, and J. Hofkens, "Defocused Wide-field Imaging Unravels

Structural and Temporal Heterogeneity in Complex Systems," *Advanced Materials*, vol. 21, no. 10-11, pp. 1079–1090, 2009.

[143] J. Jasny and J. Sepioł, "Single molecules observed by immersion mirror objective. A novel method of finding the orientation of a radiating dipole," *Chemical physics letters*, vol. 273, no. 5, pp. 439–443, 1997.

[144] M. Böhmer and J. Enderlein, "Orientation imaging of single molecules by wide-field epifluorescence microscopy," *JOSA B*, vol. 20, no. 3, pp. 554–559, 2003.

[145] D. Patra, I. Gregor, and J. Enderlein, "Image analysis of defocused single-molecule images for three-dimensional molecule orientation studies," *The Journal of Physical Chemistry A*, vol. 108, no. 33, pp. 6836–6841, 2004.

[146] X. Brokmann, M.-V. Ehrensperger, J.-P. Hermier, A. Triller, and M. Dahan, "Orientational imaging and tracking of single CdSe nanocrystals by defocused microscopy," *Chemical physics letters*, vol. 406, no. 1, pp. 210–214, 2005.

[147] R. Schuster, M. Barth, A. Gruber, and F. Cichos, "Defocused wide field fluorescence imaging of single CdSe/ZnS quantum dots," *Chemical physics letters*, vol. 413, no. 4, pp. 280–283, 2005.

[148] W. Lukosz, "Light emission by magnetic and electric dipoles close to a plane dielectric interface. III. Radiation patterns of dipoles with arbitrary orientation," *JOSA*, vol. 69, no. 11, pp. 1495–1503, 1979.

[149] P. A. Frantsuzov, S. Volkán-Kacsó, and B. Jankó, "Universality of the fluorescence intermittency in nanoscale systems: experiment and theory," *Nano letters*, vol. 13, no. 2, pp. 402–408, 2013.

[150] V. Klimov, J. McGuire, R. Schaller, and V. Rupasov, "Scaling of multiexciton lifetimes in semiconductor nanocrystals," *Physical Review B*, vol. 77, no. 19, p. 195324, 2008.

[151] C. Galland, Y. Ghosh, A. Steinbrück, J. A. Hollingsworth, H. Htoon, and V. I. Klimov, "Lifetime blinking in nonblinking nanocrystal quantum dots," *Nature communications*, vol. 3, p. 908, 2012.

[152] S. Vezzoli, S. Shojaii, S. Cialdi, D. Cipriani, F. Castelli, M. G. Paris, L. Carbone, P. Davide Cozzoli, E. Giacobino, and A. Bramati, "An ensemble-based method to assess the quality of a sample of nanocrystals as single photon emitters," *Optics Communications*, vol. 300, pp. 215–219, 2013.

[153] G. Nair, J. Zhao, and M. G. Bawendi, "Biexciton quantum yield of single semiconductor nanocrystals from photon statistics," *Nano letters*, vol. 11, no. 3, pp. 1136–1140, 2011.

[154] C. Bradac, T. Gaebel, N. Naidoo, M. Sellars, J. Twamley, L. Brown, A. Barnard, T. Plakhotnik, A. Zvyagin, and J. Rabeau, "Observation and control of blinking nitrogen-vacancy centres in discrete nanodiamonds," *Nature nanotechnology*, vol. 5, no. 5, pp. 345–349, 2010.

[155] X. Brokmann, *Propriétés de fluorescence de nanocristaux de CdSe individuels*. PhD thesis, Université Pierre et Marie Curie-Paris VI, 2004.

[156] M. Kuno, D. Fromm, H. Hamann, A. Gallagher, and D. Nesbitt, "Nonexponential "blinking" kinetics of single CdSe quantum dots: A universal power law behavior," *The journal of chemical physics*, vol. 112, no. 7, pp. 3117–3120, 2000.

[157] X. Brokmann, J.-P. Hermier, G. Messin, P. Desbiolles, J.-P. Bouchaud, and M. Dahan, "Statistical aging and nonergodicity in the fluorescence of single nanocrystals," *Physical review letters*, vol. 90, no. 12, p. 120601, 2003.

[158] K. Shimizu, R. Neuhauser, C. Leatherdale, S. Empedocles, W. Woo, and M. Bawendi, "Blinking statistics in single semiconductor nanocrystal quantum dots," *Physical Review B*, vol. 63, no. 20, p. 205316, 2001.

[159] I. Chung and M. G. Bawendi, "Relationship between single quantum-dot intermittency and fluorescence intensity decays from collections of dots," *Physical Review B*, vol. 70, no. 16, p. 165304, 2004.

[160] A. A. Cordones and S. R. Leone, "Mechanisms for charge trapping in single semiconductor nanocrystals probed by fluorescence blinking," *Chemical Society Reviews*, vol. 42, no. 8, pp. 3209–3221, 2013.

[161] C. Galland, Y. Ghosh, A. Steinbrück, M. Sykora, J. A. Hollingsworth, V. I. Klimov, and H. Htoon, "Two types of luminescence blinking revealed by spectroelectrochemistry of single quantum dots," *Nature*, vol. 479, no. 7372, pp. 203–207, 2011.

[162] P. A. Frantsuzov, S. Volkán-Kacsó, and B. Jankó, "Model of fluorescence intermittency of single colloidal semiconductor quantum dots using multiple recombination centers," *Physical review letters*, vol. 103, no. 20, p. 207402, 2009.

[163] J. Zhao, G. Nair, B. R. Fisher, and M. G. Bawendi, "Challenge to the charging model of semiconductor-nanocrystal fluorescence intermittency from off-state

quantum yields and multiexciton blinking," *Physical review letters*, vol. 104, no. 15, p. 157403, 2010.

[164] S. Rosen, O. Schwartz, and D. Oron, "Transient fluorescence of the off state in blinking CdSe/CdS/ZnS semiconductor nanocrystals is not governed by auger recombination," *Physical review letters*, vol. 104, no. 15, p. 157404, 2010.

[165] P. Spinicelli, S. Buil, X. Quelin, B. Mahler, B. Dubertret, and J.-P. Hermier, "Bright and grey states in CdSe-CdS nanocrystals exhibiting strongly reduced blinking," *Physical review letters*, vol. 102, no. 13, p. 136801, 2009.

[166] A. V. Malko, Y.-S. Park, S. Sampat, C. Galland, J. Vela, Y. Chen, J. A. Hollingsworth, V. I. Klimov, and H. Htoon, "Pump-intensity-and shell-thickness-dependent evolution of photoluminescence blinking in individual core/shell CdSe/CdS nanocrystals," *Nano letters*, vol. 11, no. 12, pp. 5213–5218, 2011.

[167] R. Tenne, A. Teitelboim, P. Rukenstein, M. Dyshel, T. Mokari, and D. Oron, "Studying Quantum Dot Blinking through the Addition of an Engineered Inorganic Hole Trap," *ACS nano*, vol. 7, no. 6, pp. 5084–5090, 2013.

[168] D. Strauch, "CdS: lattice parameters," in *New Data and Updates for several III-V (including mixed crystals) and II-VI Compounds* (U. Rössler, ed.), vol. 44E of *Landolt-Börnstein - Group III Condensed Matter*, pp. 99–102, Springer Berlin Heidelberg.

[169] R. Verberk, A. M. van Oijen, and M. Orrit, "Simple model for the power-law blinking of single semiconductor nanocrystals," *Physical Review B*, vol. 66, no. 23, p. 233202, 2002.

[170] C. H. Crouch, O. Sauter, X. Wu, R. Purcell, C. Querner, M. Drndic, and M. Pelton, "Facts and artifacts in the blinking statistics of semiconductor nanocrystals," *Nano letters*, vol. 10, no. 5, pp. 1692–1698, 2010.

[171] G. Messin, J. Hermier, E. Giacobino, P. Desbiolles, and M. Dahan, "Bunching and antibunching in the fluorescence of semiconductor nanocrystals," *Optics Letters*, vol. 26, no. 23, pp. 1891–1893, 2001.

[172] J. Bernard, L. Fleury, H. Talon, and M. Orrit, "Photon bunching in the fluorescence from single molecules: A probe for intersystem crossing," *The Journal of chemical physics*, vol. 98, no. 2, pp. 850–859, 1993.

[173] L. Fleury, J.-M. Segura, G. Zumofen, B. Hecht, and U. Wild, "Nonclassical photon statistics in single-molecule fluorescence at room temperature," *Physical review letters*, vol. 84, no. 6, p. 1148, 2000.

[174] M. Pelton, D. G. Grier, and P. Guyot-Sionnest, "Characterizing quantum-dot blinking using noise power spectra," *Applied physics letters*, vol. 85, no. 5, pp. 819–821, 2004.

[175] M. Pelton, G. Smith, N. F. Scherer, and R. A. Marcus, "Evidence for a diffusion-controlled mechanism for fluorescence blinking of colloidal quantum dots," *Proceedings of the National Academy of Sciences*, vol. 104, no. 36, pp. 14249–14254, 2007.

[176] T. D. Krauss, S. O'Brien, and L. E. Brus, "Charge and photoionization properties of single semiconductor nanocrystals," *The Journal of Physical Chemistry B*, vol. 105, no. 9, pp. 1725–1733, 2001.

[177] L. P. Watkins and H. Yang, "Detection of intensity change points in time-resolved single-molecule measurements," *The Journal of Physical Chemistry B*, vol. 109, no. 1, pp. 617–628, 2005.

[178] R. Verberk and M. Orrit, "Photon statistics in the fluorescence of single molecules and nanocrystals: Correlation functions versus distributions of on-and off-times," *The Journal of chemical physics*, vol. 119, no. 4, pp. 2214–2222, 2003.

[179] H. J. Kimble, M. Dagenais, and L. Mandel, "Photon Antibunching in Resonance Fluorescence," *Phys. Rev. Lett.*, vol. 39, pp. 691–695, Sep 1977.

[180] R. Loudon, *The quantum theory of light*. Oxford university press, 2000.

[181] G. Leuchs, "Photon statistics, antibunching and squeezed states," in *Frontiers of Nonequilibrium Statistical Physics*, pp. 329–360, Springer, 1986.

[182] J. Zhao, O. Chen, D. B. Strasfeld, and M. G. Bawendi, "Biexciton quantum yield heterogeneities in single CdSe (CdS) core (shell) nanocrystals and its correlation to exciton blinking," *Nano letters*, vol. 12, no. 9, pp. 4477–4483, 2012.

[183] O. A. Shcherbina, G. A. Shcherbina, M. Manceau, S. Vezzoli, L. Carbone, M. D. Vittorio, A. Bramati, E. Giacobino, M. V. Chekhova, and G. Leuchs, "Photon correlations for colloidal nanocrystals and their clusters," *Opt. Lett.*, vol. 39, pp. 1791–1794, Apr 2014.

[184] T. Sh Iskhakov, A. Pérez, K. Yu Spasibko, M. Chekhova, and G. Leuchs, "Super-bunched bright squeezed vacuum state," *Optics letters*, vol. 37, no. 11, pp. 1919–1921, 2012.

[185] J. Wang, M. S. Gudiksen, X. Duan, Y. Cui, and C. M. Lieber, "Highly polarized photoluminescence and photodetection from single indium phosphide nanowires," *Science*, vol. 293, no. 5534, pp. 1455–1457, 2001.

[186] J. S. Kamal, R. Gomes, Z. Hens, M. Karvar, K. Neyts, S. Compernolle, and F. Vanhaecke, "Direct determination of absorption anisotropy in colloidal quantum rods," *Physical Review B*, vol. 85, no. 3, p. 035126, 2012.

[187] I. Hadar, G. B. Hitin, A. Sitt, A. Faust, and U. Banin, "Polarization properties of semiconductor nanorod heterostructures: From single particles to the ensemble," *The Journal of Physical Chemistry Letters*, vol. 4, no. 3, pp. 502–507, 2013.

[188] D. B. Tice, D. J. Weinberg, N. Mathew, R. P. Chang, and E. A. Weiss, "Measurement of Wavelength-Dependent Polarization Character in the Absorption Anisotropies of Ensembles of CdSe Nanorods," *The Journal of Physical Chemistry C*, vol. 117, no. 25, pp. 13289–13296, 2013.

[189] B. T. Diroll, A. Koschitzky, and C. B. Murray, "Tunable Optical Anisotropy of Seeded CdSe/CdS Nanorods," *The Journal of Physical Chemistry Letters*, vol. 5, no. 1, pp. 85–91, 2013.

[190] B. T. Diroll, T. Dadosh, A. Koschitzky, Y. E. Goldman, and C. B. Murray, "Interpreting the Energy-Dependent Anisotropy of Colloidal Nanorods Using Ensemble and Single-Particle Spectroscopy," *The Journal of Physical Chemistry C*, vol. 117, no. 45, pp. 23928–23937, 2013.

[191] J. Avelin *et al.*, *Polarizability analysis of canonical dielectric and bi-anisotropic scatterers*. Helsinki University of Technology, 2003.

[192] A. Sihvola, "Dielectric polarization and particle shape effects," *Journal of Nanomaterials*, vol. 2007, 2007.

[193] A. H. Sihvola, *Electromagnetic mixing formulas and applications*. No. 47, Iet, 1999.

[194] C. Lethiec, F. Pisanello, L. Carbone, A. Bramati, L. Coolen, and A. Maître, "Polarimetry-based analysis of dipolar transitions of single colloidal CdSe/CdS dot-in-rods," *New Journal of Physics*, vol. 16, no. 9, p. 093014, 2014.

[195] C. Lethiec, *Emission polarisée de nanoémetteurs: excitation de plasmons sur une surface métallique*. PhD thesis, Paris 6, 2014.

[196] S. Chuang and C. Chang, "kâ p method for strained wurtzite semiconductors," *Physical Review B*, vol. 54, no. 4, p. 2491, 1996.

[197] L. Biadala, B. Siebers, R. Gomes, Z. Hens, D. Yakovlev, and M. Bayer, "Tuning Energy Splitting and Recombination Dynamics of Dark and Bright Excitons in CdSe/CdS Dot-in-Rod Colloidal Nanostructures," *The Journal of Physical Chemistry C*, 2014.

[198] A. Politi, M. J. Cryan, J. G. Rarity, S. Yu, and J. L. O'Brien, "Silica-on-silicon waveguide quantum circuits," *Science*, vol. 320, no. 5876, pp. 646–649, 2008.

[199] J. L. O'Brien, A. Furusawa, and J. Vučković, "Photonic quantum technologies," *Nature Photonics*, vol. 3, no. 12, pp. 687–695, 2009.

[200] M. Law, D. J. Sirbuly, J. C. Johnson, J. Goldberger, R. J. Saykally, and P. Yang, "Nanoribbon waveguides for subwavelength photonics integration," *Science*, vol. 305, no. 5688, pp. 1269–1273, 2004.

[201] D. J. Sirbuly, M. Law, H. Yan, and P. Yang, "Semiconductor nanowires for subwavelength photonics integration," *The journal of Physical Chemistry B*, vol. 109, no. 32, pp. 15190–15213, 2005.

[202] R. Yan, P. Pausauskie, J. Huang, and P. Yang, "Direct photonic–plasmonic coupling and routing in single nanowires," *Proceedings of the National Academy of Sciences*, vol. 106, no. 50, pp. 21045–21050, 2009.

[203] M. T. Borgström, V. Zwiller, E. Müller, and A. Imamoglu, "Optically bright quantum dots in single nanowires," *Nano letters*, vol. 5, no. 7, pp. 1439–1443, 2005.

[204] M. Heiss, Y. Fontana, A. Gustafsson, G. Wüst, C. Magen, D. O'Regan, J. Luo, B. Ketterer, S. Conesa-Boj, A. Kuhlmann, *et al.*, "Self-assembled quantum dots in a nanowire system for quantum photonics," *Nature materials*, vol. 12, no. 5, pp. 439–444, 2013.

[205] Y. Fedutik, V. Temnov, O. Schöps, U. Woggon, and M. Artemyev, "Exciton-plasmon-photon conversion in plasmonic nanostructures," *Physical review letters*, vol. 99, no. 13, p. 136802, 2007.

[206] J. Claudon, J. Bleuse, N. S. Malik, M. Bazin, P. Jaffrennou, N. Gregersen, C. Sauvan, P. Lalanne, and J.-M. Gérard, "A highly efficient single-photon source based on a quantum dot in a photonic nanowire," *Nature Photonics*, vol. 4, no. 3, pp. 174–177, 2010.

[207] V. Sallet, S. Agouram, F. Falyouni, A. Marzouki, N. Haneche, C. Sartel, A. Lusson, S. Enouz-Vedrenne, V. Munoz-Sanjose, and P. Galtier, "Structural characterization of one-dimensional ZnO-based nanostructures grown by MOCVD," *physica status solidi (b)*, vol. 247, no. 7, pp. 1683–1686, 2010.

[208] K. Postava, H. Sueki, M. Aoyama, T. Yamaguchi, C. Ino, Y. Igasaki, and M. Horie, "Spectroscopic ellipsometry of epitaxial ZnO layer on sapphire substrate," *Journal of Applied Physics*, vol. 87, no. 11, pp. 7820–7824, 2000.

[209] T. Voss, G. T. Svacha, E. Mazur, S. Müller, C. Ronning, D. Konjhodzic, and F. Marlow, "High-order waveguide modes in ZnO nanowires," *Nano letters*, vol. 7, no. 12, pp. 3675–3680, 2007.

[210] V. J. Sorger, N. Pholchai, E. Cubukcu, R. F. Oulton, P. Kolchin, C. Borschel, M. Gnauck, C. Ronning, and X. Zhang, "Strongly enhanced molecular fluorescence inside a nanoscale waveguide gap," *Nano letters*, vol. 11, no. 11, pp. 4907–4911, 2011.

[211] X. Liu, Q. Zhang, Q. Xiong, and T. C. Sum, "Tailoring the lasing modes in semiconductor nanowire cavities using intrinsic self-absorption," *Nano letters*, vol. 13, no. 3, pp. 1080–1085, 2013.

[212] M. H. Huang, S. Mao, H. Feick, H. Yan, Y. Wu, H. Kind, E. Weber, R. Russo, and P. Yang, "Room-temperature ultraviolet nanowire nanolasers," *science*, vol. 292, no. 5523, pp. 1897–1899, 2001.

[213] S. Chu, G. Wang, W. Zhou, Y. Lin, L. Chernyak, J. Zhao, J. Kong, L. Li, J. Ren, and J. Liu, "Electrically pumped waveguide lasing from ZnO nanowires," *Nature nanotechnology*, vol. 6, no. 8, pp. 506–510, 2011.

[214] G. Bulgarini, M. E. Reimer, M. Hocevar, E. P. Bakkers, L. P. Kouwenhoven, and V. Zwiller, "Avalanche amplification of a single exciton in a semiconductor nanowire," *Nature Photonics*, vol. 6, no. 7, pp. 455–458, 2012.

[215] Y. Amit, A. Faust, I. Lieberman, L. Yedidya, and U. Banin, "Semiconductor nanorod layers aligned through mechanical rubbing," *physica status solidi (a)*, vol. 209, no. 2, pp. 235–242, 2012.

[216] D. V. Talapin, E. V. Shevchenko, C. B. Murray, A. Kornowski, S. Förster, and H. Weller, "CdSe and CdSe/CdS nanorod solids," *Journal of the American Chemical Society*, vol. 126, no. 40, pp. 12984–12988, 2004.

[217] S. Gupta, Q. Zhang, T. Emrick, and T. P. Russell, ""Self-corralling" nanorods under an applied electric field," *Nano letters*, vol. 6, no. 9, pp. 2066–2069, 2006.

[218] H. Qi and T. Hegmann, "Impact of nanoscale particles and carbon nanotubes on current and future generations of liquid crystal displays," *Journal of Materials Chemistry*, vol. 18, no. 28, pp. 3288–3294, 2008.

[219] H.-S. Chen, C.-W. Chen, C.-H. Wang, F.-C. Chu, C.-Y. Chao, C.-C. Kang, P.-T. Chou, and Y.-F. Chen, "Color-tunable light-emitting device based on the mixture of CdSe nanorods and dots embedded in liquid-crystal cells," *The Journal of Physical Chemistry C*, vol. 114, no. 17, pp. 7995–7998, 2010.

[220] M. Mukhina, V. Danilov, A. Orlova, M. Fedorov, M. Artemyev, and A. Baranov, "Electrically controlled polarized photoluminescence of CdSe/ZnS nanorods embedded in a liquid crystal template," *Nanotechnology*, vol. 23, no. 32, p. 325201, 2012.

[221] C. Blanc, D. Coursault, and E. Lacaze, "Ordering nano-and microparticles assemblies with liquid crystals," *Liquid Crystals Reviews*, vol. 1, no. 2, pp. 83–109, 2013.

[222] J.-P. Michel, E. Lacaze, M. Alba, M. De Boissieu, M. Gailhanou, and M. Goldmann, "Optical gratings formed in thin smectic films frustrated on a single crystalline substrate," *Physical Review E*, vol. 70, no. 1, p. 011709, 2004.

[223] K. Becker, J. M. Lupton, J. Müller, A. L. Rogach, D. V. Talapin, H. Weller, and J. Feldmann, "Electrical control of Förster energy transfer," *Nature Materials*, vol. 5, no. 10, pp. 777–781, 2006.

[224] M. Scheibner, T. Schmidt, L. Worschech, A. Forchel, G. Bacher, T. Passow, and D. Hommel, "Superradiance of quantum dots," *Nature Physics*, vol. 3, no. 2, pp. 106–110, 2007.

[225] C.-L. Hsieh, S. Spindler, J. Ehrig, and V. Sandoghdar, "Tracking single particles on supported lipid membranes: multimobility diffusion and nanoscopic confinement," *The Journal of Physical Chemistry B*, vol. 118, no. 6, pp. 1545–1554, 2014.

[226] B. Lounis and M. Orrit, "Single-photon sources," *Reports on Progress in Physics*, vol. 68, no. 5, p. 1129, 2005.

[227] N. Gisin, G. Ribordy, W. Tittel, and H. Zbinden, "Quantum cryptography," *Reviews of modern physics*, vol. 74, no. 1, p. 145, 2002.

[228] J. L. O'Brien, "Optical quantum computing," *Science*, vol. 318, no. 5856, pp. 1567–1570, 2007.

[229] L. Biadala, F. Liu, M. D. Tessier, D. R. Yakovlev, B. Dubertret, and M. Bayer, "Recombination dynamics of band edge excitons in quasi-two-dimensional CdSe nanoplatelets," *Nano letters*, vol. 14, no. 3, pp. 1134–1139, 2014.

[230] X. Brokmann, M. Bawendi, L. Coolen, and J.-P. Hermier, "Photon-correlation Fourier spectroscopy," *Optics express*, vol. 14, no. 13, pp. 6333–6341, 2006.

[231] L. Coolen, X. Brokmann, and J.-P. Hermier, "Modeling coherence measurements on a spectrally diffusing single-photon emitter," *Physical Review A*, vol. 76, no. 3, p. 033824, 2007.

[232] L. Coolen, X. Brokmann, P. Spinicelli, and J.-P. Hermier, "Emission characterization of a single CdSe-ZnS nanocrystal with high temporal and spectral resolution by photon-correlation Fourier spectroscopy," *Physical review letters*, vol. 100, no. 2, p. 027403, 2008.

[233] J. Cui, A. P. Beyler, T. S. Bischof, M. W. Wilson, and M. G. Bawendi, "Deconstructing the photon stream from single nanocrystals: from binning to correlation," *Chemical Society Reviews*, vol. 43, no. 4, pp. 1287–1310, 2014.

[234] M. Sondermann, R. Maiwald, H. Konermann, N. Lindlein, U. Peschel, and G. Leuchs, "Design of a mode converter for efficient light-atom coupling in free space," *Applied Physics B*, vol. 89, no. 4, pp. 489–492, 2007.

[235] N. Lindlein, R. Maiwald, H. Konermann, M. Sondermann, U. Peschel, and G. Leuchs, "A new 4π geometry optimized for focusing on an atom with a dipole-like radiation pattern," *Laser Physics*, vol. 17, no. 7, pp. 927–934, 2007.

[236] R. Maiwald, D. Leibfried, J. Britton, J. C. Bergquist, G. Leuchs, and D. J. Wineland, "Stylus ion trap for enhanced access and sensing," *Nature Physics*, vol. 5, no. 8, pp. 551–554, 2009.

[237] R. Maiwald, A. Golla, M. Fischer, M. Bader, S. Heugel, B. Chalopin, M. Sondermann, and G. Leuchs, "Collecting more than half the fluorescence photons from a single ion," *Physical Review A*, vol. 86, no. 4, p. 043431, 2012.

[238] I. Gonoskov, A. Aiello, S. Heugel, and G. Leuchs, "Dipole pulse theory: Maximizing the field amplitude from 4 π focused laser pulses," *Physical Review A*, vol. 86, no. 5, p. 053836, 2012.

[239] G. Leuchs and M. Sondermann, "Light–matter interaction in free space," *Journal of modern optics*, vol. 60, no. 1, pp. 36–42, 2013.

[240] G. Alber, J. Bernád, M. Stobińska, L. Sánchez-Soto, and G. Leuchs, "QED with a parabolic mirror," *Physical Review A*, vol. 88, no. 2, p. 023825, 2013.

[241] A. Drechsler, M. Lieb, C. Debus, A. Meixner, and G. Tarrach, "Confocal microscopy with a high numerical aperture parabolic mirror," *Optics express*, vol. 9, no. 12, pp. 637–644, 2001.

[242] M. Lieb and A. Meixner, "A high numerical aperture parabolic mirror as imaging device for confocal microscopy," *Optics express*, vol. 8, no. 7, pp. 458–474, 2001.

[243] J. H. Atwater, P. Spinelli, E. Kosten, J. Parsons, C. Van Lare, J. Van de Groep, J. G. de Abajo, A. Polman, and H. A. Atwater, "Microphotonic parabolic light directors fabricated by two-photon lithography," *Applied Physics Letters*, vol. 99, no. 15, p. 151113, 2011.

[244] D. T. Schoen, T. Coenen, F. J. García de Abajo, M. L. Brongersma, and A. Polman, "The planar parabolic optical antenna," *Nano letters*, vol. 13, no. 1, pp. 188–193, 2012.

Abstract. Wet-chemically synthesized colloidal nanocrystals are promising room temperature non-classical light sources. In such structures, the strong quantum confinement of the charges induced by the small dimensions results in an atomic-like emission spectrum. Strong Coulomb interactions between the charge carriers lead to fast nonradiative relaxations of the carriers and ultimately to a sub-poissonian photon statistics. A major drawback of such nanoemitters is the blinking of their photo-luminescence, when excited the emission randomly turns on and off.

This work is devoted to the study of the optical properties of a particular type of colloidal nanocrystals, called dot-in-rods, in which a spherical Cadmium Selenide (CdSe) core is surrounded by a rod-like Cadmium Sulfide (CdS) shell. By studying single dot-in-rods at room-temperature with a confocal microscope, a complete characterization of the optical, and especially quantum optical, properties of dot-in-rods is provided for several geometrical parameters.

We first study the blinking statistics of such emitters. We show that dot-in-rods with thick shells are characterized by a reduced blinking that happens on fast timescales, typically on millisecond timescales. We demonstrate that two states of emission are involved in this blinking process. The role of the geometry of the nanostructure in the blinking process is investigated. More particularly, the delocalization of the electron allowed by the shell material is shown to play a major role in explaining the reduced blinking. We then go on with a detailed characterization of the photon statistics of dot-in-rods. A complete description of the photon statistics taking into account the blinking process is realized. The polarization of the emission is also investigated. We show that the emission polarization can be tuned by engineering the geometry, more particularly by controlling the size of the core.

Finally, we also present experiments where we couple dot-in-rods with various photonic devices. We demonstrate the possibility of excitation of a single emitter using a Zinc Oxyde (ZnO) nanowire. Guiding laser light or exciting the nanowire can efficiently trigger the emission of single photons by a dot-in-rod placed at one end of the nanowire. Using defects in liquid crystals, we also show that we are able to efficiently orientate single nanoemitters.

***Keywords**:* colloidal nanocrystals, dot-in-rods, emission intermittency, photon statistics, polarization, coupling.

Résumé. Les nanocristaux colloïdaux synthétisés par voie chimique sont des sources prometteuses de lumière non-classique à température ambiante. Ces émetteurs sont caractérisés par un fort confinement des porteurs de charge due aux dimensions nanométriques de ces structures. Cela leur confère un spectre d'émission discret de type atomique. Des intéractions coulombiennes intenses entre les porteurs de charge conduisent à des relaxations non radiatives très efficaces, ceci induit une statistique d'émission de photons sous-poissonienne. Un inconvénient majeur de ces nanoémetteurs est le clignotement de leur photoluminescence, l'émission d'une telle structure s'avère être fluctuante entre différents états d'émission.

Ce travail est consacré à l'étude des propriétés optiques d'un type particulier de nanocristaux colloïdaux, appelé cœur-bâtonnet, dans lequel un noyau de Seleniure de Cadmium (CdSe) sphérique est entouré d'une coquille de Sulfure de Cadmium (CdS) de forme cylindrique. En étudiant des particules de type cœur-bâtonnet à température ambiante avec un microscope confocal, une caractérisation complète des propriétés optiques de ces émetteurs est réalisée. L'importance de la géométrie de la structure pour expliquer les mécanismes d'émission est notamment mise en avant.

Nous étudions d'abord la statistique de clignotement de ces émetteurs. Nous montrons que les émetteurs cœur-bâtonnet avec des coquilles épaisses se caractérisent par un clignotement réduit sur des échelles de temps courts, inférieurs à quelques millisecondes. Nous démontrons que deux états d'émission sont impliqués dans ce processus de clignotement. Le rôle de la géométrie de la structure dans le processus de clignotement est étudié. Plus particulièrement, la réduction du clignotement peut être expliquée par la délocalisation de l'électron dans le matériau formant la coquille à géométrie cylindrique. Ensuite, une caractérisation détaillée de la statistique de photons des émetteurs cœur-bâtonnet tenant compte du phénomène de clignotement est réalisée. La polarisation de l'émission est également étudié. Nous montrons que la polarisation d'émission peut être controlée en changeant la géométrie de la structure, en particulier en contrôlant la taille du cœur.

Enfin, nous présentons également des expériences de couplage de ces émetteurs avec des dispositifs photoniques. Nous montrons la possibilité d'exciter un émetteur cœur-bâtonnet en utilisant un nanofil d'oxyde de Zinc (ZnO), soit par guidage d'une lumière laser ou par excitation du nanofil. Le déclenchement de l'émission de photons uniques par un émetteur cœur-bâtonnet placée à une extrémité du nanofil est démontré. Nous montrons aussi que nous sommes en mesure d'orienter efficacement des nanoémetteurs uniques en utilisant la formation controlée de défauts dans des cristaux liquides.

Mots-clés *:* nanocristaux colloidaux, coeur-bâtonnets, clignotement, statistique de photons, polarisation , couplage.

Riassunto. I nanocristalli colloidali sintetizzati chimicamente sono sorgenti promettenti di luce non classica a temperatura ambiente. Tali emettitori sono caratterizzati da un forte confinamento delle cariche grazie alle loro dimensioni nanometriche. Presentano quindi uno spettro di emissione discreto di tipo atomico. Le intense interazioni coulombiane tra le cariche assicurano un rilassamento non radiativo molto efficiente, che permette di ottenere una statistica sub-poissoniana dei fotoni emessi. Un dei maggiori inconvenienti di questi nanoemettitori è il fenomeno detto di blinking, cioé l'interimttenza della fotoluminescenza che fluttua tra diversi stati di emissione.

Questo lavoro è dedicato allo studio delle proprietà ottiche di un particolare tipo di nanocristalli colloidali, chiamato dot-in-rod, in cui un nucleo sferico di selenurio di cadmio (CdSe) è circondato da un guscio di solfuro di cadmio (CdS) di forma cilindrica. Una caratterizzazione completa delle proprietà ottice di queste nanoparticelle a temperatura ambiente è eseguita mediante una tecnica di microscopia confocale. Gli effetti della geometria della struttura per spiegare i meccanismi di trasmissione sono particolarmente evidenziati.

Dapprima la statistica di blinking di tali emettitori è studiata in dettaglio. Dimostriamo che i dot-in-rods con gusci spessi sono caratterizzati da un bilnking ridotto su scale di tempo brevi dell'ordine di alcuni millisecondi e che due stati di emissione sono coinvolti nel processo di Blinking. Quindi, il ruolo della geometria della struttura nel processo di blinking è investigato. In particolare, dimostriamo che la riduzione del blinking può essere spiegata con la delocalizzazione degli elettroni nel materiale costituente il guscio di forma cilindrica. Una caratterizzazione completa della statistica dei fotoni emessa viene effettuata, considerando il fenomeno di blinkink. Infine la polarizzazione dell'emissione è analizzata: si dimostra che la polarizzazione può essere controllata modificando la geometria della struttura, in particolare controllando la dimensione del nucleo di CdSe

Il lavoro di tesi si conclude con la realizzazione di alcuni esperimenti in cui i nanocristalli sono accoppiati a vari dispositivi. Il primo esperimento consiste nell'accoppiamento di un singolo dot in rod con un nanofilo di ossido di zinco (ZnO). L'eccitazione del nanocristallo è ottenuta tramite il nanofilo stesso che puo'comportarsi da guida d'onda passiva (per un fascio laser) o attiva (se la luminescenza del nanofilo viene eccitata). Il nanocristallo posto all'estremità del nanofilo emette quindi un flusso di singoli fotoni. Il secondo esperimento consiste nell'orientare efficacemente singoli nanocristalli utilizzando idifetti di formazione nei cristalli liquidi.

***Parole chiave**:* nanocristalli, statistica de fotoni, fotoluminescenza intermittente, polarizzazione, accoppiamento.